AFML-TR-69-129

ANALYTICAL APPROACH TO COMPOSITE BEHAVIOR

L. J. Ebert
R. J. Fedor
C. H. Hamilton
S. S. Hecker
P. K. Wright

FOREWORD

This report was prepared by the Metallurgy Department, Case Western Reserve University and was initiated under Contract F33615-67-C-1487. The principal investigator for this project is L. J. Ebert. The work is administered under the direction of the Air Force Materials Laboratory, Metals and Ceramics Division, with Maj. J. Kershaw (MAMS) as program monitor and Dr. C. T. Lynch, Chief, Advanced Metallurgical Studies Branch.

This report covers work conducted during the second year's reporting period, 1 March 1968 through February 28, 1969, and was submitted by the authors March 1, 1969.

This technical report has been reviewed and is approved.

C. T. Lynch

C. T. LYNCH
Chief, Advanced Metallurgical Studies Branch
Metals and Ceramics Division
AF Materials Laboratory

ABSTRACT

The applicability of the binary composite model has been completely generalized for any combination and arrangement of materials. This refinement has eliminated the previous restriction where only composite cylinders in which the core member would yield before the case member could be treated analytically. It was found that the residual stresses in the composite induced during cooling from fabrication temperatures needed to be analyzed and incorporated into subsequent axial loading predictions. The residual stresses, which result from dissimilar thermal expansions of the components of composites, were predicted analytically and compared to the experimentally determined values for OFHC copper core with a 4340 steel case and OFHC copper core with a maraging steel case. The effect of tensile prestraining on the residual stress states and on subsequent stress-strain behavior of binary composites and tungsten-copper filamentary composites was experimentally investigated and analytically predicted. The fabrication-induced residual stresses were sufficiently altered to cause a substantial rise in the tensile flow stress curves upon reloading. Prestrains into the elastic-plastic behavioral region were emphasized. A double concentric model was developed to assess the seriousness of the presence of an unconstrained outer surface of the models. The double concentric model can also be used to predict the behavior under axial loading of composites which contain an interaction layer or diffusion protection coating at the fiber-matrix interface. This model has been developed for both elastic and strain-hardening plastic deformation in the components of the composites. Presentation of experimental data (of double-concentric model composites) completes the verification of this approach. The elastic response of a two component composite cylinder uniformly loaded along its axis was compared analytically to a corresponding hexagonal fiber composite element. The analytical comparison of the elastic behavior of the two composite elements provided justification and identified limitations for the use of the cylindrical approximation to the hexagonal geometry for the yielding and subsequent plastic deformation of the matrix component. The comparative elastic analysis considered the micro-stress field and its effect on the composite modulus and yielding behavior. Experimental data are given for the study of end effects in prototype (50 mil tungsten wires in copper matrix) fiber composites. Composites of both 7 and 19 wires were assembled to represent loose and close packed conditions, with precut discontinuous tungsten wires being included in different numbers and geometric configurations.

TABLE OF CONTENTS

TABLE OF CONTENTS CON'T

LIST OF TABLES

LIST OF FIGURES

LIST OF SYMBOLS

ϵ_{ij}	Strain tensor
σ_{ij}	Stress tensor
$d\epsilon_{ij}$	Strain increment tensor
$d\sigma_{ij}$	Stress increment tensor
S_{ij}	Deviatoric stress tensor
dS_{ij}	Deviatoric stress increment tensor
E	Elastic (Young's) modulus
ν	Poisson's ratio
θ	First invariant of the stress tensor
J_1	First invariant of the deviatoric stress tensor
J_2	Second invariant of the deviatoric stress tensor
$\bar{\sigma}$	Effective stress
$\bar{\epsilon}$	Effective strain
$d\bar{\epsilon}$	Effective strain increment
P	Tangent modulus
m	Poisson's ratio value in the plastic region
A_c	Area fraction of the core = $\frac{a^2}{b^2}$
A_s	Area fraction of the case = $\frac{b^2 - a^2}{b^2}$
α	Thermal expansion coefficient
T	Temperature
ΔT	Temperature increment
u	Radial displacement

w	Axial displacement
B_i	Coefficients of least-square fit of uniaxial stress-strain curves
r	Radius or subscript denoting radial direction
z	Subscript denoting axial direction
t	Subscript denoting tangential direction
K	Material constant = $\frac{E}{(1+\nu)(1-2\nu)}$
N	Number of rings in the case material
a	Radius of the core component
b	Outside radius of the rough machined composite or radius of case-ring interface
f	Outside radius of the final machined composite
e	Superscript denoting elastic component
P	Superscript denoting plastic component
σ	Normal stress component
τ	Shear stress component
ϵ	Normal strain component
F	Force
M	Moment
Ki	Material constant in the plastic region = $\frac{P}{(1+m)(1-2m)}$
V_f	Fiber volume fraction
V_m	Matrix volume fraction
V_c	Core volume fraction
V_R	Ring volume fraction
V_s	Case volume fraction

θ	Subscript denoting tangential direction
t	Subscript denoting direction along the hexagon boundary
n	Subscript denoting direction normal to the hexagon boundary
y	Subscript denoting yield point

SECTION I

INTRODUCTION

The basic theme of this research study is that the actual mechanical performance of oriented fiber composite materials can be predicted accurately from entirely analytical relations once the relations themselves are developed completely and comprehensively. The important implications of the overall goal of this study become apparent immediately when one considers the cost of the composite materials, the reliability demands placed upon them, and the unforgiving inherent nature of the materials themselves.

Initial work on the project demonstrated the feasibility of the basic concept. It also revealed, however, that a number of the assumptions made in the interest of analytical simplicity could not be tolerated in development of the ultimate fundamental relations. It showed further that several important parameters neglected in the preliminary analysis played a major role in dictating actual mechanical behavior and therefore had to be taken into account.

Specifically, the initial work proved that simulation models could in fact be employed reliably to characterize actual filamentary composites. It proved further that applied mechanics techniques, suitably modified to account for combined elastic and plastic response to applied stresses as well as materials parameters could be used to rationalize rheological interactions in the composites and to identify their specific nature quantitatively. The shortcomings of the initital efforts lay primarily in the assumption of ideally plastic behaviors after the onset of plastic flow, the presence of a free outer surface in the simulation models, the neglect of the role of the ever-present residual fabrication stresses, and the neglect of fiber end-effects in the analytical developments.

On the basis of the success achieved in the initial work, the project effort was extended in an attempt to develop the fundamental relations to take account of the above-cited shortcomings of the preliminary analytical models. This work has been carried out under contract AF 33(615)-3796. This contract has now been extended, and the objectives of this extensions are outlined in Section VII of this report. The specific analytical objectives of the present effort (reported upon herein) can be placed into the following categories:

1. Analytical determination of the intensity and distribution of residual stresses developed in fiber composite materials and modification of the fundamental relations describing the rheological interactions of the composites on subsequent loading to take account of the residual stresses actually present.

2. Refinement of the analytical models to take account of the lack of ideally plastic behavior of the component materials of real fiber composites on service loading.

3. Further development of the analytical models to assess the seriousness of the presence of an unconstrained (free) outer surface of the models, and the modification of the basic relations as warranted.

4. Inclusion of fiber end-effects (broken fibers, etc.) into the analytical relations as warranted.

Significant progress has been made in attaining the above objectives in the two-year period during which the work has been under way. In particular, it is felt that the first three goals have been essentially accomplished and work on the fourth is in full-swing. The results of the first year's work on the present contract were fully reported in March of 1968 (Technical Report AFML-TR-68-71). These results, together with those contained in this document, represent a complete summary of the progress to date.

As the work progressed, it became apparent that very close interrelations existed among several of the goals of the present study which are set out uniquely above. For example, consideration of residual stress effects could not be treated comprehensively by themselves without simultaneously treating the non-ideally plastic behavior of the component materials (strain hardening). By the same token, assessment of the role of the free outer surface could not be made uniquely without considering the residual stress and strain hardening parameters. As a consequence of these interrelations, it is not possible to present the results of the work under the exact topical headings and in the order used above (and also employed in the contract work description). Rather, the results are treated topically to constitute a coherent presentation.

SECTION II

REFINEMENT OF THE BINARY COMPOSITE CYLINDER MODEL

In the attempt to characterize the complete uniaxial stress-strain behavior of composite materials, the authors have previously developed a plasticity analysis for the response of a two-member composite cylinder to axial loading conditions [1,2]. This analysis, however, was limited to certain arrangements of components to comprise the composite cylinder. In particular, only composite cylinders in which the core member would yield before the case member could be treated analytically. In addition, several simplifying assumptions were necessary to allow the determination of the stress state in the case member in the plastic behavioral region. To eliminate these assumptions and completely generalize the applicability of the analytical model to any combination and arrangement of materials, a modified method of analysis was developed.

Since the basic premise of the new method rests upon the plasticity concepts introduced previously [1], a review of the most important aspect of that development will be presented.

1. Concepts of the Plasticity Analysis

The method of plasticity analysis was tailored to the particular problem under investigation, the axial loading of a composite cylinder. The complexity of general plasticity solutions makes it advisable to simplify the method of analysis to take complete advantage of individual peculiarities of each problem such as the geometric symmetry of the composite cylinder.

The stress-strain relations postulated in Reference [1] are presented by the following equations:

$$
\begin{aligned}
d\epsilon_1 &= \frac{1}{P}\left[d\sigma_1 - m\left(d\sigma_2 + d\sigma_3\right)\right] \\
d\epsilon_2 &= \frac{1}{P}\left[d\sigma_2 - m\left(d\sigma_1 + d\sigma_3\right)\right] \\
d\epsilon_3 &= \frac{1}{P}\left[d\sigma_3 - m\left(d\sigma_1 + d\sigma_2\right)\right]
\end{aligned}
\qquad (1)
$$

where $d\epsilon$ and $d\sigma$ are the total (elastic plus plastic) strain and stress increments, and P and m are the instantaneous values of the tangent modulus and Poisson's ratio in either the elastic or plastic behavioral region. The advantages of these relations over the classical Prandtl-Reuss stress-strain relations [3-5] will be discussed subsequently.

To achieve a plasticity solution in a triaxial stress state it is necessary to postulate a universal stress-strain relationship and criteria for initial and continued plastic flow. The universal

stress-strain relation postulated in Reference [1] are the effective stress($\bar{\sigma}$) and the effective strain increment ($d\bar{\epsilon}$) as given by the following equations:

$$\bar{\sigma} = \frac{1}{\sqrt{2}}\left[(\sigma_1-\sigma_2)^2+(\sigma_2-\sigma_3)^2+(\sigma_3-\sigma_1)^2\right]^{1/2} \tag{2}$$

$$d\bar{\epsilon} = \frac{\sqrt{2}}{2(1+m)}\left[(d\epsilon_1-d\epsilon_2)^2+(d\epsilon_2-d\epsilon_3)^2+(d\epsilon_3-d\epsilon_1)^2\right]^{1/2} \tag{3}$$

Physically, these functions of stress and strain are so defined that results obtained from different loading programs can be correlated by a single curve of effective stress vs. effective strain. This curve is arbitrarily chosen as the uniaxial tension stress-strain curve of the material since it is by far the easiest to obtain experimentally. The use of total strain increments in equation (1) dictates the use of a universal stress-strain curve different from that used in conjunction with the classical Prandtl-Reuss relations. In the present development, the uniaxial stress - total strain curve is utilized whereas the uniaxial stress - plastic strain curve in conjunction with the following definition of the effective plastic strain is utilized in the classical methods [3-5]:

$$d\bar{\epsilon}_p = \frac{\sqrt{2}}{3}\left[(d\epsilon_1^p-d\epsilon_2^p)^2+(d\epsilon_2^p-d\epsilon_3^p)^2+(d\epsilon_3^p-d\epsilon_1^p)^2\right]^{1/2} \tag{4}$$

The von Mises yield criterion and the postulate of isotropic hardening are employed in all plasticity considerations to describe the onset and continuation of plastic flow under triaxial stress conditions. The reader is referred to References [3-7] for a detailed explanation of these and other commonly used yield and flow criteria.

The parameters P and m of equation (1) are determined from the effective stress-effective strain curve of a material as explained in Reference [1]. In the elastic behavioral region these parameters reduce to their elastic values, e and ν respectively.

The advantages of the use of the stress-strain relations of equation (1) become apparent when the similarity between equation (1) and Hooke's law [8] is noted. The equations are the same with P replacing E and m replacing ν. The equations of equilibrium, equations of compatibility, and boundary conditions are independent of the state of a material. Hence if the form of the stress-strain relations are also the same for elastic and plastic problems, then the mathematics of the solutions will be identical.

In principle, the known elasticity solution to any problem

can be extended to include plastic behavior by changing the values of E and ν in the solution to the parameters P and m. The problem remaining is that of determining the values of P and m that correspond to the proper plastic values. In this respect, the problem differs quite drastically from the elasticity problem since P and m are not constant. The proper values of P and m are required to obtain the correct solution for the stresses and strains in the body. P and m, however, are functions of the effective strain (or the effective stress-strain curve) which, in turn, is dependent upon the strain determined from the solution of the problem.

The problem therefore becomes one which has to be solved by an iterative technique in which values of P and m are approximated and then used to obtain a solution from which the effective strain is determined. This then leads to new values of P and m. The process is repeated until convergence is achieved, at which point the last solution will be the correct solution to the plasticity problem. Hence, a solution is achieved by the method of successive approximations much in the same manner as that utilized by Mendelson [3] who approximated and iterated the plastic strain components. It is important to note that in the present approach, one must continuously check for the onset of plastic flow with the aid of the von Mises yield criterion in order to determine whether the body is in an elastic or plastic state. A flow chart of the iterative scheme used in the present problem along with a discussion of convergence problems will be presented in a later section on the actual application of this method to experimental systems.

At this point in the description of the analytical development, an attempt will be made to categorize the present set of stress-strain equations as either total (deformation) or incremental (flow). Hereafter, the two theories will be referred to only by the names of "deformation" or "flow" in order to avoid confusion with the meaning of "total" in reference to "total strain", i.e., "total" referring to elastic plus plastic.

As shown in equation (1) the total strain increments, are functions of the stress increments. In the case of general loading, this behavior violates the postulate of flow theories which states that the plastic strain increment be a function of the current state of stress, not of the stress increment. In Appendix I it is demonstrated that the new stress-strain relations (1) do reduce to the Prandtl-Reuss relations [3] for the specific case of proportional loading. In the general loading case, the requirements of a flow theory necessitate the separate treatment of elastic and plastic strain components as described in the previous section.

However, it has been proposed by Budiansky [9] and Klivshnikov [10,11] that the predictions of the deformation theories might be correct for certain loading paths other than proportional ones.

For a more detailed discussion of the differences between the deformation and flow theories and their limits of application the reader is referred to several other publications which treat this problem in more detail [3,12,13].

From a practical viewpoint, there are many problems of engineering significance in which the loading path is close enough to proportional loading such that the small errors introduced are overshadowed by the gain in mathematical simplicity. Actual numerical examples are given by Lubahn and Felgar [14]. The deformation theory of plasticity can be used for general stress histories only if it is explicitly stated that, where unloading occurs, the problem is separated into loading and unloading parts with the unloading being characterized by Hooke's law.

In essence, the present method relates finite although not total (in this case referring to "total" as the opposite of "incremental") changes in strain to finite changes in stress. The approach in this respect is similar to that of Swainger [15]. Both methods are basically of the deformation type however, since they lead to the same basic contradictions as discussed for the Hencky deformation theory in Reference [16].

One such contradication is the theory's inability to account for neutral changes of stress. This has to be kept in mind when using the present method of anlaysis. It is therefore noted that the present method cannot be applied to problems in which the material exhibits no strain hardening, i.e., ideally plastic materials. Any change of the stress state (other than unloading) in such a material constitutes a neutral change of stress once the yield surface is reached since the state of stress cannot leave the yield surface.

Another consequence of using <u>total</u> strain increments in the stress-strain relations is their inability to predict the proper response to completely hydrostatic loading. Since the hydrostatic stress components are assumed not to influence plastic deformation, all strains in response to hydrostatic loading should be elastic. The plastic strain is zero and the effective plastic strain as given by equation (4) for flow theories is unaffected. Equation (1), on the other hand, depends on the values of P and m upon loading. These values cannot be determined in their regular manner [1] since the effective strain increment is zero. This type of loading must therefore be treated in a manner similar to that of unloading. Whenever a hydrostatic load increment is added to an existing state of stress the values of P and m have to be equated to the elastic values E and ν. The strain increments of equation (1) would therefore be completely elastic and will coincide with flow theory predictions.

2. Elasticity Solution of the Composite Cylinder

Knowledge of the complete elastic solution to a problem is of added importance when use of the above developed plasticity analysis is contemplated. The elasticity solution of a two-component composite cylinder under axial loading was achieved in closed form by Ebert and Gadd [17]. A look at the physical nature of the response of the cylinder upon the incidence of plastic flow aids in preparing the proper mathematical formalities for a complete solution.

The stress state in a composite cylinder loaded into the elastic region is presented graphically in Figure 1. Examination of the stress state shows that plastic flow will occur simultaneously across the entire core diameter, whereas it will begin at the case-core interface in the case, and then move progressively outward to the outside surface. The solution will therefore have to be able to account for the movement of a yield front through the case material.

The strain-hardening nature of the materials to be considered in this study will further complicate the situation. The problem is no longer one of the progression of a single yield front through the case (as is the situation for ideally plastic composites or thick-walled tubes), but rather it becomes one of the progression of an infinite number of "flow" fronts through the case. Each one of these flow fronts eminates from the interface when the effective strain at that point reaches any point on the effective stress-effective strain curve, since the curve is composed of an infinite number of flow fronts. The term "flow" is used to denote the flow stress of a material for a given strain rather than the initial yield stress.

If this process is envisioned as occurring in finite increments rather than infinitesimally, an additional complication becomes apparent. Each increment of radius in the case material will have a different effective strain. Its incremental Poisson's ratio (or in physical terms - its contractile tendency) and modulus will be different. Hence, each of the increments will interact (to set up transverse stresses) with one another as well as with the core. This results from the fact that the Poisson's ratio values for each will be different, and it is precisely this difference in Poisson's ratio which causes the mechanical interaction.

It is quite apparent then, that the elastic solution of the simple two-component composite cylinder could not be extended to account for the additional complexities introduced by the advent of plastic flow. An elastic solution was developed, therefore, for a composite cylinder in which the case component can be divided into N rings or increments of different elastic properties. The interaction developed as a result of axial extension of the composite cylinder would be influenced by the separate properties of the core

and each ring in the case. This solution can then be extended to include plastic response of a two-component composite with the aid of the plasticity analysis developed above.

The method of solution is one of classical elasticity theory, simplified tremendously by the axial symmetry of the composite cylinder. In brief, the equilibrium of forces equation is expressed in terms of the radial displacement with the aid of compatibility and stress-strain relations, and the resulting second order ordinary differential equation is solved utilizing boundary conditions.

It is in the application of the boundary conditions that this solution differs from that presented by Ebert and Gadd [17]. Their two-component cylinder required four boundary conditions. Hence, four equations had to be solved simultaneously for complete solution. The solution was therefore achieved in closed form which had the advantage of permitting physical rationalization of the resulting stress states. In the present case, however, there are N+1 components (the core and N rings in the case) and hence 2N+2 boundary conditions and 2N+2 simultaneous equations to be solved. For a value of N greater than three this becomes an impossible task in closed form. Since in general, N should be large, the solution of the 2N+2 simultaneous equations was achieved numerically with the aid of a Gaussian elimination method [18]. The details of this solution are presented in Appendix II along with a sample matrix of the Gaussian elimination method for N=4.

To complete the elasticity solution, the stresses and strains in the entire composite were related to the constants which were to be evaluated from the boundary conditions by the Guassian elimination method. Solution of the problem was achieved with a Univac 1108 digital computer.

3. Application of the Plasticity Solution

The extension of the elasticity solution developed above to include plastic material response is now a matter of making the proper substitutions of P and m for E and ν in the elastic solution (equation (A6)) and solving the problem by an iterative technique.

It is important to note that the uniaxial stress-strain curves of the component materials were approximated by least-square polynominal fits of the experimental data. The iterative scheme utilized in the present method is presented in Figure 2. The loading path was separated into increments by dividing the applied axial strain (which in essence controls the loading path) into a number of increments. The composite cylinder was divided into N+1 stations. These stations correspond to the radii of the core and the N rings into which the case has been divided. For each load increment and each station, steps 1 through 7 in Figure 2 were followed.

The first approximation for P and m was obtained by guessing a value of $d\bar{\epsilon}$ for each station and then computing P and m from knowledge of the uniaxial stress-strain curve of the individual components (steps 2 and 3). Note that despite the fact that there are N+1 stations, only two basic stress-strain curves are required since only two distinct materials exist. Thus, even though each station in the case might possess a different effective strain, and hence different values of P and m in the plastic behavioral region, these values are nevertheless determined from a single curve, the uniaxial tension stress-strain curve of the case material. An educated guess was made for the first, namely the corresponding axial strain increment.

Step 4 consists of the elastic-like solution (Appendix II) of the composite cylinder problem. The solution affords only the increments of stresses and strains ($d\sigma_{ij}$ and $d\epsilon_{ij}$) at all stations. Total stresses and strains have to be determined by adding these results to the existing stresses and strains at the beginning of the present load increment (step 5).

With a solution of the problem in hand, a new $d\bar{\epsilon}$ or $\bar{\epsilon}$ is calculated with the aid of equation (3) from the strains of step 4 ($d\epsilon_{ij}$). The entire iteration process will now be repeated if the newly determined $d\bar{\epsilon}$ at each station is not sufficiently close to the previous one computed at each station. The term δ in step 7 of Figure 2 controls the degree of coincidence of the two $d\bar{\epsilon}$'s. If condition 7 is met, then the next load increment will be imposed. Success of this method is naturally dependent upon convergence and the rapidity of convergence. Convergence is controlled by the four computational parameters discussed above, the load increment, the initial guess, the number of stations in the case (N), and the value of the iteration cutoff (δ).

In the present problem, the size of the load increment was found to have no effect on the entire process as long as the first step was taken to the elastic strain limit of the core. This result can be explained by the fact that both components undergo proportional or radial loading. This fact will be discussed in more detail subsequently. The fact that the first guess for the effective strain increment (i.e., the axial strain increment) was very close to the finally observed value led to rapid convergence of the entire scheme. The appropriate values for N and δ were found by respectively increasing N and decreasing δ until the answers differed by less than 0.01%. The values used for N and δ for the composite systems investigated in this study were N=5 for the small case area fraction samples, N=7 for the large case area fraction samples, and δ = .0005 for all calculations.

Close examination of the iteration scheme of Figure 2 reveals that there are two different possibilities for the calculation

of the effective stress, $\overline{\sigma}$. The one actually used in the program is shown in step 2; it is calculated from the effective stress-strain curve by knowing the value of $\overline{\epsilon}$. The other can be calculated from σ_{ij} in step 5 by the use of equation (5). The two need not necessarily be the same. In fact, the two are different until convergence to the correct solution is achieved.

Reference was made above to the fact that both components were loaded proportionally (or radially). A convenient way in which to demonstrate this is that of showing the loading path for each component in the π plane of the Haigh-Westergaard stress space. (The reader is referred to textbooks on the theory of plasticity [3-5] for the details of the construction of the loading path in the π plane). In this study it will suffice to explain that the von Mises yield criterion is represented by a circle in this plane and that proportional loading paths are represented by radial lines (hence the auxiliary name of radial loading).

Two composite cylinder systems were actually fabricated and tested. Details of the experimental procedures as well as actual testing results were explained in a previous report [2]. The composite systems consisted of an OFHC copper core and 4340-steel case in one system and an OFHC copper core and 18% maraging steel case in the other. The above developed plasticity analysis was applied to both systems and the resulting stress state for one of the OFHC copper 4340 steel composite specimens was reduced to the π -plane representation. Figure 3 and 4 show that the resulting stress path in both components was indeed radial for the application of axial loads. This is true for both elastic and plastic deformation. Elastic loading is represented by loading entirely within the initial von Mises yield locus. Plastic flow occurs as soon as this boundary is transgressed. In Figure 4, this boundary is transgressed by such a slight amount that it is not possible to detect it on the scale used for the drawing. In actuality, however, all points for axial strains greater than 0.0066 in/in are outside the initial yield locus because in the analytical calculations it was assumed that the linear curve which describes the uniaxial tension stress-strain behavior of the 4340 steel in the plastic range did have a finite slope.

In summary of the application of the analytical model to composite cylinders for axial loading, the entire stress and strain distributions in the composite were determined. Presentation of these results and their effect on the axial stress-strain behavior of the composites will not be made at this point, since it was shown previously [2] that the presence of residual stresses affect these results. Discussion of the axial stress-strain behavior for all composite systems investigated will therefore be postponed until the next section. Discussion of the detailed plasticity analysis in this section was necessitated by the fact that it serves as the basis

for the residual stress study of the subsequent section.

4. Tensile Strengths of Composite Cylinders

The analytical model described above is applicable only in the small strain region and hence cannot be utilized to predict the ultimate tensile strengths of composites in which both components are ductile. The ultimate tensile strengths were measured on the two composite cylinder systems investigated. The results will be compared to the Rule of Mixtures predictions which can be represented by the following equation:

$$\sigma_u^{COMP} = A_s \sigma_u^{CASE} + A_c \sigma_*^{CORE} \qquad (5)$$

where σ_u refers to the ultimate strength, A_c and A_s to the area fractions of the core and case respectively, and σ_*^{core} to the stress in the core at the strain which corresponds to the maximum load in the case.

The strain to achieve maximum load in uniaxial tension was observed to be approximately 2.6% for the maraging steel and 4.2% for the 4340 steel. These strains correspond to stresses of approximately 14,000 to 16,000 psi in the copper core. These values were used to determine the Rule of Mixtures predictions of equation (5) for both composite systems. The results of these predictions as well as the experimental results are shown by the dashed lines in Figure 5. It is apparent that all experimental values fall above the Rule of Mixtures predictions.

If the experimental results of the composites and the case component are extrapolated to the core, it then seems that the copper core actually carries a load of 25,000 to 30,000 psi. The increase in composite tensile strength could possibly be a result of the increased load-carrying capacity of the core resulting from the interaction between the components. However, it could also be a result of a more complex interaction which delays the onset of instability in the case component as a result of the presence of the core. In the OFHC copper maraging steel system, one composite sample (A_s=0.339) actually reached a strain of 4% before it reached its maximum load. (The full strains could not be measured because the strain gages failed). As noted above, however, the maraging steel component when tested by itself experienced strains of only 2.6% up to maximum load. These results indicated quite clearly that necking is indeed delayed in the composites.

SECTION III

RESIDUAL STRESS STUDY

The prediction of composite stress-strain behavior is dependent upon knowledge of the complete uniaxial stress-strain characteristics of the components. All factors which influence these characteristics must be understood and evaluated. Previous work by the authors [2] has shown that residual stresses which result inherently from composite fabrication procedures are among the most important of these factors.

Residual stresses in composite materials arise from the very nature of the materials, that is, the combination of two materials with vastly different physical properties into one integral unit. The fact that the component materials will most likely possess quite different thermal expansion coefficients, along with the necessity of high processing temperatures for their mechanical and metallurgical union, leads to the inevitable creation of residual stresses. The accuracy of the analytical prediction of composite behavior upon axial loading of as-fabricated composites therefore depends critically upon the successful rationalization and evaluation of the induced residual stresses.

The approach to this problem was begun with the study of the origin of residual stresses and their effect on composite stress-strain behavior in the two-component composite cylinder model described in the previous section. This model was chosen for study because of the rational stress-strain behavior analyzed previously.

Initial attempts to study residual stresses were made by experimentally measuring the stresses and incorporating these results into the analytical model for axial loading by an approximate technique. The experimental details of fabrication and testing of the composite cylinders are described in Reference [2]. The residual stresses in as-fabricated composite cylinders were determined by measuring the axial and circumferential surface strains relieved during the drilling-out of the center core component. The analysis for the interpretation of the strain data into residual stresses was developed in Reference [1]. During the present period of study the authors have developed a new analysis which yields the same results but is based on fewer assumptions, The mathematical analysis is presented in Appendix III. The method of analysis is essentially an extension of the method proposed by Sachs [20] for homogeneous materials.

The major assumption in the analysis is one of a stress-free case upon the complete removal of the core by drilling. Since the high hardness of the steel case material did not allow drilling-out of the component to justify this assumption, the stresses

remaining in the steel shells were checked by deflection techniques instead. The steel shells remaining after the removal of the copper core were split longitudinally. In all tests, no change in diameter was observed, therefore indicating that there were no remaining tangential stresses. The longitudinal stresses could not be checked since the small diameter of the shells did not allow the utilization of the standard deflection techniques. However, it is difficult to rationalize the existence of axial stresses if no tangential stresses exist.

Results of the residual stresses determined from drilling-out measurements were given in a previous report [2] for the composite systems consisting of OFHC copper-4340 steel and OFHC copper-maraging steel. The residual stresses at several geometric points in the composites are presented in Figures 6-8 for the two composite systems. The experimental values are given by the error bars and the analytical values will be discussed subsequently.

The residual stresses in both the core and case components in the composite specimens were found to be large. The residual stresses in the core were found to be tensile, while the case possessed radial tensile residual stresses and axial and tangential compressive residual stresses. These residual stresses can be rationalized from their physical origin. Upon cooling from fabrication temperatures, the core material (copper with $\alpha = 9.2 \times 10^{-6}$ in/in/°F) will tend to contract more than the case material (either 4340 steel with $\alpha = 6.5 \times 10^{-6}$ in/in/°F or maraging steel with $\alpha = 5.6 \times 10^{-6}$ in/in/°F) will permit, because the core has the higher thermal expansion coefficient. The core material will therefore be under residual tensions and the case under residual compressions. The magnitudes of the stresses as shown in Figure 6 to 8 are high enough that they would appreciably affect subsequent composite behavior upon axial loading. Therefore, a method of incorporating the as-fabricated residual stress distributions into subsequent axial loading predictions was needed. Since none existed, a suitable method was developed.

Initial efforts during this contract period were reported in Reference [2]. These efforts consisted of incorporating the measured residual stress distribution as an initial condition. The effective residual stress in each component was determined and further deformation was continued from that point on the effective stress-strain curve. This method breaks down, however, if anywhere during the fabrication history the composite was unloaded. If this were the case, then knowledge of the effective stress alone does not uniquely determine the proper position on the stress-strain curve since there are an infinity of such positions.

In the next section an attempt will be made to predict analytically the residual stress distribution and examine all other fabrication procedures which might influence the residual stress

distribution.

1. Prediction of Residual Stresses by Thermal Stress Analysis

Residual stresses in composites are the result of different thermal expansion coefficients between the two components. The incorporation of thermally induced strains into a suitable mechanics development should therefore lead to the prediction of residual stresses during cooling of the composite.

a. Elasticity Analysis

Since thermally induced strains affect only the normal strain components [21] they can be incorporated into Hooke's law in the following manner:

$$\epsilon_{ij} = \frac{1+\nu}{E}\sigma_{ij} - \delta_{ij}\left(\frac{\nu}{E}\theta - \alpha T\right) \qquad (6)$$

where α is the thermal expansion coefficient and T the temperature above some arbitrary reference temperature.

Using these stress-strain relations and the fact that T (or actually the temperature difference) now becomes the loading parameter, the elasticity problem of the creation of stresses and strains upon cooling (or negative thermal loading) of the composite cylinder can be solved.

The analysis is similar to that developed for the axial loading of a composite cylinder with two exceptions. First, the solution of the stresses and strains must be re-derived with the new stress-strain relations. Second, an additional boundary condition is required, since in this case, the axial strain increment is not known as it was for the axial loading case. This new boundary condition can be derived from the fact that the composite cylinder must meet the equilibrium of forces equation in the axial direction. In mathematical terms this means

$$\int_0^a \sigma_z^{CORE}\, r\,dr + \int_a^b \sigma_z^{CASE}\, r\,dr = 0 \qquad (7)$$

With these two changes in the solution, it is possible to determine the resultant stress and strain distribution in the composite upon cooling. The detailed elasticity solution, which as in

the previous case of axial loading is again set up for a composite with N rings in the case, is presented in Appendix IV.

The residual stresses induced in a composite upon cooling can be determined from the numerical solution of the 2N+3 boundary condition equations and the general relations for the stresses (equation (A63)) in terms of the unknown constants. Careful examination of all these equations shows that the build-up of residual stresses is a function of both the differences between the thermal expansion coefficients and the Poisson's ratio values of the individual components. Residual stresses can be avoided only if the thermal expansion coefficients of the components are identical.

As discussed in Appendix IV, a general solution to the thermal loading problem must include the elastic and physical properties of the components as functions of temperature. Only in the case where the temperature change is very small can the properties be considered independent of temperature. In this problem the temperature range over which stresses build up is much too large to permit this assumption. Inclusion of the temperature dependence of the elastic and physical properties (E, ν, and α) was handled as described below.

The entire problem of the Gaussian elimination method and the solution of the stresses and strains (equation (A63)) was programmed on the 1108 Univac Computer. The temperature of 850°F (actually 875°F for computational convenience, the level of thermal stresses generated by the extra 25° drop to 850°F being shown to be negligible) was chosen as the stress-free temperature for the OFHC copper-4340 steel compoiste system. This choice of temperature was based upon the fact that composites were tempered at 850°F for one hour. It was felt that the time at this temperature would permit complete stress relief in both components while they were at temperature. From 875° the temperature was lowered to room temperature in finite increments. At each temperature the Gaussian elimination method was used to solve the boundary equations, and all stresses and strains were determined. The elastic and physical properties were determined at each temperature from a linear approximation of available literature data on their variation with temperature. The actual values used and the appropriate references are given in Table 1.

The correct solution to this problem could be obtained only if the temperature increments were infinitesimal since the properties vary continuously with temperature. To obtain this condition the computer program was run with various temperature increments and the results of the stresses were plotted against the appropriate temperature increments. Figure 9 shows this graphical representation for the stresses in the core of an OFHC copper 4340 steel composite (A_s= 0.504). Extrapolation of the curves to zero temperature increment results in the correct elasticity solution to the problem.

This approach is equivalent to including the actual temperature variation of the properties by representing the properties as functions of temperature in all the equations of Appendix IV and then solving the problem in one step from the stress-free temperature to room temperature. The latter is a much more cumbersome process since the bookkeeping of the already involved equations of Appendix IV becomes even more complex.

Comparison of the residual stresses in the core predicted by the elasticity solution method (Figure 9) to experimental results (Figure 6) shows that the predicted axial stress is much too high. Also, from the computer solution it was found that the effective strain in the core was larger than the uniaxial elastic strain limit of the core. These results indicate that the core undergoes plastic deformation during cooling from the tempering temperature and hence the elasticity solution to the problem is not sufficiently accurate.

b. Plasticity Analysis

The results of the elasticity solution necessitate an elastic - plastic analysis of the problem. The first attempt at the solution was by a rigorous method which included mechanical and physical property variations with temperature.

(1) Incorporation of Property Variations with Temperature.

In the plastic behavior region of a material it is necessary to determine the change in the entire effective stress-strain curve with temperature along with the elastic and physical property variations. Data for all property variations with temperature were taken from the available literature. These data are presented in Appendix V along with the appropriate references. It is important to note that for the thermal loading problem, the effective stress-strain curve of the copper was approximated by three linear regions as shown in Figure 10.

The plasticity solution of this problem was attempted with the aid of the elasticity solution of Appendix IV, the iterative method for plasticity solutions graphically presented in Figure 2, and the component property data presented in Appendix V. The method of solution is very much like the one for the case of axial loading presented above. However, in the case of thermal loading, the concept of a universal stress-strain curve no longer suffices. Instead of postulating a single curve which typifies all stress states (effective stress-strain curve), it is necessary to postulate a universal surface in the three dimensional space of effective stress, effective strain, and temperature. Any given stress and strain state at any temperature can be reduced to this surface by equations (2) and (3) and knowledge of the temperature. This universal surface can be determined from experimentally measured uniaxial stress-

strain curves at various temperatures. It can be constructed from the experimental data presented in Appendix V.

The numerical solution to the plasticity problem was achieved in a manner similar to that of the elastic solution of the previous section. The stress-free temperature was again chosen as 850°F (actually 875°F) and the analysis consisted of lowering the temperature in finite increments to room temperature and computing the stress and strain states at each temperature. For each temperature (or loading) increment the properties of the temperature at the end of the increment were used. To obtain the universal stress-strain relationship, a cut was made through the effective stress-effective strain-temperature surface at that temperature. Hence, in the actual solution of the problem, the universal surface discussed above was approximated by a finite number of effective stress-strain curves at given temperatures. Figure 10 shows several of the curves for the OFHC copper at their respective temperatures.

This approximation led to difficulties in the numerical solution. As explained in Section II, the plasticity method is dependent upon the proper determination of the plasticity parameters P and m. To compute these, it is necessary to know the points on the effective stress-strain curve which correspond to the stress and strain state of the previous load increment and the stress and strain state of the present load increment. Of course, both of these have to be on the same curve because the derivations of the tangent modulus and Poisson's ratio associated with that curve are based on these points. In the case of thermal loading, however, these points are <u>not</u> on the same curve. The previous stress state was calculated at some temperature and is located on the stress-strain curve peculiar to that temperature. The new stress state which can only be different if the temperature has changed (because temperature is the loading parameter) is located on the curve peculiar to that temperature. This curve is necessarily different from the first curve. Figure 11 illustrates this problem.

In Figure 11 point A refers to the stress and strain state at the end of the first load (temperature) increment which was chosen to be 50°F. Calculation of the stress and strain state at the end of the second temperature increment (T=775°F) depends upon the calculation of P and m from the effective stress-strain curve at 775°F. However, the stress and strain state of the previous load increment cannot be correctly represented on the 775°F curve, because it is on the 775°F curve which corresponds to the same effective stress and strain as that of point A in Figure 11. P and m, however, cannot be computed without the previous load increment point. An approximation therefore has to be made to transfer the point A from the 825°F curve to the 775°F curve.

Figure 11 shows two such possible approximations, Paths 1

and 2. Path 1 corresponds to keeping the effective strain constant, and Path 2 to keeping the effective stress constant. Neither path is correct since both correspond to changing the values of either the effective stress or strain without changing the actual stress and strain distributions. Hence, the effective stresses and strains did not correlate at the end of the temperature loading path. Both paths were utilized in separate approximations to the thermal loading problem. The residual stresses predicted were virtually the same for both approximations.

The residual stresses in the core of an OFHC copper-4340 steel composite (A_s=0.504) are shown in Figure 12 as a function of the size of the temperature increment used in the analytical treatment. Similar results of calculations on the other three case area fraction composites of this composite system are presented in Table 2. Comparison of these results to the experimentally measured residual stresses (Figure 6) shows fair agreement. In most cases, however, the analytical values are higher than those experimentally measured.

A possible reason for the disagreement is the fact that at the beginning of the study the assumption of time independence of all materials was made. In the present study, the composite cylinders were cooled at an extremely slow rate (furnace cool) to avoid residual stresses which result from non-uniform cooling. It is entirely possible therefore, that as a result of this slow cooling rate, residual stresses due to differences in thermal expansion coefficients do not build up during cooling until some temperature, which could be substantially below 875°F, is reached. The slow cooling process could account for a stress relieving action, by a creep (time-dependent) mechanism, thus allowing no stress build-up. This process could easily occur in the copper since 875°F is approximately 100°F above one-half the absolute melting point, the temperature at which creep effects are known to be pronounced in metals [22,23].

The above developed thermal stress analysis would therefore be most applicable to a composite undergoing moderate cooling. A low cooling rate would introduce the creep effects discussed above while a fast cooling rate would introduce residual stresses by non-uniform cooling; neither of these effects can be treated by the above analysis.

For the purpose of the present study it was most important to determine the correct residual stress distribution in the composite (be the method experimental or analytical) in order to determine its effect on subsequent axial loading. To achieve this aim, a new semi-empirical model was developed to predict the residual stresses in composites upon cooling.

(2) Approximate Approach

The method is based on the same principles as those for the method described above. However, the mechanical properties of the composite were assumed to be equal to the room temperature properties and the thermal expansion coefficient was taken as the average of that at room temperature and that at the initial (stress-free) temperature. The empirical input was made by determining the initial temperature from the criterion of best fit of the resulting residual stress distribution to that measured experimentally. For the OFHC copper-4340 steel system and for a case area fraction of 0.329, it was found that the use of a starting temperature of 675°F gave good correlation with experimental data. This temperature was therefore utilized for all calculations for the other experimentally investigated composites of different case area fractions. For the OFHC copper-maraging steel composites it was found that the starting temperature of 575°F gave good agreement with experiment. The method of solution is the same as the one discussed above. In this case, however, the problems of contradicting effective stresses and strains are absent because all calculations are made with reference to only one curve, the uniaxial stress-strain curve of the copper at room temperature.

Before presenting actual results of this method, it is important to consider one additional fabrication procedure which influences the residual stress state in composite tensile specimens. Examination of the fabrication procedures will show that the composite specimens were not heat treated with final dimensions. They were, instead, heat treated with a diameter of 0.020" over the final test section diameter. Subsequent to the final heat treatment this extra material was machined off by the final grinding operation. For an exact solution of the residual stress state of the tensile test specimen, it is therefore necessary to determine the residual stress state in a composite cylinder of rough machining dimensions and then determine the effect of machining to final dimensions upon the existing residual stress state. The experimentally measured residual stresses are the result of both of these, since measurements were made on samples which were machined to final dimensions.

c. Residual Stress Changes Caused by Machining

Removal of the 0.020" rough machining stock necessarily changes the boundary conditions. The exact analysis of the amount of residual stress change is very similar to the Sachs type of analysis. In this case, the change in residual stresses is related to the residual stresses present prior to machining. The analysis is an elastic analysis and is presented in detail in Appendix VI.

The results of this analysis and its effect on the residual stress distribution and subsequent axial loading will be discussed

in the next section.

2. Complete Composite Cylinder Characterization

In this section all the theoretical work of the previous sections will be utilized to characterize completely the behavior of a composite cylinder upon axial loading. The approximate thermal stress analysis of Section III-2-6-(1) and the machining analysis of Section V-1-c and Appendix VI will be used to predict the residual stress state in a final machined composite tensile specimen. This residual stress state will then be incorporated into the elastic-plastic analysis of composite cylinders in axial tension discussed in Section II.

The general objective is that of combining all the above analyses into one general computer-programmed model which can predict composite response under thermal loads, machining, or axial loads, or any combination of the three.

a. Residual Stresses Resulting from Cooling

The approximate thermal loading analysis developed in Section II-1-b-(1) will be applied to the experimental composite systems of OFHC copper-4340 steel and OFHC copper-maraging steel. The thermal load increments represent the first loading step in the general program.

The composite cylinder is divided into a number of stations for bookkeeping purposes. The first station is at the case-core interface. The case material is divided into N rings. These rings are spaced at arbitrary intervals between the interface and the final test section diameter of radius f. The last ring extends from this radius to the outside radius b.

The composite with rough machining dimensions is now cooled analytically from a stress-free temperature to room temperature in certain temperature increments. At each temperature increment, the complete stress and strain distributions in the composite are calculated by the plasticity analysis developed above. The stresses and strains calculated at each increment are added to those existing at the previous increment. For the OFHC copper-4340 steel system, an initial temperature of 675°F was chosen and the temperature increment of 50°F was found to be sufficiently small to avoid appreciable error.

The stress and strain distribution at the end of this thermal loading program (room temperature) represents the residual stress and strain distribution in the composite as a result of cooling. Figures 13 and 14 present the entire residual stress distributions in two OFHC copper-4340 steel composites with case area fractions of 0.228 and 0.666 respectively. The dashed curves represent the residual stresses as a result of cooling and before final machining. It is apparent

that the stresses in the core are tensile while the radial stress in the case is tensile and the axial and tangential stresses in the case are compressive. This stress distribution is a result of the higher thermal expansion coefficient of the copper core in comparison to the steel case.

b. Consideration of Machining Effects

The next step in the general program is that of submitting the composite to an analytical removal of the outside ring in the case. As discussed above, this step would simulate the physical machining operation since the outermost ring of the composite corresponds to the amount of case material which is removed by the final grinding operation.

At the end of thermal loading in the general program all the stresses and strains are known at each station. At this point, the next load increment becomes the machining analysis described in Appendix VI. Since at the end of all loading increments the stresses and strains are added to those of the prior interval, the negative values of the machining results have to be computed in this calculation. This procedure must be followed because the stresses initially present (σ_{ij}) must be related to the stresses removed during machining (σ'_{ij}) and the stresses remaining after machining (σ''_{ij}) by

$$\sigma_{ij} = \sigma'_{ij} + \sigma''_{ij} \tag{8}$$

The present procedure is equivalent to

$$\sigma''_{ij} = \sigma_{ij} + (-\sigma'_{ij}) \tag{9}$$

The values for the two known parameters σ_r^* and σ_z^* of Appendix VI are therefore taken as the negative of the values of σ_r and σ_z at the station r=f at the end of the thermal loading. The stress and strain distribution at the end of this load increment (machining) represent the actual residual stress and strain distributions in the final machined composite tensile specimen of outside radius f.

The solid lines in Figures 13 and 14 represent the residual stress distributions calculated for the OFHC copper-4340 steel composites with A_c equal to 0.228 and 0.666 respectively. The magnitudes of the stresses in the core have been decreased from those present after thermal loading. In the case, the radial stresses were decreased (becoming zero at r=f) whereas the axial and tangential

stresses were increased in magnitude. The effect is seen to be very large for the A_s=0.228 sample where the material removed constituted a large part of the composite cross-sectional area, whereas the effect is very small for the large case area fraction specimen (A_s=0.666).

The stresses present at this point of the general loading program, as mentioned above, are the final residual stresses present in composite tensile specimens. The values of these stresses at various points throughout the composite (in the core and O.D. of the case) are presented in Figures 6 to 8 as circles for all the different case area fractions of both the OFHC copper-maraging steel composite systems. The good agreement with experimentally measured stresses is not accidental, of course, since the initial temperature of thermal loading was chosen so that these values do indeed fit the experimental values for each composite system.

c. Axial Loading

The next step in the general program is the application of axial loads (or in effect application of axial strain increments) to the composite cylinders with the existing residual stress state. It should be remembered that this stress state is fully known, since the stresses are those of the last load increment which are known at every station throughout the composite.

The problem of axial loading of composites has been solved in Section II. However, it was assumed that both the case and the core components were initially in an unloaded condition. This assumption no longer holds in the present case, since it was shown that both components are pre-loaded by the presence of residual stresses. It now becomes necessary to examine the effect that the presence of residual stresses has on the use of several of the plasticity concepts discussed previously.

(1) Use of the Effective Stress-Strain Curve

It is apparent that the thermal loading and machining have influenced the use of the effective stress-strain curves for subsequent axial loading. During thermal loading, the effective stresses and strains increase progressively in both components. To calculate these terms, use is made of the following expressions:

$$\bar{\sigma} = \frac{1}{\sqrt{2}}\left[(\sigma_1-\sigma_2)^2+(\sigma_2-\sigma_3)^2+(\sigma_1-\sigma_3)^2\right]^{1/2} \qquad (2)$$

$$\bar{\epsilon} = \frac{\sqrt{2}}{2(1+m_t)} \left[(\epsilon_1 - \epsilon_2)^2 + (\epsilon_2 - \epsilon_3)^2 + (\epsilon_1 - \epsilon_3)^2\right]^{1/2} \qquad (10)$$

where m_t is the total Poisson's ratio defined by equation

$$m_T = 1/2 - (1/2 - \nu)\frac{\sigma}{E\epsilon} \qquad (11)$$

Use of these equations is made possible by the fact that the loading path for the core is necessarily radial and the entire loading of the case is elastic.

During the thermal loading process, the effective stresses and strains of the components increase continuously along the respective effective stress-strain curves of the components up to some final value. Figure 15 shows this path for the core component of an A_s=0.228 OFHC copper-4340 steel composite. The behavior of the steel component is similar except that it remains elastic. It is important to note that as a result of the non-uniform stress distribution in the case (Figure 13) during cooling, the effective stress varies continuously throughout the case, being the greatest at the inside and decreasing towards the outside surface.

The effect of the machining operation is that of producing an actual decrease in the effective stress in the core computed by equation (2). This action constitutes unloading of the core component. Hence the actual solution of the changes of the stress states must be elastic and the change in the effective strain must be computed from elastic considerations rather than equation (10). The new effective strain was calculated as follows:

Let $\bar{\epsilon}_T$ and $\bar{\sigma}_T$ denote the effective strain and stress after thermal loading and $\bar{\sigma}_M$ the effective stress after machining, then $\bar{\epsilon}_M$, the effective strain after machining, is given by

$$\bar{\epsilon}_M = \bar{\epsilon}_T - \frac{\bar{\sigma}_r - \bar{\sigma}_m}{E} \qquad (12)$$

where E is the elastic modulus. Again, Figure 15 demonstrates what happens in the copper core after the machining operation. The steel case, on the other hand, did not experience unloading during machining. Instead, it experienced a slight increase in effective stress and strain.

Consideration of subsequent axial loading must include all of these observations. The effective stress-strain curve used for the copper core (for the A_s=0.228 specimen) must follow the path BAC of Figure 15. Hence, despite the fact that the copper core was loaded into the plastic region during thermal loading, it will exhibit an initial elastic response upon axial loading because of the unloading caused by the machining operation. The effective stress-strain curves of all the other specimens must be modified in a similar manner. The representative curve for the steel case also changes. Since the case is loaded only elastically during thermal loading and machining, the shape of the curve does not change. Only the starting point on the curve is different. It will correspond to whatever the values of the effective stresses and strains are at that instant. The only effect this will have upon subsequent axial loading is that of shortening the elastic behavioral region of the case, that is, yielding will occur at a strain lower than that with no residual stresses present.

(2) The Question of Proportional Loading

In the axial loading analysis of Section II it was found that both components of the composite experienced proportional loading during the entire application of axial loads as shown in Figures 3 and 4. The nature of the loading path for combined thermal loading, machining, and axial loading needs to be examined. As discussed previously, the core is necessarily loaded proportionally. The case, however, presents a different problem. Reduction of the thermal loading analysis to the geometrical representation in the π -plane indicates that the case also experiences proportional loading during cooling. The actual physical situation must now be considered to understand what happens during subsequent axial loading.

After thermal loading (and machining) the stresses in the case are given in Figure 13. It is apparent that the radial stress is the largest principal stress (σ_1), the axial stress is σ_2 and the tangential stress σ_3 . On subsequent axial loading the axial stress will eventually change from compression to tension. The radial stresses will increase slightly (however, σ_r at r=f must remain zero), and the tangential stresses will become more negative. Hence, there will be some applied strain at which the axial stress becomes σ_1 (this strain will vary for different stations in the case), and the radial stress σ_2 , while the tangential stress remains σ_3. With this type of variation the stress path can obviously not be proportional. It is important to note, therefore, that upon yielding of the case material, the present plasticity analysis is only an approximation to the actual behavior since the flow theory discussed in Section II would have to be used. As pointed out in references (5) and (14), however, the deformation and flow theories are sufficiently close for engineering predictions if the stress path is not drastically different from proportional loading. It will be shown subsequently

that the actual stress path for the composite case is not drastically different from a proportional loading path.

In general loading situations, the effective stresses and strains must be determined from equations (2) and (10) at each loading increment. Determination of $d\bar{\sigma}$ and $d\bar{\epsilon}$ at each increment and addition to the previous values of $\bar{\sigma}$ and $\bar{\epsilon}$ does not necessarily lead to the correct values.

(3) Computational Procedures

With the consideration of the concepts described above it is now possible to study the axial loading of composite cylinders containing residual stresses.

The axial strain was applied analytically to the composite in certain increments. The first increment was taken to be equal to the effective strain which was relieved during machining (Line BA in Figure 15). From this point to the onset of yielding in the case, the increment was taken as 0.0002 in/in. The small increment used during the yielding of the case was necessary because the present analysis is only an approximation to the flow theory in this region. All other computational parameters and mechanical properties used were the same as those used for the axial loading analysis of Section II. As in the case of thermal loading and machining, the stresses and strains were computed at each increment and added to the existing stress and strain states. The corresponding effective stresses and strains were computed with the aid of equations (2) and (10).

Inclusion of axial loading concludes the general program designed to predict composite behavior. The general computer program is presented in Appendix VII. It is presented (without the actual print-out of results) for the sake of completeness. It is important to mention that the program is set up to solve any of the three problems of thermal loading, machining, or axial loading of composites separately or in any combination by the substitution of appropriate data cards. It is also generalized to include variation of properties with temperature.

This computer program, therefore, achieves the main objective of the cylindrical composite study - the prediction of composite response to an applied load from knowledge of the uniaxial stress-strain properties of the basic components and knowledge of the fabrication history.

3. Application of General Model to Present Composite Systems

The computer programmed model was used to predict the residual stresses as a result of fabrication (cooling and machining) and to predict the composite response to subsequent axial loading

for all the composite systems experimentally investigated and reported previously [2]. For each composite cyclinder the entire stress and strain distributions were calculated at a number of stations throughout the cross section of the composite. These calculations were made at all loading increments, each of which included the inputs from thermal loading from the initial temperature to room temperature, the machining operation, and all the increases in applied axial strain.

Representation of all these data is impossible because of their voluminous nature. Only a few typical representations of the theoretical results for some of the composite cylinders are presented. These representations are shown in Figures 16 to 26 and they will be used subsequently to explain the composite behavior. The rest of the data will not be presented. Only the results of the final composite axial stress-strain behavior and transverse strain behavior will be presented for each composite specimen experimentally tested. These two representations of the composite behavior are those which are experimentally measurable and, in fact, have been presented for all the composite sytems in Reference [2].

a. Discussion of Analytical Results

Figures 16 to 18 represent the stress paths in the π-plane. Figure 16 represents the copper core of an OFHC copper-4340 composite (A_s=0.228). The illustration shows that the loading is radial (proportional) in the core during thermal loading, machining, and subsequent axial loading. It also shows the precise effect of the machining on the stress state after temperature loading. The subsequent axial loading is represented by a series of points which correspond to different applied axial strain.

Figure 17 represents the loading path in the 4340 case material for the same composite system. It can be seen that the loading path during the thermal loading is indeed radial. The effect of the machining operation is too small to be detected on this particular representation. Application of axial loads is seen to change the direction of the stress path so that the loading is no longer radial. This result is caused by the relative change in magnitudes and sign of the principal stresses upon axial loading. This change also necessitated the labeling of the axes as S_z, S_r, and S_t rather than S_1, S_2, and S_3. Again the axial loading path is represented by a number of points corresponding to particular applied axial strains.

Figure 18 represents the same type of diagram for the case component of an OFHC copper-maraging steel composite (A_s=0.502). Its interpretation is the same as the one for the 4340 case.

Figure 19 shows the theoretical predictions of the axial and transverse stresses in the copper core of an OFHC copper-4340

steel composite (A_s=0.228) for the entire loading program. Thermal loading is represented on the horizontal axis as ΔT (where ΔT refers to the difference from the reference temperature-taken as zero for room temperature). During thermal loading the transverse stresses and the axial stress increases as shown. The drop in the curves at the zero point on the axis represents the effects of the machining operation. The right hand side of the graph demonstrates what happens to those stresses upon subsequent axial loading. Both stresses increase up to a strain of approximately 0.0065 in/in at which point the transverse stresses remain essentially constant. This effect is caused by the yielding of the case material which, upon attaining the plastic behavioral region, increases its instantaneous Poisson's ratio toward that of the copper, thus eliminating further interaction.

The dashed curve in Figure 19 represents the uniaxial stress-strain curve of the copper core. For the Rule of Mixtures prediction, it is this curve which represents the behavior of the copper core. It is assumed for those predictions that there are no transverse stresses present. The accompanying curves representing the analytical predictions show how erroneous this assumption is. It is apparent that the axial stress in the core is much larger than that predicted by the uniaxial curve. The copper core will therefore contribute a greater stress to the composite behavior than would be predicted by the Rule of Mixtures assumption.

Figure 20 shows the same type of representation for the 4340 steel case of the same composite cylinder. The axial stress is negative during thermal loading and constant across the case cross section. The tangential stress is also negative, but it varies from the interface to the outside diameter, being greatest at the interface. The radial stress, not shown on the diagram, is zero on the outside surface and positive throughout the remainder of the case. The effect of machining is again illustrated. Both the axial and tangential stresses decrease during machining. During subsequent axial loading the axial stress changes from compression to tension after a certain amount of axial strain. At the incidence of plastic flow in the case, the axial stress actually splits into an infinite number of curves. This is caused by the non-uniform elastic stress distribution (σ_t and σ_r) in the case. The inside radius of the case experiences the highest effective stress and hence yielding will occur first at that point. As soon as yielding occurs, of course, the representative axial stress-strain curve behaves plastically. At this point the outside of the case is still elastic, and hence its stress-strain curve will still rise in an elastic manner until the yield front reaches the outside. The resulting split in the axial stress is shown for the inside and outside diameters in Figure 20.

The tangential stress in the case, Figure 20, is necessarily

non-uniform for all loading regions. The values at the I.D. and O.D. are shown for all three stages of loading. The magnitude of the stresses is seen to increase during all stages except at the yield point of the case, the stresses staying relatively constant since there is very little additional interaction. Again, as for the core component, the dashed line represents the uniaxial tension curve in the component.

The axial stress curve, for the case material of the composite is seen to be drastically different from the uniaxial curve of that material. Unlike that in the core material, the axial stress in the case in the composite is lower than the stress taken from the uniaxial curve of the case material. The interactions during thermal loading act to lower the contribution of the case to the overall composite stress-strain curve. Hence, as in the situation of axial loading alone, the effect on the composite behavior will be a balance between a large ameliorating effect in the core and a large weakening effect in the case. Numerical results will be discussed in the next section.

The transverse stresses are found to be essentially equal to one half the magnitude of the axial stresses.

Figures 21 and 22 show the similar results of an OFHC Copper-4340 steel composite with a large case area fraction (A_s=0.666). The magnitude of the stresses in the core is higher than that of Figure 19. The effect of machining is seen to be small because of the large diameter of the specimens. The transverse stresses in the case are lower than those of Figure 20. However, the values of the stresses at the I.D. and O.D. are split to a much larger extent since the case is much larger in diameter. Hence there is a greater strain range over which yielding takes place in the case material.

The behavior of the composite cylinders with maraging steel cases is similar to that of composites with 4340 steel cases. However, it is important to note that while the interaction virtually ceases upon yielding of the 4340 case, the interaction decreases only slightly for the OFHC copper-maraging steel composites because of the high strain-hardening rate in the maraging steel in the small strain range under investigation.

The previous representation of the analytical data demonstrated that the transverse stresses in composite cylinders were indeed very large, and that the axial stress was very different from that derived from the uniaxial stress-strain curves in the components. The next series of graphs (Figures 23 to 26) will present the effective stress in both components during all stages of loading and compare it to uniaxial stress-strain curves of the components.

The effective stress of a material under a general stress

state gives an indication of the yielding behavior of the material. Once the effective stress in a material reaches the value of the uniaxial yield stress in tension, plastic flow will occur. Figure 23 presents the effective stress in the copper core for an OFHC copper-4340 steel composite. From the uniaxial stress-strain curve of the copper, it can be determined that the yield stress (actually the proportional or elastic limit) is 3200 psi. Upon thermal loading (cooling) this stress is not reached until T is the equal of 400°F. The response of the copper is elastic to this point, and plastic thereafter. During machining the effective stress decreases since the core is, in effect, unloaded. From the postulate of isotropic hardening, the effective stress at the end of the thermal loading becomes the new elastic limit of the copper; that is, upon subsequent loading the copper will behave elastically until this value of effective stress is reached. Therefore, upon axial loading, the initial response is elastic up to this stress and plastic thereafter. For any given axial strain, the effective stress is greater than the stress in uniaxial tension. This behavior indicates that the effective strain is always greater than the applied axial strain and therefore yielding or flow would always occur prematurely. Note that for axial loading, the curve labeled $\overline{\sigma}$ is the curve of $\overline{\sigma}$ vs. $\overline{\epsilon}_z$, not $\overline{\sigma}$ vs. $\overline{\epsilon}$. If $\overline{\sigma}$ were plotted against $\overline{\epsilon}$ the resulting curve would necessarily be identical to the uniaxial stress-strain curve.

Figure 24 shows the similar curves for the 4340 steel case material of the same composite. The effective stress again increases during thermal loading. In the case material, the effective stress varies continuously across the case cross section. This behavior is a result of the non-uniform transverse stress distribution in the case. Figure 24 shows the effective stresses at the I.D. and the O.D. of the case. The stress at the I.D. is higher because of the nature of the transverse stresses. It is also apparent that the entire response during thermal loading is elastic since the elastic limit in uniaxial tension (183,000 psi) has not been reached. The stress change during machining is slightly positive.

Upon the application of axial strain the peculiar behavior shown in Figure 24 occurs. The effective stress increases very slowly at first and then rapidly as further axial straining occurs. In fact, there is a slight decrease in the effective stress upon initial application of axial strain. This peculiar behavior is a result of the rapidly changing relative magnitudes of the three principal stresses which corresponds to the abrupt change in the loading direction as shown in the π-plane representation of Figure 17. The relative change in the magnitudes becomes stabilized once the axial stress in the case becomes positive at a strain of 0.14% (see Figure 20). At this point the effective stress starts increasing at a rate close to that of the uniaxial stress. It is important to note that the entire behavior during this region is elastic since the elastic limit in uniaxial tension has not been reached. Figure 24 shows that this

stress is reached at a lower strain than that predicted for uniaxial tension since the effective stress of the case is larger than that predicted for uniaxial tension. It is also apparent that yielding will occur at a lower strain at the I.D. of the case than at the O.D. since the effective stress is higher at the I.D. Note, however, that during the elastic axial loading the effective stresses at the I.D. and O.D. have approached closer together than their original split after machining. Because of this effect it is impossible to apply the difference in the effective stresses as calculated from the experimental residual stress measurements to predict the onset of yielding in the case without going through the entire loading analysis.

Figure 23 and 24 also contain curves labeled S_z^D. These curves represent the deviatoric component of the axial stress. They are therefore similar to the axial stress curves in Figure 19 and 20. They are, however, much closer to the uniaxial curves since in the formulation of the deviatoric stress the hydrostatic component of the stress tensor is subtracted from the stress tensor, i.e.,

$$S_{ij} = \sigma_{ij} - 1/3\ \delta_{ij}\ \sigma_{KK} \qquad (11)$$

These curves show that the hydrostatic component of stress developed during thermal loading was large since the deviatoric curves upon subsequent axial loading are close to those of the uniaxial deviatoric curves.

Figure 25 and 26 represent the same analytical predictions as Figures 23 and 24 except they were calculated for the large case area fraction of 0.666. The behavior of the copper core is very much like the one of Figure 23. The case material (in this composite representing the bulk of the composite cross section) shows the large split in the effective stress between the I.D. and the O.D. of the composite after thermal loading. It again shows the peculiar behavior upon axial loading described previously, and the subsequent narrowing of the split between the I.D. and the O.D. Yielding in the case at the I.D. is seen to occur at an appreciably lower strain than at the O.D. or the uniaxial prediction.

b. Comparison to Experimental Results

All the theoretical predictions of the previous section will now be incorporated into predicting the average axial composite stress-strain behavior and the composite transverse strain behavior for all the composite systems investigated. The experimental results were reported earlier in the overall program [2]. The mechanical property data for the constituent composite materials are repeated in Table 3. The experimental data represented in terms of composite

axial stress-strain curves for both composite systems and all components are also repeated in Table 3. The experimental data represented in terms of composite axial stress-strain curves for both composite systems and all components are also repeated from Reference [2] in Figures 7 to 41.

In the previous work [2] the experimental results were compared to Rule of Mixtures predictions and analytical predictions which included only an approximate residual stress correction. Both the Rule of Mixtures and analytical predictions were found to be inadequate in predicting axial stress-strain behavior. The initial totally elastic composite response region observed experimentally could not be predicted by the analytical model. Predictions for the composite behavior upon the yielding of the case material were also in error (see Reference 2).

Examination of the transverse strain behavior, however, showed excellent agreement between experiment and the analytical model and also demonstrated the inadequacies of the Rule of Mixtures prediction for this type of representation.

In this section, the experimental results will be re-examined in light of the newly developed analytical model which incorporates the entire fabrication effects into axial loading predictions.

(1) OFHC Copper-Maraging Steel Composites

The OFHC copper-maraging steel composite cylinders which were processed to case area fractions of 0.339 and 0.502 will be considered first. The predictions of the general analytical model are presented along with the experimental data in Figure 28. The present analytical model incorporates residual stresses and hence predicts the premature yielding in the case which is observed experimentally. The composites also experienced an entirely elastic initial region. This region is indicated in Figure 28 by the change of slope of the stress-strain curves. Analytical agreement in this region will be discussed in the section on OFHC copper-4340 steel composites since the behavior in that system was identical to the presently investigated system and more data are available.

The general analytical model predicted transverse strain behavior which is slightly in excess of that predicted by the previous analytical model*. The new predictions, however, were so close to the previous ones (<1%) that the curves represented in Figures 30 and 31 were not redrawn. The agreement between experiment and analytical predictions for this representation is therefore still excellent.

*The analytical predictions of the transverse strain behavior in Figures 30, 31, and 38 to 41 were taken from Reference [2].

(2) OFHC Copper-4340 Steel Composites

The general analytical predictions along with experimental stress-strain curves are presented in Figures 33 to 36 for the four different case area fractions studied. The agreement up to the yielding of the case is again excellent. There is a slight discrepancy in the initial response. It was observed that the experimental curves displayed a larger elastic-elastic interaction region than was analytically predicted. Recalling previous discussions, the only reason for any elastic response in the copper is the unloading of the copper core during final machining.

Consideration should be given to this discrepancy. Figure 42(a) shows the analytical predictions of the extent of the totally elastic strain region. The experimentally observed values are shown by the error bars. The dashed line in the illustration represents the extent of the elastic strain region which should be observed if no residual stresses were present at all (the Rule of Mixtures prediction). It naturally is not a function of the case area fraction since the copper would yield at its uniaxial strain limit. It is interesting to note that the analytical model predicts only a very minute elastic region for the case area fraction of 0.666 because of the insignificant effect of the machining operation for this composite. Although it cannot be detected in Figure 36 because of the large scale of the drawing, the initial portion of the recorded load-strain curve did indeed show a very small region of high slope before changing to the slope shown in Figure 28.

Comparison of the analytical model and experiment in the region of plastic behavior in the core and elastic behavior in the case can also be made by computing the secondary modulus of the stress-strain curves of the composite. Analytical predictions are compared to experimental results for this type of representation in Figure 42(b) and the agreement is favorable.

The agreement of the analytical predictions of the region in which the case yields is not favorable, as can be seen from Figures 33 to 36. Analytical calculations in general predict a somewhat larger yield strain and a much flatter slope of subsequent composite behavior.

Immediately, the question of the applicability of the present plasticity analysis on the basis of its deformation type nature arises. It was stated previously that the stress path is not radial for axial loading of the case subsequent to thermal loading and machining. It was also noted, however, that the error introduced is not expected to be of engineering significance. The fact that the same plasticity analysis led to excellent results for the maraging steel composite systems lends credence to the assumption that

a deformation theory is sufficiently accurate for its present application to composite cylinders.

Other reasons for the lack of agreement must be sought. It was explained previously that the flat portion of the uniaxial stress-strain curve of the 4340 steel was approximated by a line with a small, but non-zero slope. Again, this assumption could only lead to insignificant errors.

The underlying problem is much more complex. It is, in fact, the basic assumptions of continuum mechanics which must be questioned in order to explain the observed discrepancy. In continuum theories of plasticity, it is assumed that all deformation is homogeneous and hence the actual fundamental nature of the process of plastic flow is ignored.

As will be explained subsequently, the assumption of homogeneous deformation cannot be made for the initial plastic flow behavior of the 4340 steel in the condition in which it existed in the composites. Continuum mechanics predicts the circular yield fronts propagate through the case material. Axial symmetry is maintained, and the case is composed of a number of homogeneous regions behaving either plastically or elastically. In contrast to this, experiments on steel which undergo the same type of yield point elongation behavior as the presently investigated 4340 steel have shown that yielding actually occurs by a completely non-homogeneous propagation of slip bands, the so-called "Lüders bands" [14]. In tensile tests on flat specimens these bands appear at approximately 45° to 55° to the tensile axes. They have been observed to initiate at several points along the test length and propagate over the rest of the specimen length at constant load. Farnell [24] has shown by hardness measurements of partially-yielded tensile test specimens that irrespective of the amount of total yield observed in the specimen, the strain in each Lüders band was equal to the strain at the end of the yield plateau. The rest of the material remained in an elastic state. When the Lüders bands had propagated through the entire specimen length the load would rise again.

In the present system, however, even if the over-simplified notions of circular yield fronts is retained, the situation is quite different. Yielding occurs over only part of the load carrying cross section as the case remains elastic and the core material strain hardens plastically. The load will therefore not remain constant as in the uniaxial tensile test, since the elastic case and the core are able to sustain further loads. Extending the above experimental observations that the strain in the yielded case region is at the end of the yield point plateau, then further loading will force the strain in the region on to the strain hardening portion of the curve (see Figure 32). This behavior could account for the

fact that the experimentally observed composite behavior has an appreciable slope in the yielding region of the case as seen in Figures 33 to 36.

The behavior explained above cannot be incorporated into the analytical model, since the strain in the yeilded case does not increase according to the effective stress-strain curve but rather immediately becomes equal to the strain at the end of the yield point plateau, by non-homogeneous deformation.

In actuality, the yielding in the case does not propagate in circular fronts. Steele and Eichenberger [25] have shown that for an internally pressurized thick-wall tube, the Lüders bands propagate in the form of spikes asymmetrically located around the cylinder, and moreover, these Lüders bands penetrate to various depths into the cylinder wall. The mode of yielding in the composites under study is probably very similar to, but even more complex than, that in the tube.

It is interesting to note that Steele and Eichenberger observed that yielding in the cylinder occurred earlier than theoretical predictions (based on continuum plasticity theory) indicated and that the circumferential strains measured at the O.D. of the cylinders were actually close to theoretical predictions.

These results appear to be (at least) a partial explanation for the fact that in all cases the theoretical yield strain was larger than the experimentally observed strain, and that the experimental transverse strain behavior was predicted quite accurately by the model despite the discrepancy noted in the axial stress-strain behavior.

4. Variation of Composite Residual Stresses by Tensile Prestraining

It does not suffice only to understand and evaluate the residual stresses and their effects on subsequent axial loading of "as fabricated" composites. Once the controlling parameters are known, efforts must be made to change the residual stresses so as to utilize their existence in the optimization of composite materials behavior.

During the first year of the present contract, efforts were expended to achieve this aim by subjecting "as fabricated" materials to various amounts of tensile prestraining, followed by unloading and subsequent reloading. Subsequent loading curves were observed to be much higher than the initial ones. Changes in the actual residual stress distribution in composite cylinders were measured experimentally by drilling-out composite specimens which had been prestrained and unloaded. The analytical model for axial loading was then corrected for this residual stress state. However, as shown earlier in

this report, it is not possible to account unambiguously for the presence of residual stresses by this method if unloading has occurred anywhere during the history of the specimens. Since, in this case, unloading has occurred, the inability to predict subsequent stress-strain behavior, as was shown in Reference [2] is not suprising. The experimental work has shown, however, that mechanical prestraining has the potential to provide a material with properties above that originally envisioned.

It is the objective of this section of the study to develop an analytical procedure to account for the tensile behavior of a prestrained composite and to show that mechanical prestraining can be utilized practically to provide an ameliorating influence. In pursuit of this objective, this section will be divided into two parts. In part (a) an attempt will be made to predict the stress-strain behavior of prestrained binary composites by extending the analytical model described previously in this report. In part (b) prestraining of copper-tungsten filamentary composites will be investigated experimentally and analytically. While it has already been established in Reference [1] that prestrains into the plastic-plastic region of the tensile stress-strain behavior are beneficial for filamentary composites, the lack of ductility of the more practical fibers precludes this degree of prestrain. As a result, prestrains into the elastic-plastic behavioral region will be investigated fully to indicate whether this technique has any real practical significance. In addition an attempt will be made to apply the analytical model, developed for the two member cylindrical composites, to rationalize the behavior of filamentary composites.

a. Cylindrical Composite Behavior

In order to predict the behavior of prestrained composites, the entire loading history of the composite must be followed. This means that the stress-strain distribution must be followed analytically from cool-down from fabrication temperature, through the axial prestrain and unloading from the prestrained state, and finally through subsequent axial loading. The previously described model can be used to predict the behavior up to the end of the axial prestrain. However, a complexity arises during unloading from the prestrained state which requires the development of an extended analytical model.

McDanels, et al [19] appear to be the first to observe that upon removal of an applied axial load that the composite acts first in a fully elastic manner and then continues to unload with the matrix deforming in compression. This behavior is illustrated in Figure 43 for the copper-tungsten system. Baker [26] and Baker and Cratchley [27] qualitatively discussed this peculiar unloading behavior in analyzing the low cycle fatigue and damping properties of aluminum-silica (fiberglass) composites. Their interpretation of this cyclic loading behavior is schematically represented in Figure 44. It was assumed that

aluminum and silicon possess the same elastic modulus and that aluminum flows in an ideally plastic manner.

Upon loading, as seen in Figure 44, the silica deforms elastically along OA; the matrix elastically along OB and then plastically along BC. The composite loading curve can be approximated by two straight lines O'B' and B'C'. On unloading from A, the silica will return along AO; the matrix initially deforms elastically along C to D, at which point the load on the matrix is zero while that on the fibers is given by DP. On further unloading beyond D, the matrix continues to deform elastically along DE until at E it yields in compression. From E the matrix deforms plastically again along EF.

The composite unloading curve consists first of the line C'D'E', which is parallel to the initial all elastic slope O'B', and then the line E'F' (parallel to B'C') which represents the elastic-plastic region. When the load is completely removed at F', there is a permanent set O'F' on the system. Considering the two components separately at this state there exists a tensile stress on the fibers given by QB balanced out by a compressive stress QF on the matrix which makes the overall stress on the system zero.

The above analysis is not sufficient to account for the unloading behavior of practical metal-matrix composites. An accurate analytical model must consider the very pronounced Bauschinger effect and subsequent strain hardening behavior exhibited by typical metal matrices when exposed to reversed plastic stress. For example, Lubahn [28] has shown that the Bauschinger effect is very pronounced for pure copper, and such behavior would have a marked influence in composites in which the matrix has these characteristics. The model developed earlier in this report considers strain hardening only from the standpoint of monotonic loading. More particularly, the isotropic hardening loading function used in this analysis cannot be used when the Bauschinger effect is present. Thus, before the stress-strain behavior of prestrained composites can be predicted accurately, a refinement of this model is necessary. To find the stress state after unloading, a loading function which considers the Bauschinger effect and subsequent strain hardening must be used. Once the unloaded stress state is known, the model can be further extended in a similar fashion to compute the subsequent loading behavior.

(1) Loading Functions

The onset of plastic flow for each component during actual loading (or unloading) is determined in this study by the von Mises yield criterion. Once the material has exceeded the yield stress a loading function or work hardening law is required to describe continued plastic flow.

One of the major problems in the theory of plasticity is

that of describing the behavior of work hardening materials for complex loading histories. This is generally achieved by formulating constitutive laws related to uniaxial tensile behavior of the individual components.

The two loading functions which are most commonly used are those of isotropic and kinematic work hardening. According to Prager and Hodge [29] isotropic work hardening occurs when the initial yield surface (representing the yield criterion in stress space) expands uniformly during plastic flow. Figure 45 describes the behavior of a material which obeys the isotropic hardening loading function under cyclic uniaxial loading (along S_1). While the onset of yielding, which occurs at point A, is dictated by the von Mises criterion, subsequent plastic flow is governed by the expansion of this circle up to point B which represents the limit of prestrain. Upon removal of the tensile force and application of a uniaxial compressive force, the material will behave elastically to point C. This means if the flow stress at the end of the tensile prestrain is Sy, then upon reversing the stress, plastic flow will begin at a stress value of -Sy. According to the isotropic hardening law, subsequent compressive plastic flow beyond point C is identical (except for sign) to that in uniaxial tension beyond point B. The stress-strain behavior predicted by this rule is illustrated in Figure 46 for the OFHC copper matrix material used in this study. It is obvious that the Bauschinger effect is neglected by this theory.

According to the rule of kinematic work hardening the yield surface does not change its initial form and orientation, but merely translates in stress space. This concept has been introduced by Prager [30] in order to account for the Bauschinger effect and anisotropy due to plastic deformation. Figure 47 depicts the translation in stress space of the yield locus from the onset of plastic flow in axial tension at point A to the end of prestraining at point B. Upon reversal of the load, the kinematic theory predicts that yielding in compression will occur at point C. This dictates that the extent of elastic behavior will be twice the elastic limit in uniaxial tension. According to the kinematic theory subsequent plastic behavior will be identical to that beyond point A in uniaxial tension. As can be seen in Figure 46, the kinematic rule predicts a very pronounced Bauschinger effect and a workhardening rate equivalent to that observed in uniaxial tension.

The difference in cyclic behavior predicted by the isotropic and kinematic laws is quite large. Actual behavior lies somewhere between both theories. A recent attempt to provide a general theory (i.e. a theory based solely on uniaxial tensile behavior) to better describe complex loading histories has been developed by Mroz [31] This same concept has also been recently discussed by Iwan [32] but for purposes of this study it will be called the Mroz model since Mroz discussed it in much more detail.

The Mroz model considers the simultaneous expansion and translation of the original yield surface. For the initially isotropic material, all surfaces f_o, f_1, ...f_n are similar and concentric, enclosing the origin O. The model assumes that all surfaces are allowed to translate in the stress space without changing form and orientation. In Figure 48, when the stress point moves from O along the vertical axis (uniaxial tension), it reaches the elastic limit at A and the circle f_o moves along this axis until it contacts the circle f_1 at B. All other circles remain fixed during this period. Between A and B the plastic strain is defined by the tangent modulus E_1. When the stress point moves from B to C, the circles f_o and f_1 translate together until the point C is reached where f_o and f_1 touch the circle f_2 which up to now remained at rest; between B and C the tangent modulus is equal to E_2. From C the three circles f_o, f_1, f_2 translate with the stress point towards D. Figure 48 represents the situation upon reaching point E the end of the axial prestraining.

Upon unloading and subsequent reloading in the reverse direction, the stress point reaches G where compressive plastic flow occurs and the circle f_o translates downwards until it reaches the circle f_1 at H. This is the same result for the onset of yielding as was predicted by the kinematic work hardening rule. However, the stress difference between H and G equals twice the difference between stresses at B and A because the tangent modulus E now acts over twice the strain range. Thus, the Mroz model predicts a higher degree of work hardening than the kinematic theory. Further loading along HI corresponds in an analogous manner to the previous step BC. Thus it can be seen that the curve of inverse loading EGHI is uniquely defined by the curve of primary loading OABCDE.

The three loading functions already described can be defined completely by the behavior of a material in uniaxial tension. This is a highly desirable situation because if one of the theories is proven valid, only a limited amount of experimental data is required to predict the behavior under complex loading schemes. Of importance is the fact that all three theories predict the onset of plastic flow upon reversal of load to be independent of the amount of prestrain. The work of Lubahn [28], however, has shown that the Bauschinger effect is a function of the amount of prestrain. Thus, none of the three current theories can be expected to predict the behavior under reversed loading conditions exactly.

The most accurate loading function would be an experimentally determined effective stress-effective strain curve. This approach would require a separate investigation for each particular amount of prestrain and hence could not be considered a general behavioral model. The subsequent four parts of this section, 2-5, will compare the four described loading functions in their ability to predict total composite behavior during unloading from the prestrained state.

(2) Isotropic Work hardening Rule

Use of the isotropic work hardening rule to predict the unloading behavior of a composite is a direct extension of the model previously described. A new computer program was written, however, for this unloading prediction. Besides geometric data and uniaxial tension stress-strain data for each component, the input data included the stress and strain distributions, and effective stresses and effective strains for each ring computed at the end of the prestraining. The program treated the case material as behaving elastically for the entire unloading sequence.

The analytical stress-strain results are compared to the experimental results in Figures 49, 50, and 51. In these figures and in subsequent figures only the analytical loading curve will be given since it has been already shown that this portion of the curve can be accurately described by the model. In all cases, it can be seen that the isotropic hardening assumption greatly overestimates the region of totally elastic behavior during unloading. In effect, the occurrence of a very pronounced Bauschinger effect has been established for these model composites under a triaxial stress state. In general, the error between theory and experiment is maximum at the prediction of yielding and becomes smaller because of the combined effect of a predicted low work hardening rate and an experimentally measured relatively high work hardening rate. The difference at the end of unloading can be seen by comparing the predicted and measured amount of residual strain. This is identified as ERES in the figures and it can be seen that the isotropic loading function predicts a higher residual strain than observed in all cases.

(3) Kinematic Work Hardening Rule

The computer program written for the isotropic hardening theory was revised to allow the evaluation of the kinematic work hardening theory. The onset of yielding was established, according to the theory, at twice the uniaxial tension elastic limit of copper (0.0004"). The shape of the effective stress-effective strain curve in the plastic region is identical to that of uniaxial tension curve of the OFHC copper. A least-square fifth order polynomial fit of this curve was used to permit the analytical calculation.

Figures 52, 53, and 54 compare the experimental results with the predictions of the kinematic work hardening theory. In Figure 52 it can be seen that the prediction of the onset of yielding for the 4340 steel-OFHC coper system is in good agreement with the experimental results. At smaller strains, however, the error becomes excessive as the degree of compressive work hardening predicted by the kinematic theory is significantly less than what is actually observed. The error increases with higher volume percentage of copper since it is the behavior of only the copper core which is not being properly

characterized.

In Figures 53 and 54 it can be seen that after prestraining the maraging steel-OFHC coper composites 0.0065 in/in into the elastic-plastic region, the kinematic theory slightly underestimates the extent of fully elastic behavior. For the specimens which were prestrained 0.012 in/in into the plastic-plastic region, the prediction of the onset of yielding is even in greater error. These results indicate the magnitude of the error which is inherent in the assumption used in the kinematic theory that the Bauschinger effect is independent of the degree of prestrain. As in the 4340 steel - OFHC copper composites, the maraging steel - OFHC copper composites deviated from the kinematic predictions significantly as the unloading process proceeded. Thus, the degree of work hardening predicted by the kinematic theory is seen to be considerably in error.

(4) Mroz Model Loading Function

The kinematic theory unloading program was modified to permit the Mroz model prediction of unloading behavior. The prediction of the onset of yielding is identical to that of the kinematic model, but the strain hardening portion of the copper effective stress-effective strain curve was analytically determined according to the theory of Mroz. This was done by dividing the uniaxial tensile curve of OFHC copper into 0.0002 in/in increments, and then determining the secant modulus of each increment. For the unloading curve, each incremental modulus was plotted to extend over increments of 0.0004 in/in. A fifth order polynominal fit was used to characterize each unloading curve mathematically.

Figures 55, 56, and 57 compare the Mroz model predictions with the experimental results on the two composite systems. Figure 55 shows that, for the 0.504 volume fraction of 4340 steel, the predicted and experimental behavior are in good agreement. The prediction of the behavior of the 0.225 volume fraction, however, is still significantly in error. The maraging steel - OFHC copper system behaves in a similar manner, with error increasing with copper content. In addition, the error also increases with degree of prestrain as a consequence of the underestimated prediction of the onset of yielding.

(5) Experimental Effective Stress-Effective Strain Approach

The required effective stress-effective strain curve for the OFHC copper had to be determined experimentally. In order to generate this curve, tensile-compression specimens had to be fabricated and tested. The machined configuration is shown in Figure 58. The top surfaces had to be flat to act as a compression surface while the lateral surface had to be concentric to insure proper tensile loading.

The OFHC copper rods used for the tensile-compression specimens

were heat treated for four hours at 1750°F and then oil quenched. 4340 steel buttonheads were then brazed onto the ends of the copper pins. The specimens were then machined to the dimensions shown in Figure 58. A stress relief for two hours at 850°F in dry hydrogen followed the machining. This heat treatment schedule was used to yield a grain size equal approximately to the grain size obtained in the core of the binary composites. Two longitudinal strain gages were placed 180° apart and connected in series to minimize the measurement of bending effects.

Specimens were fabricated with length to diameter ratios of 3 to 1, 5 to 1, and 8 to 1 in order to find an optimum size. However, in each size, considerable scatter was observed from specimen to specimen. This problem was circumvented by only using those curves which exhibited the expected initial uniaxial tensile results. The observed scatter is believed to be due largely to the effects of bending. While the strain gage system, tensile fixtures, and specimen configuration were all devised to minimize the bending effects, considerable error in measuring the plastic behavior of the very soft copper was still possible.

The appropriate effective stress-effective strain curve was obtained in the following manner:

1. Prestrain in tension to the effective strain analytically computed to account for both thermal loading and tensile prestraining.

2. Unload from tension.

3. Reload in compression

The curve required for the analysis is obtained from steps 2 and 3 above. The onset of yielding was taken as the first deviation from linearity during unloading. This in effect is the onset of the hysteresis loop normally seen in a single component unloading curve. The balance of the unloading curve and the compression curve were assumed to be continuous. These curves were characterized at low strain by a fifth order polynomial fit and at high strain by a linear approximation.

Using these experimentally determined effective stress-effective strain curves for the copper core, the composite unloading curves were computed. Figure 59 shows that good agreement exists between experimental and analytical results for the 4340 steel-OFHC copper composites which were prestrained into the elastic-plastic region. The ability to predict the measured residual strain closely is additional evidence of the suitability of the technique. Similar good agreemnt as seen in Figure 60 and 61 was seen in the maraging steel-OFHC copper composites prestrained into the elastic-plastic

region. Initially the maraging steel-OFHC copper samples which were prestrained into the plastic-plastic region did not show good agreement with experimental results. The source of the disagreement was the neglect to account for the hysteresis behavior of the maraging steel. In order to rectify the error, single component maraging steel tensile specimens were fabricated. They were prestrained an amount equal to the analytically computed effective strain which existed in the case at the end of the prestrain. Upon unloading from the prestrained state the hysteresis behavior was measured experimentally. In effect, for prestraining into the plastic-plastic region both the core and case had to be characterized by an experimentally determined effective stress-effective strain curve. Figures 60 and 61 show that good agreement between analytical and experimental results existed once the hysteresis behavior of the case was included in the analytical prediction.

As stated previously, all composites were instrumented with both axial and circumferential strain gages. This allowed an additional test of the model i.e., a comparison of the analytically predicted and the actually measured surface tangential strain as a function of axial strain. Figures 62, 63, and 64 show these comparisons for the prestrain cycle. Relatively good agreement is seen for the composites prestrained into the elastic-plastic region; however, only fair agreement can be seen on those composites prestrained into the plastic-plastic region. This error does not appear to be related to the unloading analysis but to the experimental measurement of tangential strain.

Since the experimentally determined effective stress-effective strain curve can be used to represent the unloading behavior of composites adequately, a close look at the calculated residual stress state at the end of the unloading analysis is warranted. Figures 65, 66, 67, and 68 compare the residual stress state in each component computed in the "as fabricated" condition and after the prestraining into the elastic-plastic region. It can be seen that there is little difference in the radial and tangential stresses before and after prestraining. However, the alteration of the axial stress of each component is of importance. The mechanical prestraining causes the copper core material to have a significantly reduced axial stress. Correspondingly the axial stress in the case is increased by the prestraining step.

The real significance of the alteration in the axial stress in the core is seen if the axial deviatoric stress is considered. This stress is the difference between the axial stress and the hydrostatic stress component for the system. In the "as fabricated" condition, the axial deviatoric stress is positive, representing the tensile stress state induced by thermal loading. After prestraining, however, the axial deviatoric stress is negative. This is seen in Figures 65, 66, 67, and 68 where the tangential and radial stresses after pre-

straining are larger in magnitude than the axial stress. In effect, the negative deviatoric stress represents the compressive state of the core after prestraining.

Figures 69 and 70 illustrate the residual stress distributions before and after prestraining into the plastic-plastic region. In general, they are similar to the results noted for the smaller degree of prestrain, except that the case axial stress varies with distance from the interface and the changes in the axial stresses are larger in magnitude.

(6) Reloading Analysis

Since the experimental effective stress-effective strain curves used for the unloading analysis yielded an adequate representation of the unloading behavior, the same approach was used to determine the response to subsequent axial loading. The appropriate effective stress-effective strain curve for the copper core was obtained using tensile-compression specimens identical to those used in the unloading analysis. The loading procedure used on these specimens was as follows:

1. Prestrain in tension to the effective strain analytically computed to account for both thermal loading and tensile prestraining.

2. Unload from tension.

3. Reload in compression an amount equal to the axial prestrain, minus the amount of strain in step 2, minus the residual strain observed after the prestrain cycle.

4. Unload from compression.

5. Reload in tension.

The curve obtained in steps 4 and 5 is the required effective stress-effective strain curve for copper in the reloading analysis. A typical loading function determined in this manner is shown in Figure 71. The numbers in the figure refer to the five steps given above. It is obvious that the totally elastic behavioral region of the reloaded copper is significantly larger than that in the initial uniaxial tensile loading. The unloading computer program was modified for the reloading prediction. Input data included the complete stress and strain distribution of each component after unloading.

Figures 72, 73, and 74 show the composite stress-strain curves predicted by the reloading analysis. Good agreement is seen in all cases between the analytical and experimental results. Compared to the "as-fabricated" tensile curves shown in Figures 28, 33,

and 35, the reloaded curves exhibit a significant increase in load carrying capacity. This is directly related to the increase in fully elastic behavior which resulted from loading the copper core from a state of compression. It should be noted that the reloading curves were translated to a new origin so that the effect of the residual strain after prestraining is not observed.

Figures 75, 76, and 77 show the experimental and analytical predictions for the ratio of tangential to axial strain. Good agreement is seen in all cases. It is not known why the experimental difficulties regarding this measurement that were observed in the prestraining cycle did not appear upon reloading.

The good agreement in predicting both the axial stress-axial strain curve and the tangential strain-axial strain curve indicates that the experimentally determined effective stress-effective strain approach used in this study represents the behavior of prestrained cylindrical composites adequately. In addition, it has been clearly shown by this approach that the increase in load carrying capacity which results from prestraining occurs from a rational alteration of the residual stress state of the model composites.

b. Filamentary Composite Behavior

The previous analytical description and experimental study of the effect of mechanical prestraining on two-member cylindrical composites has demonstrated the importance of the residual stress state in optimizing the tensile behavior of the composite. While the cylindrical model has provided a complete physical rationalization of the behavior of each component, the consequence of the geometry approximation to real fiber composites must be considered.

There are three areas of prime concern in extrapolating analytical results obtained for the simple two-component cylindrical model to typical filamentary composites. First, the matrix regions in either close or loose packed arrays are not circular. Second, a characteristic repeating unit of the real composite does not have a free surface as the cylindrical model does, but has a boundary subject to stresses and strains necessary to maintain the material continuity. Third, fiber cross-over and catenary is to be expected in real composites. For these reasons, it is necessary to evaluate the effect of mechanical prestraining on actual filamentary composites experimentally. Once this has been done, the analytical model can be applied to predict the real composite behavior. The success of this effort will signify the engineering value of the analytical model in the design of improved performance filamentary composites.

The fiber composite system chosen for this study was the tungsten-copper system. In selecting this system the following factors were considered essential:

1. The elastic and plastic behavior of each component must be representative of actual fiber composite materials.

2. The stress-strain behavior of component materials must be obtainable in the same metallurgical condition in which they exist in the composite.

3. A strong metallurgical bond between the components must be attained.

4. Limited diffusion and an absence of third phase formation at the component interface is required.

5. A proven fabrication technique must be available.

Tungsten-copper composites, fabricated by the vacuum infiltration technique, have been used as a model composite system in several major investigations [19,33,34]. In fact the generally accepted current theory of the tensile behavior of metal matrix composites is based mainly on the observed behavior of this system.

(1) Fabrication

High purity OFHC copper identical to that used in the model composites was used as the matrix material. Its chemical composition is given in Table 5. General Electric Type 218 CS (cleaned and straightened) tungsten wire of 0.005" diameter was used as the reinforcement.

The tungsten wires were cut into 4.5" lengths and cleaned by pickling in an aqueous solution of 40% nitric acid-20% hydrofluoric acid. The copper was cleaned with a 50% nitric acid solution. The number of wires required to achieve about 20, 40, or 60 volume fraction were packed into a graphite mold of 0.188" inside diameter. Sufficient copper was placed above the wires to insure complete filling of the mold. The graphite mold was placed into a quartz tube and vacuum degassed overnight (about 16 hours) prior to casting. The long degassing period appears to be necessary to vent the graphite mold of entrapped gas properly.

The quartz tube was placed into a tube furnace preheated to 2200°F. After about five minutes, sufficient time for the copper to become molten, a low frequency air vibrator, which was clamped to the quartz tube, was activated for five minutes. This technique prevented the occurrance of any "as cast" porosity. The specimen was held at 2200°F $\pm$ 25°F for one hour, then the furnace was turned off. After five minutes the specimen was lowered through the heat zone so that solidification could occur from the bottom. This procedure did not completely eliminate a center shrinkage cavity, but was successful in moving the cavity to the top of the specimen where the excess copper

solidified. Thus, it did not affect the integrity of the composites.

The quartz tube was furnace cooled to about 1200°F, removed from the furnace, and air cooled to room temperature while still under the vacuum. If the mold cooled completely to room temperature, the specimen was readily removed from the mold without damaging the mold. The filament spacings achieved by this process are shown in Figures 78, 79, and 80.

These composites were converted into tensile test coupons by silver brazing 4340 steel buttonheads to the composite ends. All of the samples were ground to the final configuration shown in Figure 81 to ensure concentricity and alignment in the tensile tests.

(2) Testing

The tensile stress-strain behavior of the 0.005" diameter tungsten filament by itself was determined after the wire was exposed to 2200°F for 1 hour in vacuum, to duplicate the treatment given to the filaments in the composite. For testing purposes, the wire was attached to small aluminum tabs with sealing wax. The tensile test was then conducted on an Instron tensile machine, using the aluminum tabs for gripping. The strain recorded during the test was based upon the cross-head motion; consequently any elastic strain in the fixture, grips, and tabs was included in the recorded strain. To eliminate the gripping and fixture error, i.e., to establish the accurate elastic modulus the system of extrapolated infinite gage length was employed. Tests were conducted in wires of various gage lengths, and a plot of modulus as a function of the reciprocal gage length was prepared. Since the strain in the fixtures is independent of gage length, an extrapolation to infinite gage length could be expected to indicate the true elastic modulus. The modulus was therefore established by extrapolation of the reciprocal gage length to zero. A modulus value of 58×10^6 psi was determined by this manner.

Tensile testing of the filamentary composites was conducted in a manner similar to that used for the cylindrical two-component composites described previously. Both longitudinal and tangential strains were measured by strain gages as a function of applied load.

Since most potential fiber materials (including tungsten) are essentially brittle, prestrains into the elastic-plastic region were emphasized. For each volume fraction specimens were prestrained 0.001 in/in and 0.003 in/in, unloaded, and reloaded to failure.

The elastic-plastic regions occurred roughly over the strain range from 0.0001 in/in to 0.0035 in/in for these composites. In addition, several composites of each volume fraction were cycled at the above prestrains until stabilization occurred (i.e. the hysteresis loop became closed) and then loaded to ultimate failure.

(3) Test Results

Results on 20.75 volume per cent tungsten specimens are shown in Figures 82 and 83. Substantial increase in load carrying capacity is achieved with both 0.001 in/in and 0.003 in/in prestrain cycles. The 0.003 in/in cycle yields a greater improvement than the 0.001 in/in cycle, but not in proportion to the amount of strain. Further cycling cycling raised the stress-strain curve further but the effect damped out in only three cycles for the 0.001 in/in strain cycle and in six cycles for the 0.003 in/in strain.

The end of fully elastic behavior (the elastic limit of the copper) in the "as fabricated" state is about 0.00007 in/in. One 0.001 in/in prestrain cycle increased the elastic-elastic behavior to about 0.00022 in/in. A similar increase was seen with the 0.003 in/in prestrain. Further cycling at either 0.001 in/in or 0.003 in/in increased the elastic limit to about 0.00040 in/in. Since both amounts of prestrain yielded about the same increase in elastic behavior, the higher elastic-plastic behavior for the 0.003 in/in prestrained samples must be attributed to a higher strain hardening rate in the copper. Of most importance, however, is the fact that very significant improvement in behavior can be attained with relatively small amounts of prestrain. With a prestrain cycle around 0.001 in/in there is little likelihood that even the most brittle fibers would be fractured in the prestrain operation.

Figure 84 illustrates the results obtained by prestraining 43 volume per cent tungsten composites. Again an increase in load carrying ability is seen for the composites prestrained both 0.001 in/in and 0.003 in/in. The 0.001 in/in prestrain cycle formed a closed hysteresis loop after three cycles as it did in the 20.75 volume per cent samples. However, the relative increase in composite stress-strain behavior is less than for the lower volume fraction specimens. After one 0.003 in/in cycle very little increase in composite stress-strain behavior was observed. It can be seen that one 0.003 in/in cycle yields slightly better results than three 0.001 in/in cycles. The increase in elastic limits for the 43 volume per cent tungsten specimens is similar to that seen in the lower volume per cent specimens.

The effect of tensile prestraining 64 volume per cent tungsten specimens is seen in Figure 85. Data are presented for only one cycle at both 0.001 in/in and 0.003 in/in prestrains because further increase upon recycling was negligible. At this high fiber volume fraction, the prestraining is not as effective at improving the total composite behavior as it was with the lower volume fraction composites. Changes in the extent of fully elastic behavior are virtually impossible to measure because of the overwhelming influence of the very high strength tungsten, i.e., the onset of plastic flow in the relatively weak copper has a small effect on total composite behavior.

(4) Application of Analytical Model

The analytical model which predicted the behavior of prestrained two-member cylindrical composites adequately will be applied to the fiber composite systems described in the previous section.

For the 64 volume percent tungsten specimens the model will be used as it was for the previous two-component model in which the copper was the core material and the fiber material was the case or outer sleeve. This application represents a "close-packed" configuration where the matrix is under high constraint because of its proximity to the fibers. As can be seen in Figure 80, the average fiber separation is not greater than the fiber diameter, thus the "close-packed" assumption appears valid.

For the 20.75 and 43 volume percent tungsten fiber composites, the simulation model is reversed. The copper is now on the outside and the tungsten is the core material. This represents the condition of "loose packing" where the fibers are assumed to be separated sufficiently, so that at some point or region between the fibers, the matrix does not "feel" the presence of the fibers. The analytical work of Hamilton [13] predicted that this conditon is true up to about 55 volume percent of fiber. It can be seen in Figures 78 and 79 that the average interfiber separation is relatively large. Thus the assumption of "loose packing" appears to be valid.

The computations for the "close-packed" model are similar to those performed for the model composite. In order to characterize the behavior of the copper core material during the complex loading scheme, only one effective stress-effective strain curve was required for each loading sequence. This is a result of the fact that, for the core, the stress and strain distributions are not a function of radius. However, for the "loose packed" model, the stresses and strains vary with the radius. Thus a different effective stress-effective strain curve is required for each ring of the case. Since this curve must be determined experimentally, it would require a vast number of experiments to characterize the case behavior completely. However, a more expedient method was utilized in this analysis. The description of this method follows.

One effective stress-effective strain curve was determined at an average value of the computed effective strain in the case at the end of the prestrain. This curve was then translated along the strain axis by an amount equal to the difference between the average case effective strain and the actual effective strain at each ring at the end of the prestrain. The largest error involved in this approximation is that it is assumed that the Bauschinger effect determined for the average effective strain is constant over the strain range to which it is applied. This error is quite small, however, since the largest range of effective strain over the case which was computed

was only 0.00025"/" and the change in the Bauschinger effect over this strain range is almost negligible. Using this technique, the computational process could be carried out in a rather straightforward manner once the new computer program was written.

a. "As Fabricated" Residual Stresses

The thermal loading problem was solved for the three different volume fractions by assuming a stress free temperature of 850°F. This is identical to the stress free temperature used in the thermal loading of the model composites. For the fiber composites, the thermal loading was achieved during cool down from the brazing temperature of about 1300°F. This cooling took place at about an average rate of 20°F per minute.

The variation in the mechanical properties of the copper with temperature were utilized in the thermal loading analysis. The elastic properties of the tungsten, however, were assumed not to vary over the 800°F range. The stress and strain distributions were computed in 50°F increments from 850°F to room temperature.

The "as fabricated" residual stresses are shown for the 20.75, 43, and 64 volume percent tungsten composites in Figures 86, 87, and 88. It can be seen that the copper is in tension and the tungsten is in compression in all cases. The non-uniform axial stress distribution in the copper of the loosed packed composite results from the origination of plastic flow at the case-core interface. The relatively low magnitude of all the stresses in the 20.75 and 43 volume percent tungsten composites is in sharp contrast to the results on the 64 volume percent tungsten composites. The "close-packed" model, which imposes great restraint on the core material, induces a very high hydrostatic stress into the core. However, when this is subtracted out, i.e., on a deviatoric stress basis, both models predict that after cool down from the fabrication temperature the effective stress on the copper is approximately the room temperature yield stress of the copper.

It must be noted that all the fiber composites were cleaned-up machined after brazing. The amount of machining was not constant but is known. However, both tungsten and copper were removed by the machining. This, unfortunately, makes the machining effect not applicable to an analytical computation.

The "as fabricated" residual stress state is thus assumed to be that calculated by the thermal loading analysis. This means that any unloading of the copper which would occur as a result of the machining operation (analogous to the effect of machining on the model composites) is neglected.

b. Axial Prestraining

To compute the intensification of the stresses which occurs during axial prestraining, the "as fabricated" residual stresses had to be recomputed using only the room temperature effective stress-effective strain curve of the copper. This is in accordance with the procedure described in Section I. For the "loose-packed" composites, only a single 50°F temperature increment was required while for the "close-packed" composites a 750°F effective stress free temperature was used. While these seem to be in sharp contrast, the only basic difference lies in the amount of hydrostatic stress component developed and it is known that the hydrostatic stress component does not affect the the flow properties.

Using the above procedure, the effective stresses and effective strains correlate with each other at the end of the thermal loading analysis so that the effect of subsequent axial loading can then be measured. The stresses were computed in 0.0002 in/in increments.

The loading curves for the 20.75 volume percent tungsten specimens are seen in Figures 89 and 90. The analytical curves can be seen to be lower than the experimental results. The analytical model does not predict any elastic-elastic behavior, however, about 0.00007 in/in of totally elastic behavior is experimentally observed. Better agreement would probably have been possible if the machining operation could be taken into account.

Figures 91 and 92 compare the predicted and observed loading curves for the 42 volume percent tungsten composites. Again the computed curves do not show any fully elastic behavior and as a result are somewhat lower than the experimental curves throughout the strain range. Figures 93 and 94 illustrate the loading curves for the 64 volume percent tungsten composites. Because of the overwhelming influence of the tungsten, the effect of neglecting the fully elastic behavior of the copper does not lead to much error. The relative drop in the experimental curve of Figure 93 at high strains can probably be attributed to some fiber breakage which has been observed on other specimens above 0.002 in/in of strain.

c. Unloading Prediction

In order to make a prediction of the unloading behavior of the composites, an experimentally determined effective stress-effective strain curve had to be measured for each amount of prestrain. Pure copper tensile-compresssion samples identical to those discussed in part (4a) of this section were first strained in tension to amount equal to the average effective strain computed at the end of the prestrain. After unloading, these specimens were then reloaded in compression. Using the unloading and compression curves as the effective strain-effective strain curves for the matrix, the composite unloading behavior was computed.

The predicted unloading curves are compared to the experimental curves in Figures 89-94. In each case the shape of the unloading curves are in agreement; however, the error which originated in the loading curves is carried over to offset all the computed curves from the experimental curves. It should be noted that within the accuracy of the technique the prediction of the onset of plastic flow in the matrix during unloading was in good agreement with the observed results.

Since the residual stress state is now known after the prestrain, it is worthwhile to note the effect of the mechanical prestrain on the "as fabricated" residual stresses. This is shown in Figure 86 for the 20.75 volume percent tungsten composites. It can be seen that prestraining decreases the axial stress in the copper significantly and correspondingly increases the axial stress in the tungsten. On a deviatoric stress bases, the axial stress in the copper actually changes sign. This result is similar to that seen in the model composites and certainly accounts for the beneficial effect of the prestrain. It is quite clear from Figure 86 that only 0.001"/" of prestrain is sufficient to alter the residual stress state dramatically. In Figures 87 and 88 very similar results are seen for the 43 and 64 volume percent tungsten composites.

d. Reloading Prediction

Since the residual stress state has been calculated for each volume fraction after the prestrain cycle, the effect of subsequent reloading can now be determined. The results will be shown on a new set of axes, i.e., a coordinate shift equal to the residual strain is made. As was the case of the model composites, an experimentally determined effective stress-effective strain curve had to be determined. The curves used for the unloading analysis were extended by unloading from compression and reloading into tension. These final unloading and reloading curves were used to determine the response to reloading after the prestrain cycle.

Figure 95 compares the predicted and observed composite reloading curves for the 20.75 tungsten volume fraction specimens. Good agreement is seen in predicting the amount of totally elastic behavior, however, deviations are seen at large strain for both the 0.001"/" and 0.003"/" prestrained specimens. The error appears to be systematic, and is related to underestimating the strain hardening behavior of the copper. In turn, this is probably a result of underestimating the effective strain at the end of the axial prestrain, as would be the case if the stresses generated during cool down were underestimated. The effect of non-uniform cooling could account for this disparity. This observed difference could also be related to the non-uniform packing of the fibers. This non-uniformity would result in a portion of the matrix being stressed higher than the average and a portion being stresses lower than the average. It has

been shown in Reference 13 that the higher loaded portion of the matrix would be loaded to a larger degree than expected on a weight average while the remaining portion of the matrix would be loaded on about a weight average. Thus the total effect of the non-uniform packing would be to stress the matrix to a greater extent than predicted.

The reloading behavior of the 43 volume percent tungsten composites is shown in Figure 96. Once again the fully elastic behavior is well predicted. The elastic-plastic behavior is underestimated for the sample prestrained 0.001"/" in a manner similar to that shown in Figure 95 for the 20.75 volume percent tungsten composite. However, the observed behavior of the 0.003"/" prestrain specimen actual falls below the predicted curve at high strains. In this case, there is evidence that some fiber fracture occurred above .002"/" strain. This seems to indicate that the prestrain step, while significantly improving the low strain range behavior, can also cause brittle fiber fracture to occur earlier than what would normally be expected. This would be a consequence of changing the sign of the "as fabricated" residual stress in the tungsten from compression to tension by prestraining.

The observed behavior of the 64 volume percent tungsten composites is compared to the analytical predictions in Figure 97. Good agreement over the full strain range is observed. It appears that the error in predicting the copper behavior is not of sufficient magnitude to alter the predicted curves significantly for this high volume fraction of tungsten.

SECTION IV

COMPARATIVE ANALYSIS OF CYLINDRICAL AND HEXAGONAL ELEMENTS

The cylindrical composite models have been widely used to describe elastic behavior, and are virtually the only geometric model to which plastic behavior has been ascribed. The reason for the widespread usage of this model stems directly from the relative simplicity of the analysis for circular symmetry as compared to formidable analyses required for even the simplest of actual fiber composite configurations. Plasticity analysis of an exact array of fibers would be an exceedingly difficult undertaking, even for the simplest case of perfect plastic behavior. The cylindrical element has generally been considered reasonable in its accuracy for low fiber volume fraction composites where the effects of adjacent fibers on a given fiber are negligible. However, the limitations of the maximum fiber volume fraction for which this model may reasonably accurately permit computation of the transverse interaction stresses have not been examined in detail. It is anticipated that at some minimum fiber volume fraction the adjacent fibers will begin to cause aberrations in the simple cylindrical model stress field, and this cylindrically symmetric solution will give erroneous results. This will, of course, be true for plastic as well as elastic deformation.

The two-component cylindrical model was developed analytically by Ebert and Gadd [17] for elastic deformation, yielding, and subsequent perfect plastic deformation. This model was developed to represent close-packed fibers in a matrix material and as such considered the core component as representing the matrix and the case component as representing the fiber component. In this type of representation, the constraint which the surrounding fibers impose on the matrix component is considered to be reasonably accurately represented.

The use of this two-component cylindrical model in approximating loosely-packed composites was suggested by Ebert, Hamilton, and Hecker [1]. For this type of representation, the core and case were employed as the fiber component and matrix component respectively.

Although these models were developed to represent both close- and loose-packed fiber composites, the range of fiber volume fraction within which these models provide an accurate representation of actual fiber composites has not heretofore been evaluated. Consequently, it was believed that a detailed examination of the micromechanical effects in the cylindrical composite as compared to the hexagonal element would provide the urgently needed determination of the range of applicability of the cylindrical model.

In this section, therefore, the analytical comparison is made between the elastic responses of the cylindrical and hexagonal composite

elements loaded in axial tension, and the comparative behavior under plastic deformation is discussed.

In the case of aligned fibers in a metal matrix loaded in axial tension, the initial yielding and plastic deformation of the matrix create a decided effect on the observed behavior of the composite[17,2,35]. Not only is the strain hardening rate reflected in the load carrying ability of the matrix component during its plastic deformation, but the properties of the matrix which determine the extent of the mechanical interaction during this straining are critically dependent on the strain hardening properties of the matrix. Specifically, it has been discussed in the Introduction that the transverse stresses arise from a difference in Poisson's ratio between the two components; that is, a difference in the lateral contractile tendencies of these components. Other things being equal, the greater the difference in Poisson's ratio the greater the transverse stresses being developed at a given axial strain. For a given Poisson's ratio difference, the larger the magnitudes of either or both components' elastic moduli, the larger will be the transverse stresses resulting from this interaction. The contractile tendency and "modulus" during plastic deformation have been described in the form of instantaneous values[1]and shown to be functions of the strain-hardening rate as well as elastic constants. Thus, the extent of the mechanical interaction and consequent transverse stresses developed between the components will be strongly dependent on the plastic properties of the matrix.

Consequently, the analysis utilized to rationalize the stress field developed during plastic-elastic interactions should ideally account for the exact plastic strain-hardening behavior of the plastic component. This observation, coupled with the inherent difficulties associated with plasticity analysis of complex problems, has supported the development of the cylindrical composite element as a representation of more complex fiber composite elements such as the hexagonal element considered herein. The plasticity analysis of the cylindrical element, complex though it may be, is considerably more amenable to the incorporation of exact plastic deformation behavior than its exact geometrical counterpart.

The fiber composite element referred to herein is that basic element of a fiber composite which is repeated throughout the composite to create the continuum. Each element behaves identically so that the total composite behavior is the sum total of each element; each element will represent therefore the total composite behavior.

The composite element for the hexagonally-packed fiber composite is shown schematically in Figure 98 with its corresponding representation by a cylindrical model element. Figure 99 shows the hexagonal element with its descriptive nomenclature. It is apparent from this representation that the geometrical approximation of the

actual hexagonal element by the cylindrical element is limited to the element surface configuration where the linear segments of the hexagon have been distorted into circular arcs to form the cylindrical surface.

It is inherent from the definition of the hexagonal element that it will contain the same constituent volume fractions as the entire composite. For the cylindrical element representation, this restriction will also be used. Aside from the geometrical approximation, the cylindrical element should provide a good representation of the hexagonal element if it is exposed to similar net surface loading conditions. In fact, if the average surface loads on the two elements are identical, the only difference in the actual stress field, and consequent effects thereof, will arise from the periodic nautre of element surface forces around the circumference and their results on the internal stress field.

For a very small fiber volume fraction, the surface is well removed from the fiber-matrix interface which is the source of the internal interaction. These oscillating effects would therefore be expected to be small. On the other hand, for a densely-packed composite the element surface is close to this interface and these effects may be expected to be large. Consequently, limits of the cylindrical approximation are expected to exist for some minimum fiber volume fraction of a given composite system.

For the extremely close-packed array, the cylindrical representation of Figure 98 appears to be an extremely crude representation of the hexagonal element, and the corresponding stress fields will most certainly be quite different from the true values of such a composite. In this case, the matrix is essentially encompassed by three adjacent fibers and therefore subject to severe restrictions to lateral deformations. This particular observation was noted by Ebert and Gadd[1]who then proposed to reverse the cylindrical model so that the matrix component is in the interior. For this model, the matrix is restricted to lateral flow much the same as is the matrix in the close-packed array of fibers.

The normal boundary force which must be imposed on the cylindrical element surface to provide the desired approximation to the hexagonal element will now be considered.

If a cut is made along the boundaries of hexagonal symmetry and parallel to the fibers, as shown in Figure 100, a balance of forces and moments must be imposed on the surface to replace those of the section removed;

$$\Sigma F_x = 0$$
$$\Sigma F_y = 0 \qquad (12)$$
$$\Sigma M_z = 0$$

If the composite is large with respect to the fiber and composite element size, any surface effects will be balanced over the large interior, and such an effect will be so small as to be masked by the localized effects. Therefore, these surface effects are neglected.

Since each element in the interior is identical to any other, and must remain so during axial loading, this summation must be true on a local scale for each repeating hexagonal section. In addition, it is noted that each hexagonal boundary within the composite must experience the identical stress and strain distribution as any other, that is, any symmetry boundary is unidentifiable from any other. Additionally, the planes of hexagonal symmetry require that the stresses normal and parallel to these planes are principal stresses. Considering these factors, the force distribution on each boundary is identical, and no shear stresses may be present on these boundaries. Consequently, each boundary must be in equilibrium.

The force distribution expressed mathematically is:

$$\sigma_n^A = \sigma_n^B = \sigma_n^C = \sigma_n^D \qquad (13)$$

where σ_n is the normal stress distribution and will be a function of distance "t" along the boundary of the hexagonal face. The superscripts refer to the hexagonal face under consideration.

Summing the forces in the x direction for a unit length of the composite

$$\int_A \sigma_n^A \sin\frac{\pi}{6}\,dt + \int_B \sigma_n^B + \int_C \sigma_n^C \sin\frac{\pi}{6}\,dt + \int_D \sigma_n^D = 0 \qquad (14)$$

From (12) and (13) above

$$(2+2\sin\tfrac{\pi}{6})\int_A \sigma_n^A\,dt = 0 \qquad (15)$$

and therefore

$$\int_A \sigma_n^A \, dt = 0 \tag{16}$$

Consequently, it is shown that the normal force distribution must be such that it is balanced to zero net force over the surface of the hexagon.

A consideration of the symmetry about the center of a given hexagonal face reveals that the normal force distribution on each half-face must be identical, and therefore must be a net zero normal force. Thus, it is proven that the net normal force over each hexagonal half-face must be in equilibrium, and there is no net compression or tension acting normal to the hexagonal element faces.

In approximating the behavior of a hexagonal element by a cylindrical element, it is suggested that the element surface boundary conditions should be the same as for the hexagonal element, that is, the cylinder surface should be a free surface and experience no radial surface forces. This requirement is imposed analytically as the boundary condition requiring the surface radial stress to be zero. This is precisely the boundary condition imposed on the cylinder by Ebert et al [17,1,2] and the resulting analytical model should provide the desired approximating composite element.

Therefore, analytical calculations of internal stress states were made for given composite systems utilizing this cylindrical model and compared to results of the hexagonal model proposed by Piehler [36]. It must be noted, however, that the stresses in Piehler's model are given by an infinite series solution which must be truncated to permit calculations of the stresses. Consequently, these computed stresses will not necessarily be correct, but effect of the hexagonal geometry will be indicated.

As plastic deformation occurs in the matrix, its properties change. This will affect the resulting stress distribution within the components of the composite. However, it has been shown in Section II that for this type of composite under axial loading only, the plastic properties may be represented by instantaneous material properties analogous to the elastic properties of the material. In other words, plastic properties as expressed may be utilized in incremental plastic relations to permit the plasticity analysis. Therefore, the comparison of the elastic analysis should provide good insight into the corresponding relative results for elastic-plastic and plastic-plastic calculations. This analysis will be of definite value in indicating the validity and limitations of the cylindrical model as applied to fiber composite behavior after plastic deformation commences.

Comparative computations were made for three fiber composite systems of engineering interest, which constitute a wide range of elastic properties: beryllium fibers in aluminum matrix, boron fibers in aluminum matrix, and tungsten fibers in aluminum matrix. The elastic properties of these materials are presented in Table 4. The results of the analytical computations revealed similar comparative behavior for all these systems, albeit the magnitudes changed, and therefore only a complete and detailed discussion of the beryllium-aluminum system will be presented. Such a presentation of the results of the other systems would be repetitive and add little to the discussion. Reference to the comparative behavior of the other systems will be made occasionally and as necessary for completeness. The beryllium-aluminum system was chosen for discussion because of the large difference in Poisson's ratio which gives rise to sizeable internal interactions.

In examining the micromechanics of a fiber composite, the important effects must first be determined. A knowledge of the exact nature of the actual stress field within the composite components is certainly necessary since these stress values which constitute the field can indicate critical locations with respect to yielding, fracture, and debonding. In addition, the stress field is necessary to determine the magnitude of the axial stress which a given point is actually experiencing under a given axial strain. This latter point gives rise to the actually observed composite stress at a given axial strain, and therefore the observed elastic modulus and subsequent elastic-plastic and plastic-plastic stress-strain behavior.

On the basis of the above, this evaluation will be directed to give an insight into the approximating value of the cylindrical model in determining actual internal stresses, and corresponding yielding and flow behavior of hexagonally-packed fiber composites. To facilitate the comparision of yielding behavior, the effective stress was determined for each calculation (at an axial strain of 0.001 in/in) from the Von Mises relation[37] given in cylindrical coordinates:

$$\bar{\sigma} = \frac{1}{\sqrt{2}} \left[(\sigma_z - \sigma_r)^2 + (\sigma_r - \sigma_\theta)^2 + (\sigma_z - \sigma_\theta)^2 + 6\,\tau_{r\theta}^2 \right]^{1/2} \qquad (17)$$

considering that

$$\tau_{rz} = \tau_{\theta z} = 0$$

The difference between the effective stress and the axial stress expected in the absence of transverse stresses then provides a measure of early or delayed yielding for the stress state under consideration. In other words, yielding initiates when $\bar{\sigma} = \sigma_y$ for the given component under consideration. At this point the stress state may be such that $\bar{\sigma}$ is not equal to $E\epsilon_z$, but may be greater or lesser in value. Consequently, the yielding behavior of the various regions of the composite may be compared to the Rule of Mixtures predictions by simply comparing this effective stress to the uniaxial stress at a given elastic axial strain. To facilitate this analysis, the difference $(\bar{\sigma} - E\epsilon_z)$ was evaluated at $\epsilon_z = 0.001$ in/in for both the hexagonal and cylindrical models as an indication of yield behavior. This difference as determined is such that positive values of this difference indicate earlier yielding than expected from uniaxial comparisons, and negative values indicate delayed yielding. Correspondingly, the measure of the deviation of the axial stress from the Rule of Mixtures prediction is presented as the difference $(\sigma_z - E\epsilon_z)$. Positive values indicate an increased stress and correspondingly higher observed elastic modulus relative to the Rule of Mixtures.

Computations were made over the range of fiber volume fractions of V_f=0.01 to V_f=0.90. The larger value of V_f is very close to the theoretical limit of close-packed fibers (0.91); higher values than that have no meaning. The very low fiber volume fraction may be expected to reveal little, if any, interaction effects between fibers. The stress field for V_f=0.01 for the hexagonal model and cylindrical model should therefore be virtually identical.

The distribution of the radial and tangential stresses through the hexagonal and cylindrical composite models of the Be-Al system are shown in Figure 101. It is apparent from these graphs that the stress distributions of the two models are identical, but their magnitudes are not in agreement. The stresses computed by the hexagonal model are of the same sign as, but of greater magnitude than, those of the cylindrical model. The effects of the difference in transverse stress magnitudes is reflected in the distributions of $(\sigma_z - E\epsilon_z)$ and $(\bar{\sigma} - E\epsilon_z)$ which are shown in Figure 102.

Since the stresses drop to negligible values at the external interface, it can be concluded that the difference in stress magnitudes observed here in the two models is a consequence of the truncation of the series solution of the hexagonal model which was necessary to facilitate the calculations. The solution of the cylindrical model is of closed form and therefore should be exact within the limitations of the assumptions made.

The comparison of the cylindrical model to the hexagonal model is limited to comparing relative effects rather than specific values. This limitation does not seriously impair the value of this comparison, however, since only the corresponding magnitudes are

amplified for the hexagonal calculations, and the relative distribution of the stresses are otherwise identical.

Before comparing the effect of increased fiber volume fraction on the internal stresses, it is timely to examine the type of stress distribution which is actually present in the hexagonal element at high fiber volume fractions. The radial and tangential stress distribution are presented for $\theta = 0^o$ (see Figure 99 for identification of θ) and $\theta = 30^o$ in Figure 103, and the interface stress is shown as a function of θ in Figures 104 and 105. It is interesting to note that the radial stress, which is shown in Figure 104 to possess maximum absolute values at 0^o and 30^o, becomes tensile at 30^o while becoming increasingly compressive at 0^o. This reflects the oscillation of normal stress on the hexagonal surface. These normal stresses must also pass from tension to compression in order to allow equilibrium, as was discussed previously in this section. The in-plane shear stress, which is zero at the 0^o and 30^o lines of symmetry, passes through a maximum at about 15^o as shown in Figure 104. The radial and shear stresses at the interface are identical for both components as required from equilibrium considerations (hence, Figure 104 applies to either component), but the interface tangential stresses are different in the matrix and fiber as shown in Figure 105.

The variation of stress with θ for the composite of high fiber volume fractions, then, is the cause of differences in behavior which may be predicted between the hexagonal element and the cylindrical element. It has been shown schematically that no substantial difference exists between the two models for $V_f = 0.01$, and that for $V_f = 0.70$ significant aberrations in the stress fields are caused by the close proximity of adjacent fibers.

The effect of varying the fiber volume fraction is shown in Figures 106 - 111. To facilitate this evaluation, the interface radial and tangential stresses are shown for 0^o and 30^o, and for extreme values of $(\bar{\sigma} - E\epsilon_z)$ and $(\sigma_z - E\epsilon_z)$ for the matrix and fiber as computed by both hexagonal and cylindrical models. These comparative plots are presented for the Be-Al composite system (Figures 106 - 108) and the W-Cu composite system (Figures 109 - 111) to demonstrate that the relative effects are independent of material properties. The magnitudes of these effects, however, may be seen to depend on the properties of the components of the composite system.

Examination of the radial stresses of Figures 106 and 109 reveals an effect of the adjacent fibers at fiber volume fractions as low as 0.2. However, this effect does not appear to be substantial until the fiber volume fraction reaches 0.5 or 0.6. The tangential stress, on the other hand, does not reflect the effect of fiber proximity until the fiber volume fraction reaches 0.6 or 0.7.

The values of $(\bar{\sigma} - E\epsilon_z)$, which will predict yielding behavior,

indicate essentially no hexagonal aberrations until the fiber volume fraction approaches 0.6 or 0.7. Corresponding values of $(\sigma\text{-}E\epsilon_z)$ in Figures 108 and 111 become affected by the hexagonal symmetry at fiber volume fractions of approximately 0.3, but not substantially until 0.6 or 0.7.

Since the values of $(\bar{\sigma}\text{-}E\epsilon_z)$ and $(\sigma\text{-}E\epsilon_z)$ are strong indications of yield and stress-strain behavior, respectively, of the components of the composite, and consequently of the composite itself, it is of interest to examine the actual distribution of these values throughout the composite. To permit this evaluation on a comparative basis, corresponding 30^o sections of hexagonal and cylindrical elements, as shown in Figure 112, were selected for the presentation of results. The values of $(\bar{\sigma}\text{-}E\epsilon_z)$ and $(\sigma\text{-}E\epsilon_z)$ are shown on these sections as lines of equal value, or isograms, in Figures 113-120. Since these values within the fiber are frequently constant, the fiber area is crosshatched to indicate the region over which the value is constant.

The yielding behavior of the matrix is indicated in Figures 113-116 where the isograms of $(\bar{\sigma}\text{-}E\epsilon_z)$ are presented. In comparing these values of the cylindrical model to those of the hexagonal, it is significant to note the location of the zero isogram, which separates those regions of the matrix which will yield early and those which will yield late as compared to uniaxial considerations. On this basis, it appears that similar yielding behavior may be expected for the two models for fiber volume fractions up to at least 0.3.

Further examination of the hexagonal element in Figures 113-116 reveals that, even at high fiber volume fractions, similar volumes of the matrix are above and below the zero. This effect is shown for the entire hexagonal element in Figure 121. This indicates that the average yielding strain for the matrix is close to the uniaxial value. The corresponding effect in the cylindrical model disagrees increasingly with the hexagonal model as the V_f increases above 0.5. This model predicts that an increasing percentage of the matrix will undergo delayed yielding.

While the yielding predictions of the cylindrical model are obviously in error at large V_f, the effect of this discrepancy on the composite behavior is not as great as first considerations might indicate. In the first place, the volume fraction of the matrix becomes smaller as the discrepancy increases, thereby reducing the contribution of this error to the overall composite behavior. Secondly, the actual magnitudes of this effective stress change are so small as to be of virtually negligible effect in altering the predicted net yield stress. Thus, with the cylindrical element as with the hexagonal element, the observed average yield strain of the matrix will be very close to the uniaxial value.

The most significant difference between the matrix yielding behaviors of the two models is in the actual form of the yielding region of the matrix. The cylindrical model, for $V_f = 0.9$ for example, predicts a delay of yielding by about 0.84% above the uniaxial yield strain and subsequently the moving of a yield front through the matrix with yielding of the matrix complete at about 1.6% above the uniaxial

yield strain. In contrast to this, the matrix of the hexagonal element will begin yielding at $\theta = 0$ at about 23% less than uniaxial yield strain, and the yield front will move through the matrix to $\theta = 30^{\circ}$. Yielding will be complete at a strain of about 15% above the uniaxial yield strain[1].

The net effect of this yielding phenomenon is shown schematically in Figure 122. For this schematic presentation, the effects of the transverse stresses on elastic modulus and plastic stress-strain slope are neglected. The net effect of the yield front moving through the matrix is similar in all respects to the progressive yielding previously reported for the two component cylindrical composites [1,2]. For the ideal material exhibiting linear strain hardening as shown in Figure 122, the progressive yielding results in a region of the stress-strain curve which will show a continuously decreasing slope until yielding is complete and this slope becomes that of the plastic region.

The isograms of $(\sigma - E\epsilon_z)$ presented in Figures 117-120 indicate the magnitude of the deviation from the elastic modulus. The significant observation to be made from these graphs is the opposing effects of the fiber and matrix. All areas of the matrix show an increase in modulus while the fiber generally shows a decrease. The exception to this is for $V_f = 0.85$ (see Figure 108) where the fiber begins to show a slight positive variation in modulus.

The cylindrical element shows close agreement in behavioral trends of the modulus, though magnitudes remain lower. As with the effective stress deviations, the cylindrical model appears to follow rather closely the behavior of the hexagonal model with respect to the modulus variations. The net effect of the increase in the matrix component and the decrease in the fiber component is one of producing elastic moduli which are close to, though necessarily higher than those predicted by the Rule of Mixtures. This net deviation of modulus for the overall composite from the Rule of Mixtures is shown in Figure 123 as a function of fiber volume fraction as predicted by both analytical models. The trend of composite modulus based on the cylindrical model is surprisingly similar to that computed by the hexagonal model. Again, the magnitudes of the moduli are not in close agreement, but as mentioned several times previously, much of this deviation is due to the computational approximations of the hexagonal model.

The results of this study of the cylindrical model behavior as it compares to that of the hexagonal element indicates that the

---

[1] Recall that the actual values of hexagonal element calculations may be erroneously high due to the truncation of the series solution. Although the magnitudes may be in error, the argument is nonetheless valid in respect to the effect.

overall stress-strain behavior of a hexagonally-packed composite will be reasonably predicted by the cylindrical model for most fiber volume fractions. The composite elastic moduli appear to be closely determined as does the average matrix yield strain. The cylindrical model will not, however, predict the large strain range over which the matrix components undergo progressive yielding for high fiber volume fractions. However, this contribution of the very low volume fraction of matrix for which this phenomenon occurs will constitute a small fraction of the total composite stress-strain curve, and may even be a difficult characteristic to observe experimentally. The surrounding fibers appear to increasingly disturb the cylindrically symmetric stress field at fiber volume fractions of about 0.5 and above. However, up to this fiber loading, the cylindrical model appears to provide a reasonably accurate prediction of the actual internal stresses.

The value of this study is augmented by its extrapolation into the study of plastic deformation of the matrix, yielding of the fiber, and continued plastic deformation of the fiber. Those conclusions reached on the basis of elastic deformations are expected to hold approximately for plastic deformation. Consequently, it appears that the cylindrical model should provide a suitable analytical means of determining complete stress-strain behavior of hexagonally-packed fiber composites for most fiber volume fractions. The simplicity associated with the circular symmetry of the cylindrical model as compared to the hexagonal model makes this model especially attractive. This factor coupled with the errors arising from analytical simplifications necessary to apply the more complex models (even for totally elastic deformations) certainly justifies its use for most composite systems.

At the inception of this contract, the geometrical shortcomings of the cylindrical model in representing close-packed fiber composites were recognized [1]. It was proposed at that time to develop analytically an advanced cylindrical composite, the double-concentric composite, which would provide added flexibility in the application of the more simple cylindrical composites to such as the hexagonal composites. This analytical model has been developed to provide the complete transverse stress and strain fields for elastic and plastic deformation under axial loading, and is presented in a previous report [2]. However, the results of this detailed comparative analysis shed new light on the value of the two-component cylindrical composite in representing hexagonally-packed fiber composites.

While the value of the double-concentric model appears to be diminished, as a supplementary tool for predicting stress-strain behavior of densely-packed composites, it now takes on new dimensions as a method of analysis for fiber composites in which a third material is present at the interface. Such a third interfacial component may result from diffusion reactions resulting from thermal processing

[38-46], or from the application of diffusion reaction coating applied to the fibers prior to fabrication[46].

SECTION V

DOUBLE-CONCENTRIC MODEL

The value and limitations of the cylindrically symmetric two-component model in predicting internal stresses and thus effects on stress-strain behavior of a hexagonally-packed fiber composite, were discussed in detail in the previous section. The cylindrical model was shown to provide reasonably accurate calculations for the stress field at moderate fiber volume fractions, and strong indications that the stress-strain behavior was indeed indicative of actual fiber composites up to fairly high fiber loadings. However, the actual stresses at high fiber loadings were somewhat in error, and did not reflect the periodic stress variations around the actual hexagonally-packed fiber composite. Further they did not approximate the corresponding peak tensile and compressive stresses. In general, the cylindrical element approximated average stresses.

In summary, the simple two-component composite is seen to fall short of predicting the actual local stress values for densely-packed composites which would give rise to such factors as debonding between the fiber and matrix. Since bonding between the fiber and matrix is critical to the load transfer from the matrix to the fiber, such effects are of major interest in the use of fiber composites. Consequently, the need for supplementary methods of determining specified internal stresses is indicated, particularly for plastic deformation.

In addition to the above consideration, metal-matrix composites are frequently fabricated by high temperature processing, which may result in interaction or diffusion between the two components. Such a reaction characteristically leads to the formation of a multi-component composite: a fiber, an interfacial diffusion layer or intermetallic compound, and the matrix. In the simplest case, such a reacted composite would consist of the three basic components. While the interface reaction layer may not constitute sufficient fraction of the composite to significantly alter its stress-strain behavior, it may be a brittle, weak layer and therefore could be the source of premature failure. Such a layer, being very thin, would be expected to offer little resistance to deformation at the interface, although it may be experiencing excessively high stresses. Consequently a need for an analytical technique with which to provide insight into the micromechanics of a more complex composite is again indicated.

These considerations led to the development of the double-concentric model. The analytical development and experimental evaluation of Berylco 25-OFHC copper composites has been previously reported [2]. The recent progress supporting this study has been made by experimental evaluation of double-concentric composites consisting

of maraging steel case and core components with an OFHC copper ring component (see Figure 124 for designation of components).

1. Analytical Evaluation

The analytical development of the double-concentric model has been previously reported [2] and will not be reviewed here.

2. Experimental Evaluation

The experimental study was designed to provide data which could be compared directly to the analytical model. Consequently, test coupons were fabricated to match the exact double-concentric model geometry, and the component material properties chosen so that mechanical interactions could be evaluated. For this experiment, the two principal surface strains were measured as functions of applied load to provide the necessary data for the comparison to the analytical model. These experimental results, then, provide a measure of the composite axial stress-strain and transverse straining characteristics. The selection of component materials for this evaluation is otherwise unimportant since the analytical model is completely general, and its validity should be demonstrable for virtually any combination of materials.

a. Fabrication

The maraging steel case component used for these composites was the high strength alloy (designated maraging 300 alloy) possessing a yield strength of about 300,000 psi, whereas the maraging steel core component was the somewhat weaker alloy (designated maraging 250 alloy) which exhibits a yield strength of about 250,000 psi. The ring component was fabricated of OFHC copper tubing. Chemical analyses of all three components are presented in Table 5.

The fabrication of these composites involved the cold drawing of the OFHC copper tubing onto the 250 alloy maraging steel wires, and then shrink fitting these core-ring composites into precision ground 300 alloy maraging steel cylinders. The 250 alloy maraging steel wires were cleaned by degreasing with trichloroethylene before the drawing operation. The copper tubing was cleaned with a 50% nitric acid solution, and subsequently rinsed with water and then methanol. Four different wire diameters were used to fabricate the core-ring components containing four core area fractions.

All core-ring components were cut to 4-1/2" lengths, and centerless ground to 0.2395 $\pm$ 0.0001". One end of each rod was given a 5° taper over 1/2" length to assist its insertion into the steel case cylinder. The maraging 300 alloy case components were cut to 3-3/4" length by 1-1/4" diameter; drilled along their axes, and the inside diameter honed to 0.2395 $\pm$ 0.0001". These components

were degreased by cleaning in trichloroethylene before assembly.

The core-ring rods were shrink-fitted into the steel cylinder case components by cooling them in liquid nitrogen and then rapidly inserting them into the maraging steel cylinders. The excess core-ring rods (protruding from the ends of the cylinder) were cut off, and the ends of the assembly were inert-gas welded to protect the internal interfaces during subsequent processing.

The components were diffusion bonded by heating the composite at 1750°F for four hours, and cooled by oil quenching from temperature. The oil quench was found to be necessary to prevent intergranular cracking in the copper which otherwise resulted from tensile stresses developing from the differential thermal expansion on air cooling. The rapid cooling (oil quench) caused the case cylinder to cool faster than the internal copper, and thereby maintaining a compressive constraint on the copper, and preventing it from cracking. These composites were subsequently aged at 900°F for three hours, and air cooled. This thermal treatment age hardened the maraging steel components to their rated properties.

Sixteen composites were fabricated by this technique to permit fabrication of duplicate coupons for 8 different combinations of component volume fractions. The dimensions of the components in these composites and the composite identifications are shown in Table 6. In addition to these 16 composites of the double-concentric model, two composites containing only the copper core and maraging steel case are included in the study. The data for these composites (M44 and M50) was obtained from the previous Section III. These two-component composites represent a special situation for the double-concentric model in which one component has vanished.

Samples of maraging steel alloys were processed with the composite coupons to provide the required component data for the analytical computations. The maraging steel 300 alloy case component was tested as previously reported [2]. The maraging steel 250 alloy wires were not of sufficient diameter to allow the machining of test coupons, and consequently, these components were tested in the wire form directly.

b. Testing

All testing was conducted in a manner and with equipment as discussed in detail in a previous report [2].

c. Results

The results of this experimental evaluation are presented in three different graphical forms. The axial stress is presented as a function of axial strain, and compared to corresponding

analytical and Rule of Mixtures calculations. The surface strain measurements on these composites have been used to compute the tangential stresses as a function of axial strain. These strains are principal strains and therefore provide sufficient information for this computation. Since the case component will behave plastically as well as elastically, the computational process is somewhat involved and therefore presented in Appendix VIII. The surface strains are also presented as the ratio $(-\epsilon_\theta/\epsilon_z)$ as a function of axial strain.

Both representations of the transverse straining behavior of the composite will provide a good measure of the internal interactions. If no interactions occurred, there would be no tangential surface stress. Therefore, the surface tangential stress indicates the existence of such an interaction, and its magnitude will provide a quantitative comparison between the analytical and experimental results. The surface strain ratio is effectively a measure of the composite Poisson's ratio, though this ratio cannot be expected to be constant once plastic deformation begins in any component. Again, this same parameter $(-\epsilon_\theta/\epsilon_z)$ is obtained from the analytical model for comparison to experimental results. If no interaction occurred, the surface strain ratio would simply be that of the case component. Deviation from this case component behavior will again indicate the presence and magnitude of the mechanical interactions.

The cross section of a typical maraging steel-copper double-concentric composite is shown in Figure 125. Good bonding was achieved with this composite system as is shown by the fracture cross section in Figure 126 and corresponding micrographs of the interfaces presented in Figure 127. A thin diffusion zone may be seen in the copper at the interfacial areas, and results from the dissolution of the maraging steel constituents during the diffusion bonding treatment. This diffusion zone undoubtedly possesses different mechanical properties than the three basic component materials, but constitutes such a minor volume fraction of the total composite that it is not expected to affect the measured stress-strain or transverse strain properties. Such a thin interfacial layer would be expected to affect the composite behavior by causing debonding or cracking prematurely. Neither of these phenomenon were observed, and its effect on the composite properties is therefore discounted.

The component mechanical properties are listed in Table 7, and the stress-strain curves for all components are shown in Figure 128.

The results of tensile tests on the composites are presented in Figures 129 through 148. The results of duplicate coupons are presented in each figure. The analytical computations based on the double-concentric model are presented with the experimental results in each graph, and the Rule of Mixtures calculations are also presented with the axial stress-strain presentations for comparison. The Rule of Mixtures is not defined for the transverse strain measurements

and hence does not appear on these graphs.

Scatter in the measured and computed results is encountered periodically between duplicate test coupons containing the same component volume fractions. This scatter is believed to be caused by undetected errors in the measuring and/or recording instrumentation. A slight variation in diameters between duplicate samples (see Table 6) would contribute to the scatter, but this source of error is considered to be a minor contribution. The fabrication and processing are not believed to contribute significantly to the scatter since these procedures were identical for all samples. Bonding between components in this composite system is excellent, and debonding was observed only in the immediate fracture area. Consequently, debonding is not considered to have contributed to the scatter. Since all test samples were welded at the ends, load transfer to the inner components should be enhanced, thereby reducing or eliminating end effects. The St. Venant's effect which may arise from the effects of the change in geometry at the button-heads of the coupons would not vary between duplicate samples since the geometries of these coupons are identical.

The axial stress-strain behavior of these composites appears to agree well with both the analytical and Rule of Mixtures predictions for the many components area fractions tested. With these composites, as with the two-component composites[1], the analytical predictions are higher than the Rule of Mixtures predictions, but this difference is so slight as to be bearly perceptible.

It is noted that the experimental results for the axial stress-strain behavior of the two-component composites, shown in Figures 137 and 147, fall somewhat below the analytical prediction. This behavior has been examined in detail, both analytically and experimentally in Section III, and was traced to the presence of residual stresses arising from differential thermal contractions during cooling of the composite from processing temperatures. This behavior is constrasted by the stress-strain characteristics of the double-concentric composites which show curves consistently closer to and in some cases higher than, the analytical predictions. It therefore appears that the presence of the core component altered the residual stress state (as compared to that of the two-component composite) sufficiently that it imposed no larger effect on the subsequent stress-strain behavior.

Although some of the stress-strain curves are above the analytical predictions, this effect is not consistent and is generally accompanied by some variation in duplicate results. These observations indicate that the high curves are the result of measurement or recording instrumentation error.

The surface tangential stresses and surface strain ratios

also show agreement with the analytical predictions. A characteristic of the surface tangential stress curves, Figures 130 through 148 (odd numbered figures only), is the small initial axial strain region during which no measurable tangential stresses are reported. This is the small strain region during which the components all deform elastically, and the small difference in Poisson's ratio precludes the formation of measurable mechanical interactions. A second interesting characteristic of this graphical representation is the decrease in slope at an axial strain of about 0.009 in/in. This corresponds to the yielding of the maraging steel case. The surface tangential stress levels out at this strain because the Poisson's ratio of the case changes from the elastic value and approaches 0.5, the approximate Poisson's ratio for the copper ring component. The difference in Poisson's ratios of the components again becomes small and the resulting interaction between components becomes negligible.

The surface strain ratio ($-\epsilon_\theta/\epsilon_z$), shows a rapid increase corresponding to the beginning of plastic deformation in the ring component. After this rapid rise, the curve forms a plateau and this surface strain ratio becomes nearly constant for increasing strain. The nearly constant surface strain ratio is a consequence of the fact that the copper ring component, as well as the steel core and case component, is deforming with a linear strain hardening behavior as may be observed from its component curve, Figure 128. Corresponding to these linear stress-strain regions of the components are constant values of the incremental Poisson's ratio and incremental modulus.

This surface strain ratio increases rapidly at an axial strain of about 0.008 in/in or 0.009 in/in, which corresponds to the incidence of plastic flow in the steel case and core components. The increase in the composite surface strain ratio reflects the rapid increase of the steel components' Poisson's ratios as they rise toward the plastic value of 0.5. The two representations of the transverse strain measurements presented adjacent as they are, provide a rather clear representation of the micromechanical interactions as the composite components undergo the various states of elastic and plastic deformation.

The magnitudes of tangential stresses and the surface strain ratios are functions of the volume fractions of the components, as well as their mechanical properties. For example, samples MCT 1-1, MCT 2-1, MCT 3-1, MCT 4-1 and M 50 were fabricated to have identical case component dimensions. The corresponding size of the core component was decreased, and the matrix inside diameter decreased to accommodate the decreasing core size. The resulting surface tangential stresses and surface strain ratios, shown in Figures 130, 132, 134, 136, and 138 increase accordingly as the core size decreases (and the ring size increases).

Exactly the same relative behavior is shown for the samples MCT 1-3, MCT 2-3, MCT 3-3, MCT 4-3, and M 44 for which the core component also decreases correspondingly in size. The transverse strain effects for these samples are shown in Figures 140, 142, 144, 146 and 148 respectively.

It is apparent from all of these graphs in which the transverse strain effects are presented that the analytical model calculations show good agreement with not only the curves shapes, but also the actual magnitudes of the effects.

SECTION VI

DISCONTINUITY AND END-EFFECT STUDIES

The analytical and experimental studies pursued in the initial effort of the subject contract have limited the considerations to a highly specialized case wherein the composites were assumed to consist of infinitely long fiber components. End effects, discontinuous fibers, and fractured fiber components were not considered. Such assumptions were vital for the analysis undertaken, and have provided the basis for thorough studies within the limits of those assumptions.

However, fiber composites as engineering materials will not be of infinite length, and thus the end effects of the composite structural materials must be understood. In addition, discontinuous fibers can be used to advantage to permit fabrication of imaginative composite materials which are more difficult or impossible to fabricate of continuous filaments. Finally, broken filaments within composites may be present as a result of processing, fabrication, loading in service, or other factors.

The high probability of encountering discontinuous filaments in structural composite materials underlines the need for a thorough understanding of their effects on the composite material properties and their corresponding response to structural service. Consequently, this phase of study of the micro-mechanics of composite materials, which is concerned with the end-effects and discontinuities, represents a logical continuation of previous analytical and experimental studies.

Studies in this area were initiated during an earlier reporting period (Reference [2]), in which the investigators fabricated and tested several prototype tungsten fiber-copper matrix composites with single discontinuous fibers, as well as several continuous "control" composites. The results indicated that the effects of the fiber discontinuity, as reflected in composite stress-strain behavior and transverse strain ratio, could be seen as reduced stress and transverse surface strain at any axial strain level, although internal debonding of the composites may have affected transverse strain values. It was also noticed that discontinuity effects diminished rapidly away from the discontinuity location.

The approach utilized in continuing this investigation was basically the same as that of the previous work, that is, an experimental determination of the effect of the introduction of discontinuous fibers in various numbers and locations in the composite on the axial stress-strain and transverse strain behavior. It was hoped that a sample of a broad variety of situations could lead to a definition

of some of the more important variables, so that subsequent testing could be concentrated in specific areas.

It was felt that the prototype system of large diameter fibers was most amenable to such a study, combining fibrous characteristics of filamentary composites with sufficient size so as to be able to control accurately dimensions and geometry of the end configurations. Thus, use of the 0.050 inch diameter tungsten fiber-copper matrix prototype system was continued.

1. FABRICATION

The immediate goal was that of obtaining data indicating the effects of the following parameters under conditions of discontinuous fibers: 1) proximity of neighboring fibers to a discontinuity, i.e., closeness of fiber packing; 2) number of discontinuities present; 3) relative location of the discontinuities by variation in lateral and longitudinal distances to neighboring discontinuities; 4) fiber end geometry, specifically fiber end shape and proximity of ends of the halves of each discontinuous fiber. Not all of these configurations could be evaluated completely because of the very large number of composites needed to represent every combination. In addition, some configurations posed complex fabrication problems. Table 8 indicates the configurations which contribute to the present discussion.

Composites were fabricated by assembling 19 cleaned tungsten fibers into close packed hexagonal cross sections, as shown in Figure 149. Loose packed arrays were made by utilizing two of these short fiber bundles at each end to hold seven long fibers in the configuration shown in Figure 150. Discontinuities were introduced by substituting end wise fiber segments precut to known lengths in place of an original continuous fiber. By careful fabrication and tabulation, the location of the discontinuities could be followed through all stages in fabrication. Composites were then liquid infiltrated with copper in graphite molds according to the procedure described in Reference [2], and steel buttonheads were brazed onto each end. The excess copper was machined off to give a final diameter of 0.260 inches, yielding fiber volume fractions of 70.2% and 25.9% for close and loose packing, respectively.

2. TESTING

Strain gages were placed at two separate axial locations on each composite in an effort to obtain more data from each configuration. This gaging was the same at each location as used in previous work, permitting measurement of both axial and tangential surface strains at a cross section. The axial location of the gages varied from specimen to specimen, but generally one set of gages was located over a discontinuity plane and another set some distance away to observe the

longitudinal extent of crack effect. The composites were tensile-tested in precision aligned fixtures, and the surface strains were recorded as functions of applied load on x-y recorders.

Stress-strain data for component material is taken from Ref. [2] and is shown in Figure 151. Other mechanical properties are shown in Table 3. All materials used were of the same lots and treatment as in that investigation, so that material properties were identical to those reported previously. Data for control samples of continuous fiber composites are also from Reference [2]. The results presented below include those previously unreported as well as some pertinent data from Reference [2].

3. RESULTS AND DISCUSSION

Results discussed in this section pertain only to the close packed 19 fiber configuration, since the results from 7 fiber composites fabricated in this period are not yet complete.

Figures 152 through 154 show composite stress strain behavior for composites with one, three, or four discontinuities. All fiber separations were in the same cross sectional plane and the experimental curves portrayed were derived from data generated by strain gages in this plane. Aside from the tendency to decrease secant modulus and fracture strain with the increasing number of cracks, it is seen that the relative lowering of the strain curves (with the exception of the single crack specimen) is less than one might expect assuming that all the decrease in stress-strain behavior is associated with the effect of the decreased fiber fraction at the crack plane. The exception of the single crack specimen could be the result of either nontypical data for the specimen, or differences in fabrication techniques between the discontinuous and continuous composites (the latter of which were fabricated by other investigators). This surmise is being evaluated by the fabrication of a new set of continuous composites.

A word is in order about computation of the "expected" stress-strain curves. Since the prototype tungsten-copper system shows a large "synergystic" effect over the straight Rule of Mixtures predictions, it is not strictly correct to make comparisons between different volume fraction behaviors using Rule of Mixtures values. This was circumvented in part by using the continuous fiber composite curve as a basis, reducing it to proportions of fiber fractions of 18, 16, and 15 fibers apiece (corresponding to one, three, and four cracks in a plane), and assuming that the fiber is replaced by well bonded copper. In some cases, the copper was not well bonded to the fibers, as seen by debonding of copper from the fiber ends at the fracture. However, considering the effective increase in fiber fraction resulting from this factor does not significantly raise the

expected stress strain curve toward the observed. Such an increase, then, in the observed, over the expected, stress level at any axial strain would imply that the copper was carrying more stress than expected, or that a stress concentration effect was present. However, this conclusion may be nullified by the observation that the reduced fiber fraction does not extend over the entire axial gage length, and so the gage "sees" some fiber fraction intermediate between the continuous and the "expected" value as calculated. This alone could raise the stress-strain curve recorded by the gage, obscuring the effect of any stress concentration.

Typical surface transverse strain ratios for two locations on a discontinuous fiber composite are shown in Figure 155. The composite shows a higher transverse strain ratio at the crack plane than in the main body of the composite. This would indicate more elongation at the discontinuity than for the continuous fibers at the same level of axial strain. This trend is substantiated by data from other composites, plotted in Figure 156. For convenience in comparison, the transverse strain is normalized by plotting the ratio of the transverse strain value of interest to the transverse strain shown by continuous composites at the same axial strain as the y-axis. Normalized transverse strains less than 1.0 indicate the possibility of debonding or voids inside the composite.

Here again, the observed trend is predicted by consideration of the lowered volume fraction of fibers, (or increased fraction of copper) in the crack plane, since the copper, being in a plastic flow state, has a greater contractile tendency than do the fibers. However, the magnitude of the effect seen is within the values of transverse strain predicted by the analytical model for the lowered fiber fraction, and thus any effect other than that of decreasing effective fiber fraction is not readily identifiable. Possible reasons for this are that fiber-matrix bonding is poor, (as is probable in some of the composites since they show abnormally low transverse strains), and the realization that the transverse gages, like the axial gages, are seeing some average of the reduced and non-reduced fiber fractions. Both of these factors will tend to lower observed strains below expected values, thus obscuring a possible effect of stress concentration.

Effects of a discontinuity in close-packed composites diminish rapidly with distance from the discontinuity, as is seen in the transverse strain data for locations not on a crack plane (Figure 156) and also stress-strain behavior (Figures 152 through 154). Gages 0.2" or more from a discontinuity all showed substantially the same response, although decreased slightly, as the continuous composites (evidence for non-representativeness of the continuous composites).

The one gage set at 0.1 inch from a crack showed an axial strain behavior similar to continuous composites, but an increased transverse strain reading. These observations are compatible, since

it is known that transverse strain ratios are a more sensitive measure of composite interaction than stress-strain behavior.

The rapidity of decay of discontinuity effects with distance from the defect is a measure of the stress transfer ability at the discontinuity since the smaller the distance in which stress in the fibers is built up to its nominal value, the smaller is the area in which non-continuous behavior is seen. Thus, for these composites, the transfer distance, as seen from the surface of the composites, seems to be 0.2 inch or less. Since the fibers are .050 inches in diameter, this yields a critical aspect ratio of 8. This compares well with the value of 7.2 calculated by the analysis of Kelly and Tyson (reference [33]), using the material values determined in this investigation.

There is some evidence that the transfer length may be even smaller based on the fracture of one of the specimens. This specimen was fabricated with three discontinuities in one plane, and a fourth in another fiber in another plane 0.1" distant axially. The composite fractured at the plane of the three cracks. The fourth fiber also fractured in that plane, rather than pulling out the remaining 0.1" length. Thus, the stress in this fourth fiber must have built up sufficiently in the 0.1" length from its end to reach the fiber tensile strength, i.e, the 0.1" length was greater than the critical half length. This implies a critical aspect ratio as low as 4. Such a low critical aspect ratio means that contrary to the assumptions of Kelly and Tyson's analysis, stress transfer by the copper through the ends of the fibers is important, at least with the well bonded copper-tungsten interfaces and very short fiber end to fiber end distances used in this composite.

It is also of note in discussing stress transfer ability around discontinuities that not one of the close packed composites fabricated with only a single discontinuity fractured at the discontinuity. This attests to the ability of the matrix to transfer load successfully under such a condition, so that the fiber break is no weaker than a natural fiber defect.

SECTION VII

FUTURE WORK

With the complete development of both the elasticity and the plasticity elements of the analytical model, and capability of handling thermal loading and machining effects in the model on a theoretical basis, it is now possible to employ the basic model as an analytical tool to evaluate the parametric effects that are intrinsic in oriented fiber composite materials. Such evaluation will permit the inclusion of these parametric effects into the model to achieve the ultimate goal - a workable analytical model based on first principles with which to be able to predict and thus optimize fiber composite performance.

To achieve this end, the work of the study has been extended for a two year period. The specific topics to be considered are the following:

1. The effect of fiber-matrix inter-diffusion at the fiber-matrix interface on total performance, both predicted and measured, will be determined by use of the double-concentric analytical model.

2. The effect of the external geometry of the composite on the total performance will be evaluated in terms of both predictions from the analytical model and also actual measurement. Modifications of the analytical model will be made to take account of geometries in which surface effects alter the basic continuum concepts.

3. The residual stress distribution introduced into metal matrix composites as a result of fabrication will be predicted and measured, and the effect of changing the residual stress intensity and distribution on composite performance will be determined in terms of both the integrated analytical model as well as actual measurement.

4. The effect of biaxial loading on the stress-strain behavior of fiber composite sheet will be determined by means of a hydraulic bulge test. The anisotropy due to the unidirectional orientation of the fibers will be measured directly.

5. The effect of fiber discontinuities will be evaluated both analytically and experimentally, and the analytical model will be modified as necessary to take account of this parametric effect.

REFERENCES

1. Ebert, L.J., Hamilton, C.H., and Hecker, S.S., "Development of Design Criteria for Composite Materials", AFML-67-95, April 1967, AD 814815.

2. Ebert, L.J., Hamilton, C.H., Hecker, S.S., "Analytical Approach to Composite Materials", AFML-68-71, March 1968.

3. Mendelson, A., Plasticity: Theory and Application, MacMillan Co., New York, 1968.

4. Hill, R., The Mathematical Theory of Plasticity, Clarenden Press, London, 1950.

5. Ford, H., Advanced Mechanics of Materials, John Wiley and Sons Inc., New York, 1963, pp. 393-478.

6. Naghdi, P.M., "Stress-Strain Relations and Thermoplasticity", Proc. 2nd Nav. Symp. on Structural Mech., 1961, pp. 123-169.

7. Lin, T.H., "Review of Some Correlations of Physical and Mathematical Theories of Plasticity", Composite Materials Workshop, Technomic Publishing Co., Stamford, Conn., 1968, pp. 65-85.

8. Timoshenko, S. and Goodier, N.J., Theory of Elasticity, McGraw-Hill Book Co., 1951.

9. Budiansky, B., "A Reassessment of Deformation Theories of Plasticity", J. Appl. Mech., Vol. 26, 1959, pp. 259-264.

10. Kliushnikov, V.D., "New Concepts in Plasticity and Deformation Theory", PMM (Translation of Prikl. Math. i. Mekh.) Vol. 23, 1959, pp. 1030-1042.

11. Kliushnikov, V.D., "On a Possible Manner of Establishing the Plasticity Relations", PMM, Vol. 23, 1959, pp. 405-418.

12. Edelman, F., "On the Coincidence of Plasticity Solutions Obtained with Incremental and Deformation Theories", Lst. U.S. Natl. Congr. Appl. Mech., 1952, pp. 493-498.

13. Ilyushin, A.A., "The Theory of Small Elastic-Plastic Deformations", Prikl. Math. Mekh., Vol. 10, 1946, pp. 347-356.

14. Lubahn, J. and Felgar, R., Plasticity and Creep in Metals, J. Wiley and Sons Inc., New York, 1961.

15. Swainger, K.H., "Compatibility of Stress and Strain in Yielded Metals", Phil. Mag., Vol. 36, 1945, pp. 443-473.

16. Handelman, G.H., Lin, C.C., and Prager, W., "On the Mechanical Behavior of Metals in the Strain - Hardening Range", Quart. Appl. Math., Vol. 4, 1947, p. 397.

17. Ebert, L.J. and Gadd, J.D., "A Mathematical Model for Mechanical Behavior of Interfaces in Composite Materials", Fiber Composite Materials, American Society for Metals, 1965, pp. 89-113.

18. Kreyszig, E., Advanced Engineering Mathematics, John Wiley and Sons Inc., New York, 1967, pp. 399-400.

19. McDaniels, D.L., Jeck, R.W., and Weeton, J.W., "Stress-Strain Behavior of Tungsten-Fiber-Reinforced Copper Composites", NASA TN-D-1881, 1963.

20. Sachs, G. and Espey, G., "Residual Stresses in Metals", Iron Age, Vol. 128, 1941, p. 63.

21. Timoshenko, S. and Goodier, N.J., Theory of Elasticity, McGraw-Hill Book Co., 1951, p. 399.

22. Reed-Hill, R.E., Physical Metallurgy Principles, D. Van Nostrand Co., Inc., Princeton, N.J., 1964, pp. 571-611.

23. Shoeck, G., Creep and Recovery, ASM Seminar, 1957, p. 199.

24. Farnell, K., "Piecemeal Yielding of Mild Steel", Engineering, Vol. 185, 1958, pp. 92-93.

25. Steele, M.C. and Eicheberger, L.C., "Nonhomogeneous Yielding of Steel Cylinders: 1 - Mild Steel", Trans. ASME, Vol. 79, 1957, pp. 1608-1618.

26. Baker, A.A., "The Fatigue of Fiber-Reinforced Aluminum", J. of Materials Science, 3, 1968.

27. Baker, A.A. and Cratchley, D., "Stress-Strain Behavior and Toughness of a Fiber-Reinforced Metal", Applied Materials Research, April 1966.

28. Lubahn, J.D., "Bauschinger Effect in Creep and Tensile Tests on Copper", J. of Metals, September 1955.

29. Prager, W. and Hodge, P.G., "Theory of Perfectly Plastic Solids", John Wiley and Sons, N.Y., 1951.

30. Prager, W., "The Theory of Plasticity: A Survey of Recent Achievements", Proc. Inst. Mech. Eng., 169, 41, 1955.

31. Mroz, Z., "On the Description of Anisotropic Workhardening", J. Mech. Phys. Solids, 15, 1967.

32. Iwan, W.D., "On a Class of Models for the Yielding Behavior of Continuous and Composite Systems", Trans. ASME, 612, Sept. 1967.

33. Kelly, A. and Tyson, W.R., "Fiber-Strengthened Materials", Proc. of the 2nd International Materials Symposium, John Wiley and Sons, N.Y., 1964.

34. McDanels, D.L., Jech, R.W., and Weeton, J.W., "Metals Reinforced with Fibers", Metal Progress, 78, 6, 1960.

35. Hill, R., J. Mech. Phys. Solids, Vol. 12, p. 213, (1964).

36. Piehler, H.R., "Fiber-Strengthened Metallic Composites", ASTM Special Technical Publication No. 427, p. 1, (1966).

37. Dieter, G., "Mechanical Metallurgy", McGraw-Hill, N.Y. (1961).

38. Alexander, J.A., Cunningham, A.L., Chueny, K.C., AFML-TR-67-391, (1968).

39. Blackburn, L.D., Burt, H.M., and Bonanno, F.R., "Strengthening Mechanism -- Metals and Ceramics", University Press, (1965).

40. Pertrasek, D.W., Signorelli, R.A., and Weeton, J.W., "Fiber Strengthened Composites", ASTM STP 427, AM. Soc. Testing Materials, p. 149, (1967).

41. Report of the Ad Hoc Committee on Composites, Materials Advisory Board Report MAB-215-M, p. 31, (1965).

42. Clark, A.B., AFML-TR-68, 42, (1967).

43. Snide, J.A., AFML-TR-67-354, (1968).

44. Report of the Ad Hoc Committee on Interface Problems in Fibrous Composites, Materials Advisory Board Report MAB-214-M, (1965).

45. Long, J.R., Quarterly Progress Report to Air Force Materials Laboratory, Contract No. F3361S-67-C-1708 BPSN 67(680100-000A-000B-600) Project No. 735107 (1968).

46. Metcalf, A.G., J. Composite Materials, Vol. 1, p. 356 (1967).

47. Metals Handbook, 7th ed. American Society for Metals, 1948, p. 1007.

48. Vasco Report, "18% Nickel Ultra High Strength Maraging Steel", Vanadium-Alloys Steel Co., Latrobe, Pa., 1966.

49. Upthegrove, C. and Burghoff, H., "Elevated Temperature Properties of Coppers and Copper-Base Alloys", ASTM STP No. 181, 1956.

50. Hill, W.H., Shimmin, K.D., and Wilcox, B.A., "Elevated-Temperature Dynamic Moduli of Metallic Materials", ASTM Proc. Vol. 61, 1961, pp. 890-906.

51 Campbell, J.E., Barone, F.J., and Moon, D.P., "The Mechanical Properties of the 18% Nickel Maraging Steels", DMIC Report No. 198, 1964.

52. North American Aviation, Unpublished Data.

53. Everett, F.L., and Milkowitz, J., "Poisson 's Ratio at High Temperatures", J. Appl. Phys., Vol. 15, 1944, pp. 592-598.

54. Eldridge, E.A. and Deem, H.W., "Physical Properties of Metals and Alloys from Cryogenic to Elevated Temperature", ASTM STP No. 296, 1961.

55. Carreker, R.P., and Hibbard, W.R., Jr., "Tensile Deformation of High-Purity Copper as a Function of Temperature, Strain Rate, and Grain Size", Acta. Met., Vol. 1, 1953, pp. 654-663.

56. Chase Brass and Copper Co., Unpublished Data.

TABLE I

ELASTIC AND PHYSICAL PROPERTIES AND THEIR RATE OF CHANGE WITH TEMPERATURE OF THE CONSTITUENT MATERIALS OF THE CYLINDRICAL COMPOSITES

Material	Room Temp. Value of E (psi)	Room Temp. Value of ν	Room Temp. Value of α in/in/^{o}F	Linear Rate of Change of E with Temperature psi/^{o}F	Linear Rate of Change of ν with Temperature ^{o}F-1	Linear Rate of Change of α with Temperature (in/in/^{o}F)/^{o}F
OFHC Copper	16.0×10^{6}	0.34	(a) 9.2×10^{-6}	(c) -1.0×10^{4}	(f) * 6.25×10^{-5}	(a) 2.22×10^{-9}
4340 Steel	28.5×10^{6}	0.286	(a) 6.5×10^{-6}	(d) -5.6×10^{3}	(f,g) 4.25×10^{-5}	(h) 2.51×10^{-9}
Maraging Steel	26.3×10^{6}	0.294	(b) 5.6×10^{-6}	(e) -8.25×10^{3}	(f,g) 4.25×10^{-5}	(b) 1.75×10^{-9}

(a) Reference 38
(b) Reference 39
(c) Reference 40
(d) Reference 41
(e) Reference 42
(f) Reference 43
(g) Reference 44
(h) Reference 45

*The data on the change of Poisson's ratio with temperature was not taken from actual experimental results, but rather it was determined by the author's generalization of test data on other materials.

TABLE 2

RESIDUAL STRESSES IN OFHC COPPER-4340 STEEL COMPOSITES PREDICTED BY THE PLASTICITY ANALYSIS WHICH CONSIDERS PROPERTY VARIATIONS WITH TEMPERATURE

Case Area Fraction A_s	Transverse Stresses Core	Axial Stress Core	Axial Stress Case	Tangential Stress Case (at O.D.)
0.228	9,300 psi	13,200 psi	-43,800 psi	-62,000 psi
0.329	13,300	17,300	-34,300	-53,000
0.504	19,700	23,800	-23,750	-39,000
0.666	25,500	29,800	-14,900	-26,000

TABLE 3

MECHANICAL PROPERTY DATA OF CONSTITUENT MATERIALS
FOR THE CYLINDRICAL COMPOSITES AND FIBER COMPOSITES

Material	Ult. Strength (psi)	0.05% Offset Yield (psi)	Prop. Limit (psi)	Elastic Modulus (10^6 psi)	Poisson's Ratio
OFHC Copper	35,000	6,000	3,200	16.0	0.34
4340 Steel	204,500	191,300	183,100	28.5	0.286
Maraging Steel	288,000	260,000	210,400	26.3	0.294
50 mil-diam. tungsten wire (a)	232,000 (b)	212,000	180,000	49	0.285 (b)
5 mil-diam. tungsten filaments (a)	273,000 (b)	247,000	180,000	58	0.285 (b)

(a) Processed at 2200°F for 1 hour under vacuum.

(b) Taken from the literature, not determined in this project.

TABLE 4

ELASTIC PROPERTY DATA OF FIBER COMPOSITE COMPONENETS
USED IN THE COMPARATIVE ANALYSIS

Component	Elastic Modulus	Poisson's Ratio
Beryllium Fiber	45×10^6 psi	0.04
Aluminum Matrix	10×10^6 psi	0.33
Tungsten Fiber	58×10^6 psi	0.285
Copper Matrix	16×10^6 psi	0.34

TABLE 5

CHEMICAL ANALYSES OF THE COMPONENT MATERIALS
USED IN THE DOUBLE-CONCENTRIC MODEL

Material	C	Mn	Si	Ni	Cu	Mo	Al	P	S	Fe	O	Co	Ti	Be
OFHC Copper	-	-	-	-	99.92 Min.	-	-	-	-	-	Nil	-	-	-
300 Alloy Maraging Steel	0.012	0.032	0.007	18.71		4.81	0.08	0.004	0.01	Bal.		9.02	0.84	-
250 Alloy Maraging Steel	0.023	0.06	0.02	18.02		4.82	0.12	0.005	0.004	Bal.		7.57	0.50	-

TABLE 6

DIMENSIONS AND VOLUME FRACTIONS OF
DOUBLE-CONCENTRIC COMPOSITES' COMPONENTS

Sample No.	Core Dia. (in.)	Ring Dia. (in.)	Case Dia. (in.)	V_c	V_R	V_s
[1] MCT 1-1	0.1555	0.2392	0.2955	0.277	0.378	0.345
MCT 1-2	0.1555	0.2392	0.2954	0.277	0.378	0.345
MCT 1-3	0.1555	0.2392	0.3404	0.209	0.295	0.506
MCT 1-4	0.1555	0.2392	0.3405	0.209	0.295	0.506
MCT 2-1	0.1034	0.2396	0.2953	0.122	0.535	0.344
MCT 2-2	0.1034	0.2396	0.2958	0.122	0.535	0.344
MCT 2-3	0.1034	0.2396	0.3404	0.0919	0.402	0.506
MCT 2-4	0.1034	0.2396	0.3404	0.0919	0.402	0.506
MCT 3-1	0.100	0.2392	0.2957	0.077	0.578	0.345
MCT 3-2	0.100	0.2392	0.2457	0.077	0.578	0.345
MCT 3-3	0.100	0.2392	0.3407	0.058	0.436	0.506
MCT 3-4	0.100	0.2392	0.3403	0.058	0.436	0.506
MCT 4-1	0.0625	0.2392	0.2956	0.045	0.611	0.345
MCT 4-2	0.0625	0.2392	0.2953	0.045	0.611	0.345
MCT 4-3	0.0625	0.2392	0.3403	0.034	0.460	0.506
MCT 4-4	0.0625	0.2392	0.3404	0.034	0.460	0.506
M 50	0	0.2395	0.3397	0	0.663	0.337
M 44	0	0.2395	0.2942	0	0.497	0.503

TABLE 7

MECHANICAL PROPERTY DATA OF THE CONSTITUENT MATERIALS
USED IN THE DOUBLE-CONCENTRIC MODEL

Material	Ult. Strength (psi)	0.05% Off. Yield (psi)	Prop. Limit (psi)	Elastic Modulus (psi)	Poisson's Ratio
OFHC Copper	35,000	6,000	4,000	16.0×10^6	0.34
250 Alloy Maraging Steel	262,000	245,000	178,000	26.5×10^6	0.294
300 Alloy Maraging Steel	288,000	260,000	210,000	26.3×10^6	0.294

TABLE 8

SCHEDULE OF CONFIGURATIONS
OF
DISCONTINUOUS FIBER COMPOSITES
COMPLETED TO DATE

Packing	Loose*	Close		
No. of Cracks	One	One	three, four	
Location of Cracks	central fiber	central fiber	a) all in one plane b) out of plane	
			1/8" between planes	3 in one plane, one 0.1" away
End Type	Squared, Zero gap, copper filled	a)notched b)squared, zero gap copper filled	squared, zero gap copper filled	

* Data from Reference 2

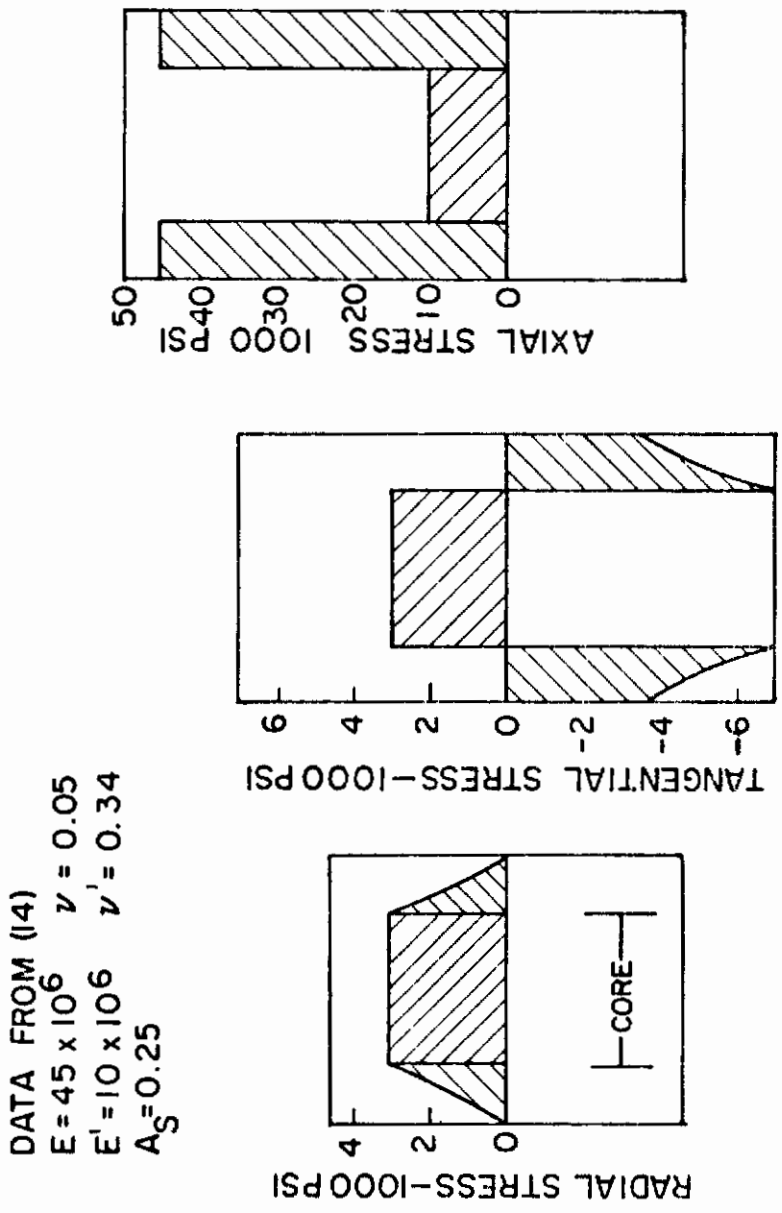

Figure 1

Stress Distribution of a Two-Component Cylindrical Composite Loaded in Axial Tension into the Elastic Behavioral Region.

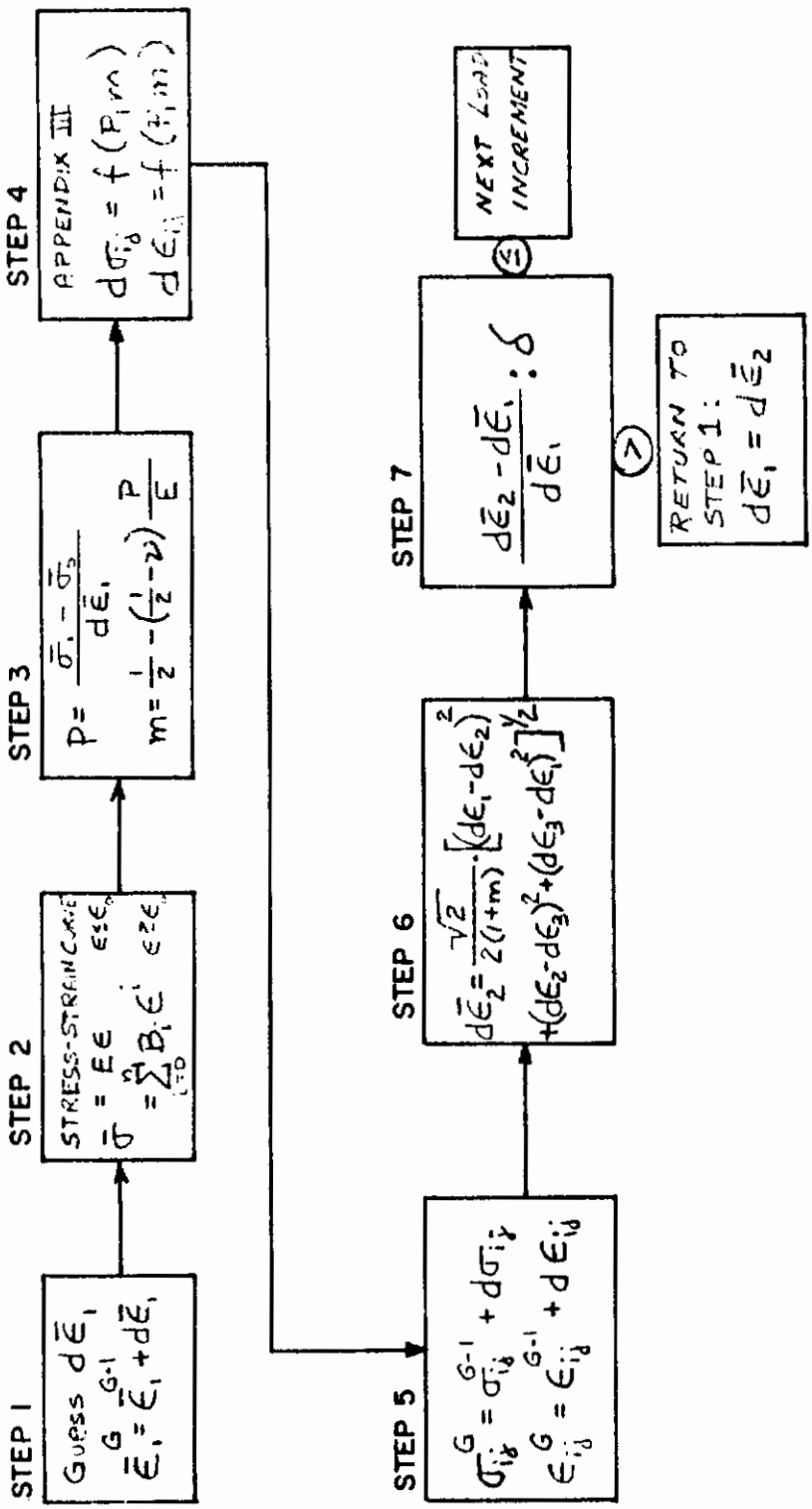

Figure 2

Iteration Scheme for the Plasticity Analysis

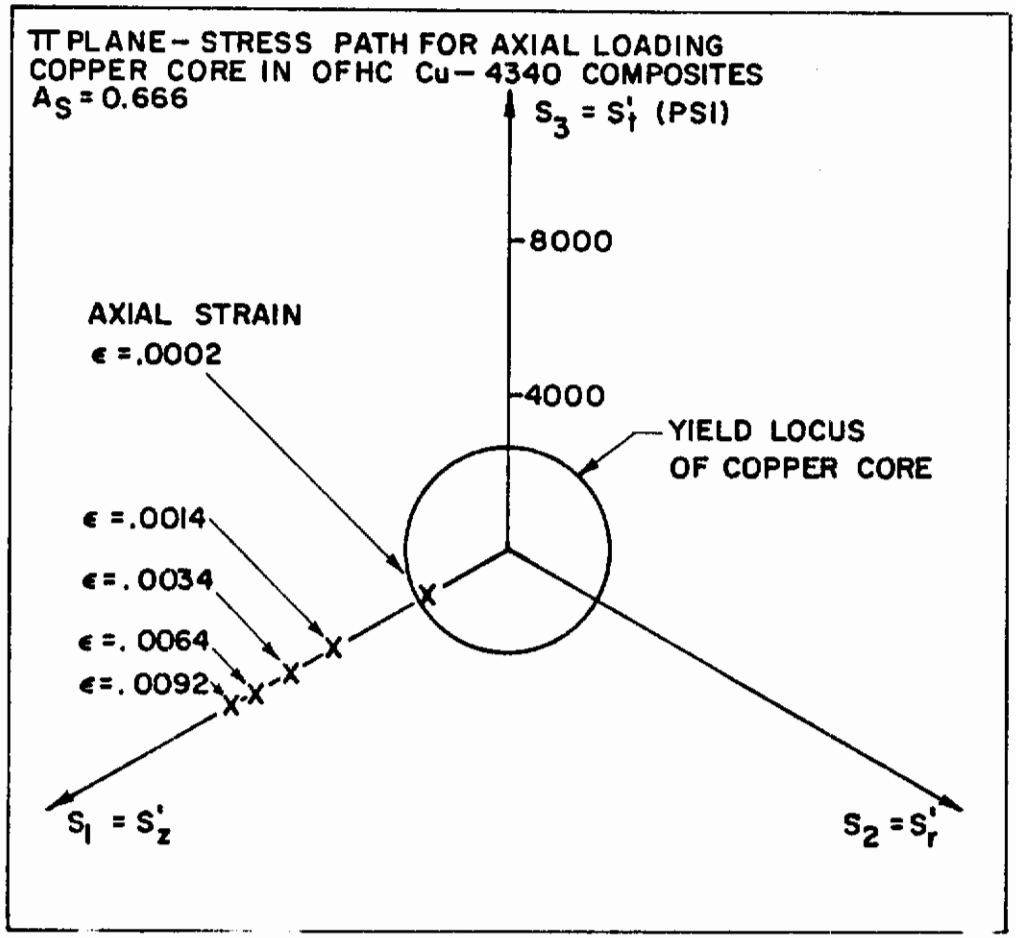

Figure 3

Axial Loading Path of the OFHC Copper Core of an OFHC Copper – 4340 Steel Composite ($A_s = 0.666$).

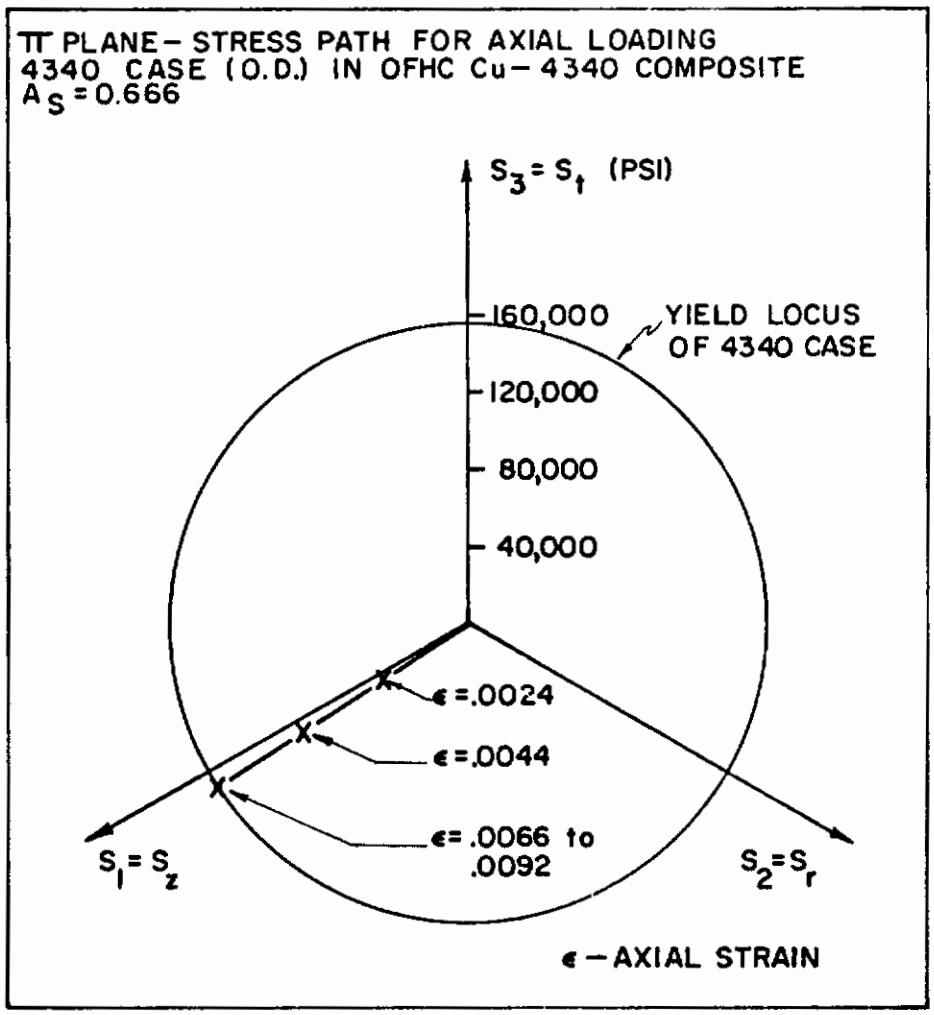

Figure 4

Axial Loading of the 4340 Steel Case of an OFHC Copper - 4340 Steel Composite (A_s = 0.666).

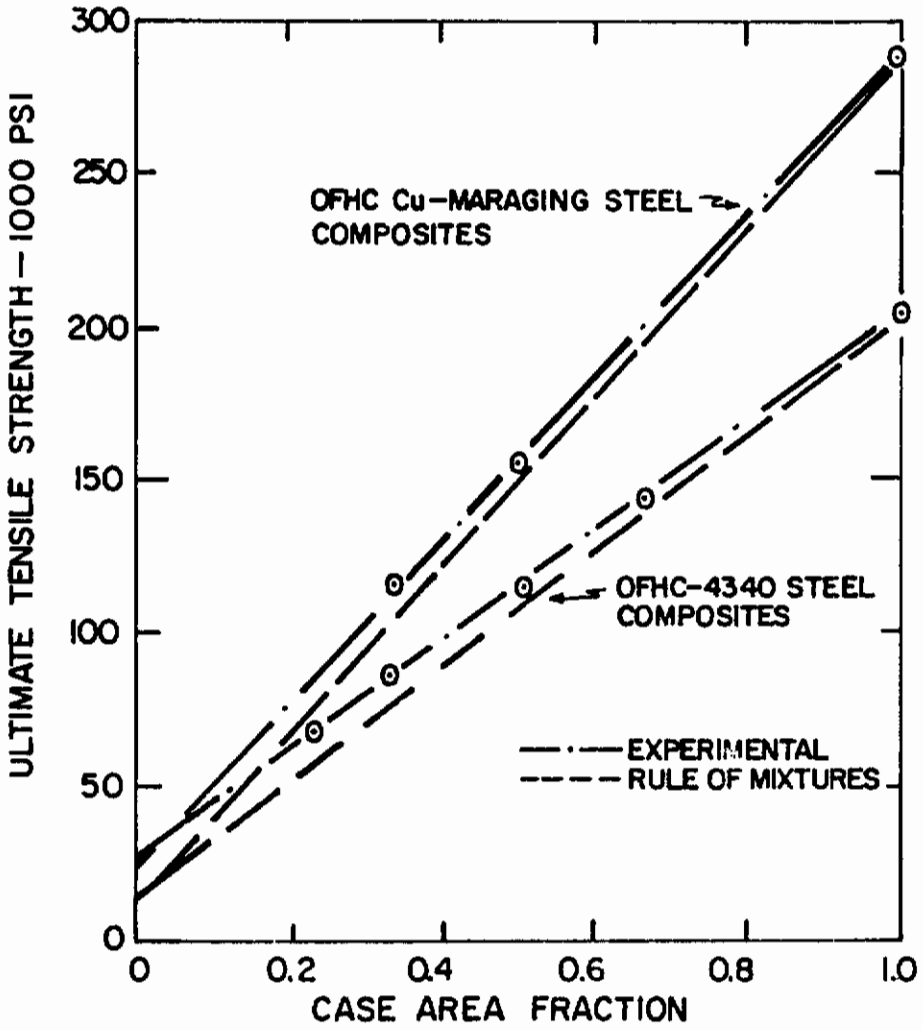

Figure 5

Ultimate Tensile Strengths for OFHC Copper - 4340 Steel and OFHC Copper - Maraging Steel Composites.

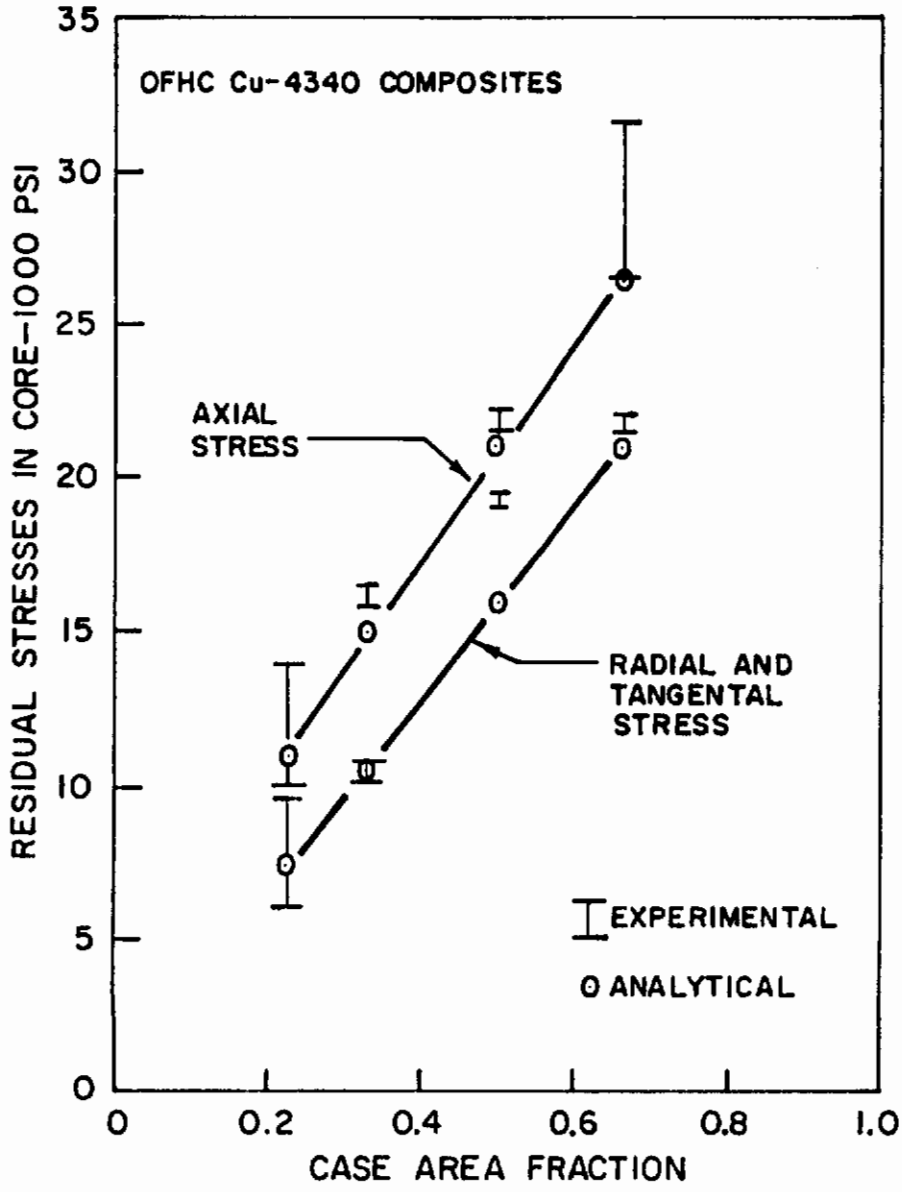

Figure 6

Residual Stresses in the Core Components of OFHC Copper - 4340 Steel Composites.

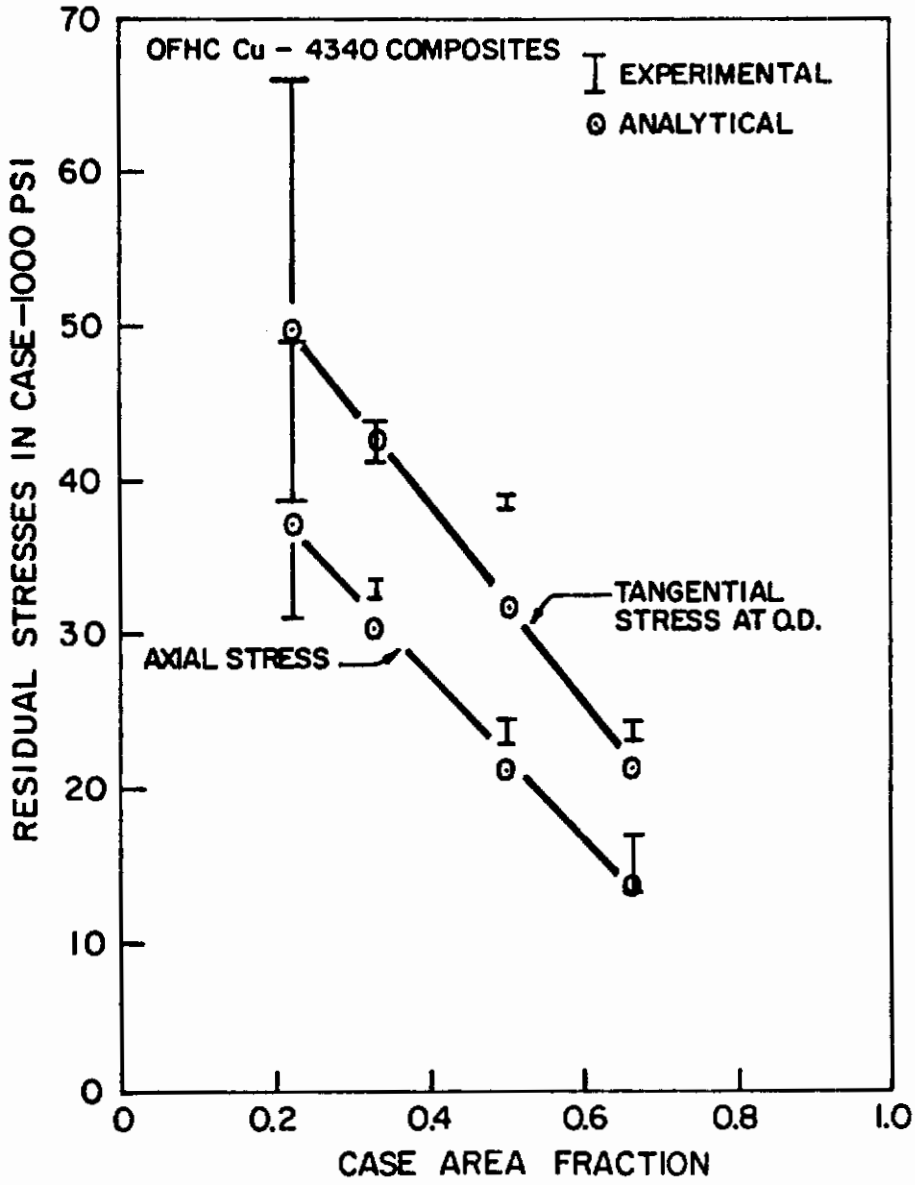

Figure 7

Residual Stresses in the Case Components of OFHC Copper - 4340 Steel Composites.

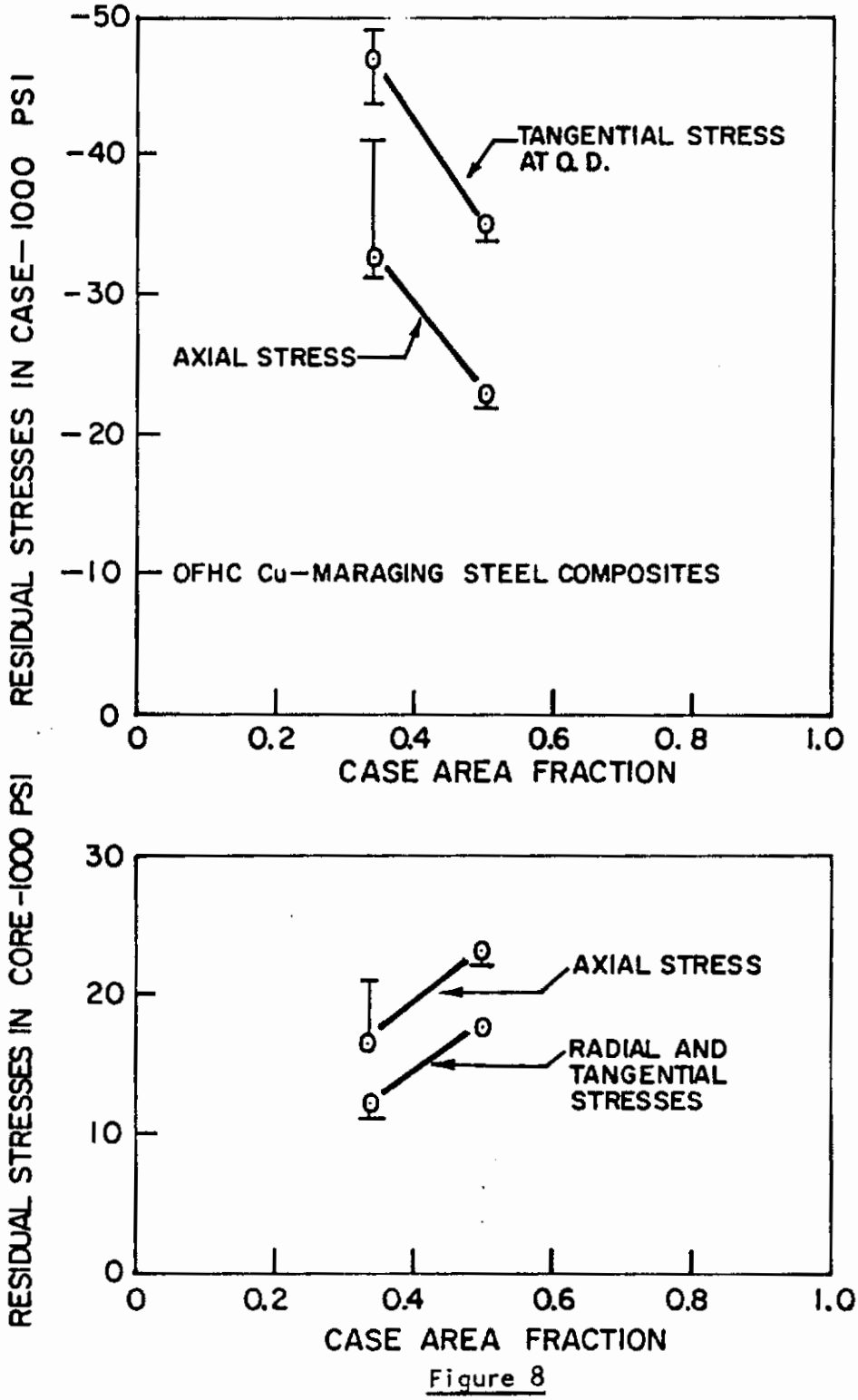

Figure 8

Residual Stresses in the Core and Case Components of OFHC Copper - Maraging Steel Composites.

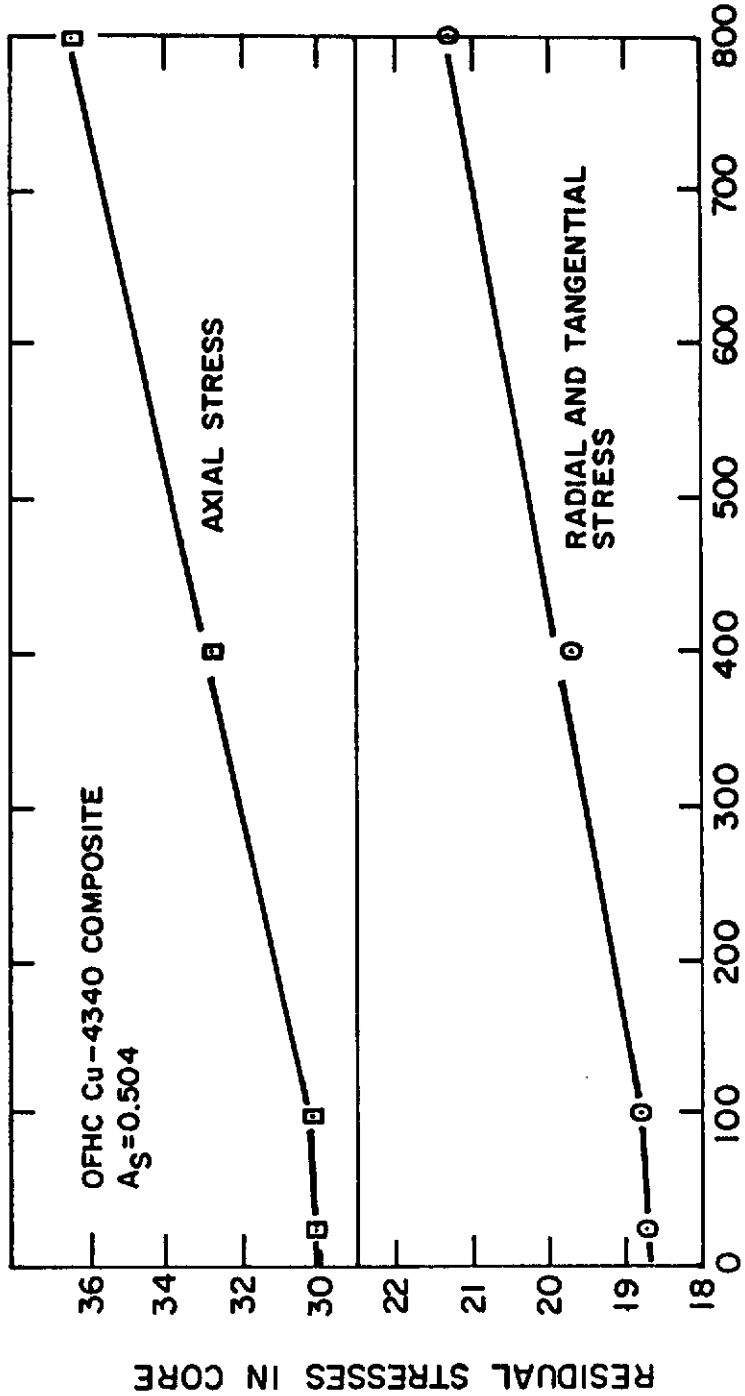

Figure 9

Residual Stresses in the Core of an OFHC Copper - 4340 Steel Composite Predicted by the Elastic Thermal Loading Analysis (A_s = 0.504).

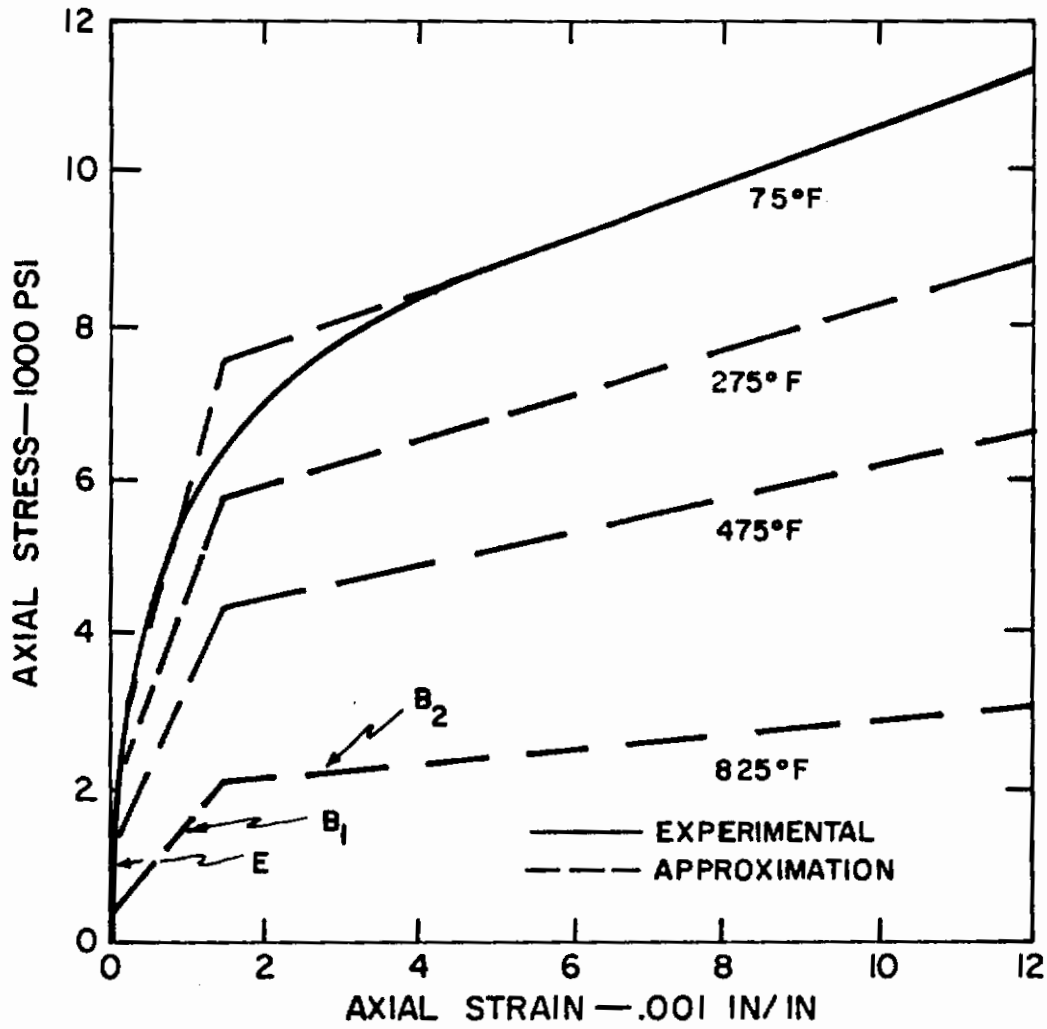

Figure 10

Experimental Stress-Strain Curve of OFHC Copper and Approximations of the Curves for Various Temperatures.

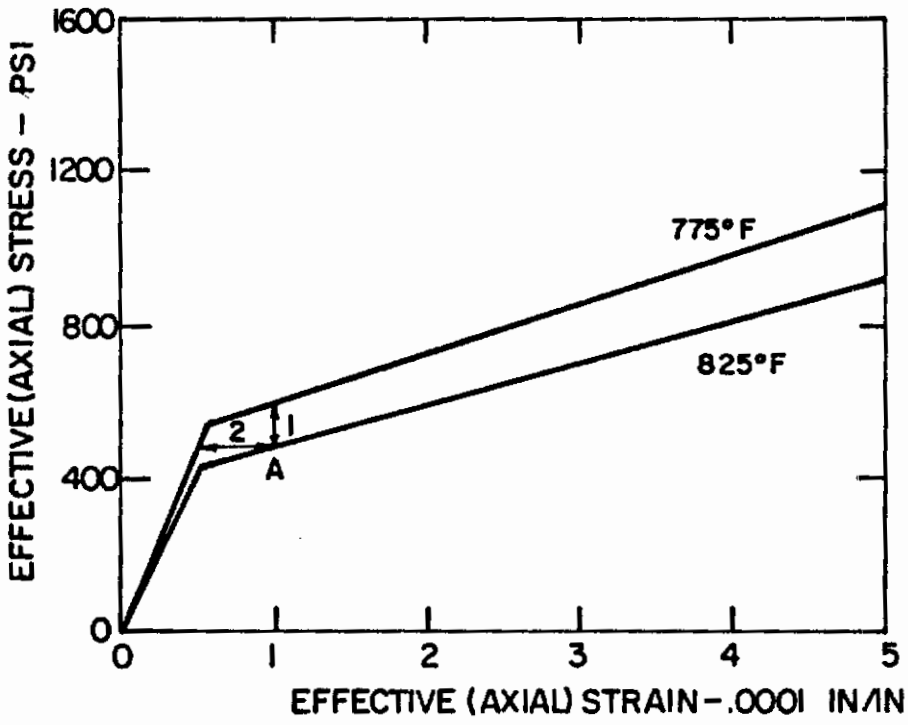

Figure 11

Effective Stress-Strain Curves of OFHC Copper at two Different Temperatures.

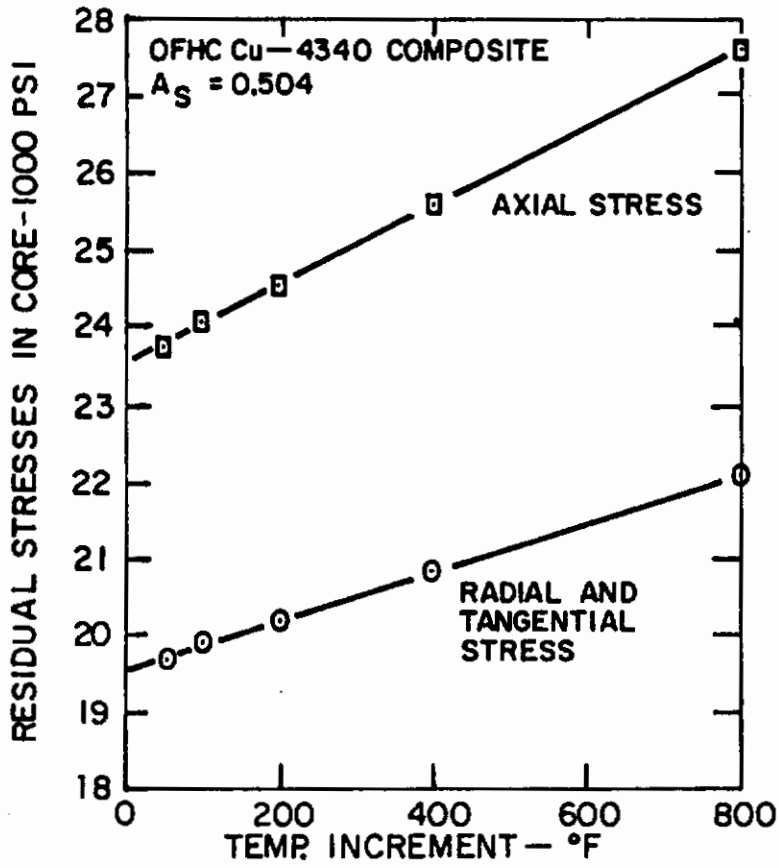

Figure 12

Residul Stresses in the Core of an OFHC Copper-4340 Steel Composite Predicted by the Plastic Thermal Loading Analysis (A_s = 0.504).

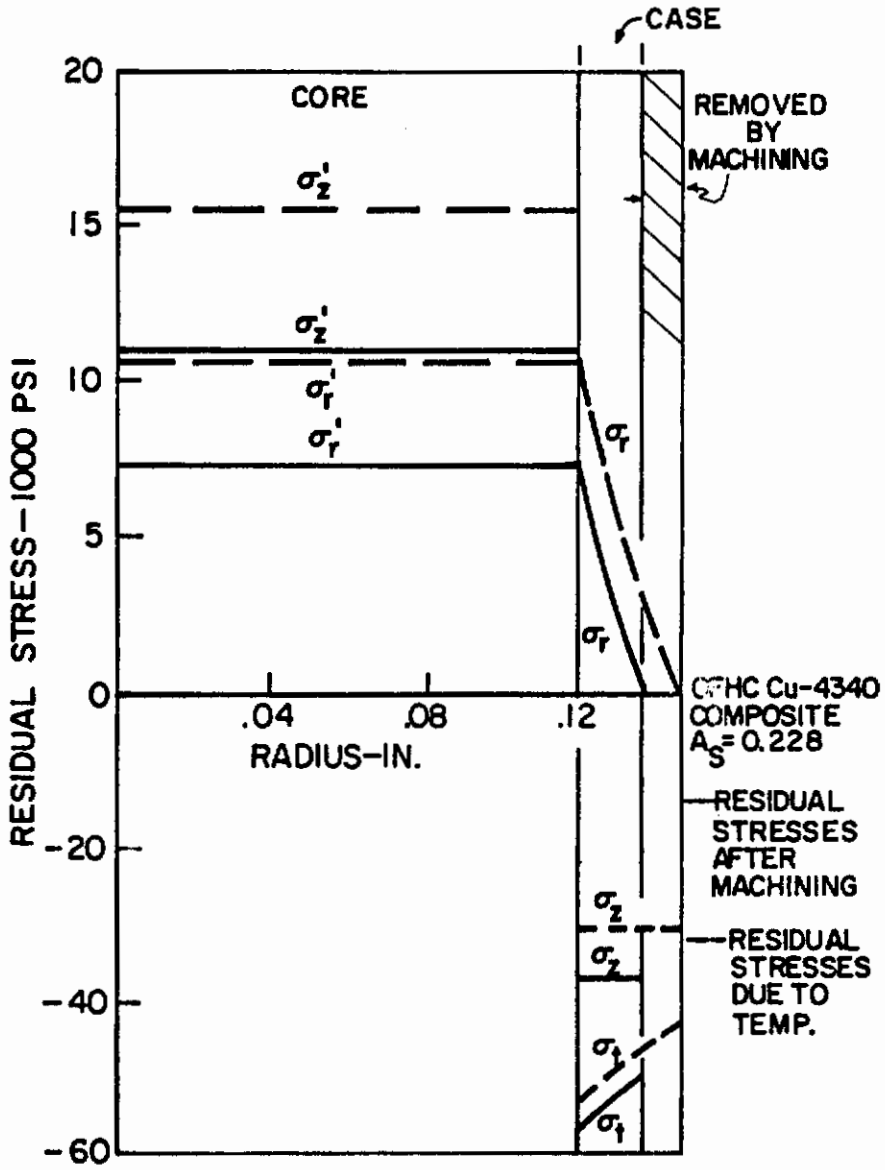

Figure 13

Residual Stress Distribution in an OFHC Copper 4340 Steel Composite Predicted by the Approximate Thermal Loading Model (A_s = 0.228).

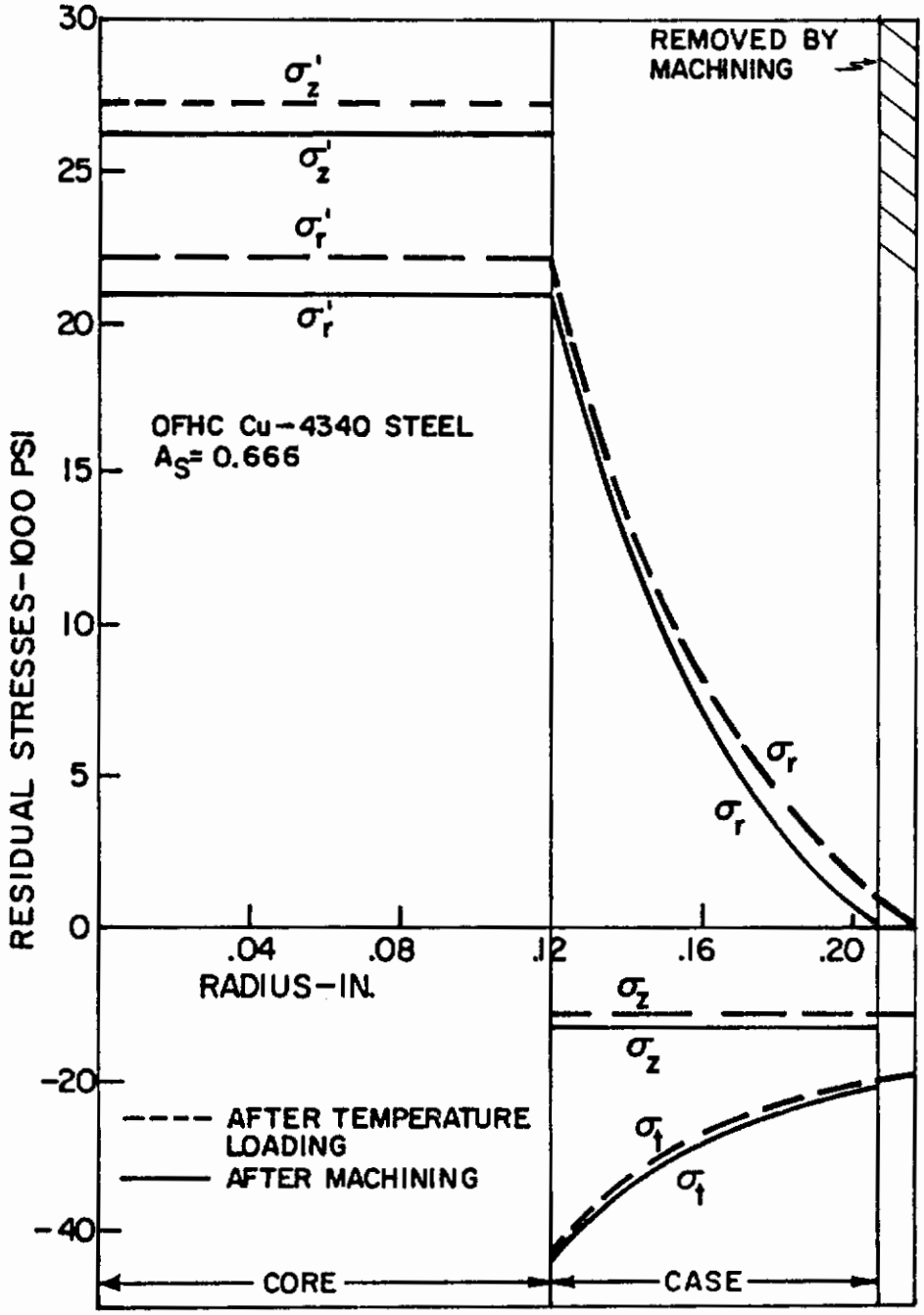

Figure 14

Residual Stress Distribution in an OFHC Copper-4340 Steel Composite Predicted by the Approximate Thermal Loading Model (A_s = 0.666).

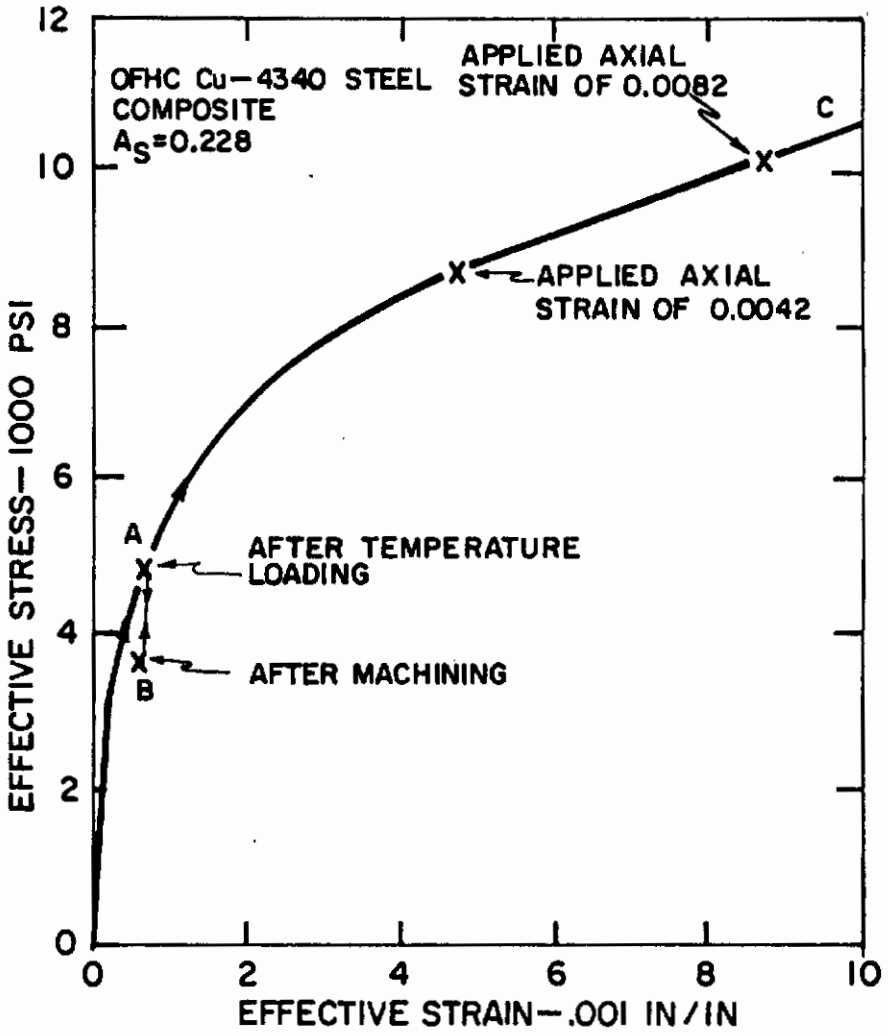

Figure 15

Loading Path on the Effective Stress-Strain Curve for an OFHC Copper - 4340 Steel Composite (A_s = 0.228).

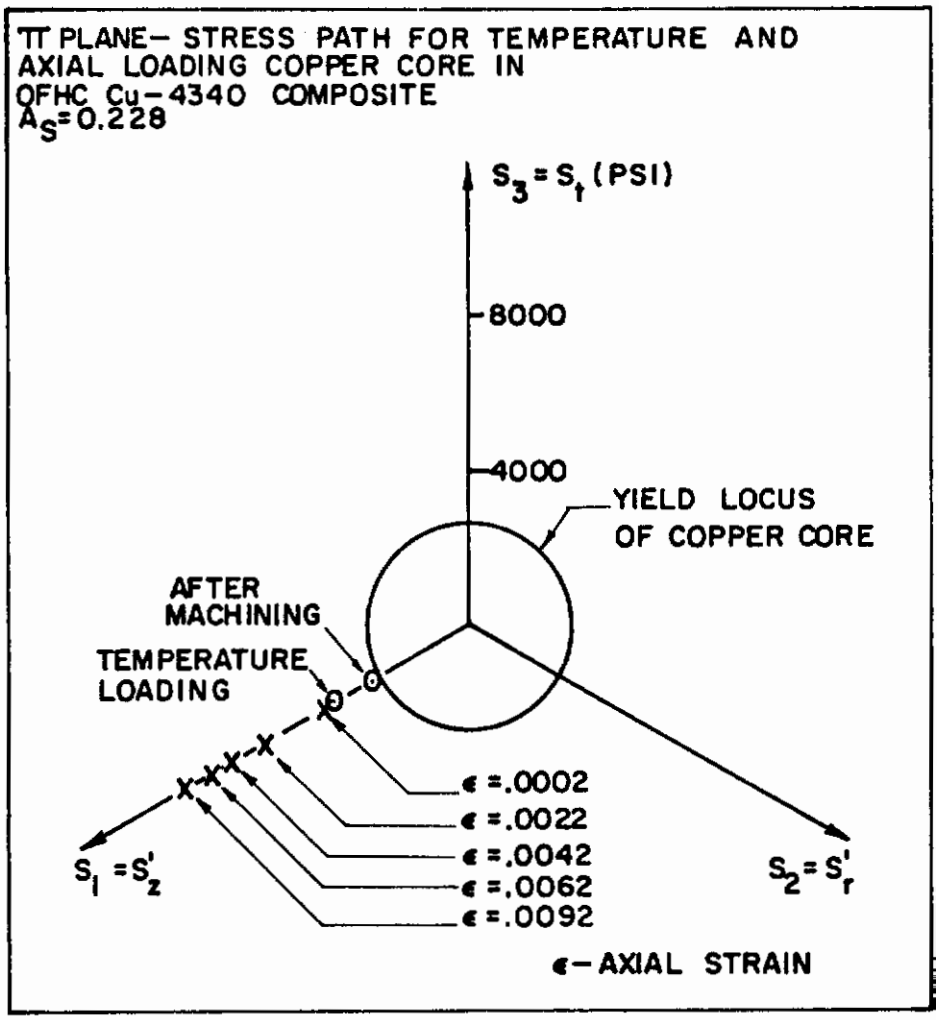

Figure 16

Loading Path for the Copper Core of an OFHC Copper - 4340 Steel Composite (A_s = 0.228).

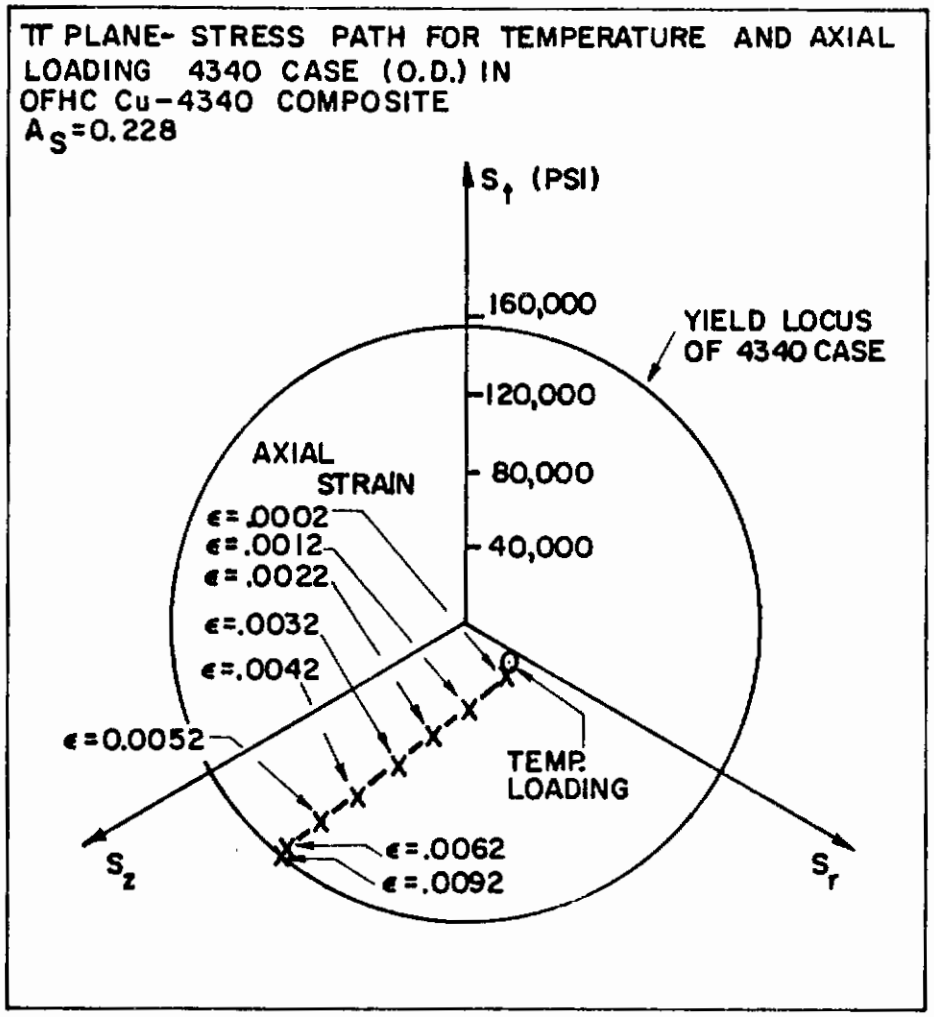

Figure 17

Loading Path for the 4340 Steel Case of an OFHC Copper - 4340 Steel Composite (A_s = 0.228).

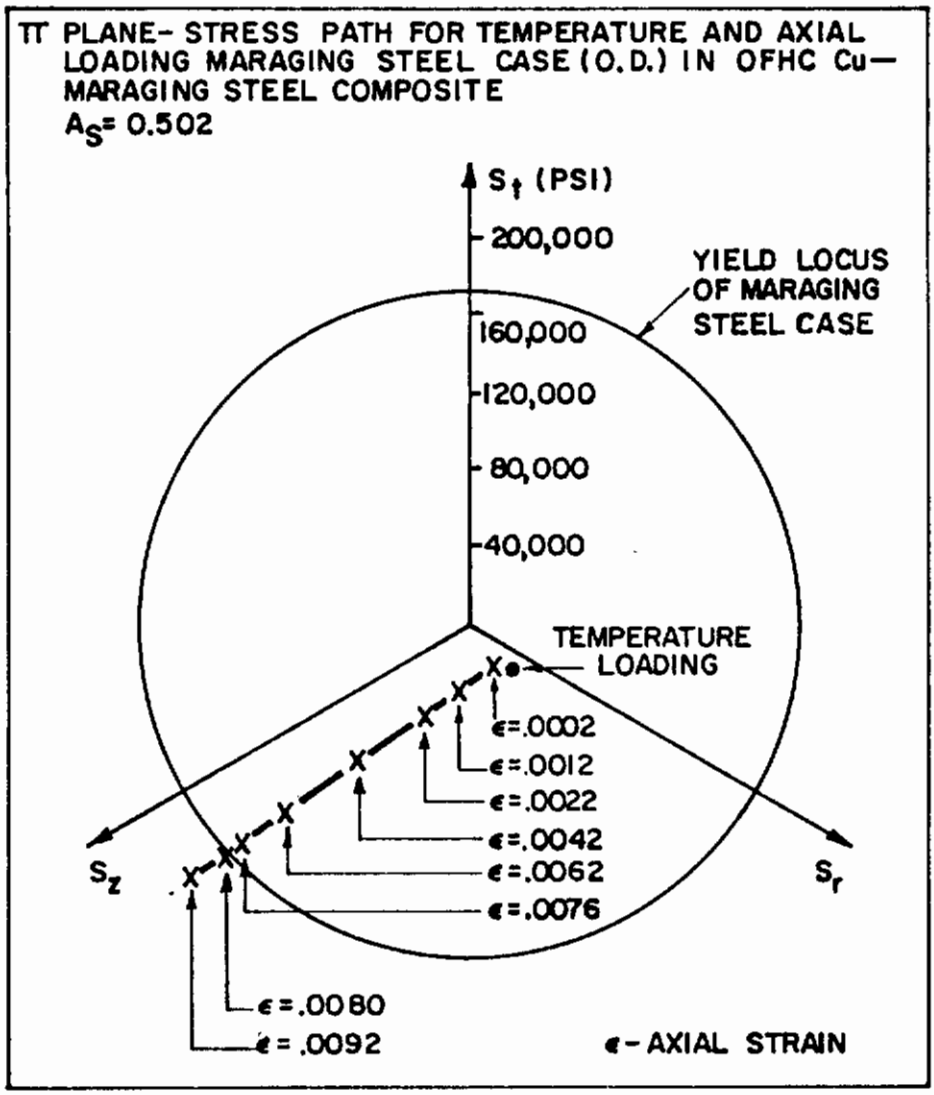

Figure 18

Loading Path for the Maraging Steel Case of an OFHC Copper - Maraging Steel Composite (A_s= 0.502).

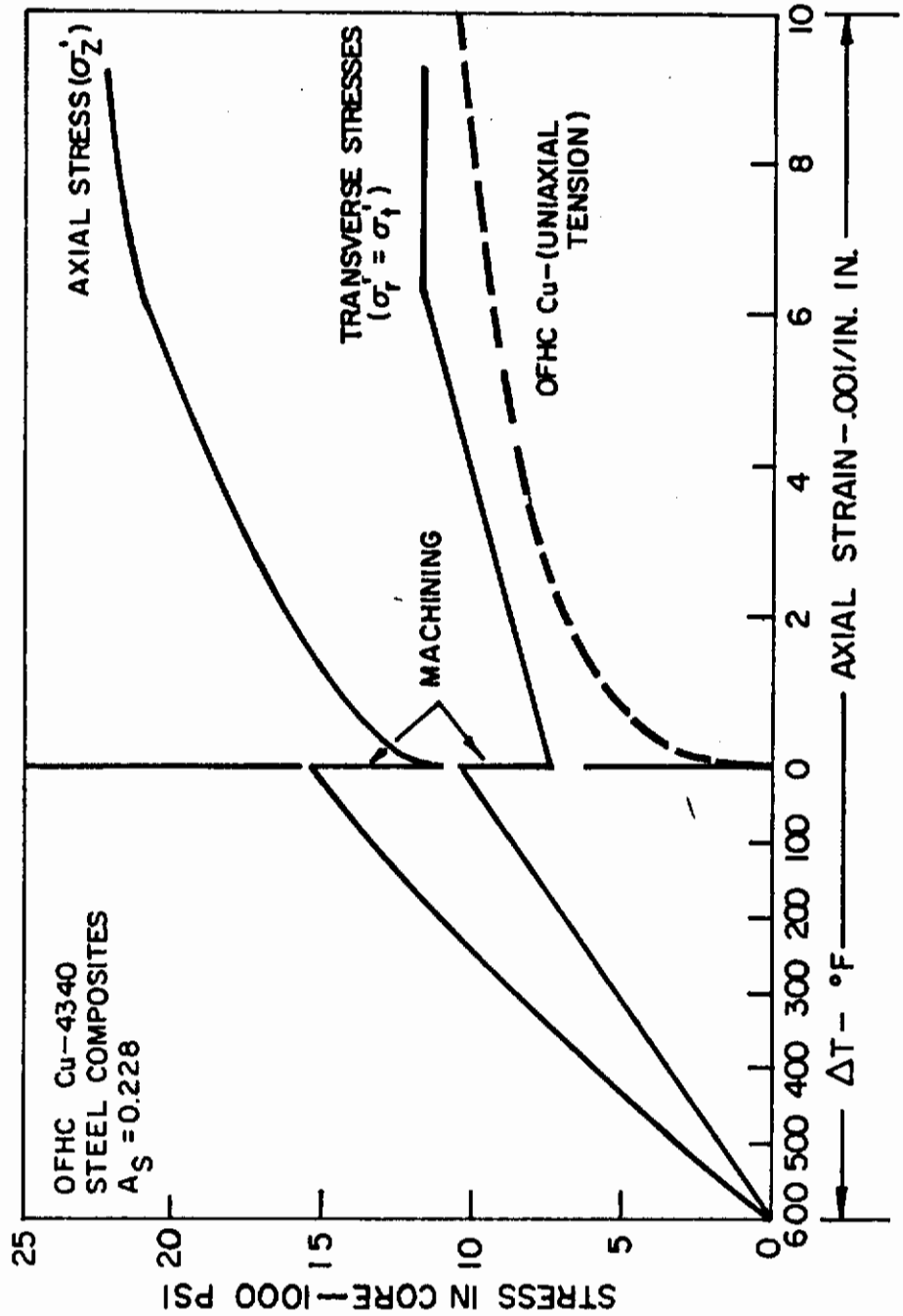

Figure 19

Stresses in the Core of an OFHC Copper - 4340 Steel Composite during All Three Stages of Loading (A_s = 0.228).

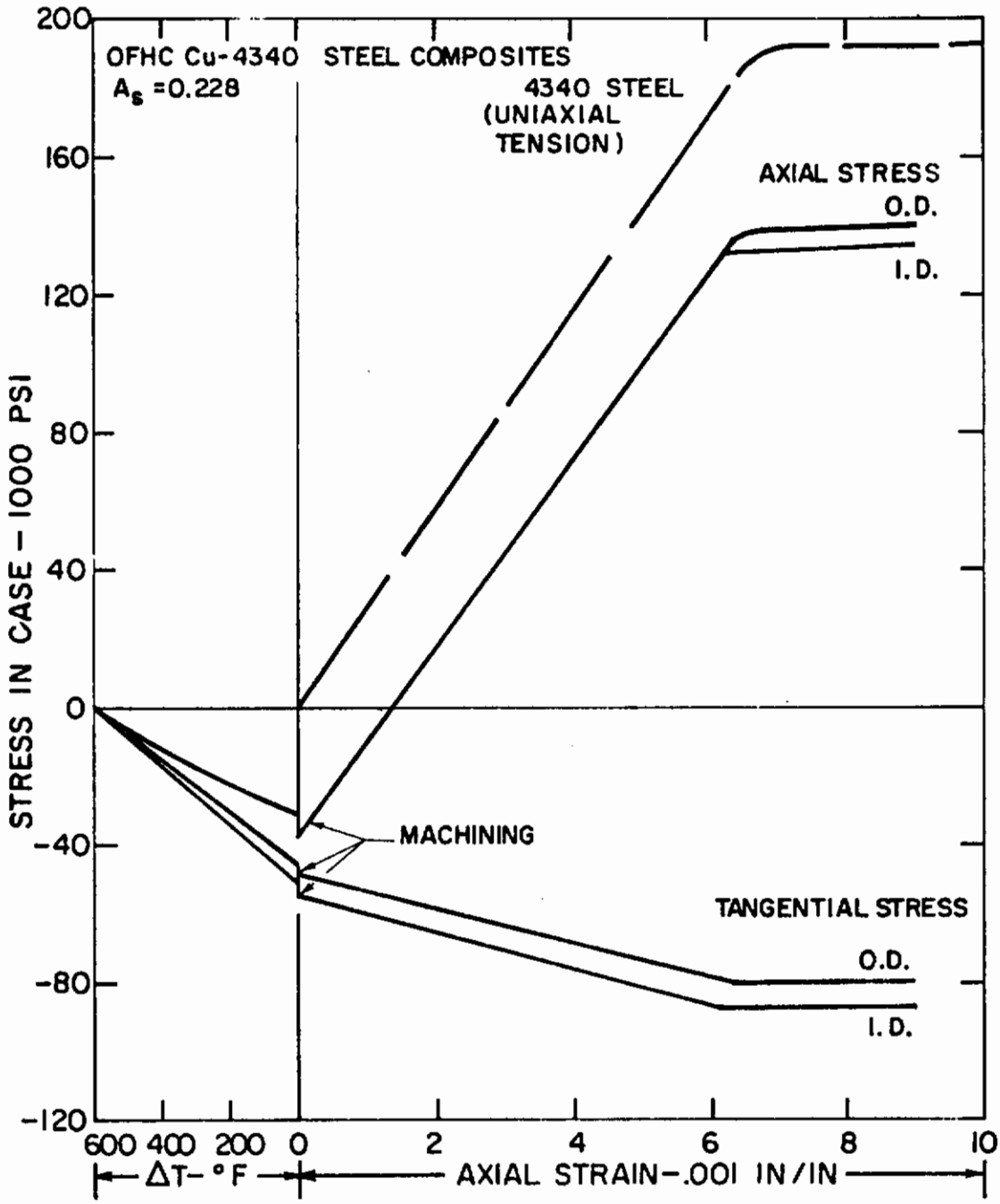

Figure 20

Stresses in the Case of an OFHC Copper - 4340 Steel Composite during All Three Stages of Loading (A_s = 0.228).

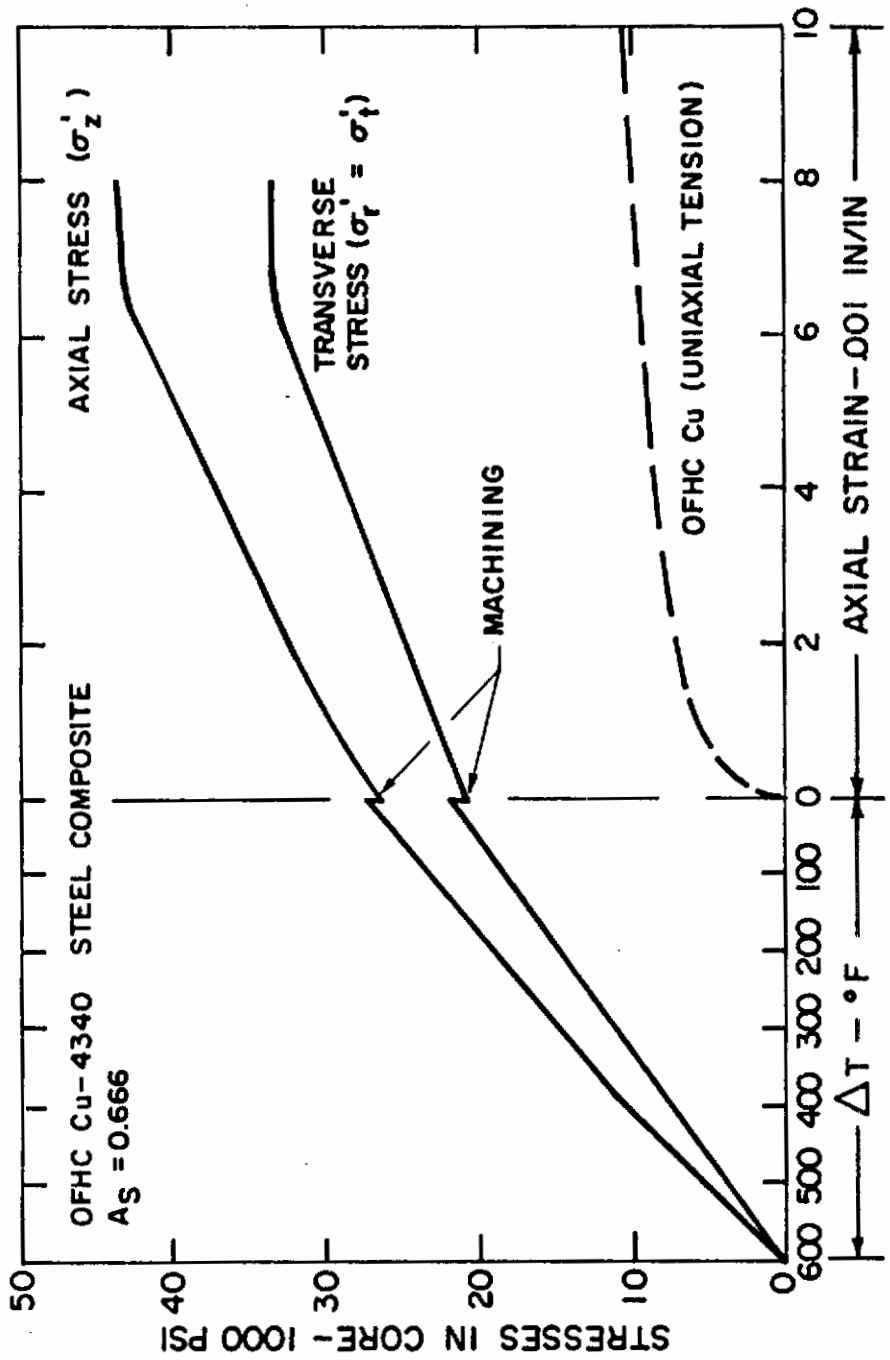

Figure 21

Stresses in the Core of an OFHC Copper - 4340 Steel Composite during All Three Stages of Loading (A_s = 0.666).

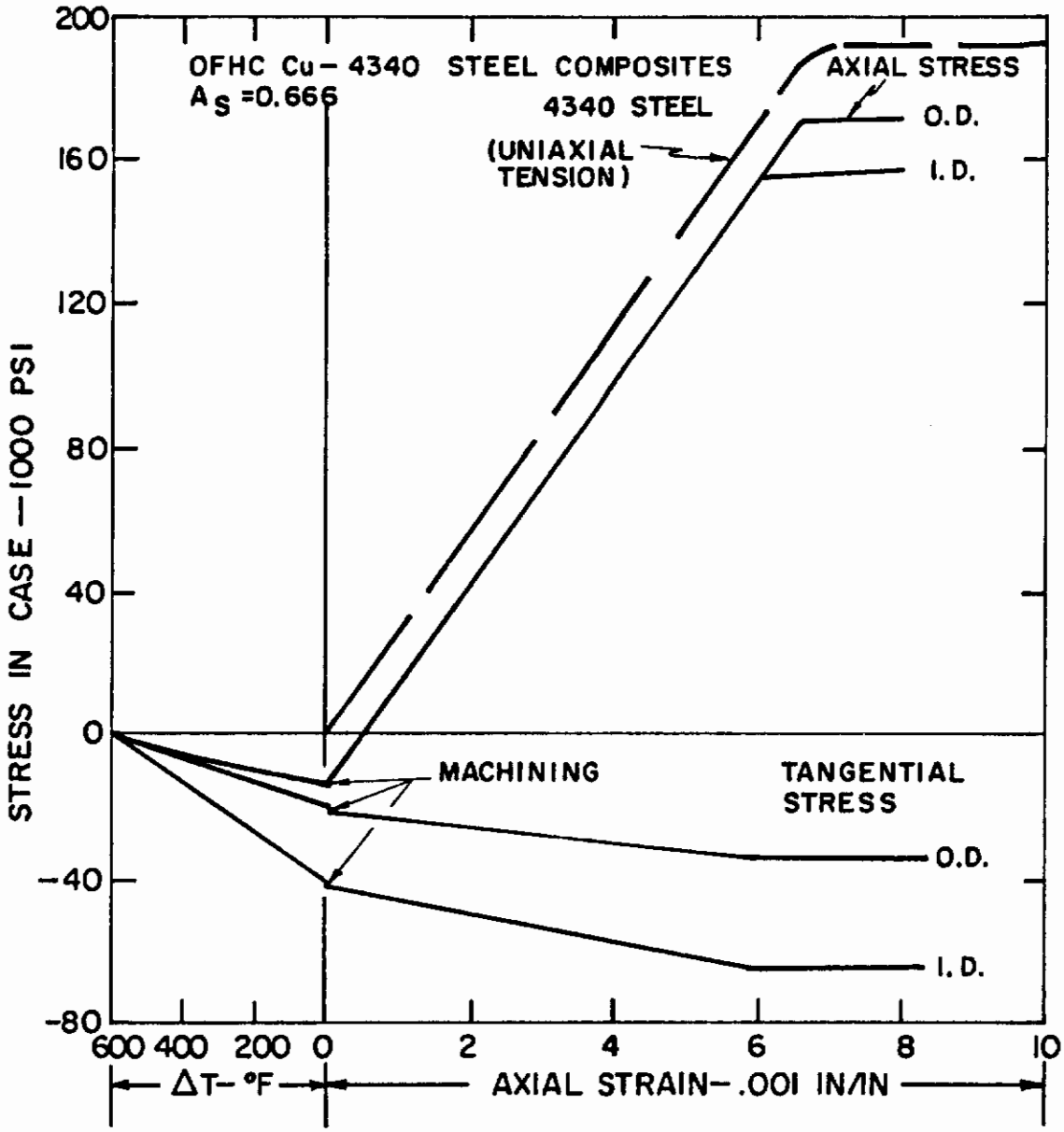

Figure 22

Stresses in the Case of an OFHC Copper - 4340 Steel Composite during All Three Stages of Loading (A_s = 0.666).

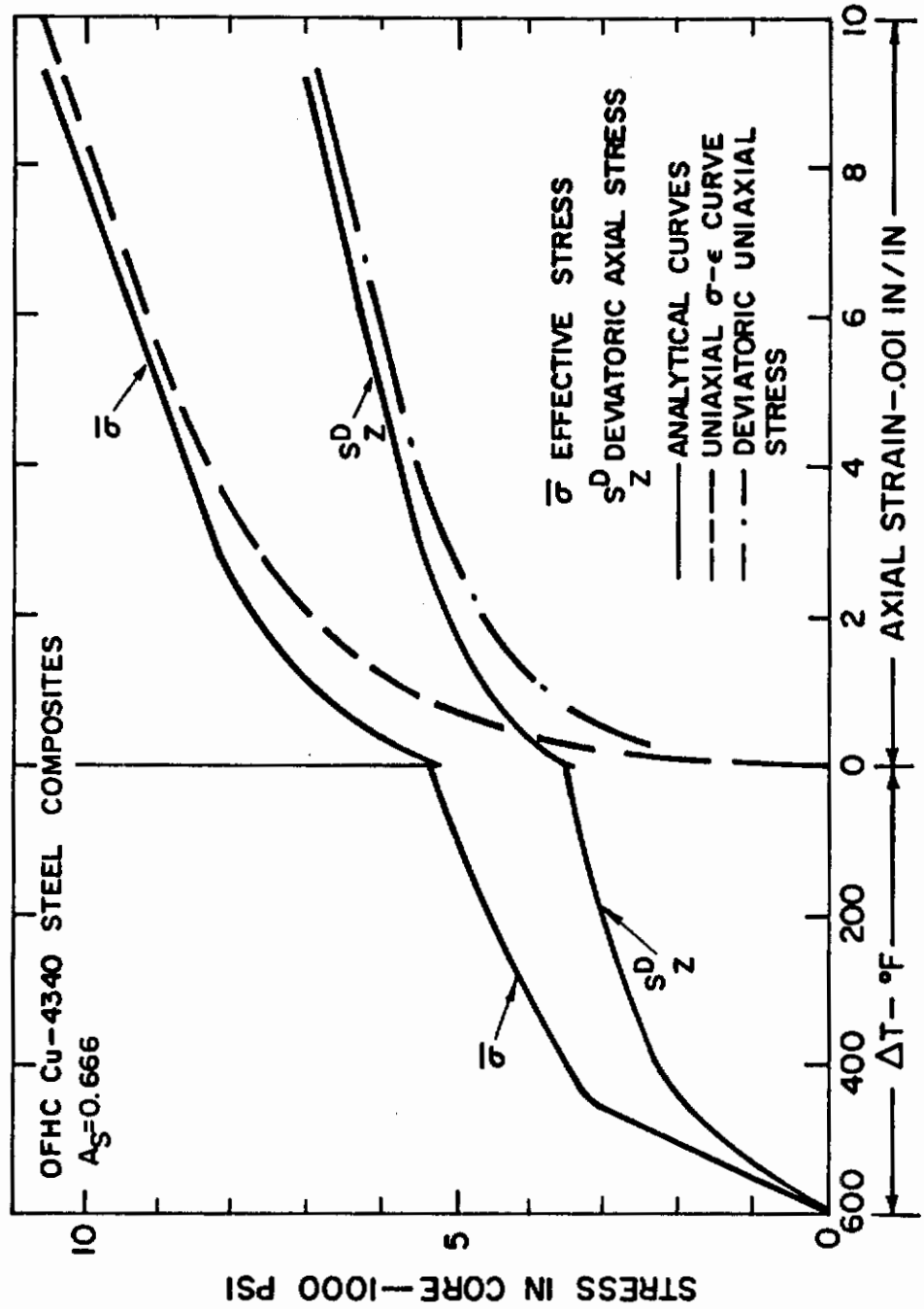

Figure 23

Effective and Axial Deviatoric Stresses in the Core of an OFHC Copper - 4340 Steel Composite during All Three Stages of Loading (A_s = 0.228).

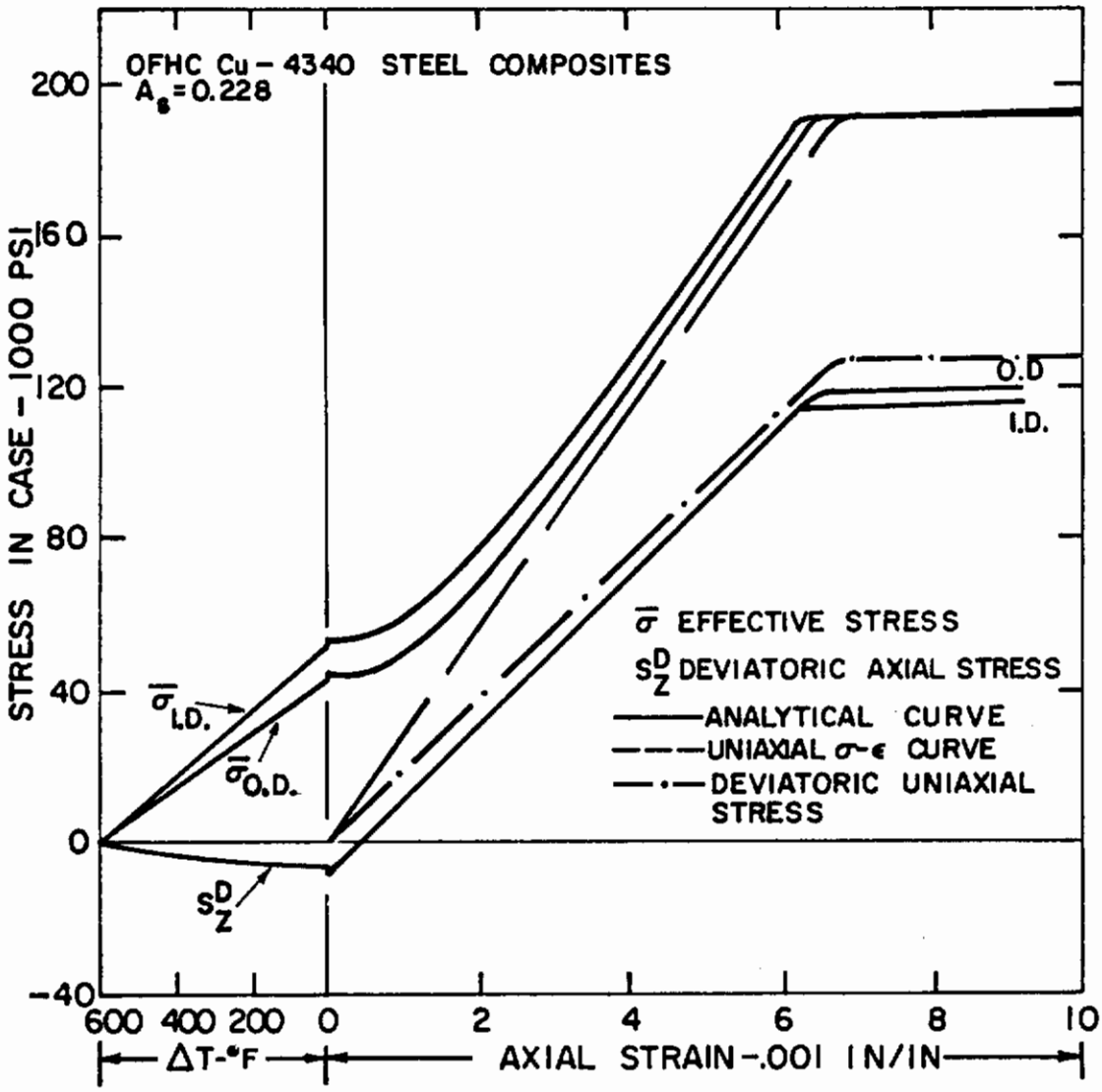

Figure 24

Effective and Axial Deviatoric Stresses in the Case of an OFHC Copper - 4340 Steel Composite During All Three Stages of Loading (A_s = 0.228).

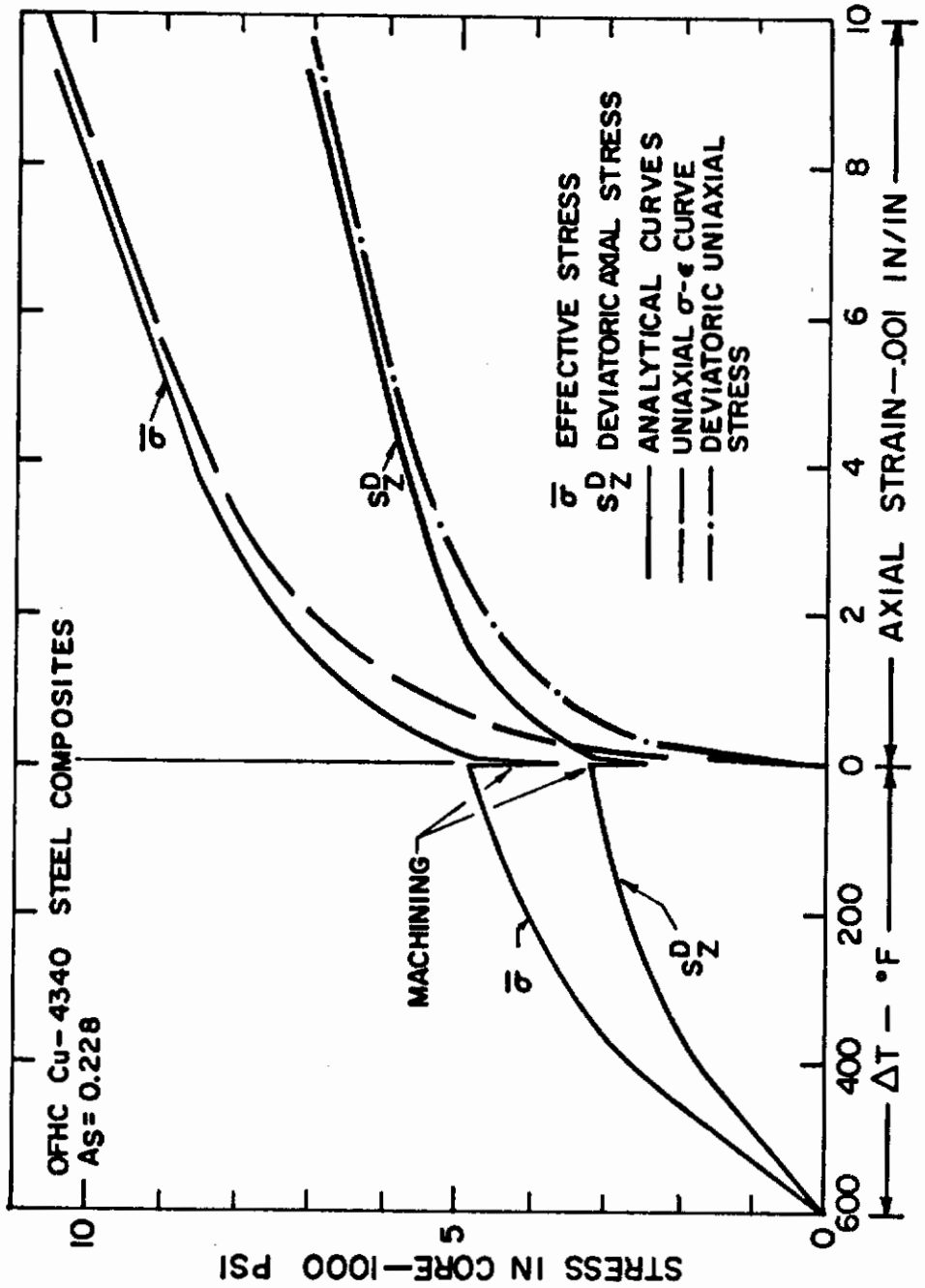

Figure 25

Loading Path for the Copper Core of an OFHC Copper - 4340 Steel Composite (A_s = 0.666).

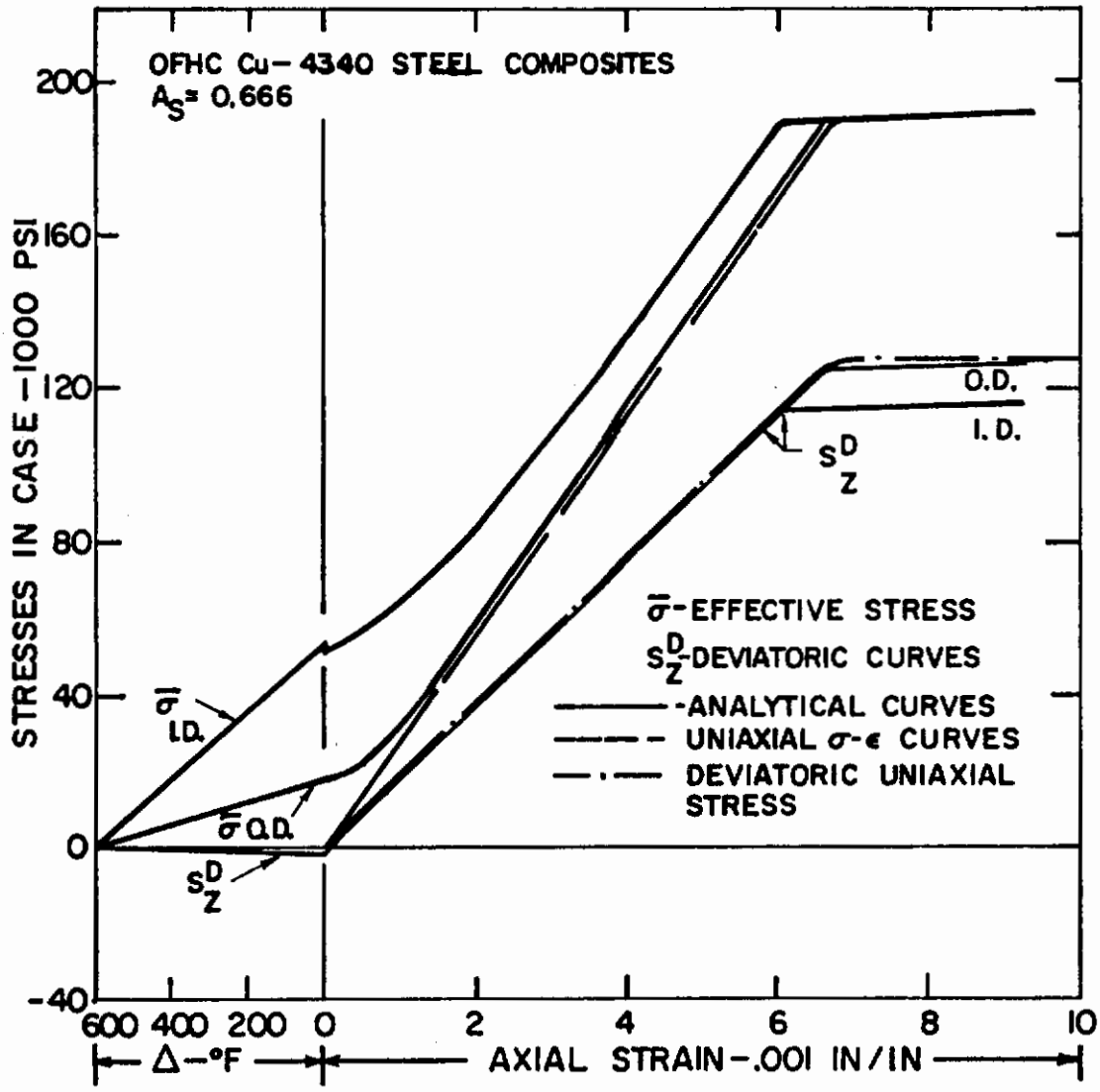

Figure 26

Loading Path for the 4340 Steel Case of an OFHC Copper - 4340 Steel Composite (A_s = 0.666).

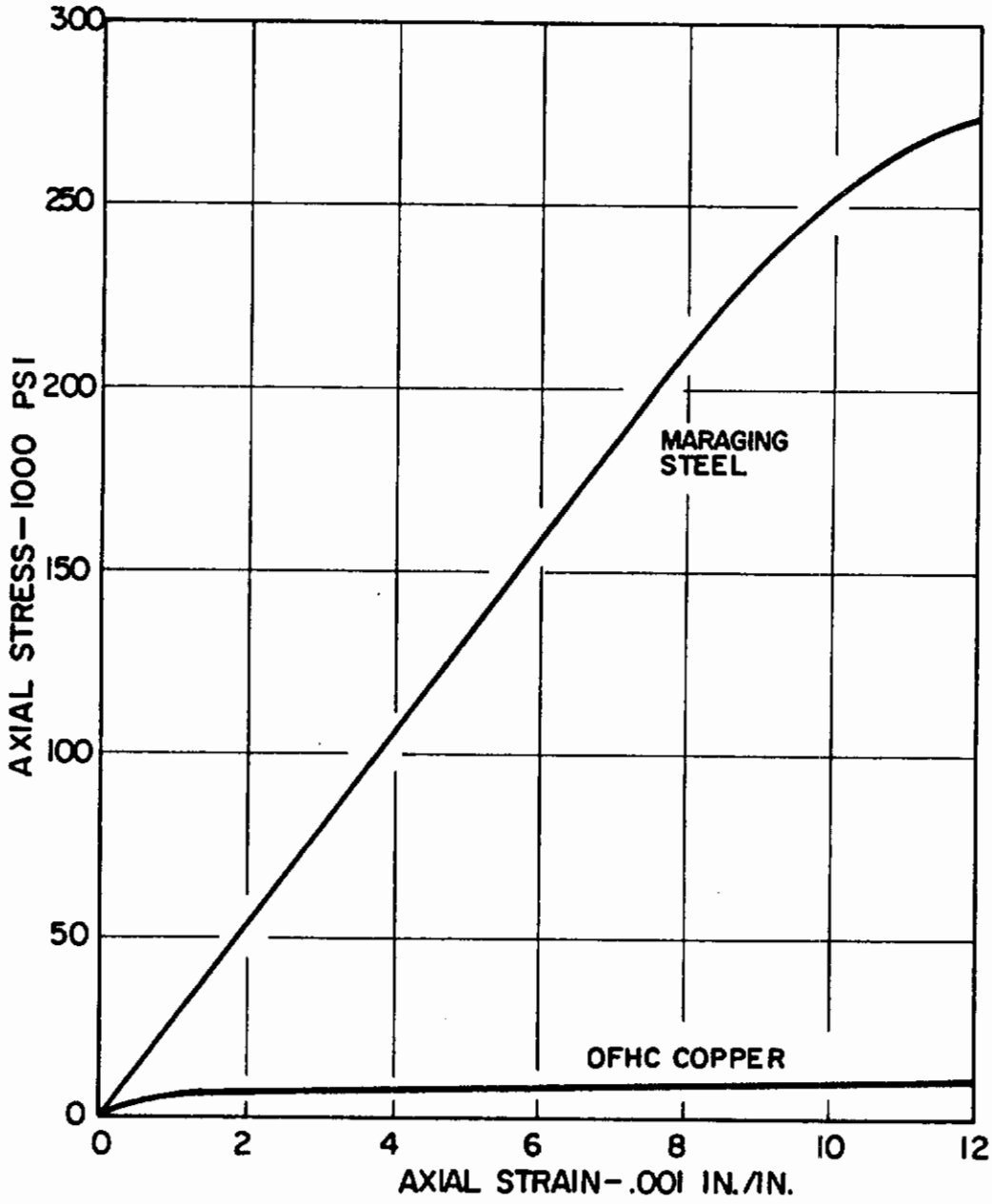

Figure 27

Experimental Stress-Strain Curves for OFHC Copper and Maraging Steel Tensile Specimens.

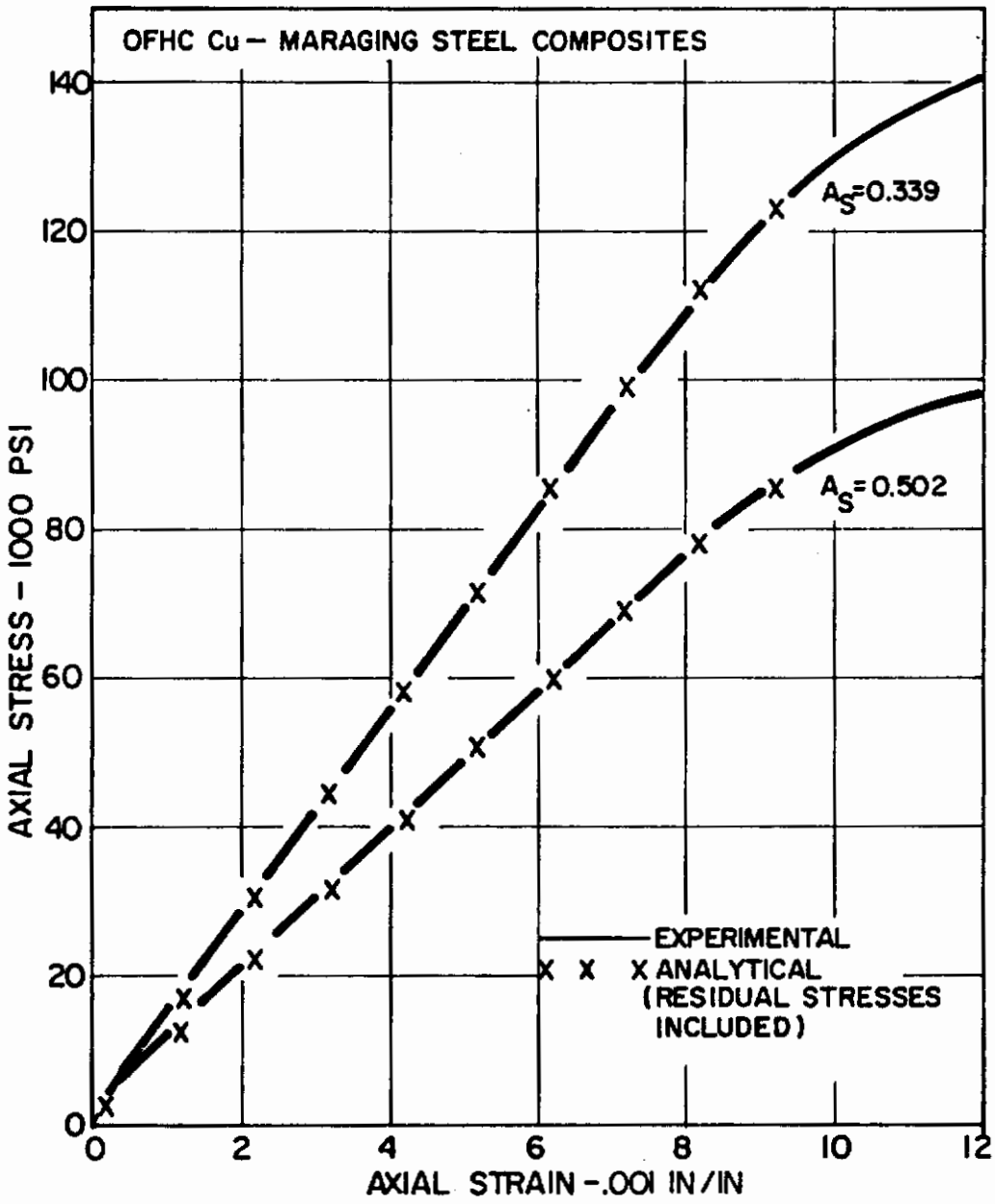

Figure 28

Experimental and Residual Stress Modified Analytical Stress-Strain Curves for OFHC Copper - Maraging Steel Composites.

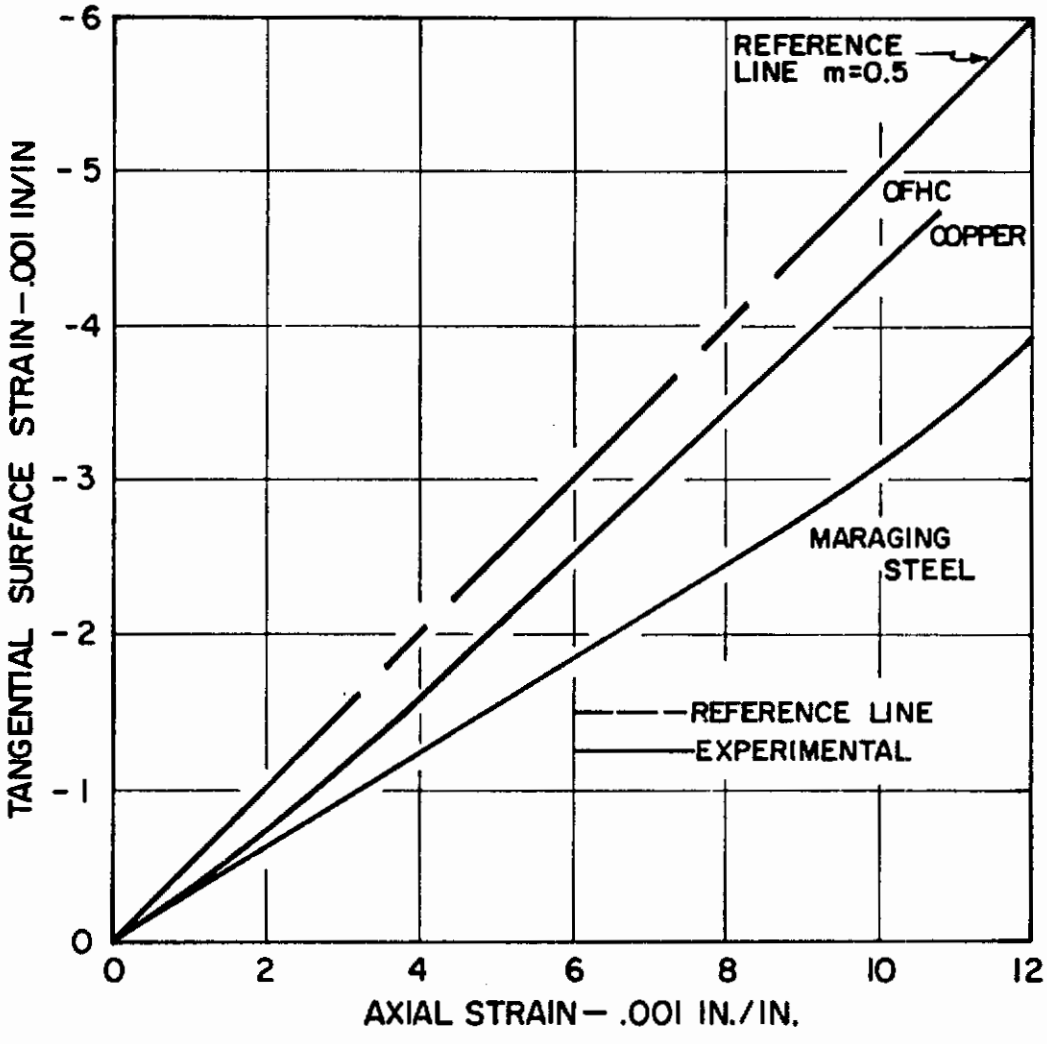

Figure 29

Tangential Surface Strain as a Function of Axial Strain for OFHC Copper and Maraging Steel Tensile Specimens.

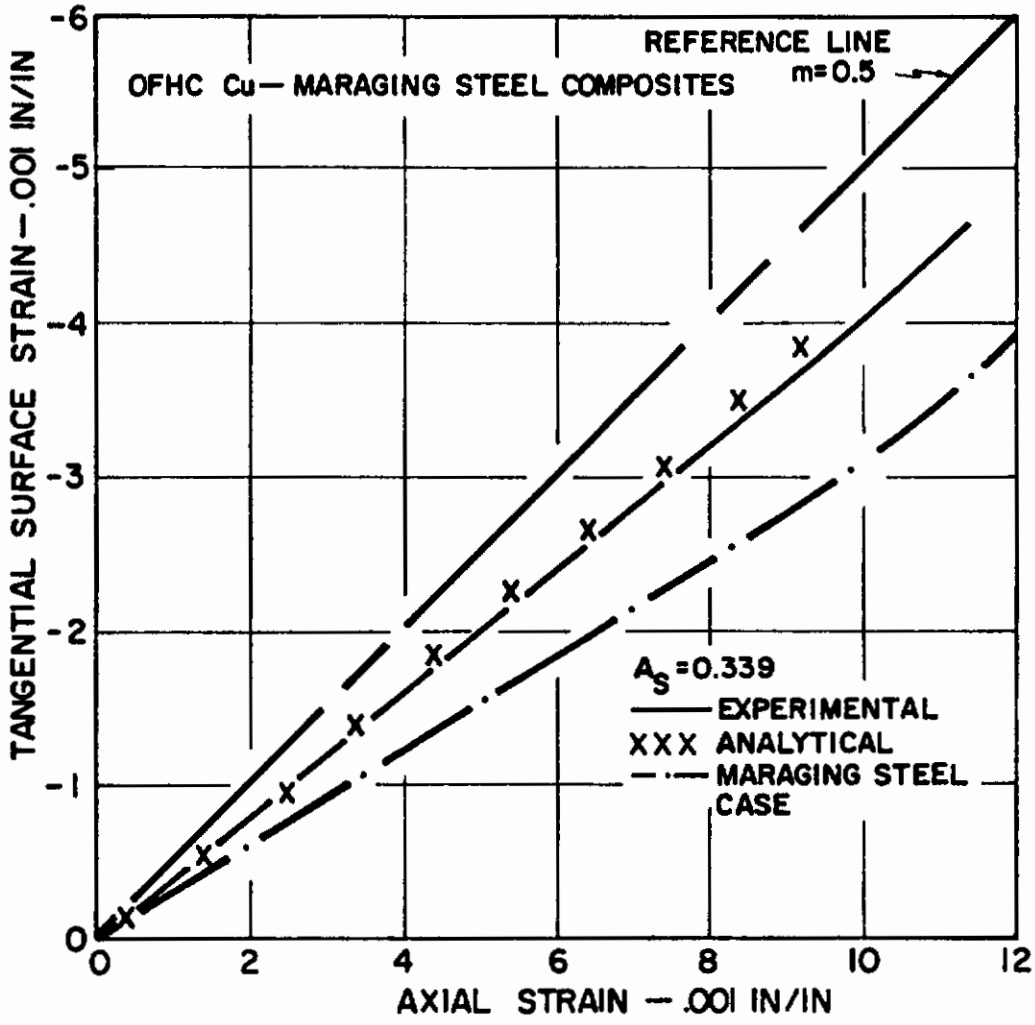

Figure 30

Tangential Surface Strain as a Function of Axial Strain for OFHC Copper - Maraging Steel Composite Tensile Specimens (A_s = 0.339).

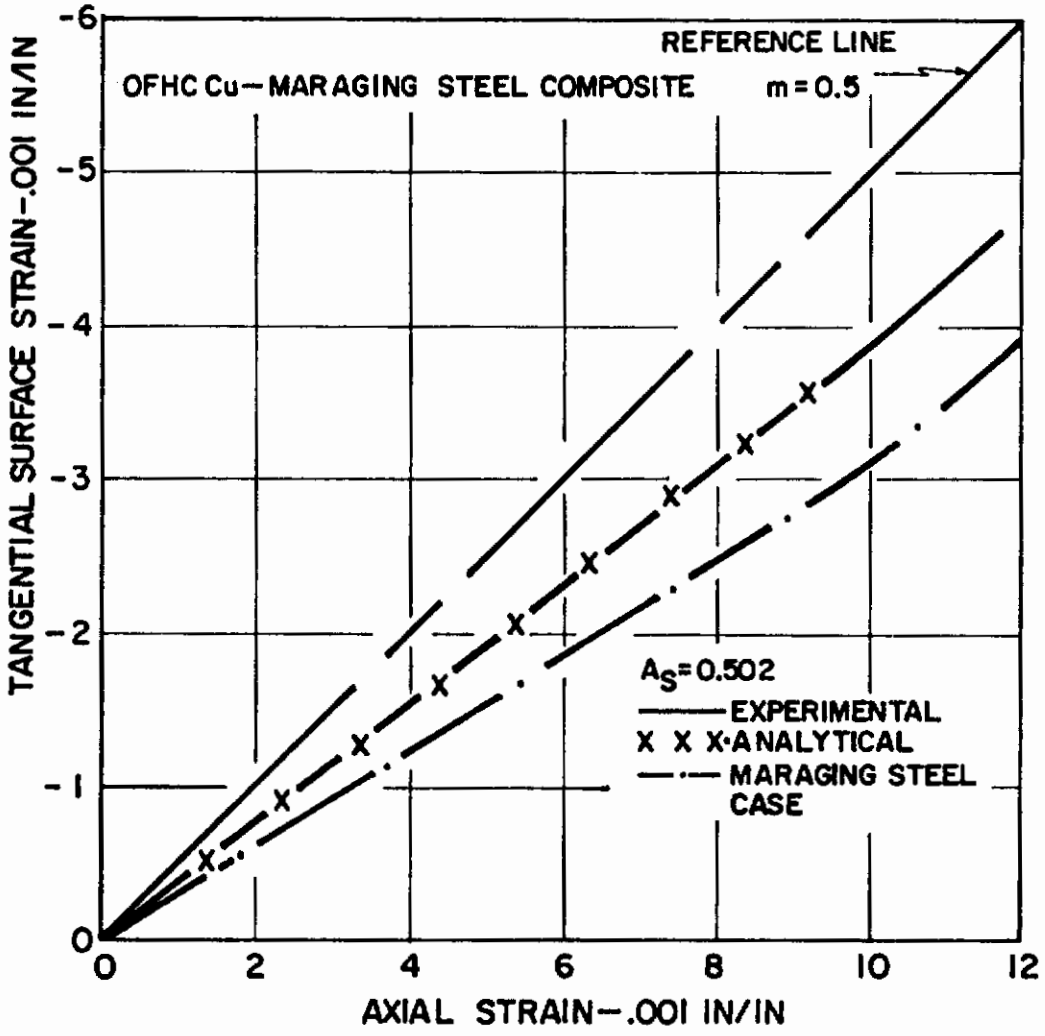

Figure 31

Tangential Surface Strain as a Function of Axial Strain for OFHC Copper - Maraging Steel Composite Tensile Specimens (A_s = 0.502).

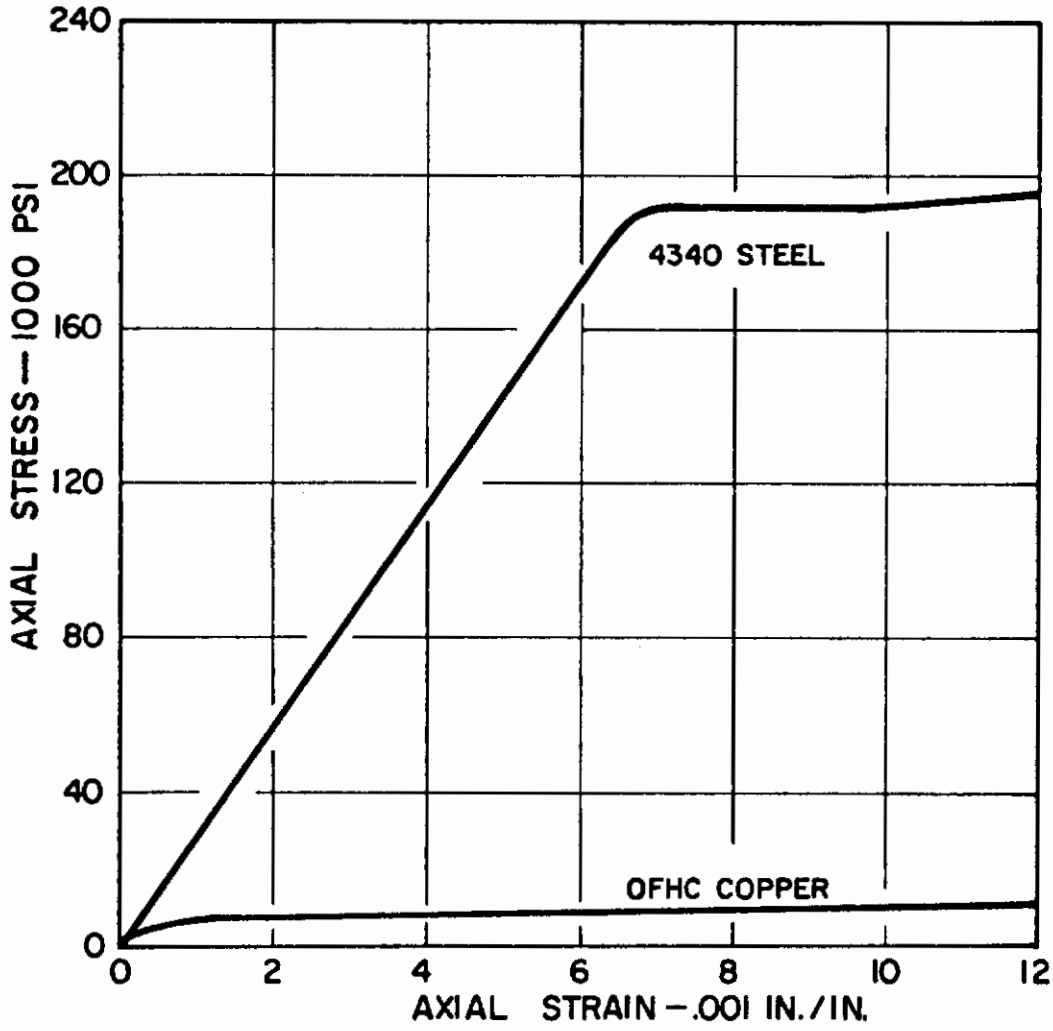

Figure 32

Experimental Stress-Strain Curves for OFHC Copper and 4340 Steel Tensile Specimens.

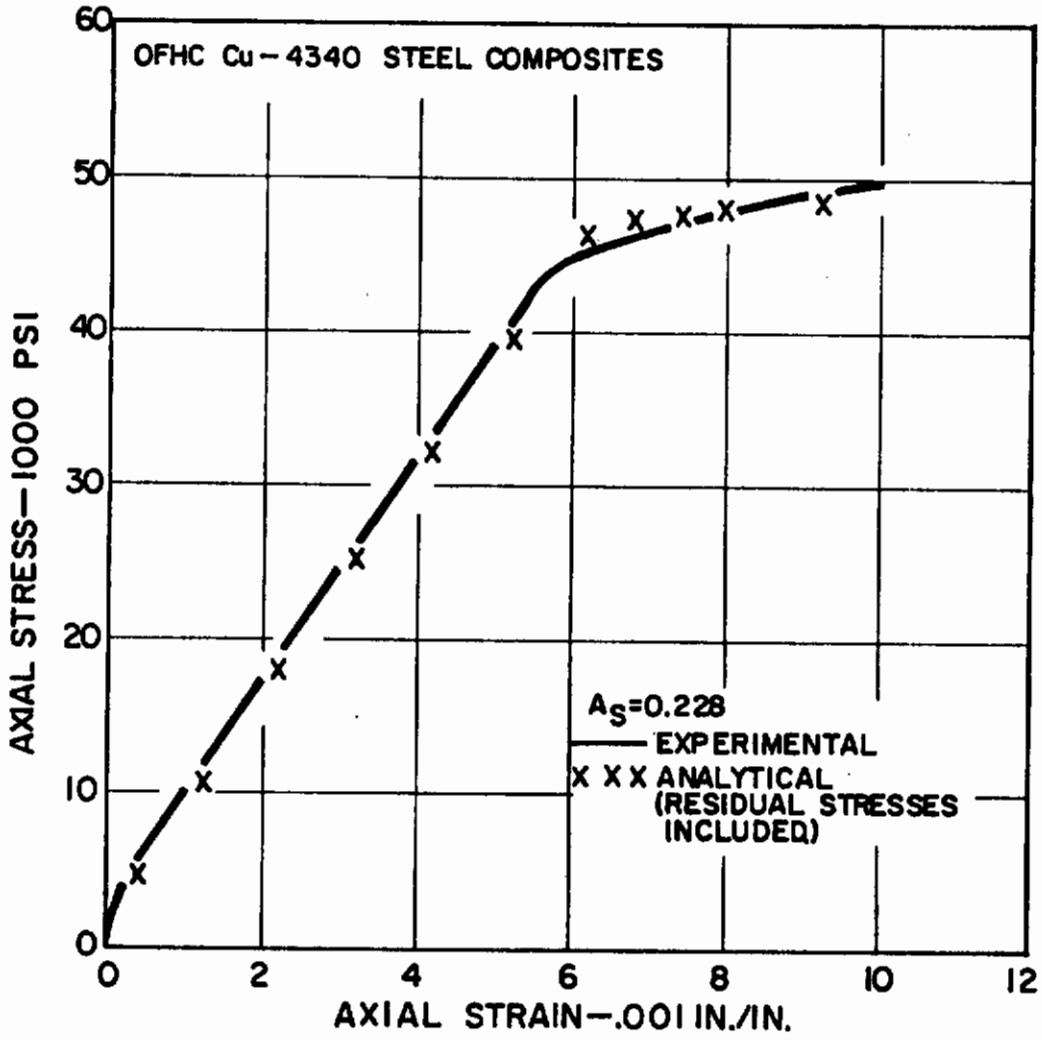

Figure 33

Experimental and Residual Stress Modified Analytical Stress-Strain Curves for an OFHC Copper - 4340 Steel Composite (A_s = 0.228).

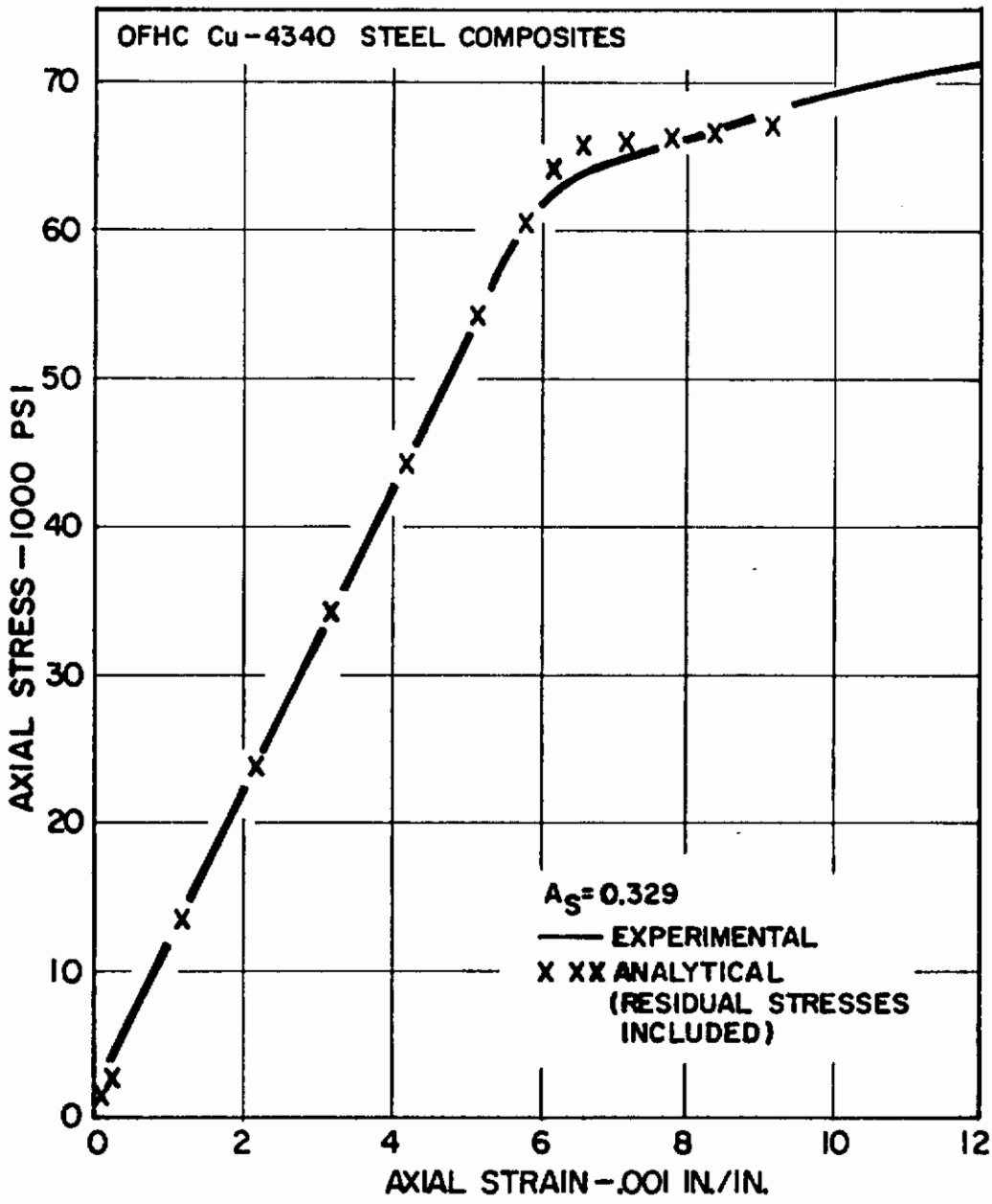

Figure 34

Experimental and Residual Stress Modified Analytical Stress-Strain Curves for an OFHC Copper - 4340 Steel Composite (A_s = 0.329).

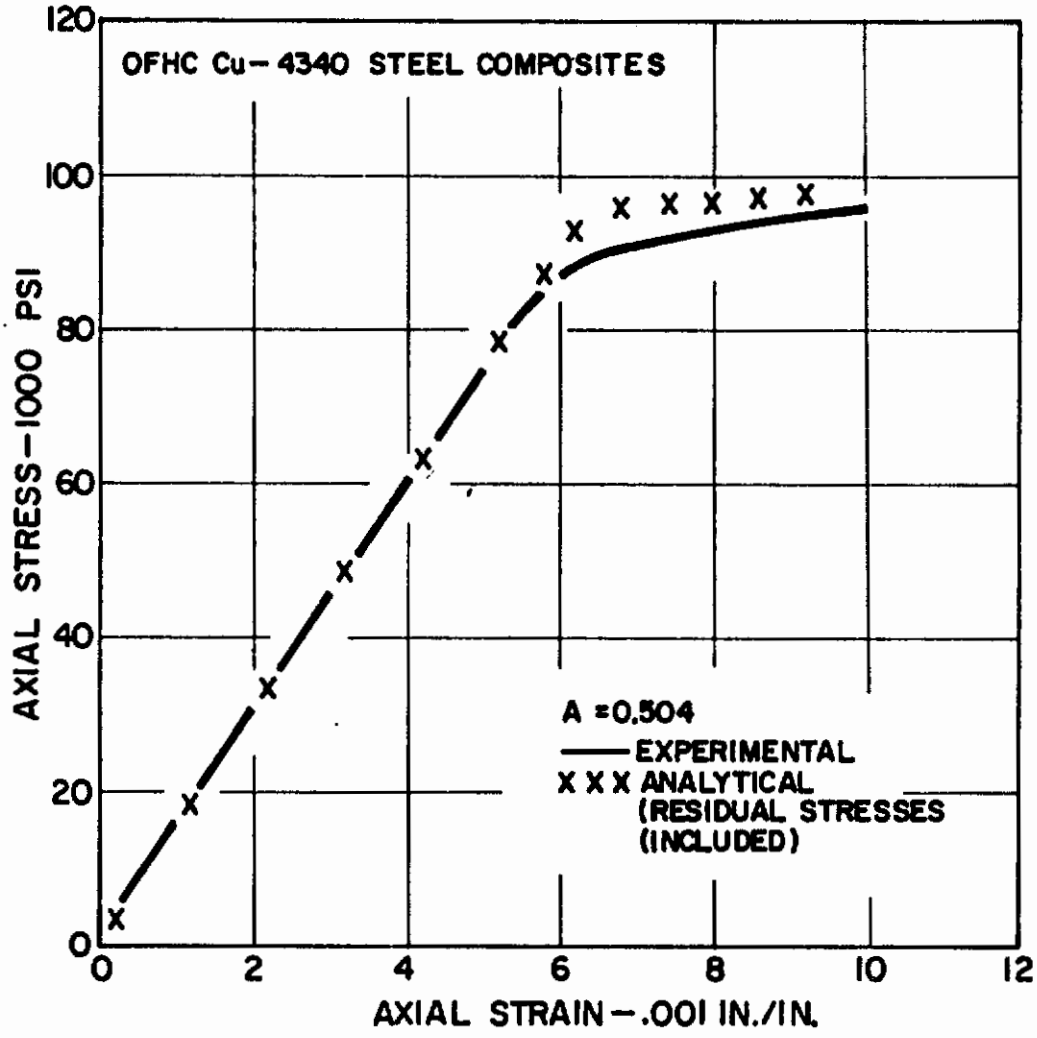

Figure 35

Experimental and Residual Stress Modified Analytical Stress-Strain Curves for an OFHC Copper - 4340 Steel Composite (A_s = 0.504).

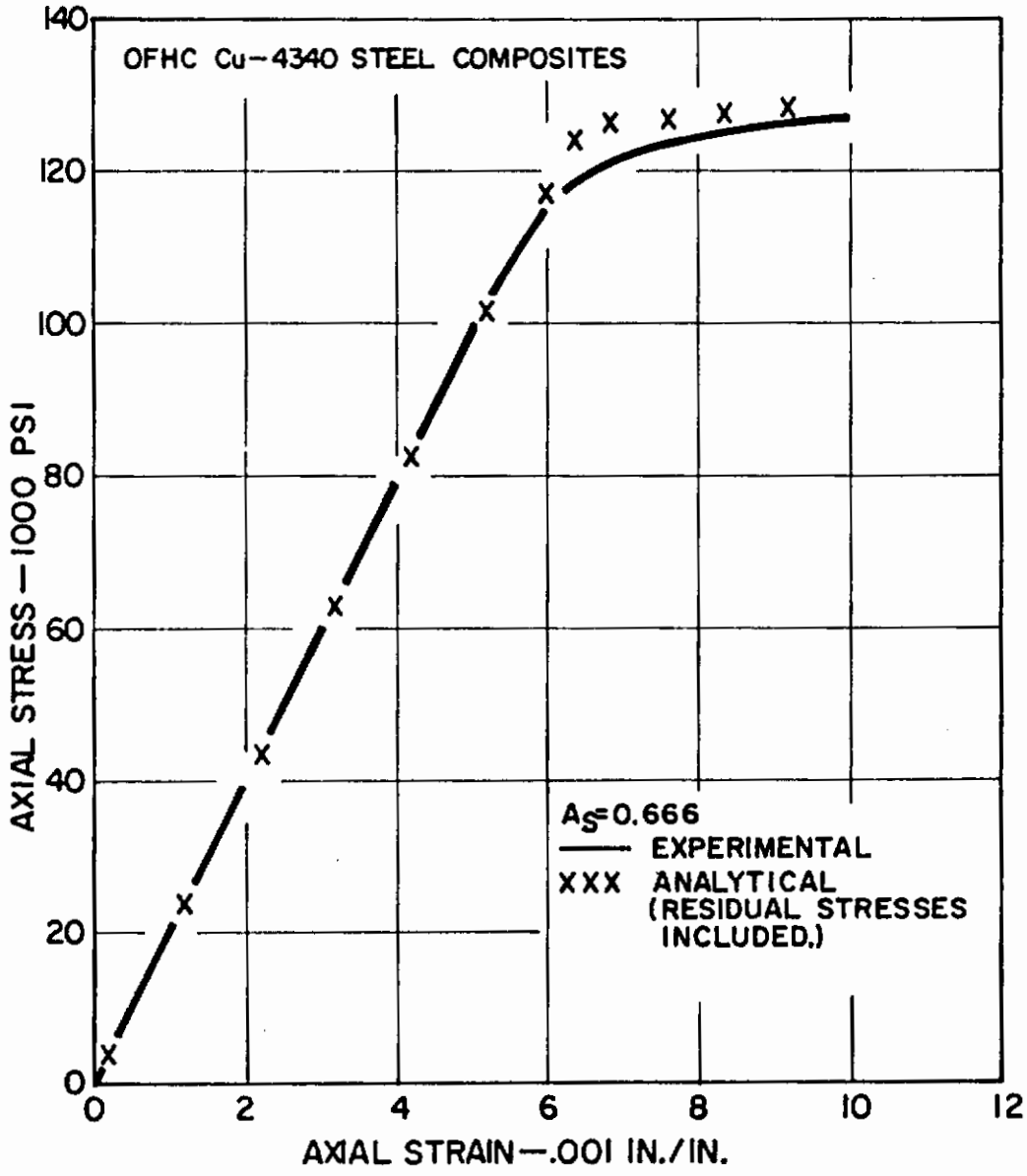

Figure 36

Experimental and Residual Stress Modified Analytical Stress-Strain Curves for an OFHC Copper - 4340 Steel Composite (A_s = 0.666).

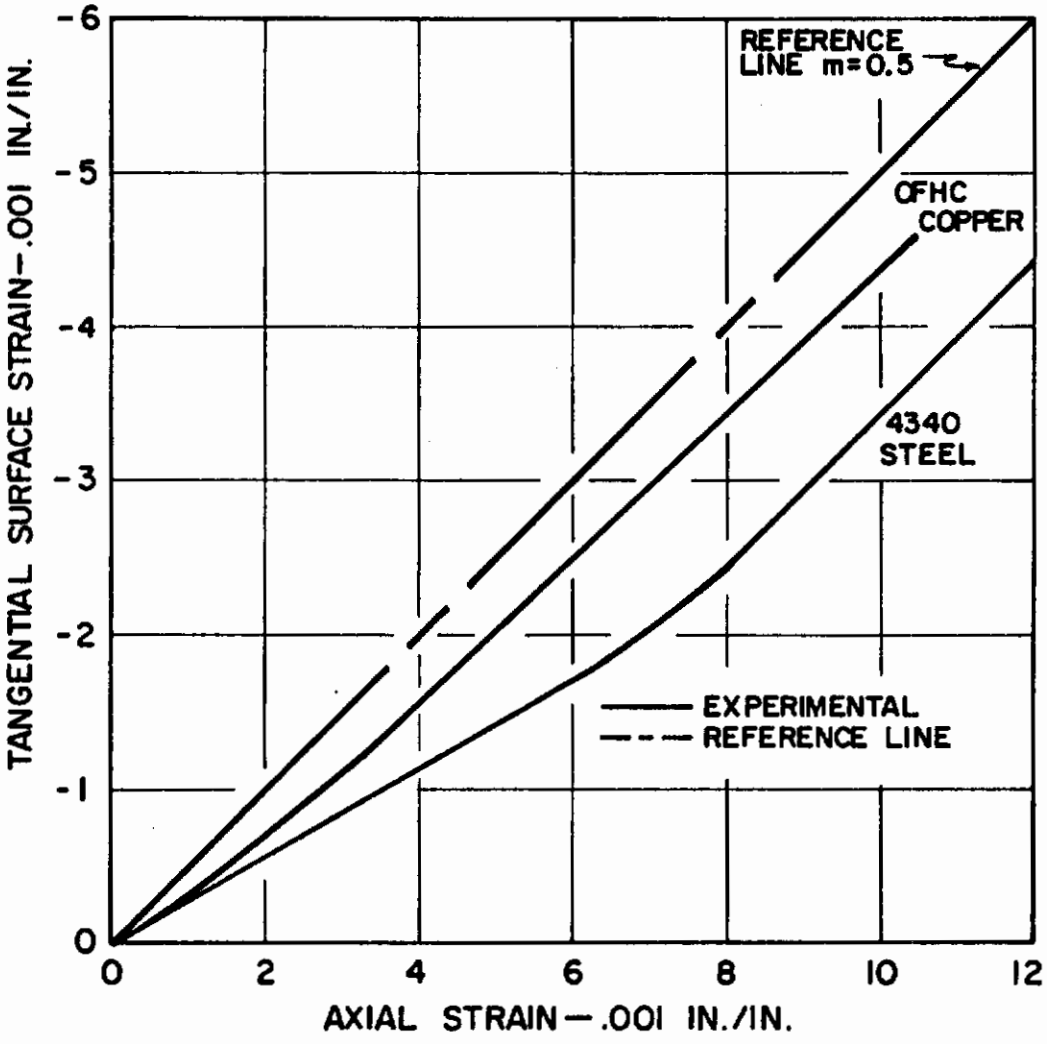

Figure 37

Tangential Surface Strain as a Function of Axial Strain for OFHC Copper and 4340 Steel Tensile Specimens.

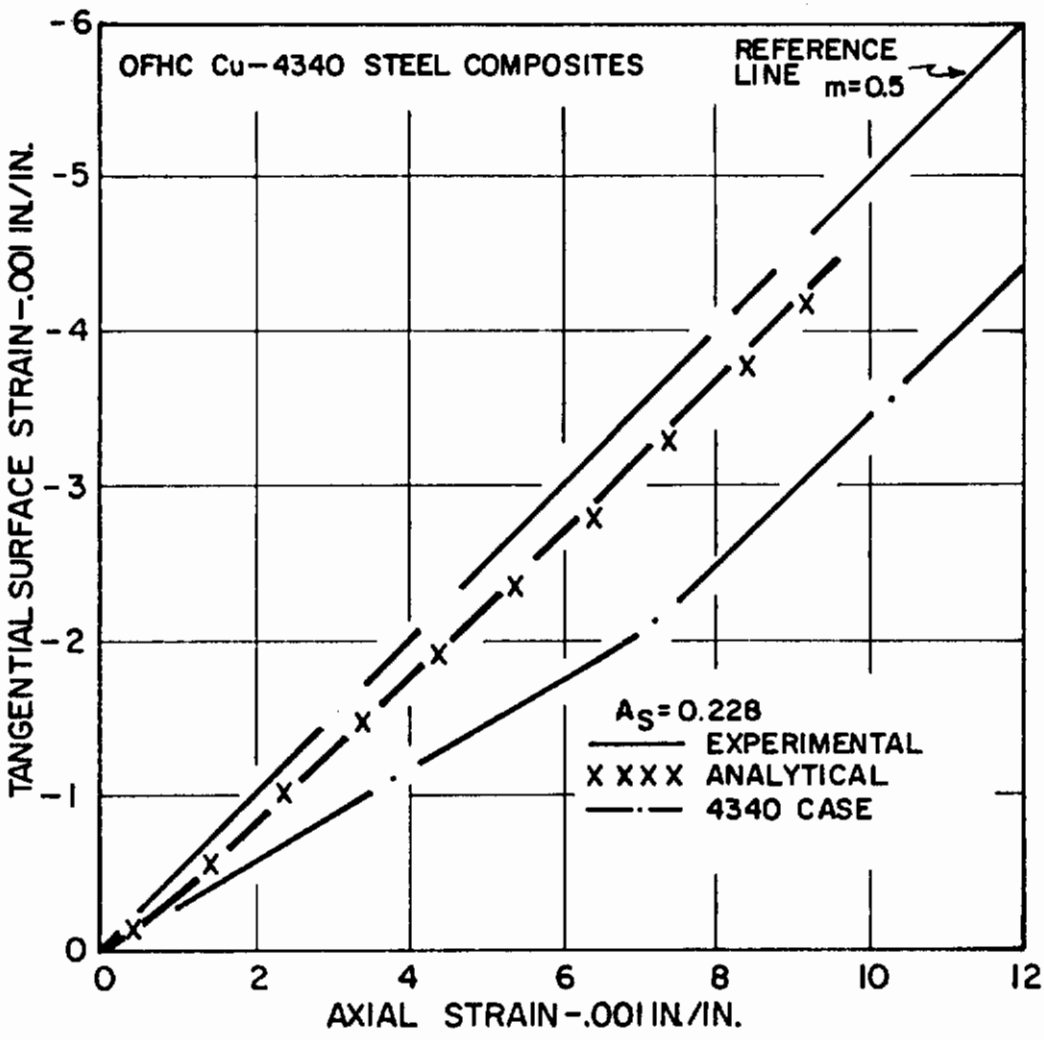

Figure 38

Tangential Surface Strain as a Function of Axial Strain for OFHC Copper - 4340 Steel Composite Tensile Specimens (A_s = 0.228).

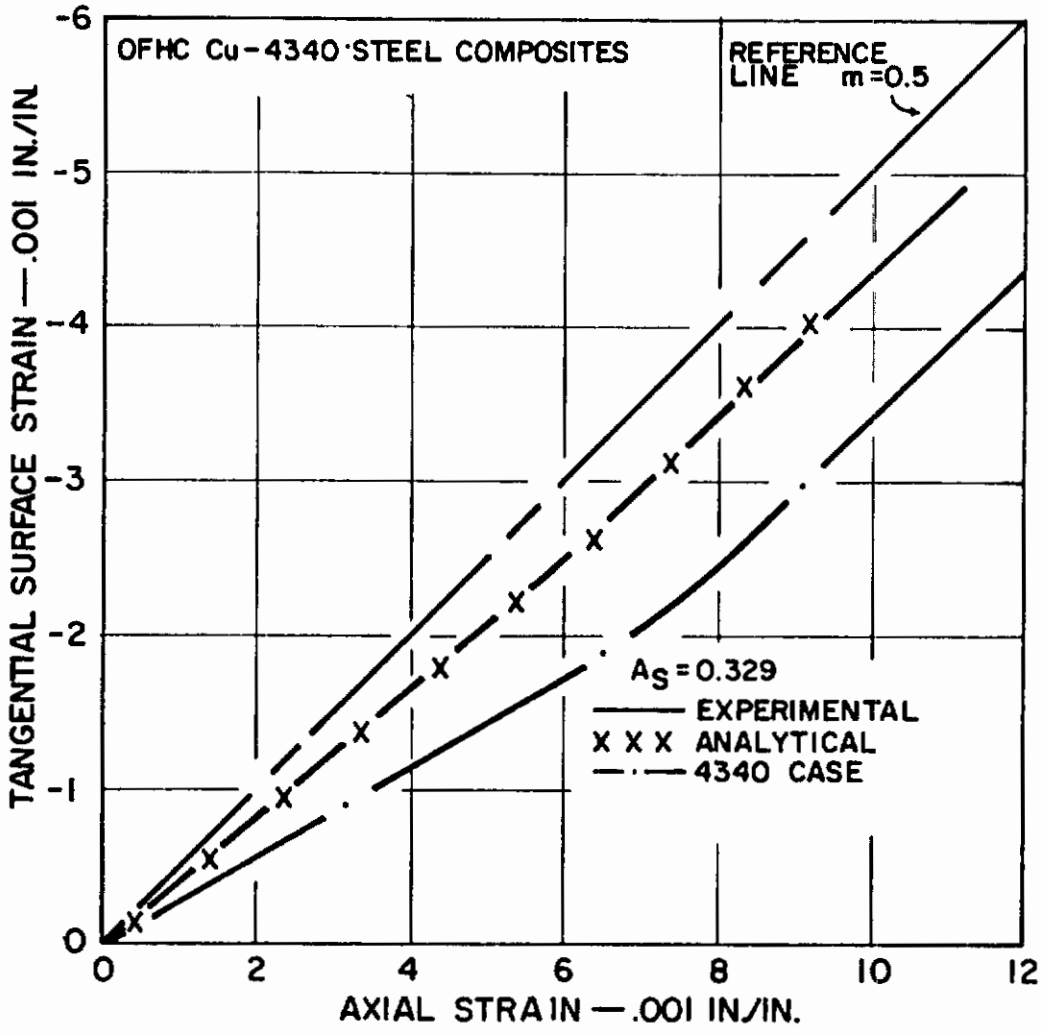

Figure 39

Tangential Surface Strain as a Function of Axial Strain for OFHC Copper - 4340 Steel Composite Tensile Specimens (A_s = 0.329).

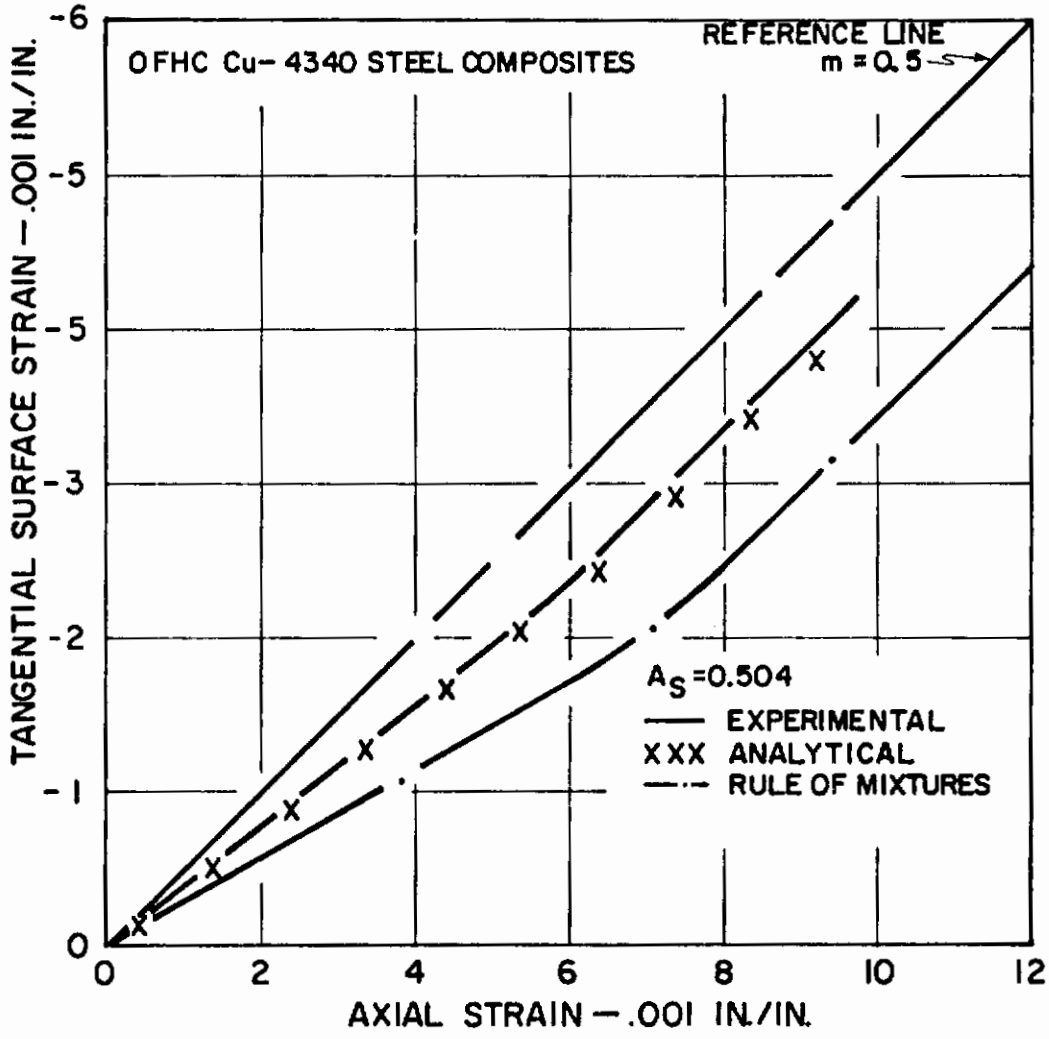

Figure 40

Tangential Surface Strain as a Function of Axial Strain for OFHC Copper - 4340 Steel Composite Tensile Specimens (A_s = 0.504).

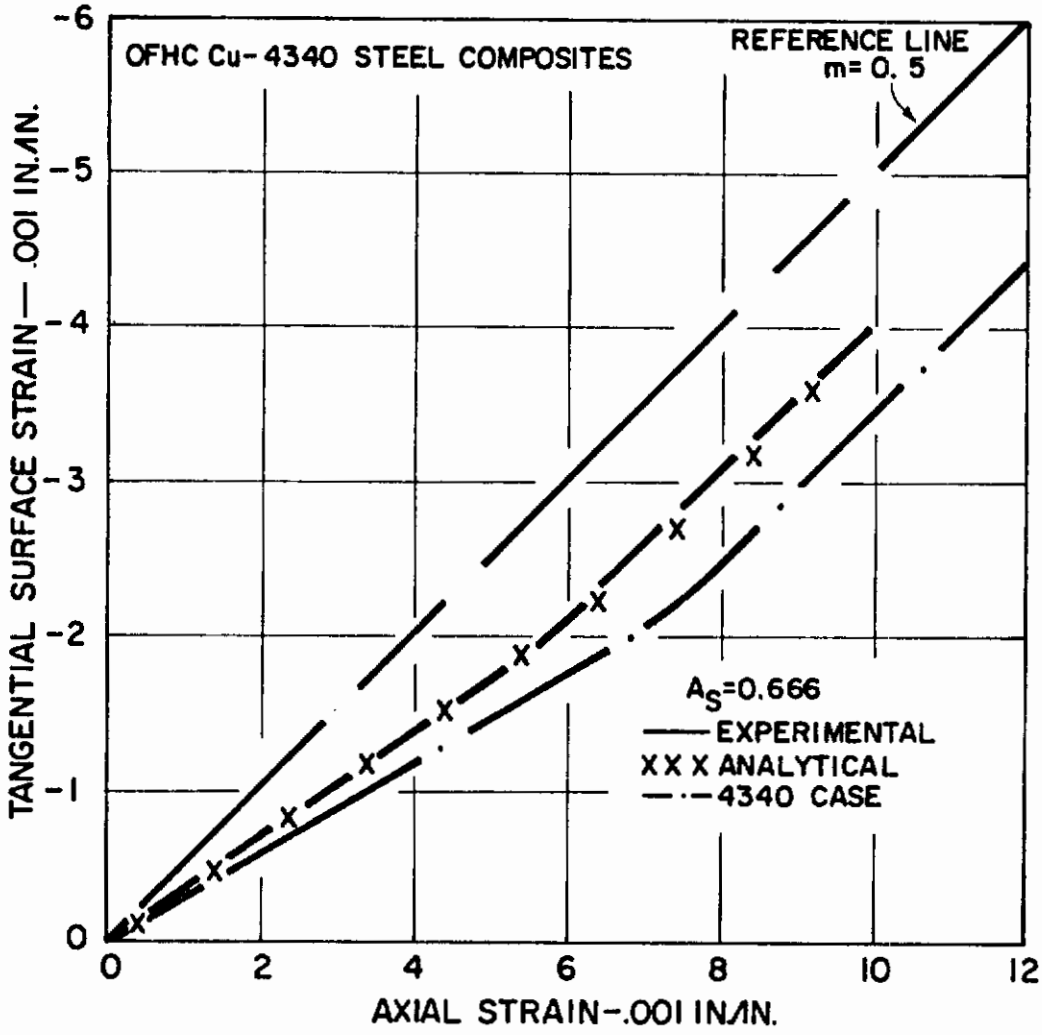

Figure 41

Tangential Surface Strain as a Function of Axial Strain for OFHC Copper - 4340 Steel Composite Tensile Specimens (A_s= 0.666).

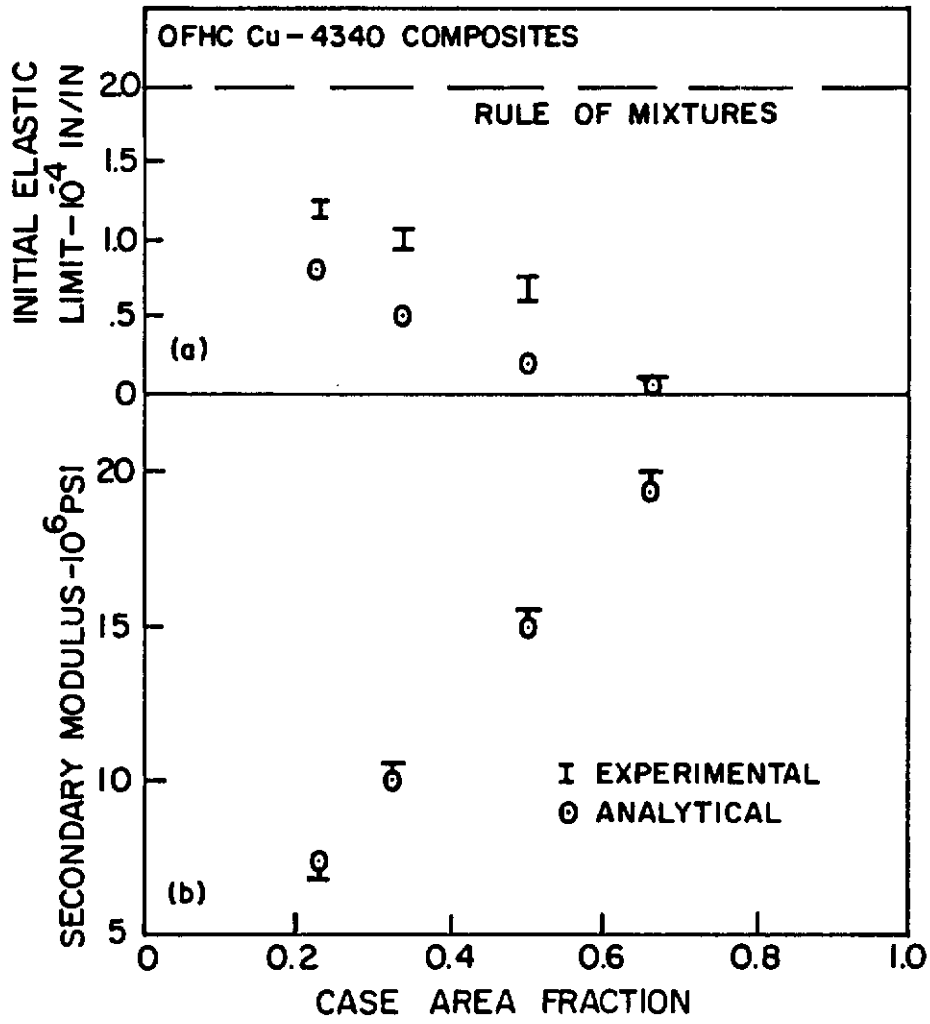

Figure 42

Initial Elastic Limit and Secondary Modulus of OFHC Copper - 4340 Steel Composites.

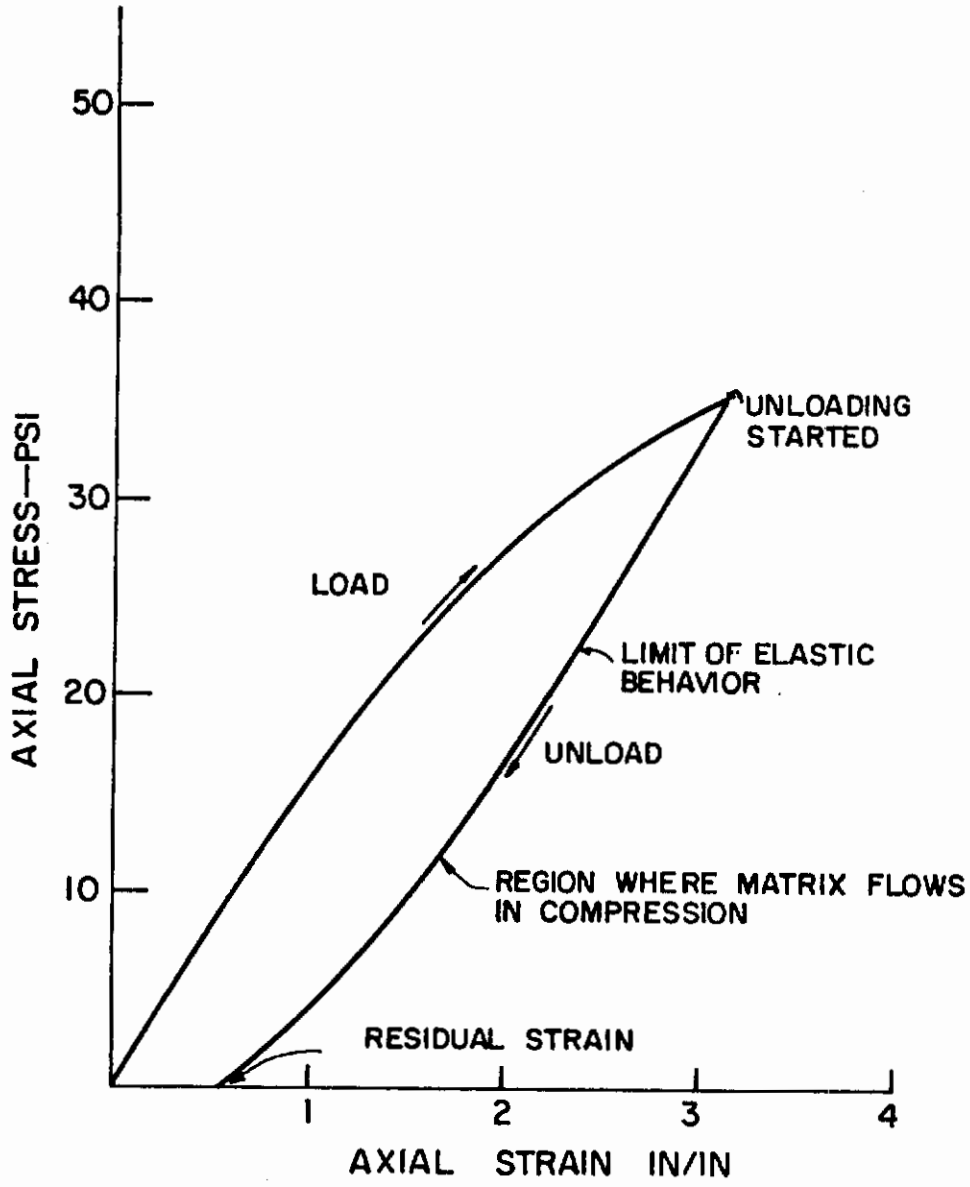

Figure 43

Behavior of Copper-Tungsten Composite During One Tensile Loading Cycle.

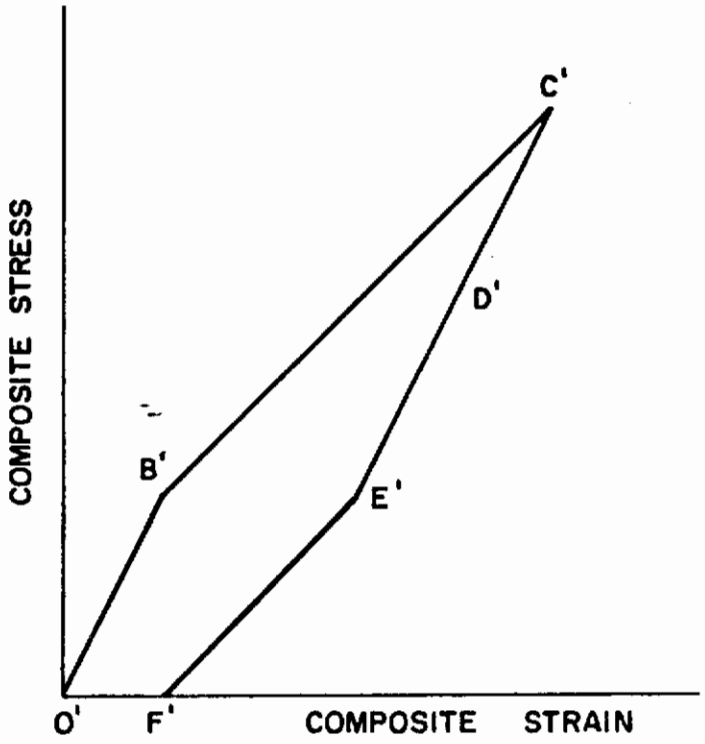

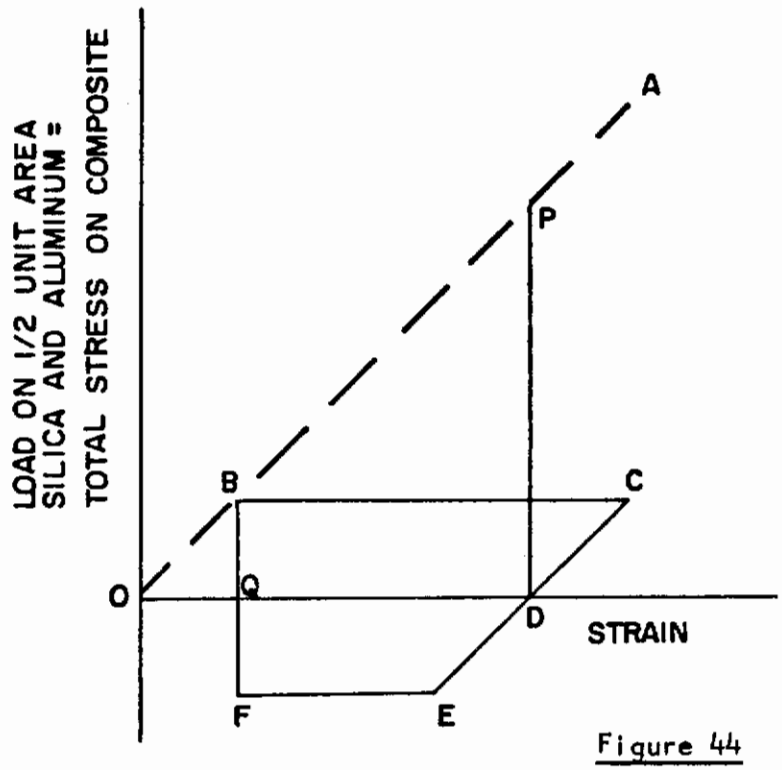

Figure 44

Component Behavior During Tensile Loading Cycle
For 50% Aluminum - 50% Silica Composite.

π PLANE REPRESENTATION

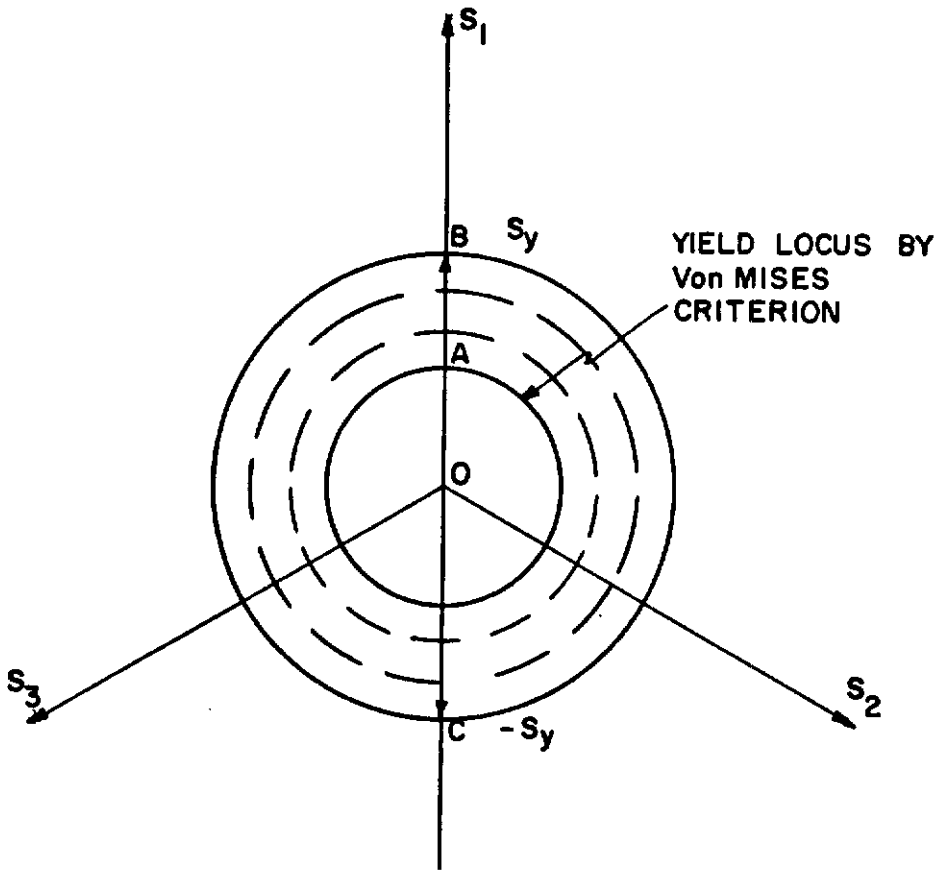

Figure 45

Illustrations of Isotropic Hardening Loading Function for Reversed Uniaxial Loading.

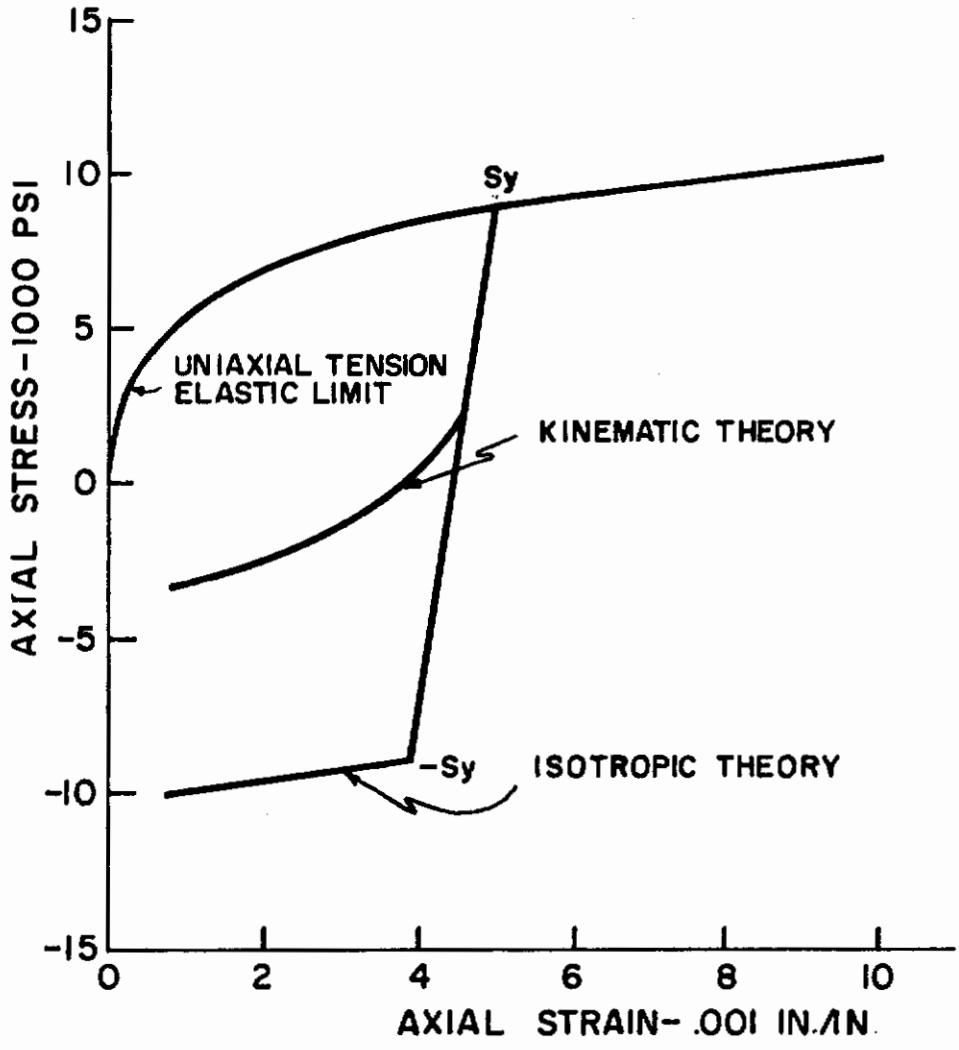

Figure 46

Stress-Strain Behavior of OFHC Copper Predicted by Isotropic and Kinematic Loading Functions.

π PLANE REPRESENTATION

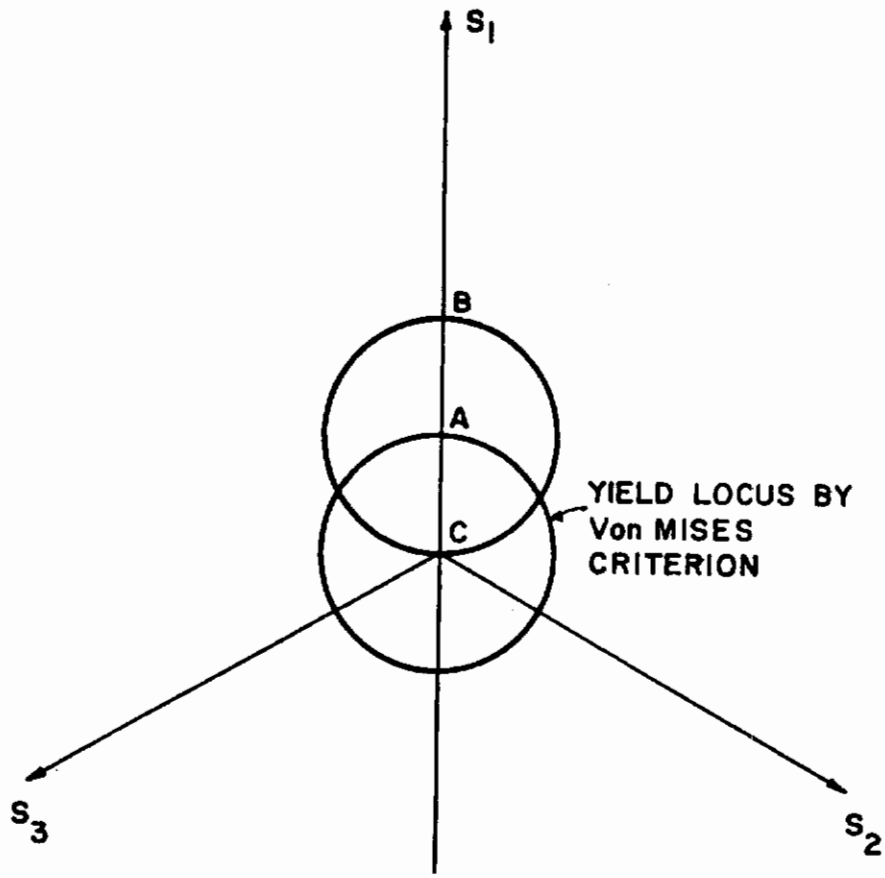

Figure 47

Illustration of Kinematic Hardening Loading Function For Reversed Uniaxial Loading.

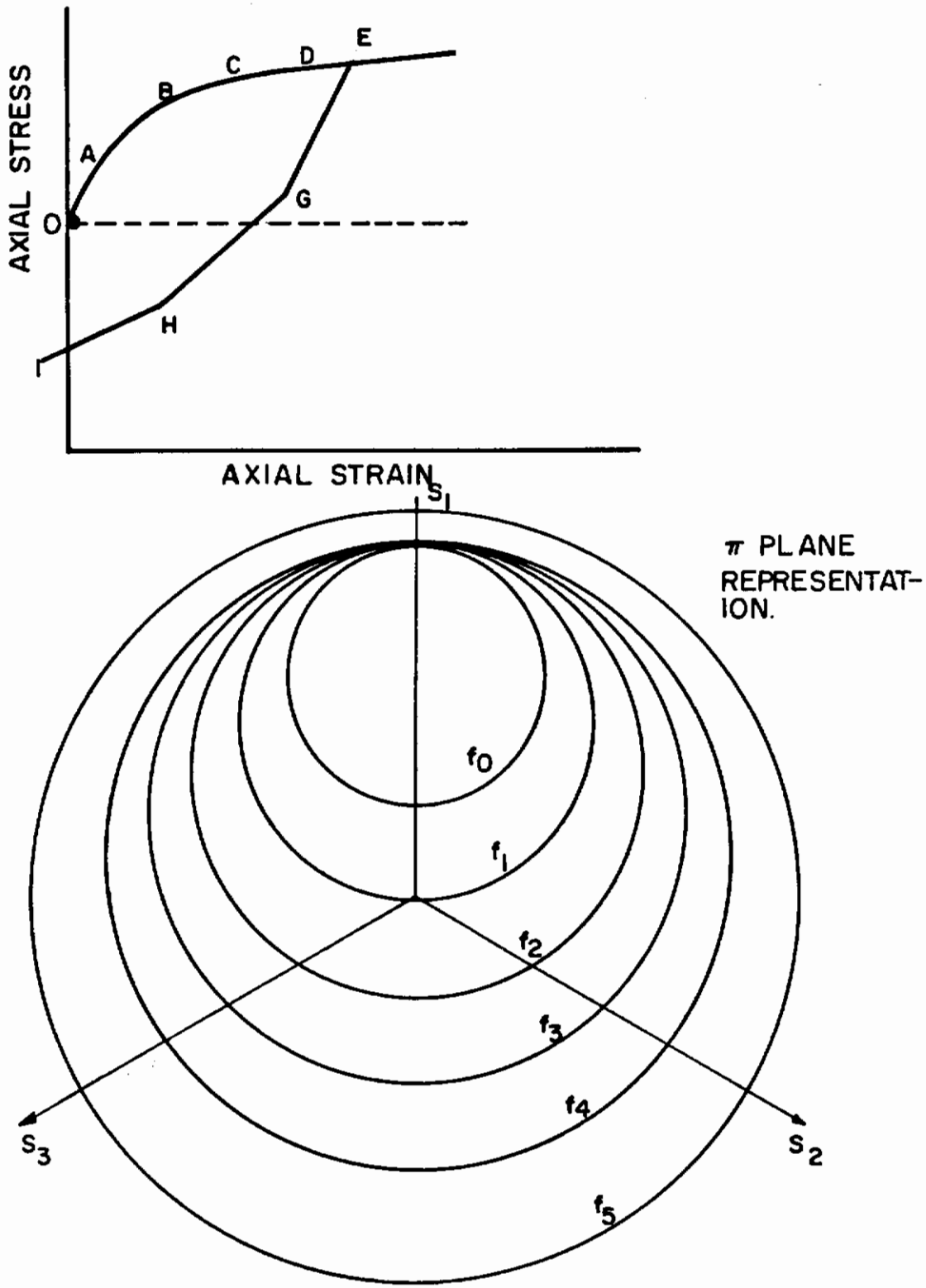

Figure 48

Representation of Mroz Model Loading Function For Reversed Uniaxial Loading.

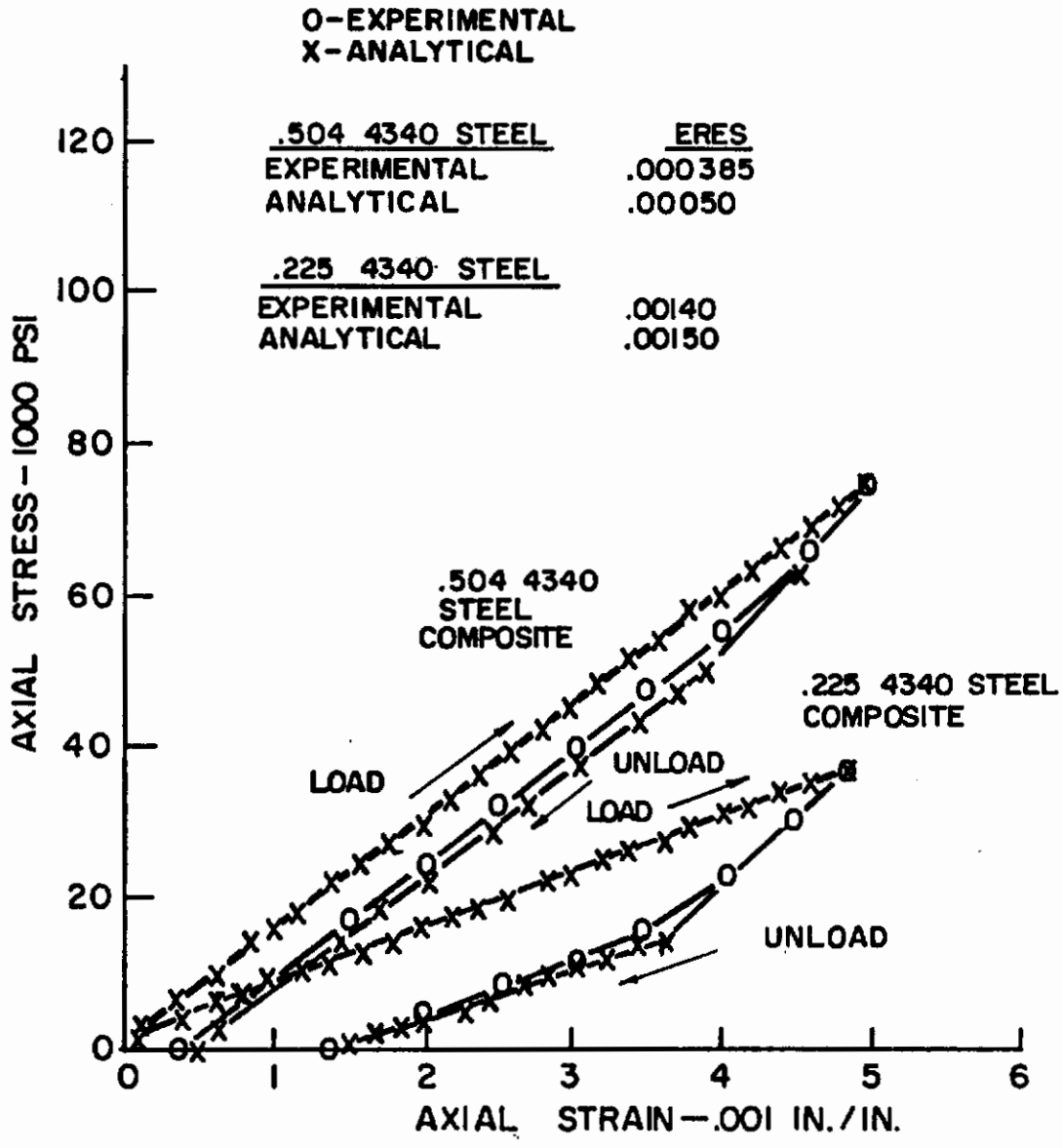

Figure 49

Isotropic Hardening Unloading Predictions of 4340 Steel-OFHC Copper Composites.

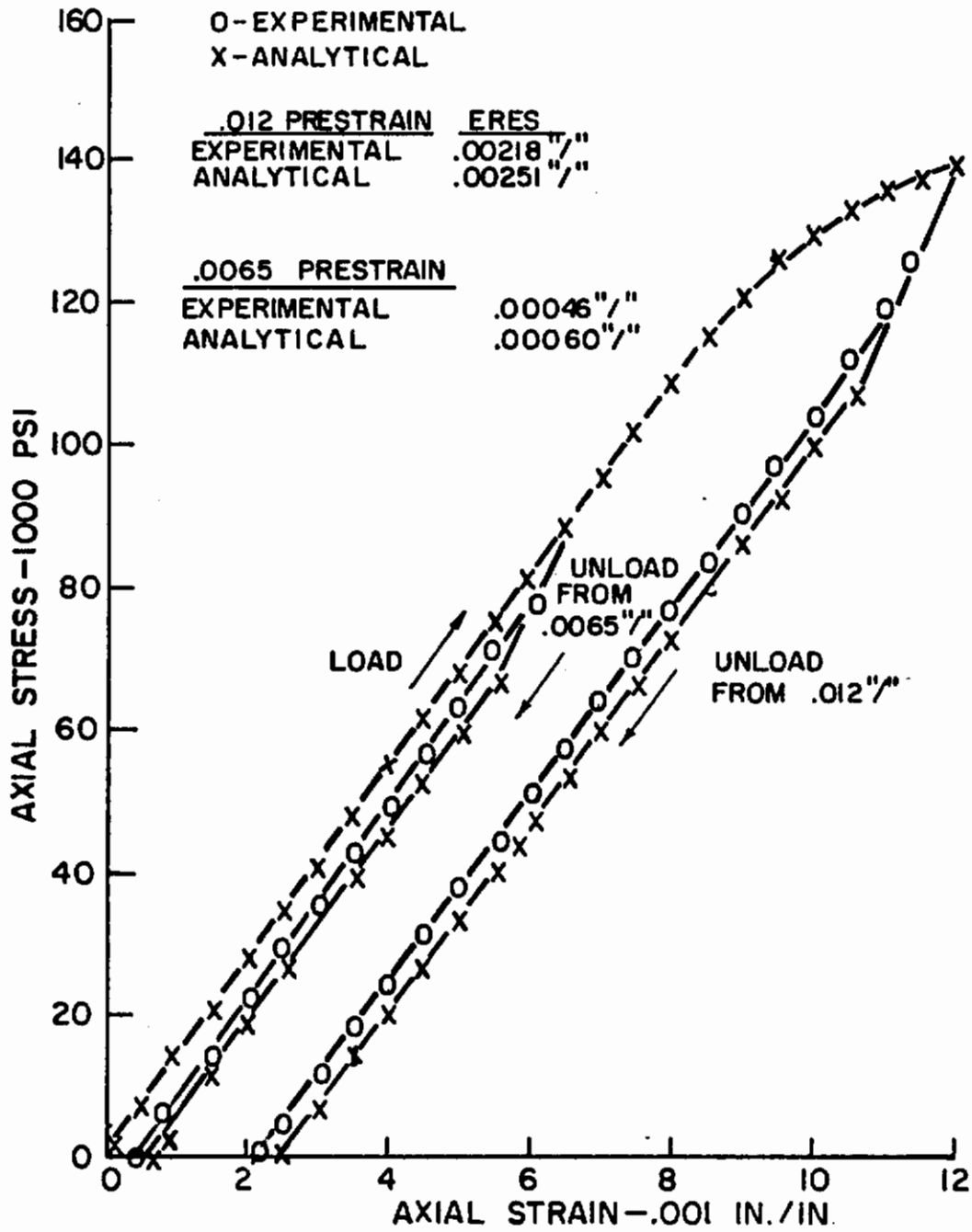

Figure 50

Isotropic Hardening Unloading Prediction of .504 Volume Fraction Maraging Steel-OFHC Copper Composites.

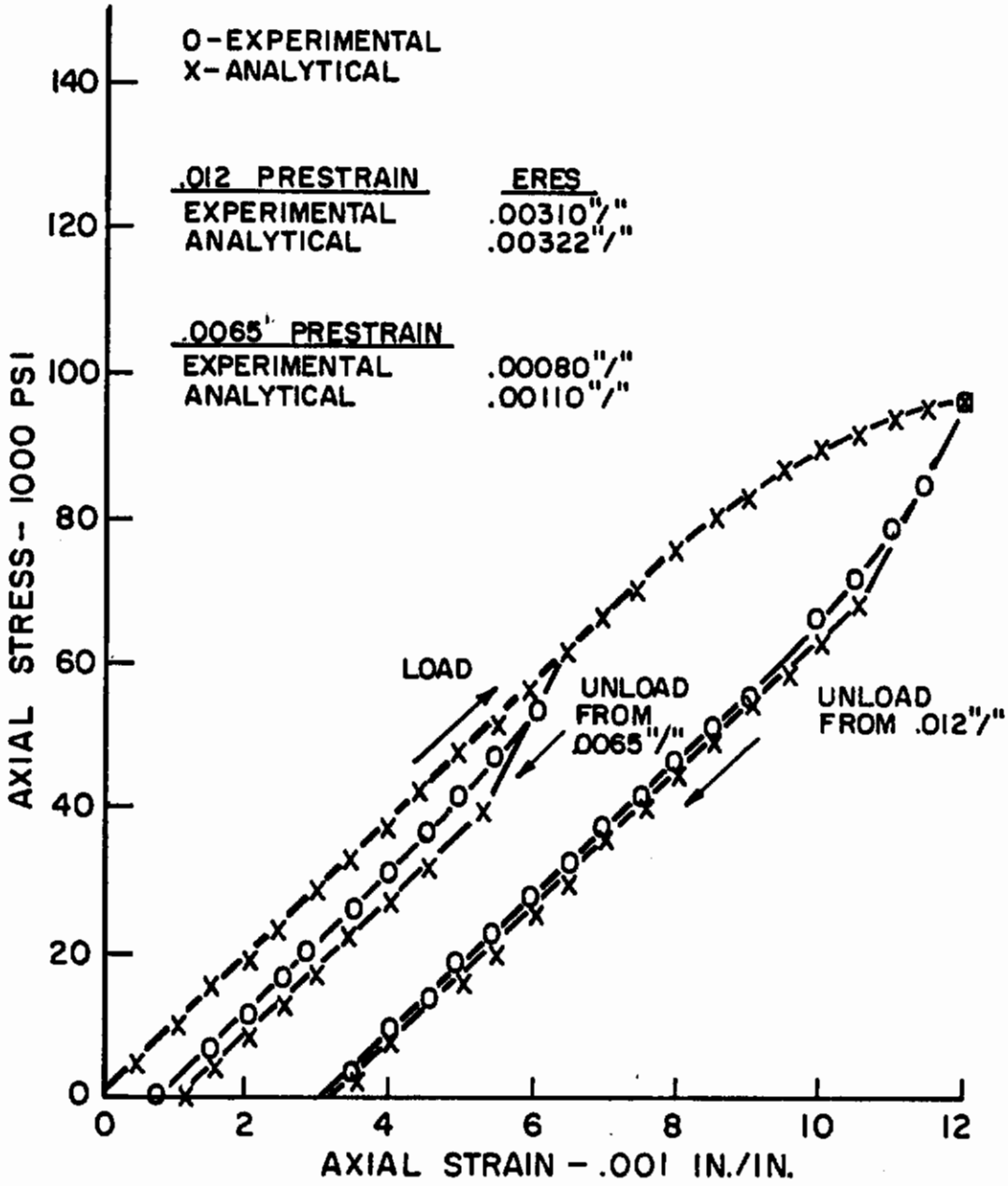

Figure 51

Isotropic Hardening Unloading Prediction of .335 Volume Fraction Maraging Steel-OFHC Copper Composites.

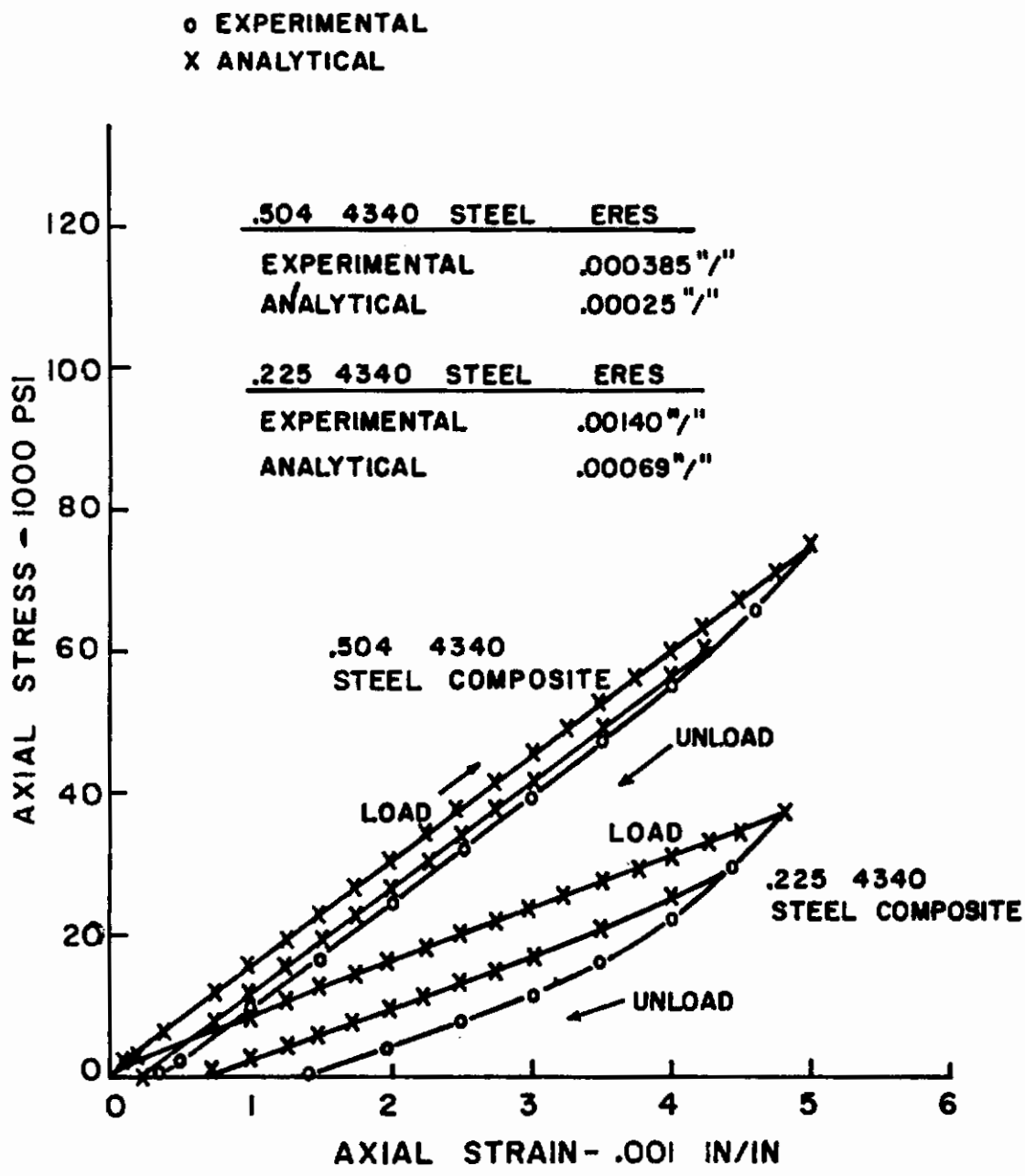

Figure 52

Kinematic Workhardening Unloading Predictions of 4340 Steel-OFHC Copper Composites.

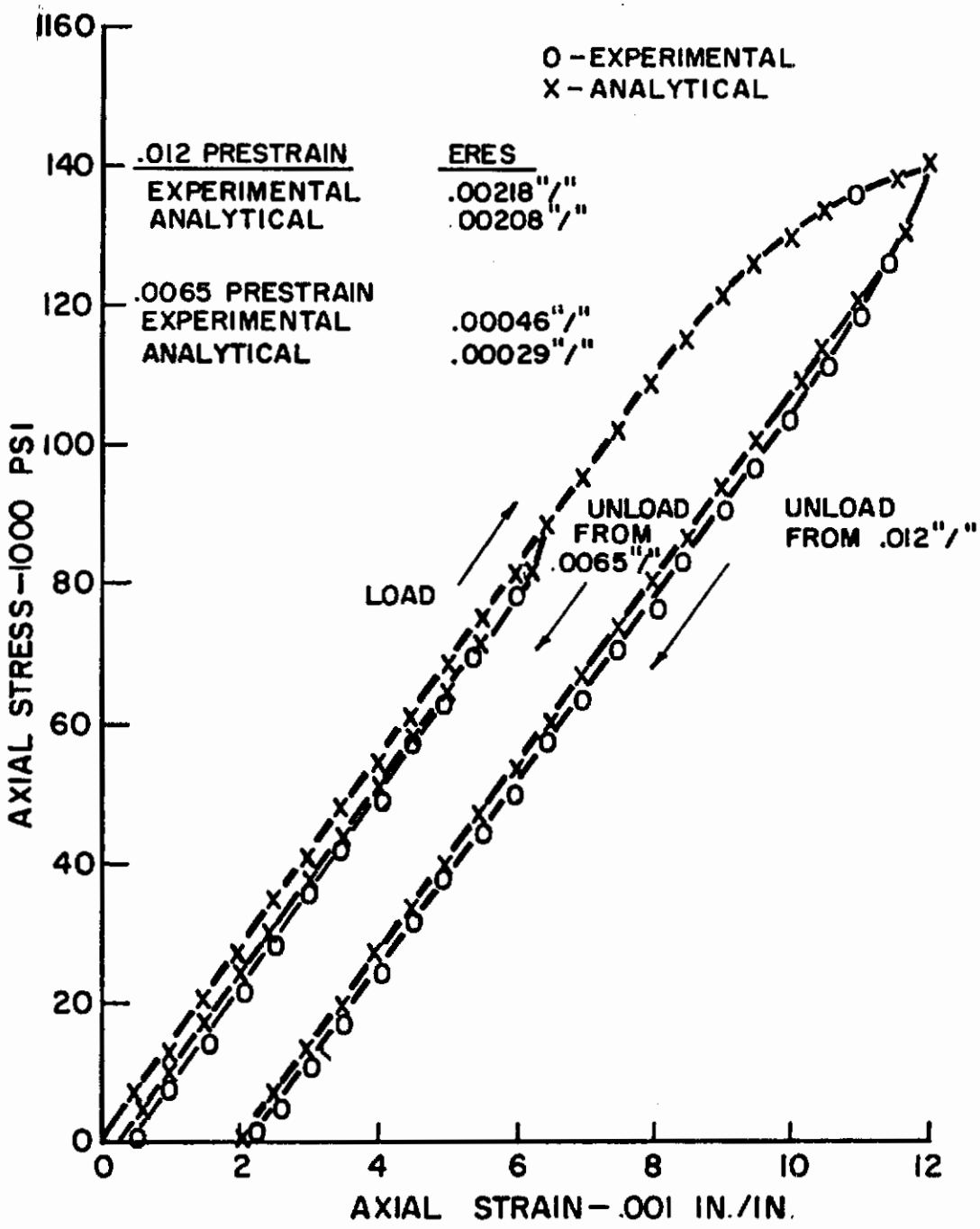

Figure 53

Kinematic Workhardening Unloading Predictions of .504 Volume Fraction Maraging Steel-OFHC Copper Composites.

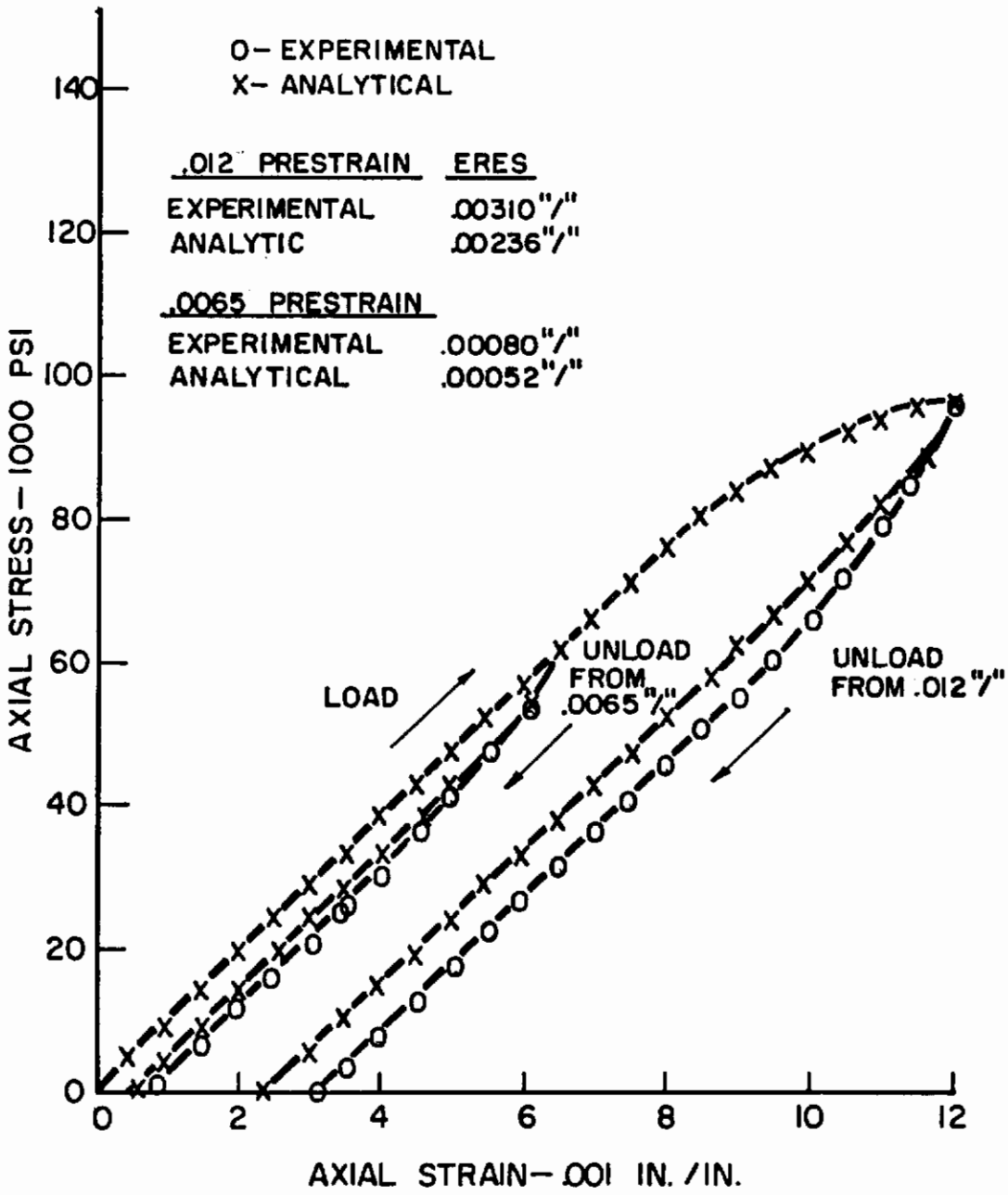

Figure 54

Kinematic Workhardening Unloading Predictions of .335 Volume Fraction Maraging Steel-OFHC Copper Composites.

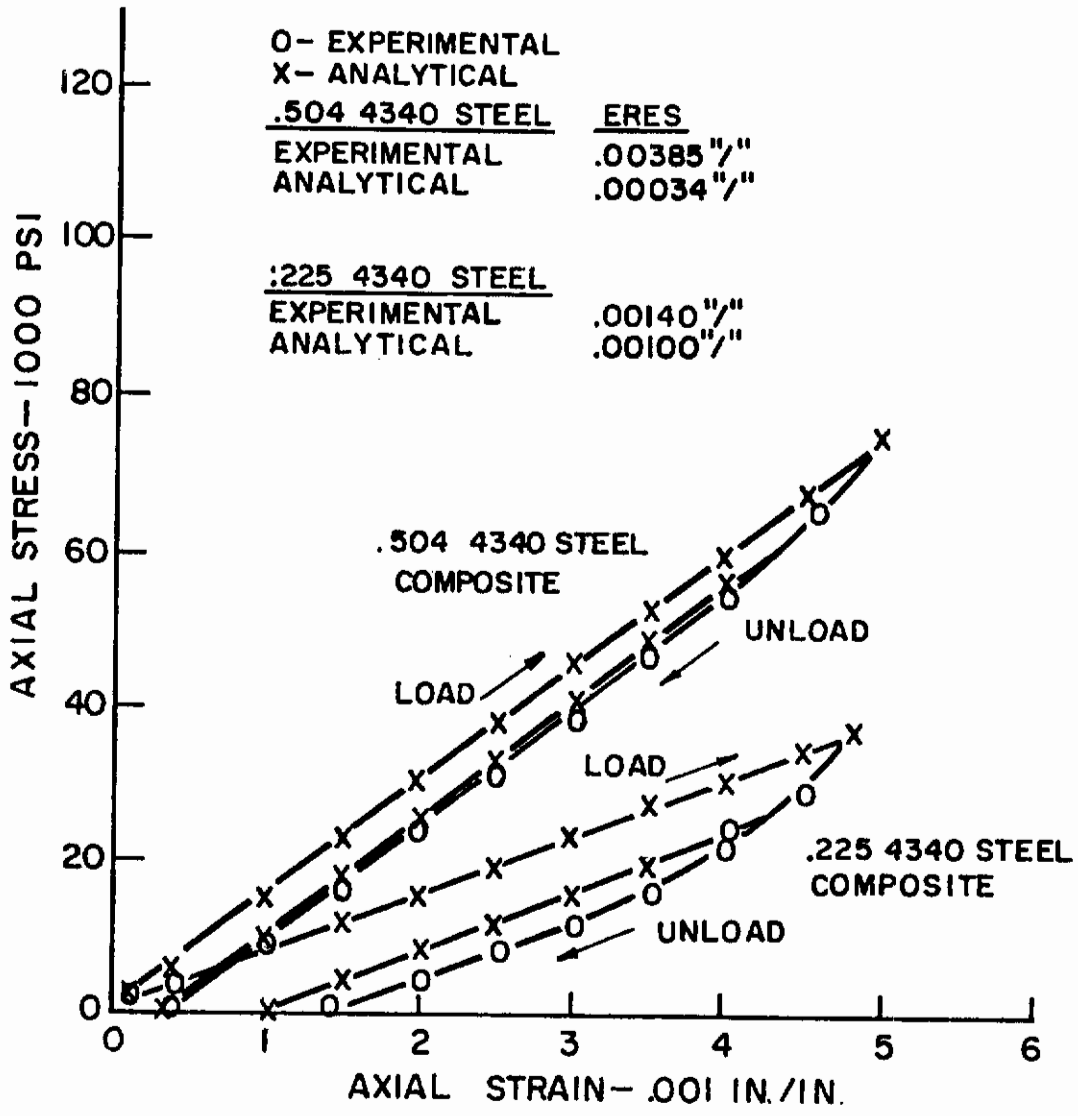

Figure 55

Mroz Model Unloading Predictions of 4340 Steel-OFHC Copper Composites.

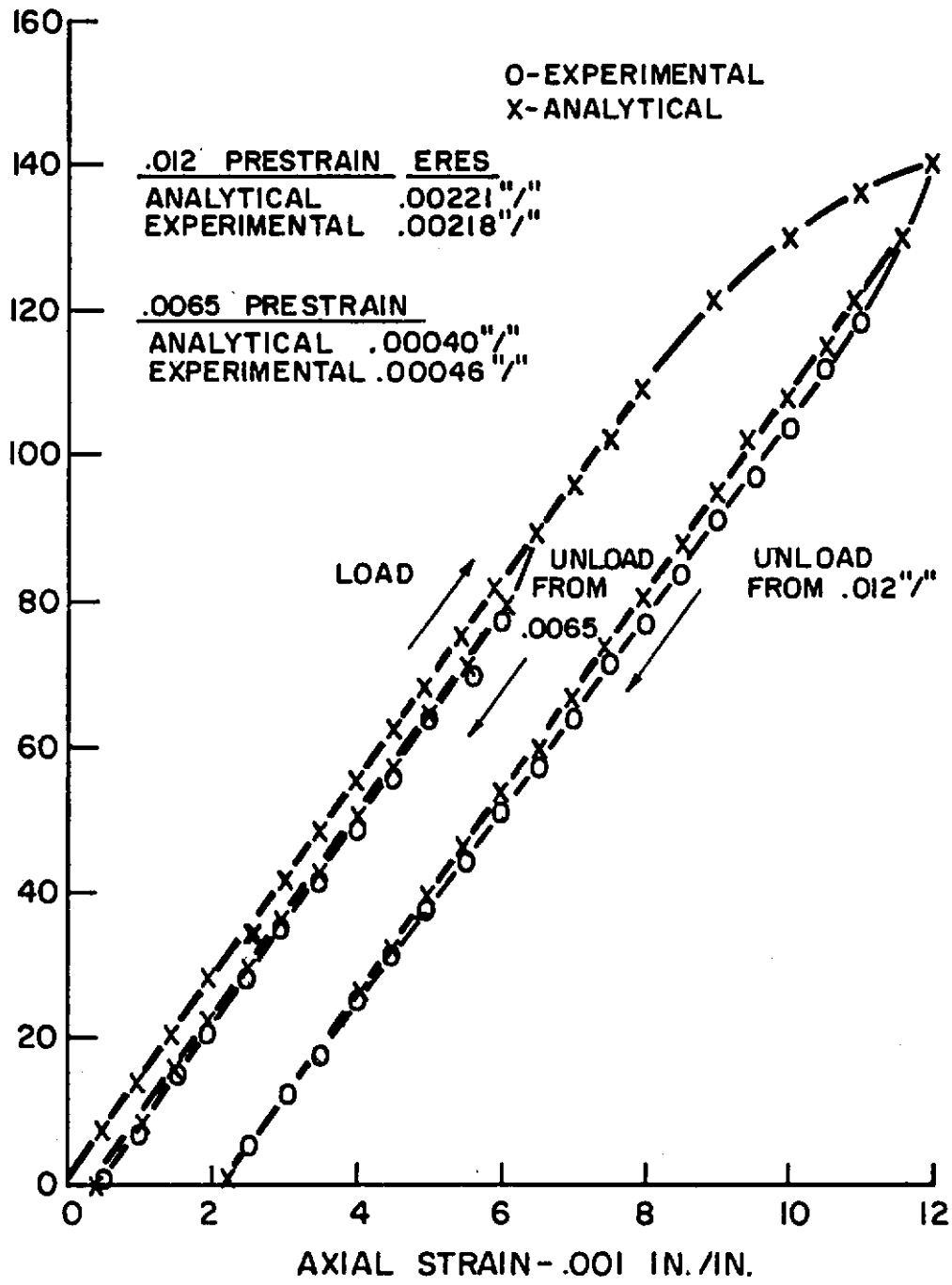

Figure 56

Mroz Model Unloading Predictions of .504 Volume Fraction Maraging Steel-OFHC Copper Composites.

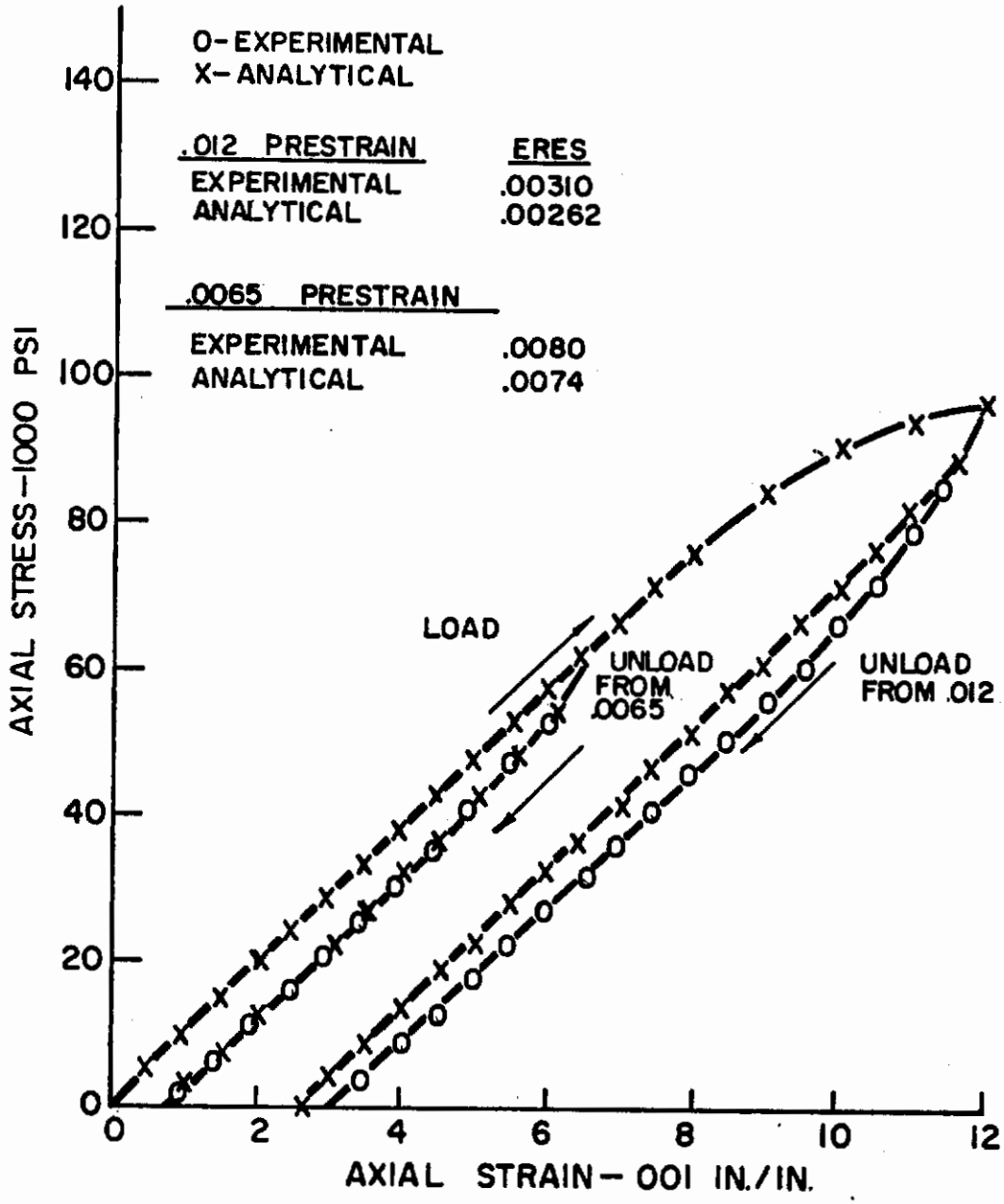

Figure 57

Mroz Model Unloading Predictions of .335 Volume Fraction Maraging Steel-OFHC Copper Composites.

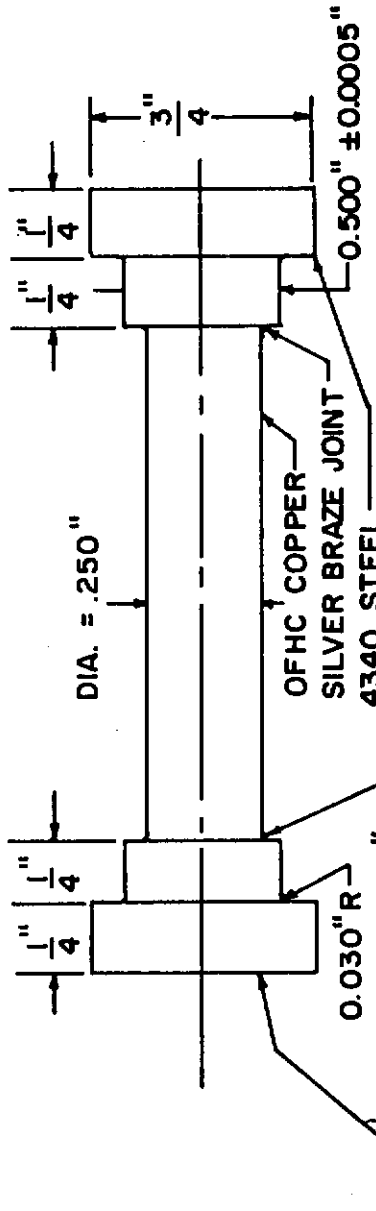

Figure 58

Tensile-Compression Specimen Configuration for Cyclic Effective Stress-Effective Strain Determination.

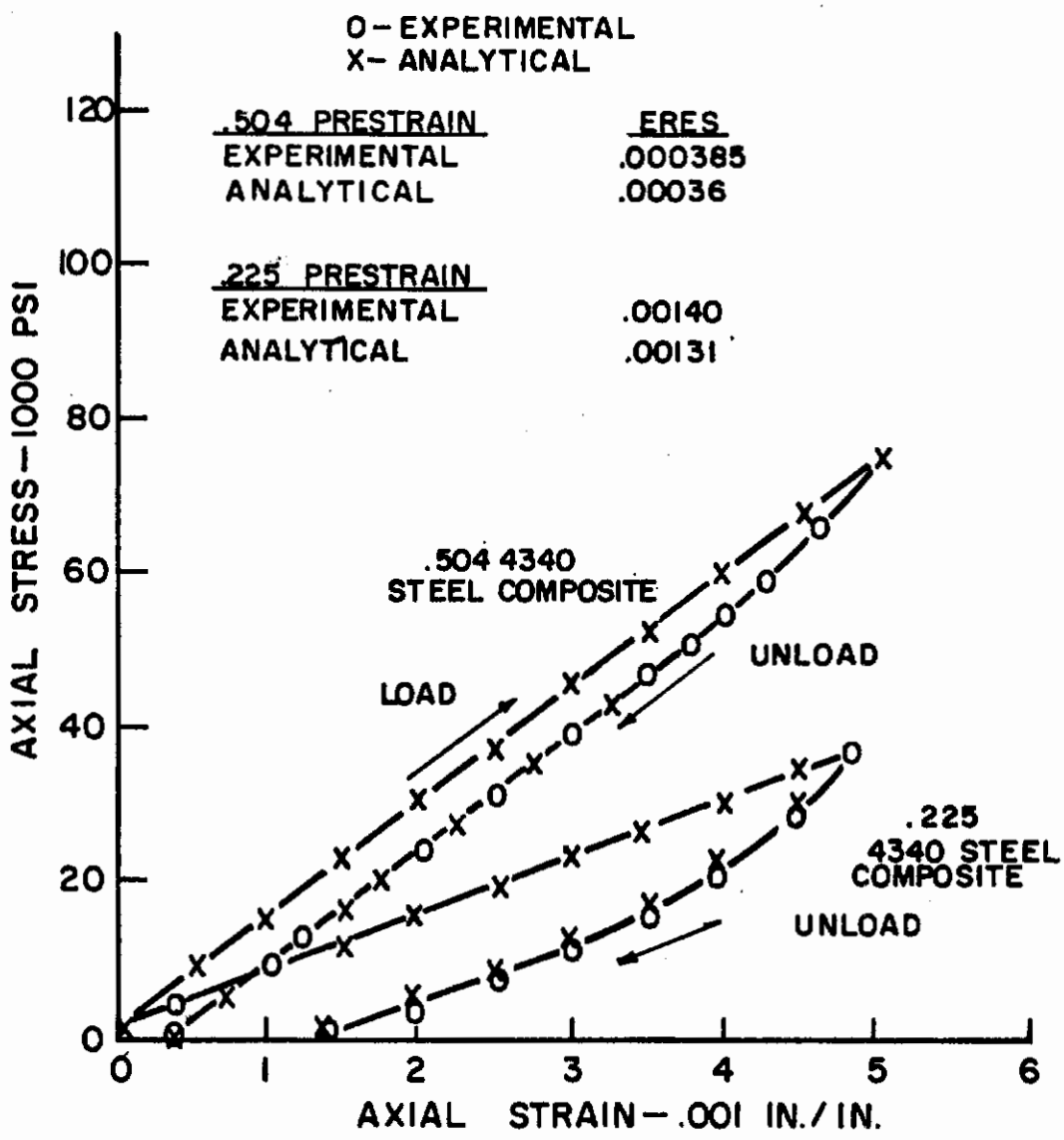

Figure 59

Effective Stress-Effective Strain Unloading Predictions of 4340 Steel-OFHC Copper Composites.

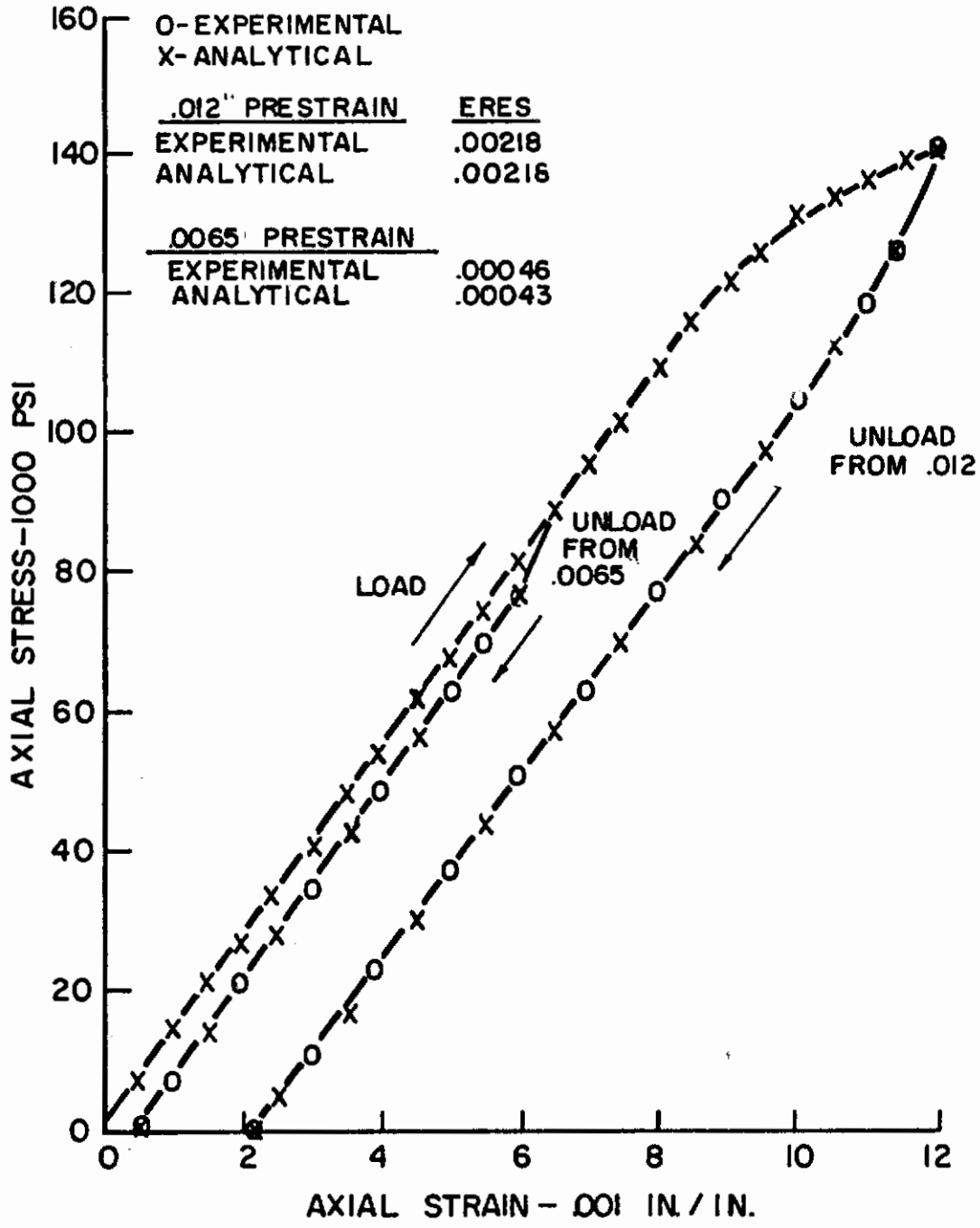

Figure 60

Effective Stress-Effective Strain Unloading Prediction of .504 Volume Fraction Maraging Steel-OFHC Copper Composites.

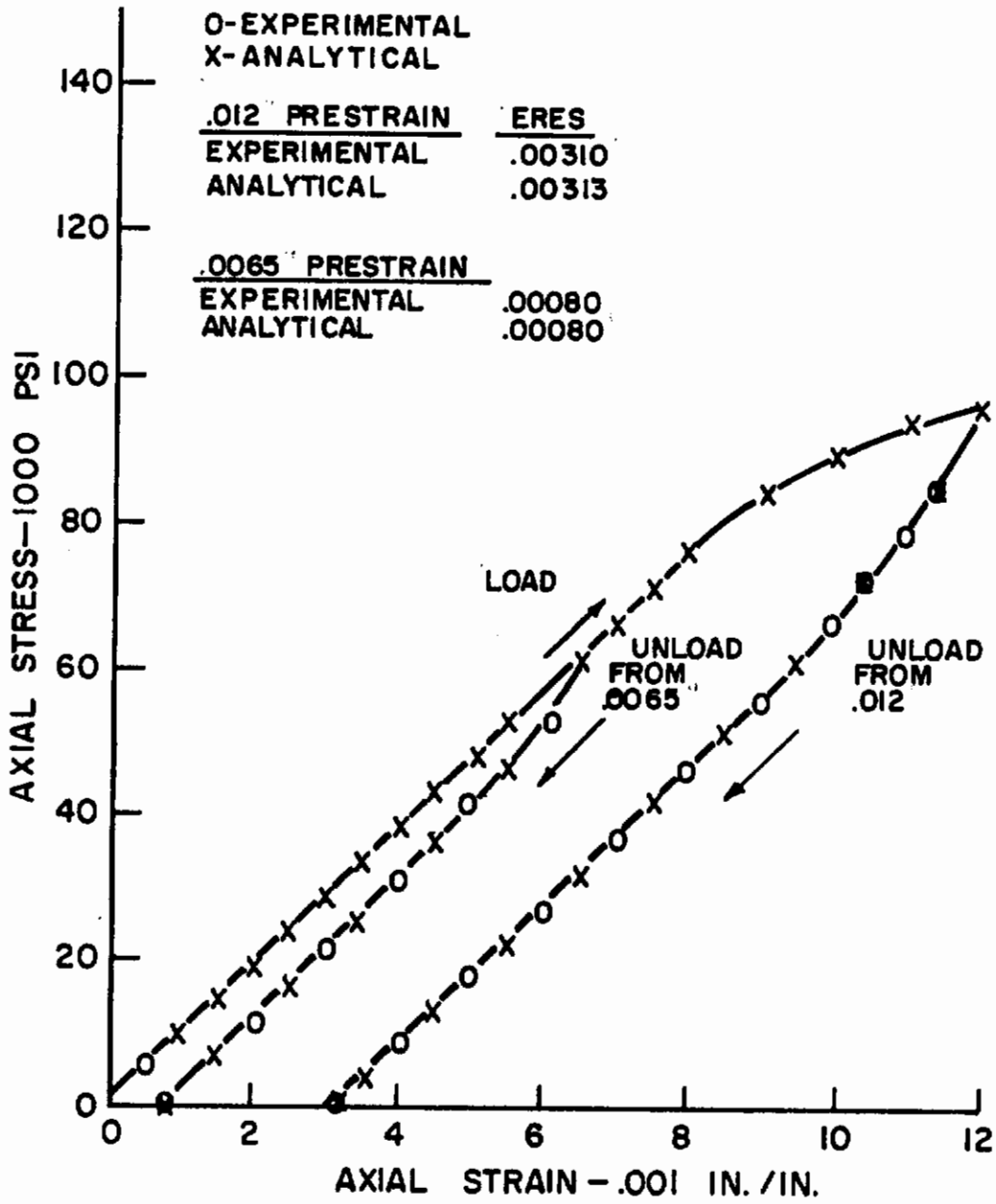

Figure 61

Effective Stress-Effective Strain Unloading Prediction of .335 Volume Fraction Maraging Steel-OFHC Copper Composites.

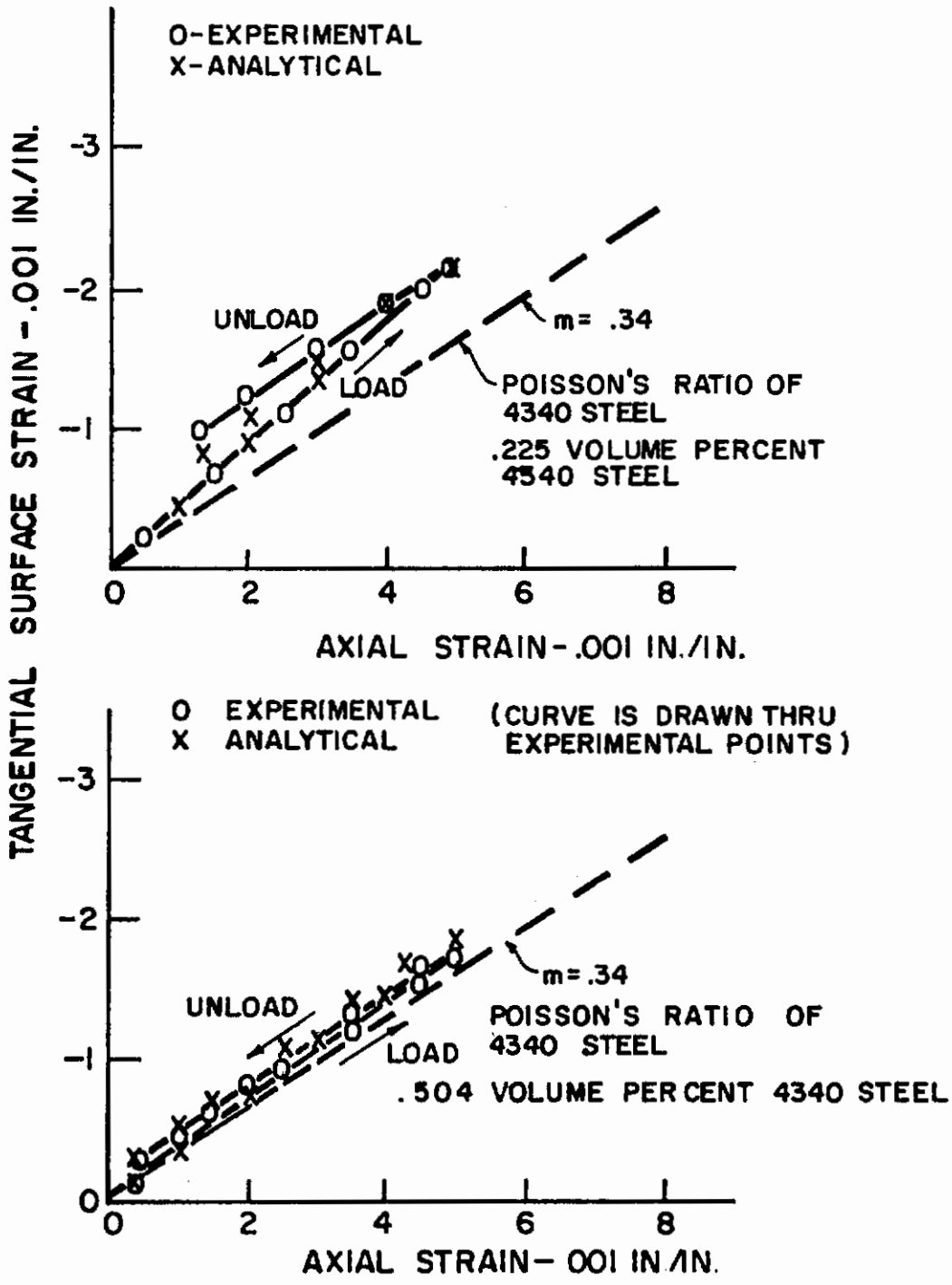

Figure 62

Tangential Surface Strain as a Function of Axial Strain During Prestraining of 4340 Steel-OFHC Copper Composites.

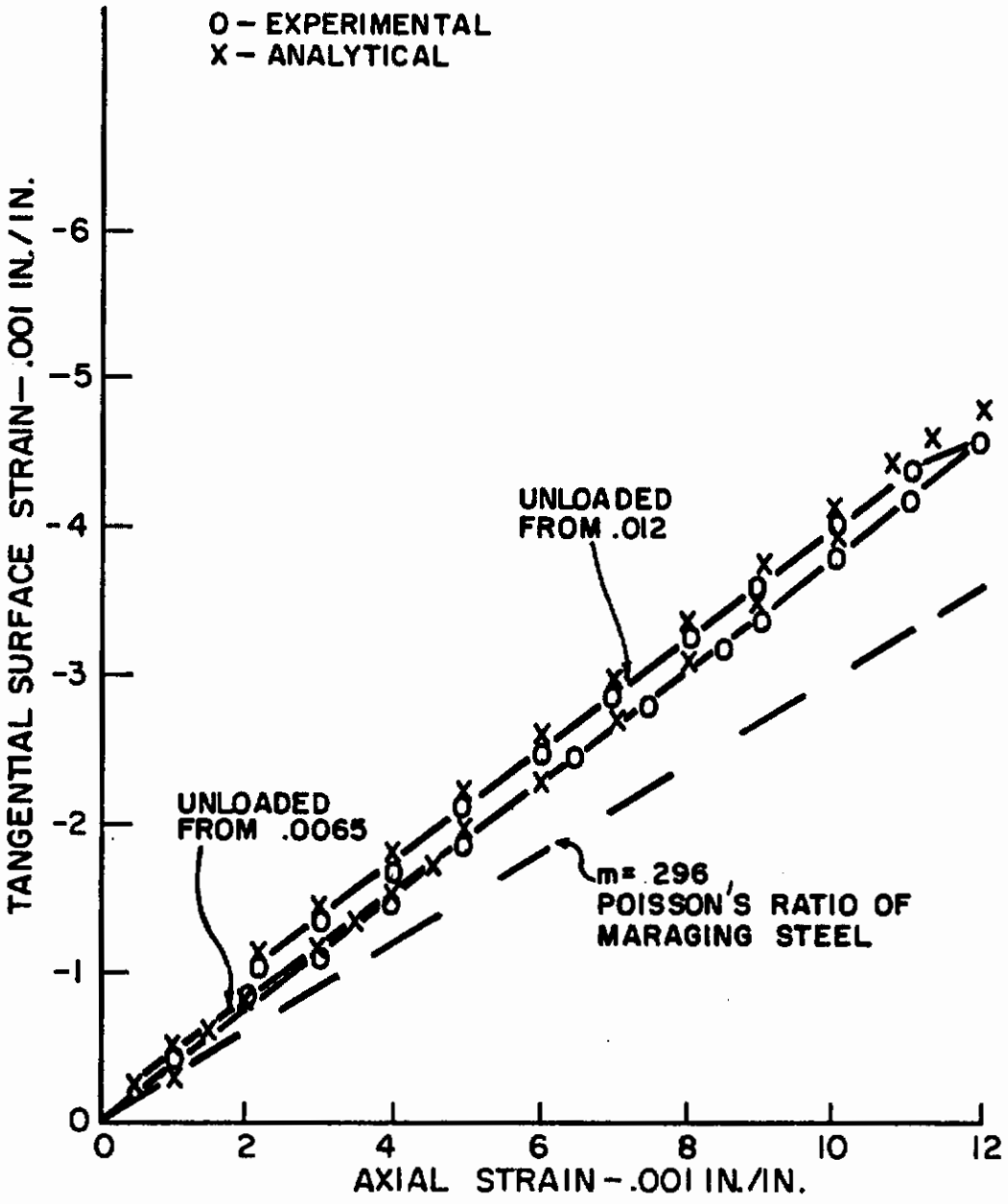

Figure 63

Tangential Surface Strain as a Function of Axial Strain During Prestraining of .504 Volume Fraction Maraging Steel-OFHC Copper Composites.

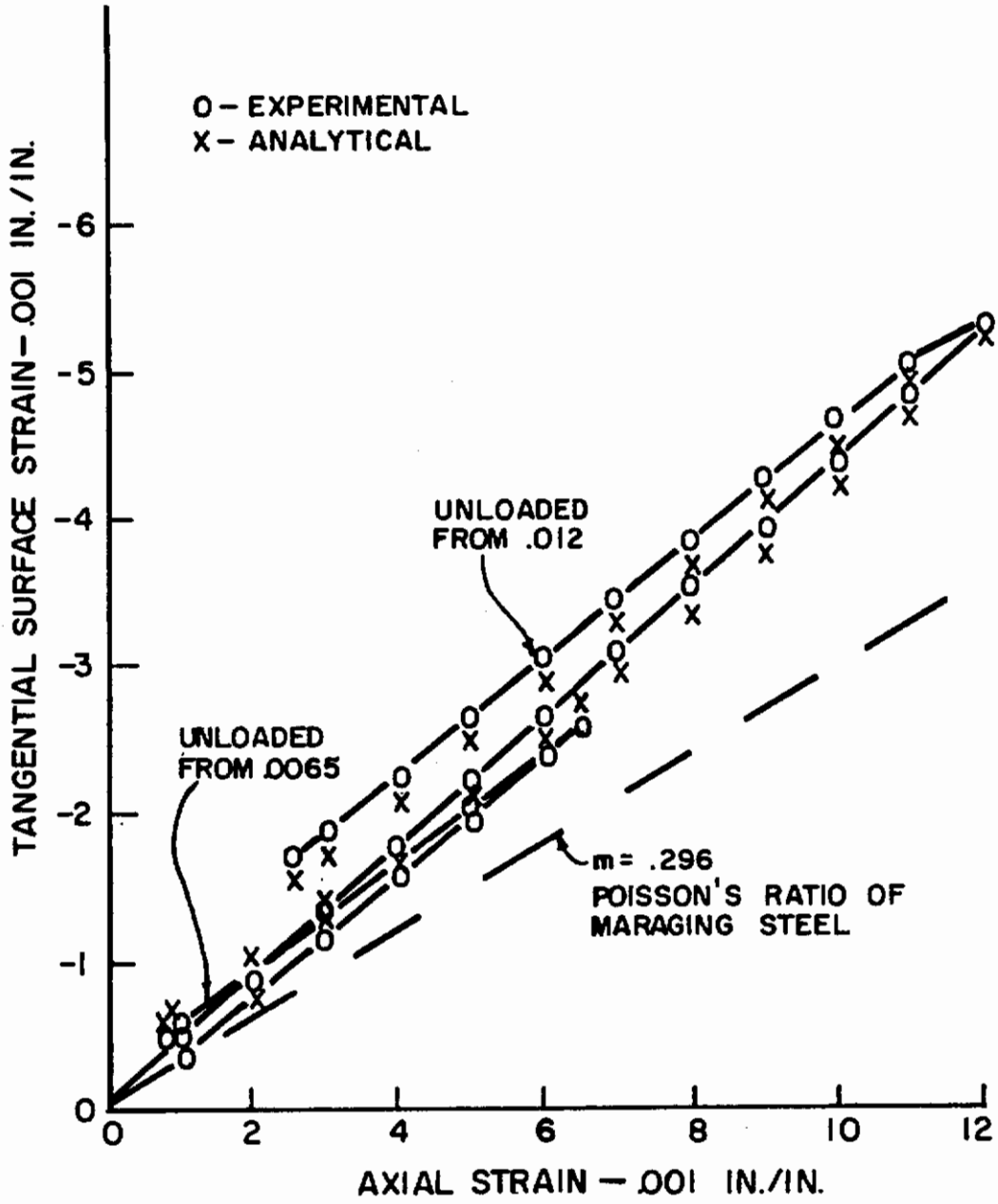

Figure 64

Tangential Surface Strain as a Function of Axial Strain During Prestraining of .335 Volume Fraction Maraging Steel-OFHC Copper Composites.

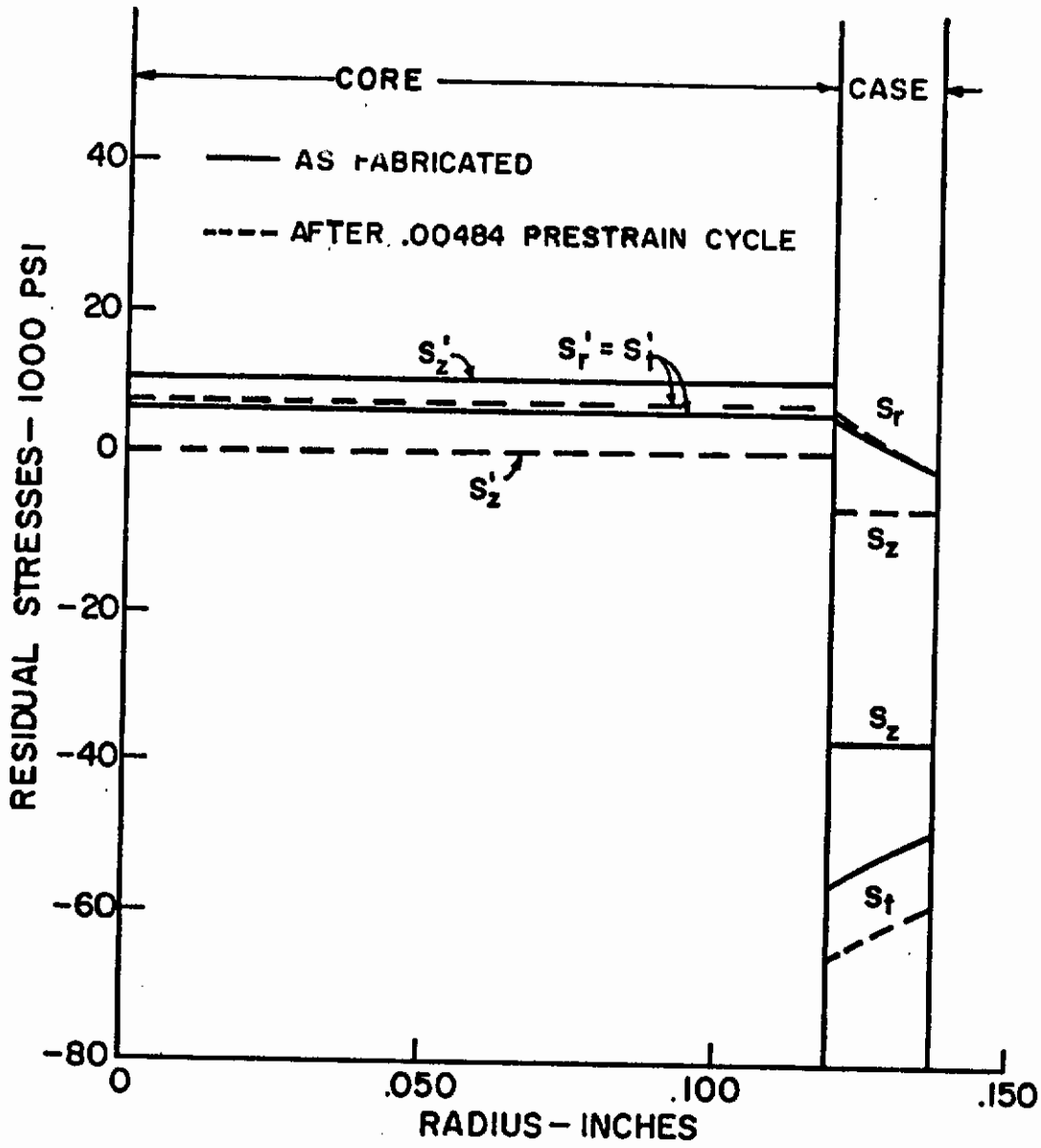

Figure 65

Residual Stress Distribution Before and After Axial Prestrain for .225 Volume Percent 4340 Steel-OFHC Copper Composite.

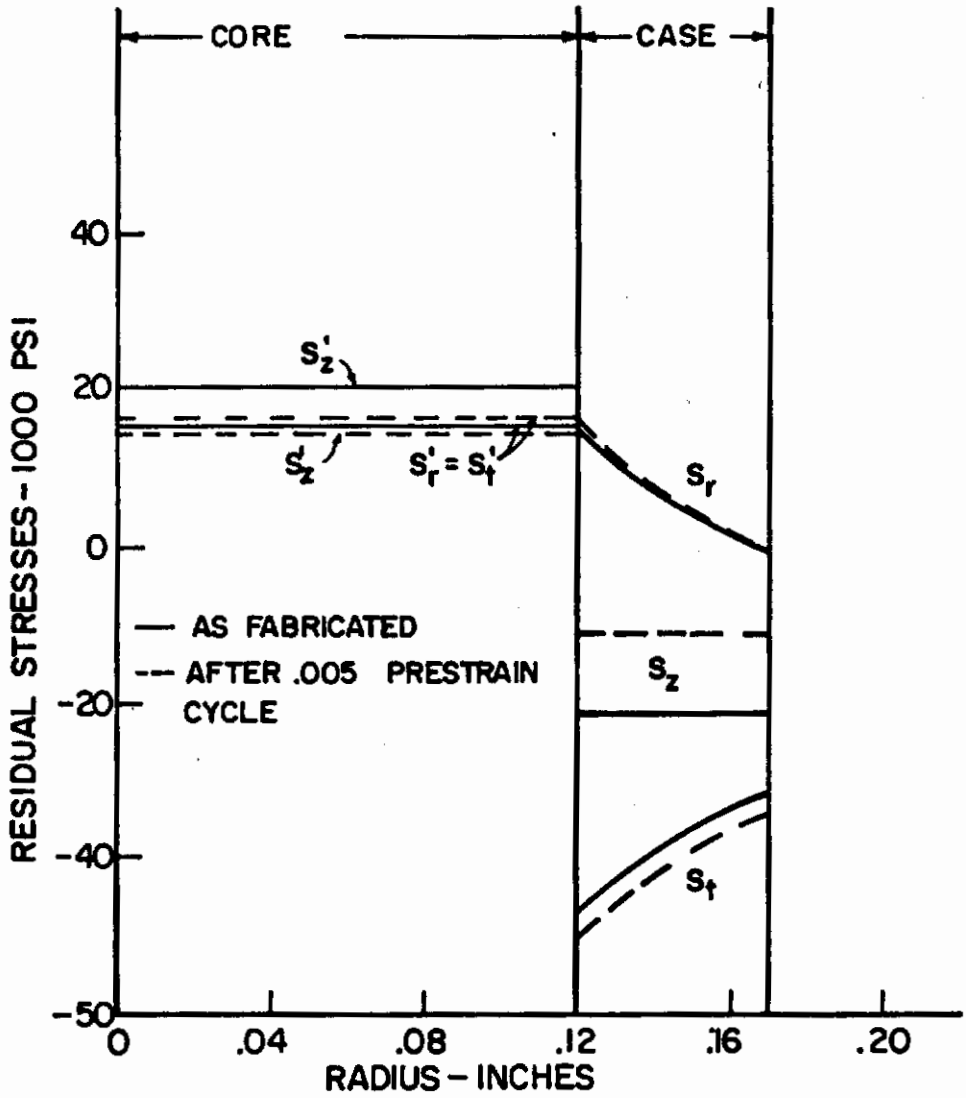

Figure 66

Residual Stress Distribution Before and After Axial Prestrain For .504 Volume Percent 4340 Steel-OFHC Copper Composite.

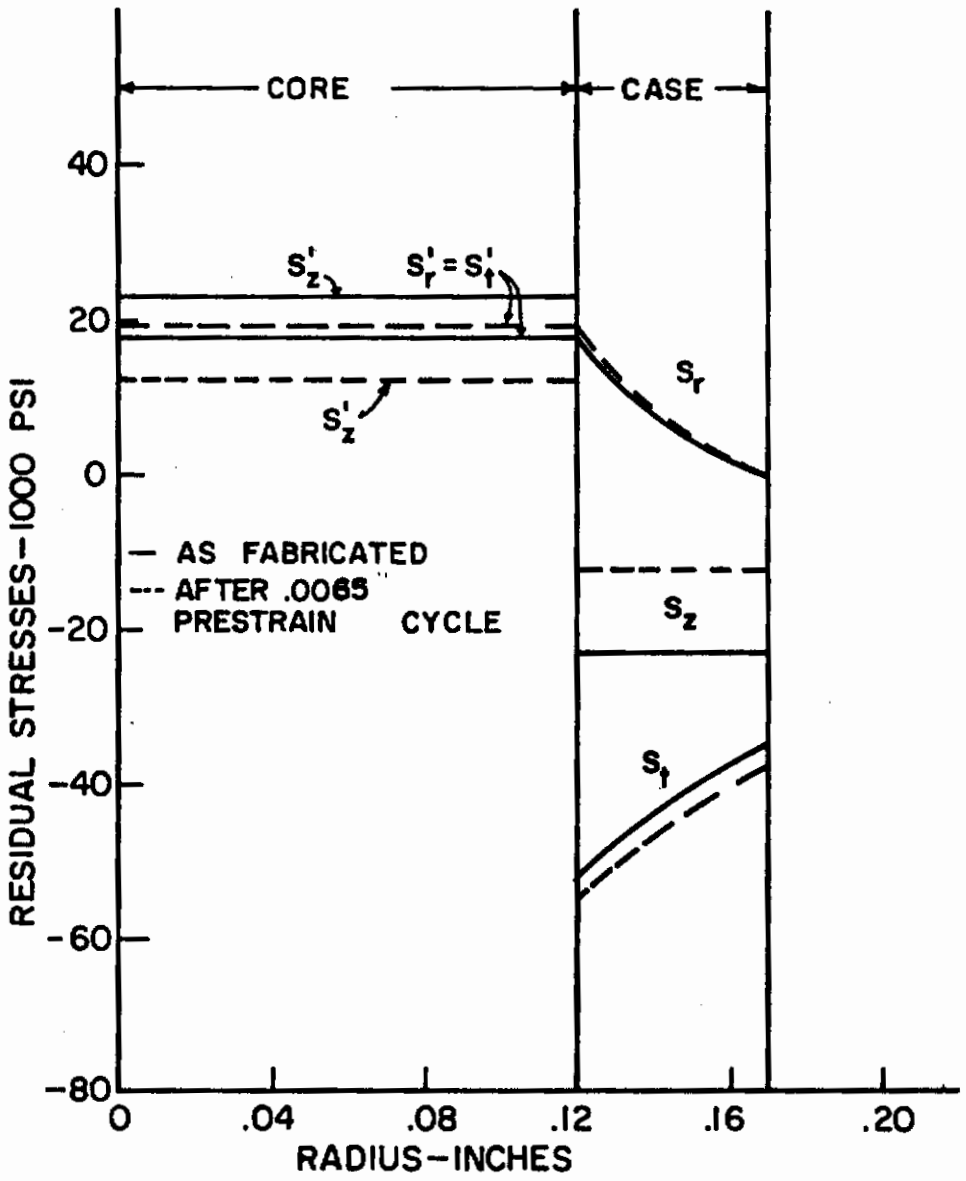

Figure 67

Residual Stress Distribution Before and After Axial Prestrain Into Stage II For .504 Volume Fraction Maraging Steel-OFHC Copper Composite..

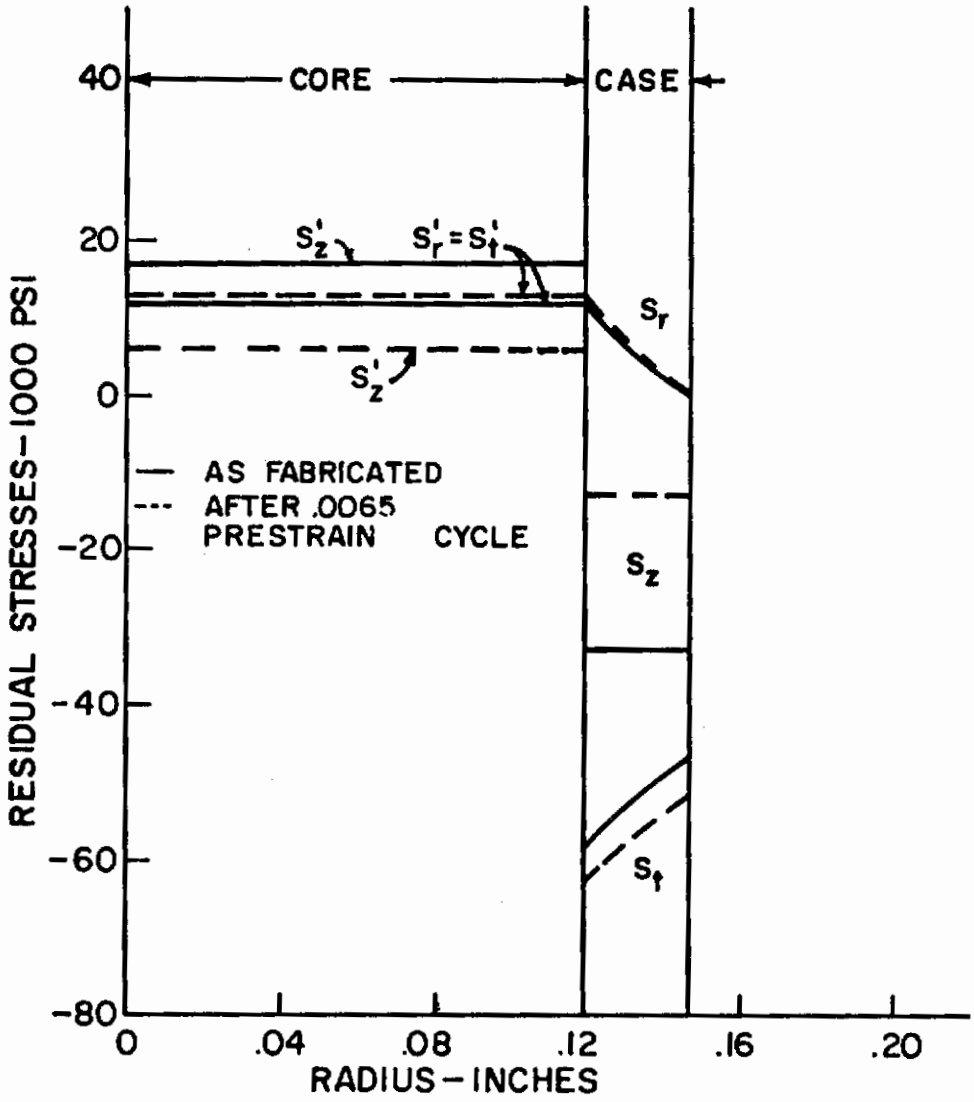

Figure 68

Residual Stress Distribution Before and After Axial Prestrain Into Stage II for .335 Volume Fraction Maraging Steel-OFHC Copper Composite.

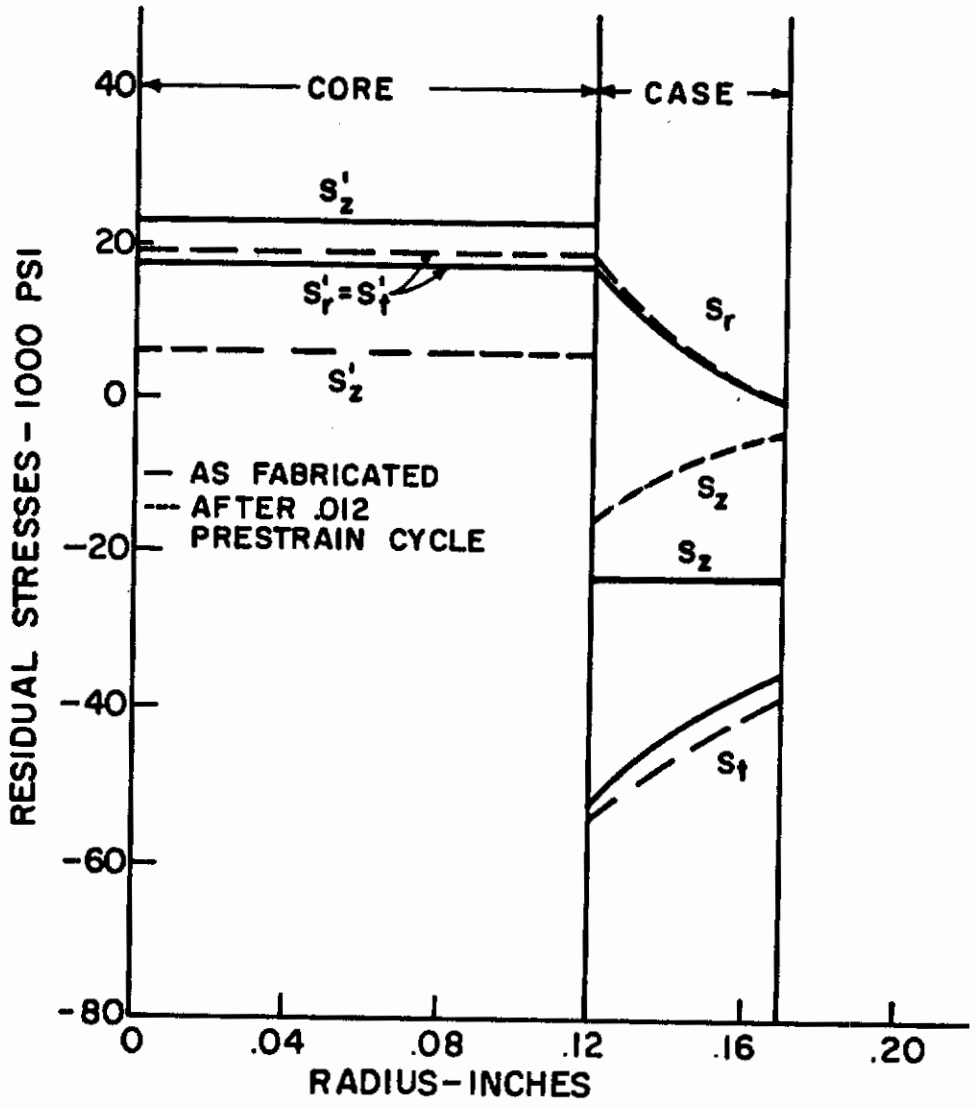

Figure 69

Residual Stress Distribution Before and After Axial Prestrain Into Stage III for .504 Volume Fraction Maraging Steel-OFHC Copper Composite.

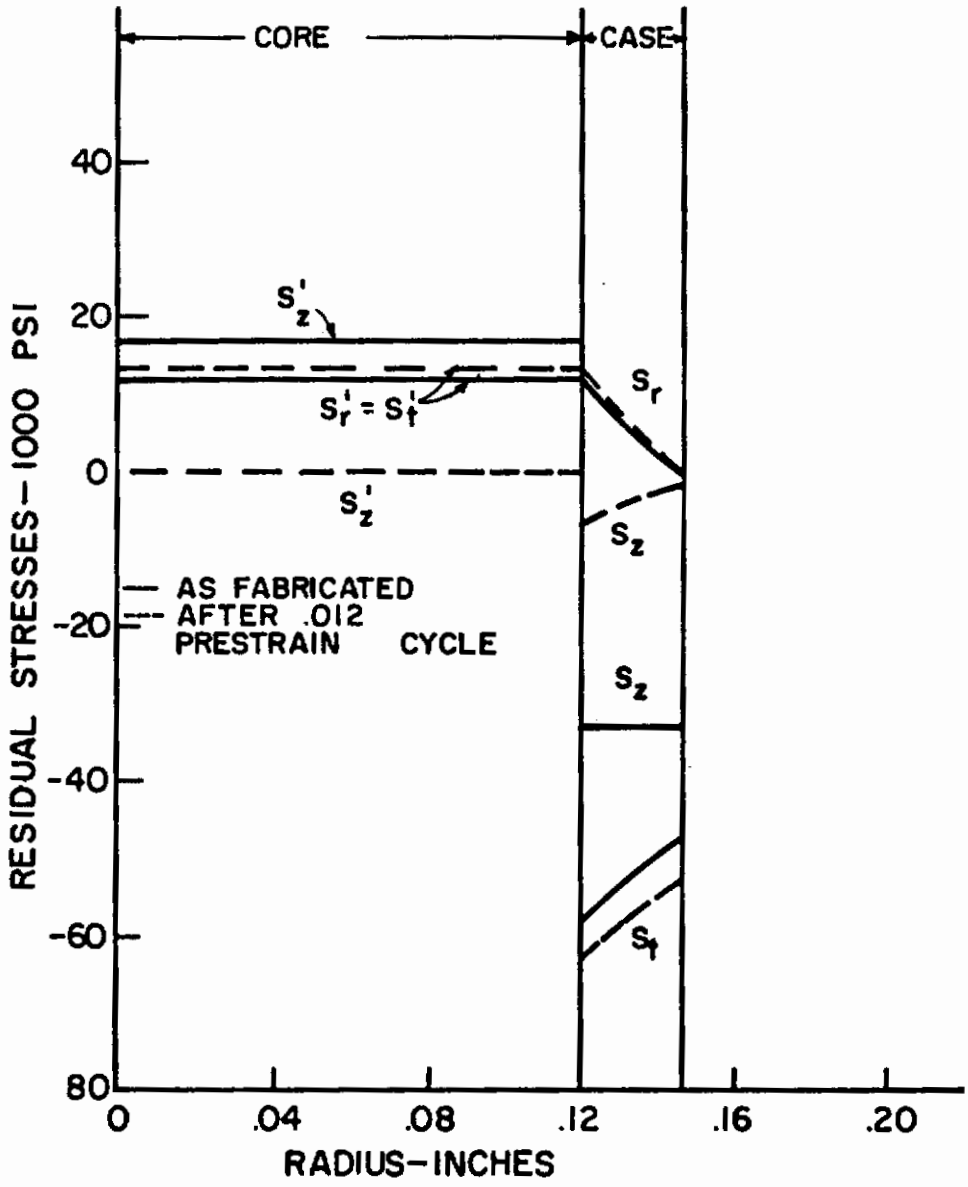

Figure 70

Residual Stress Distribution Before and After Axial Prestrain Into Stage III for .335 Volume Fraction Maraging Steel-OFHC Copper Composite.

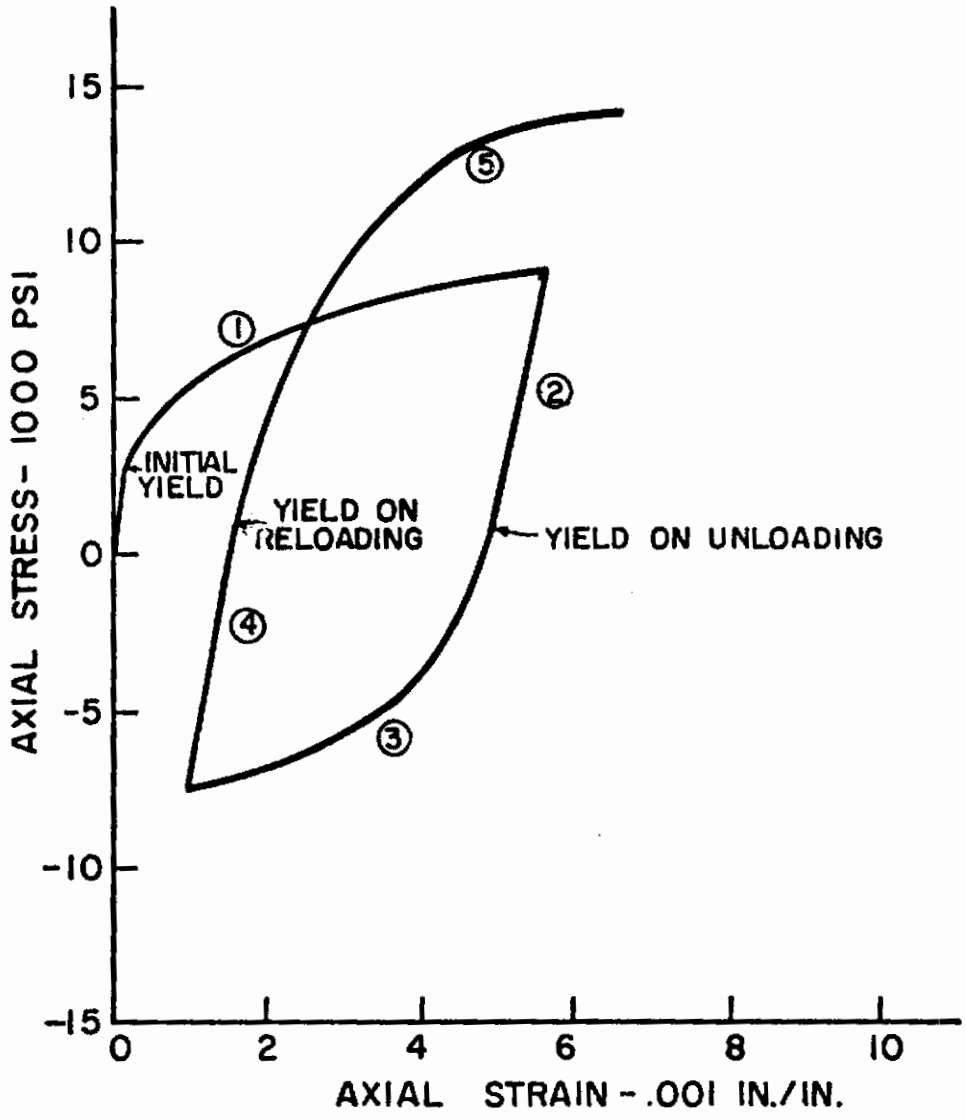

Figure 71

A Typical Experimentally Determined Effective Stress-Effective Strain Loading Function for OFHC Copper.

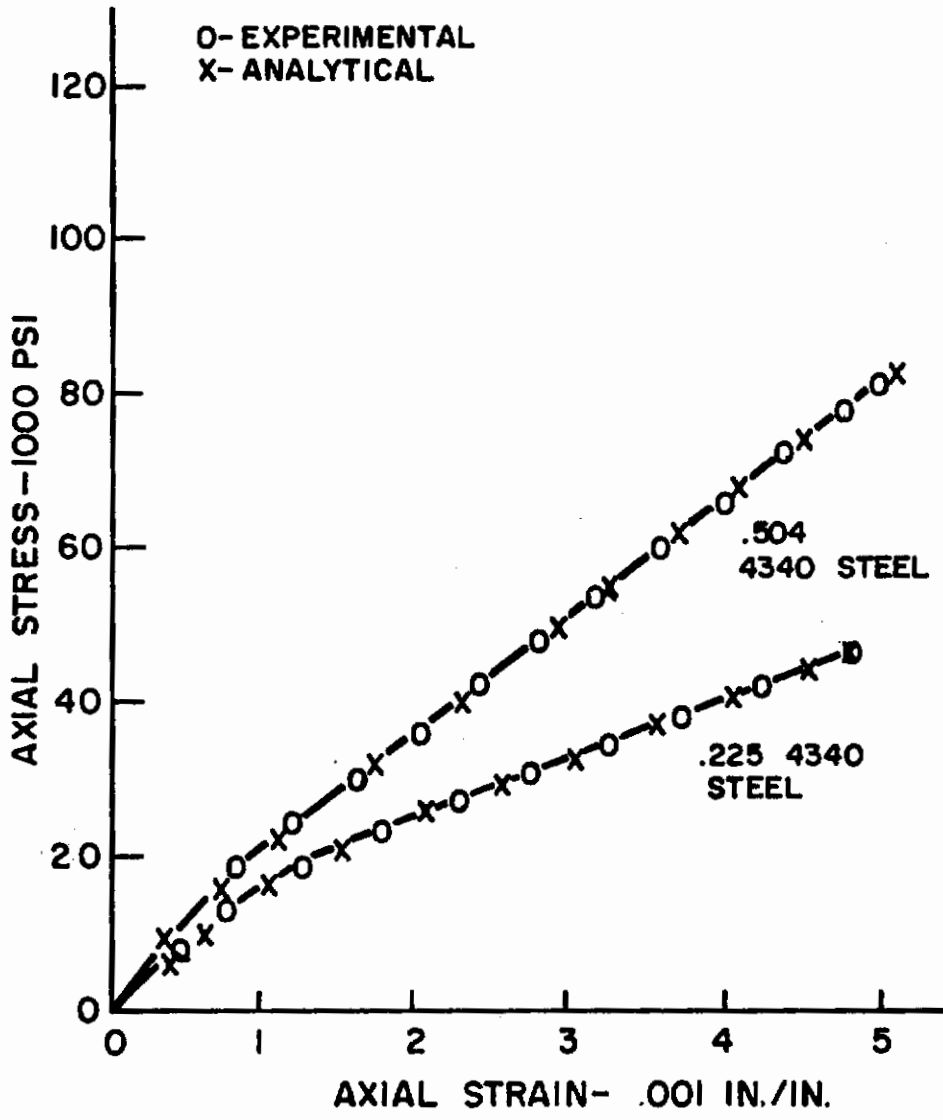

Figure 72

Experimentally Observed and Analytically Predicted Reloading Curves for 4340 Steel-OFHC Copper Composites.

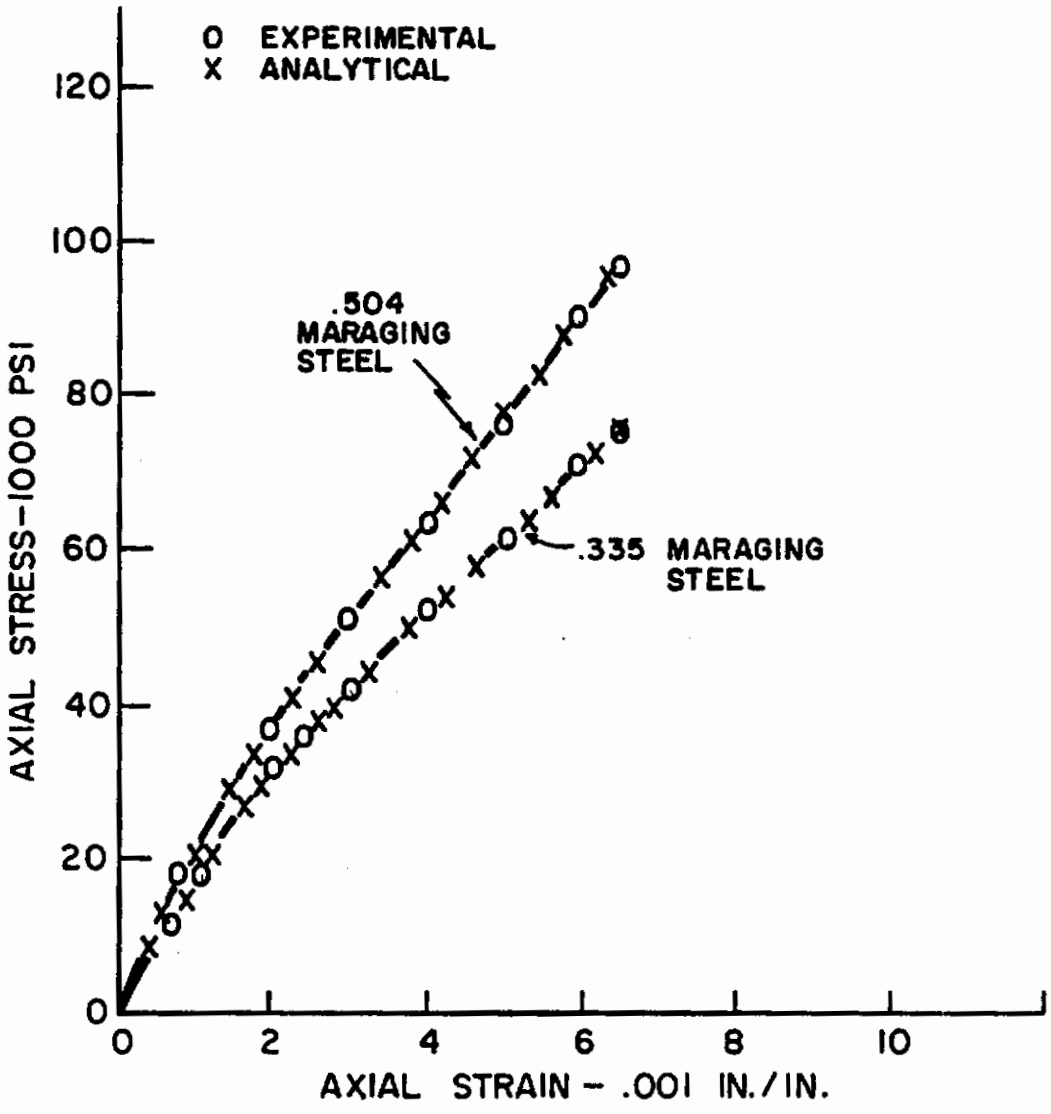

Figure 73

Experimentally Observed and Analytically Predicted Reloading Curves for Maraging Steel-OFHC Copper Composites Prestrained Into Stage II.

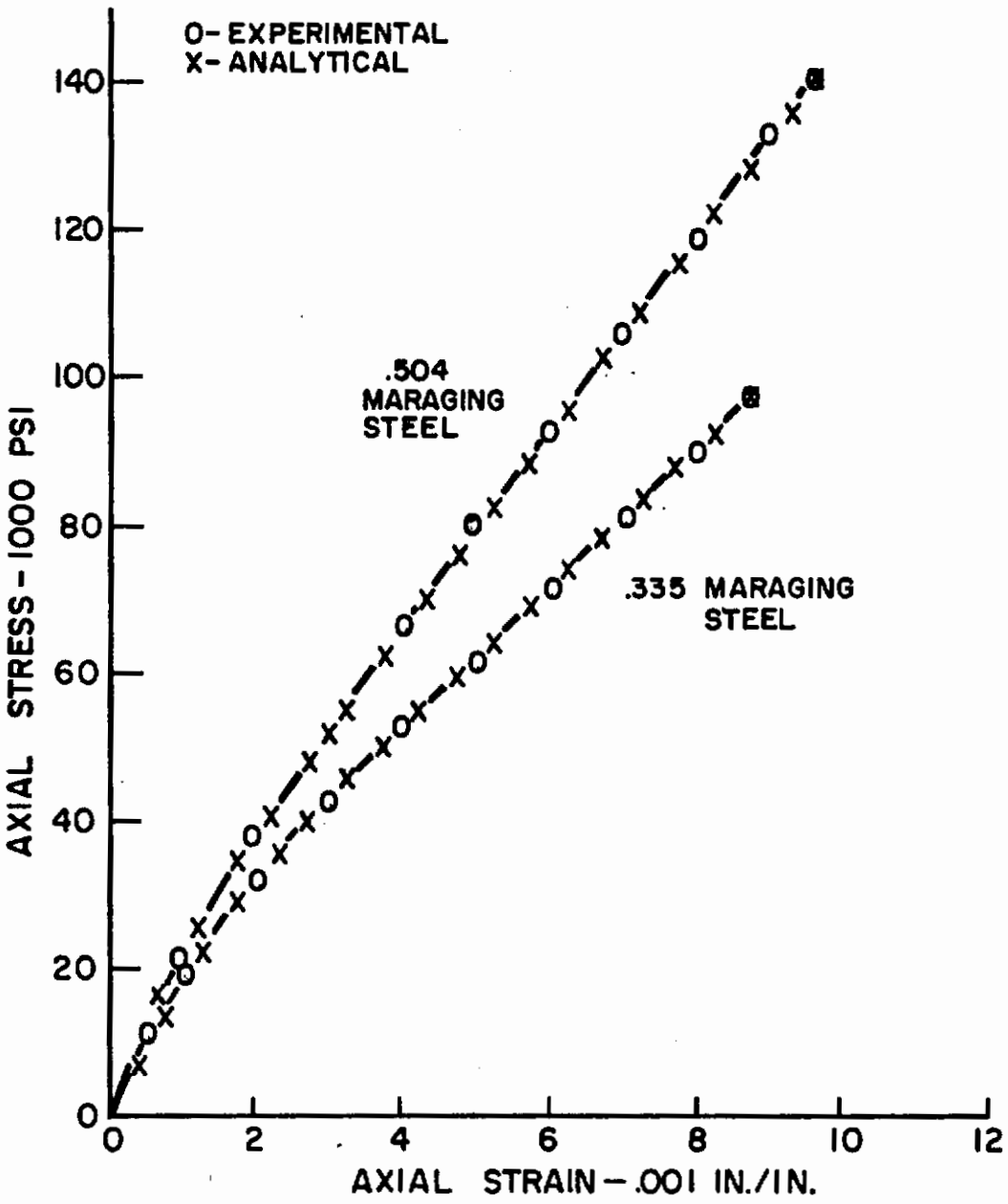

Figure 74

Experimentally Observed and Analytically Predicted Reloading Curves for Maraging Steel-OFHC Copper Composites Prestrained Into Stage III.

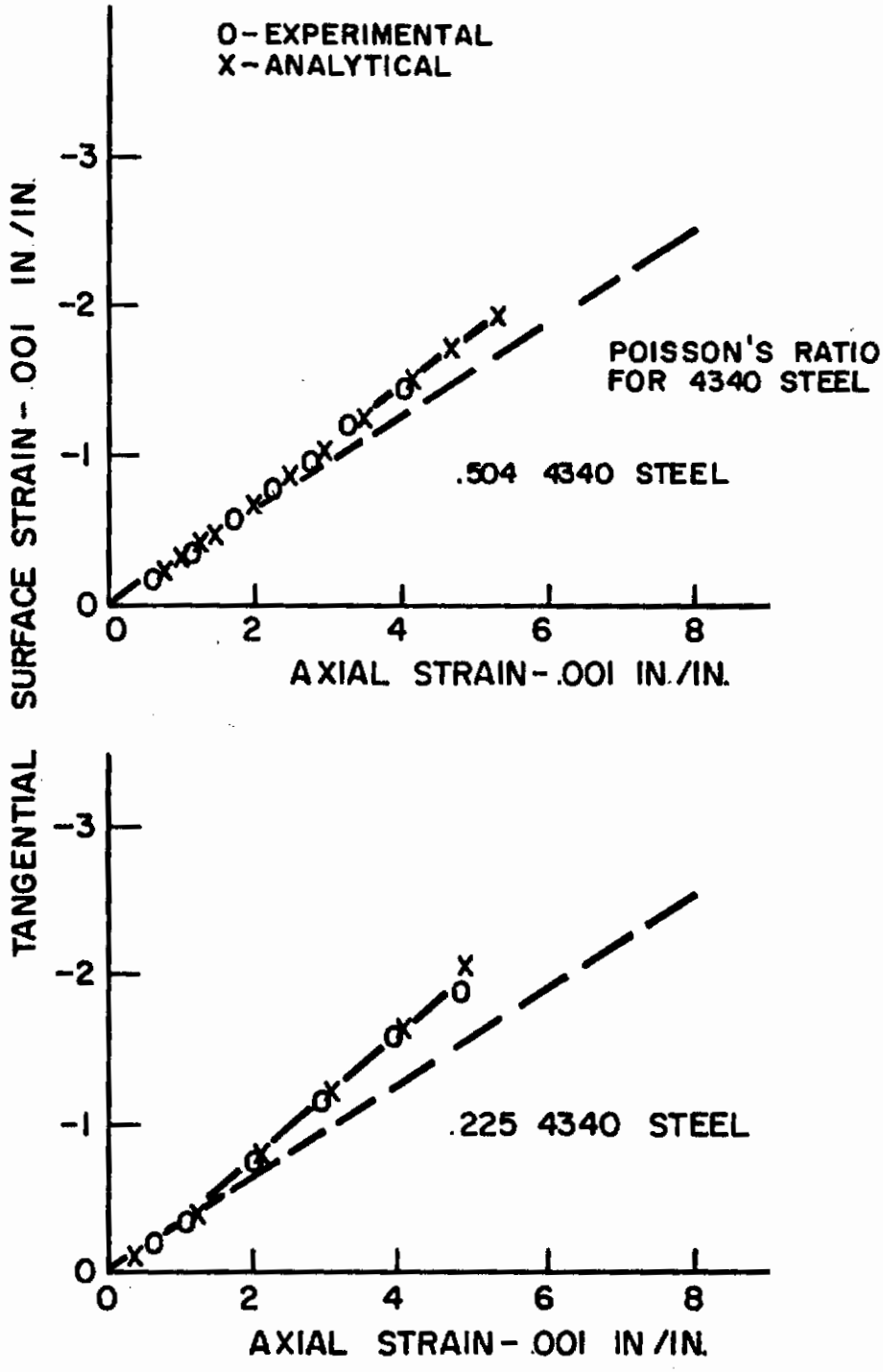

Figure 75

Surface Tangential Strain-Axial Strain Curves for Reloading 4340 Steel-OFHC Copper Composites.

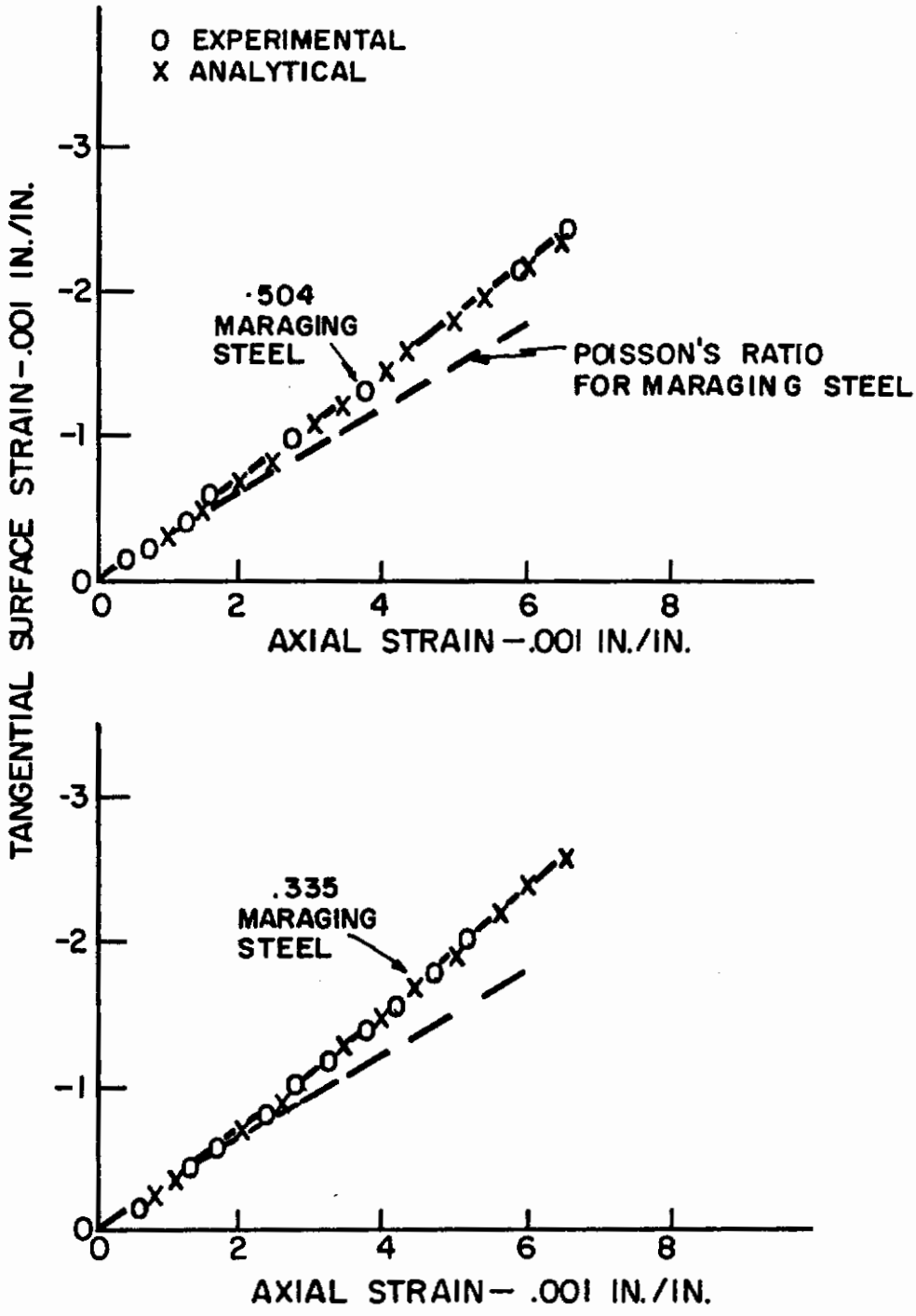

Figure 76

Surface Tangential Strain-Axial Strain Curves for Reloading Maraging Steel-OFHC Copper Composites Which were Prestrained Into Stage II.

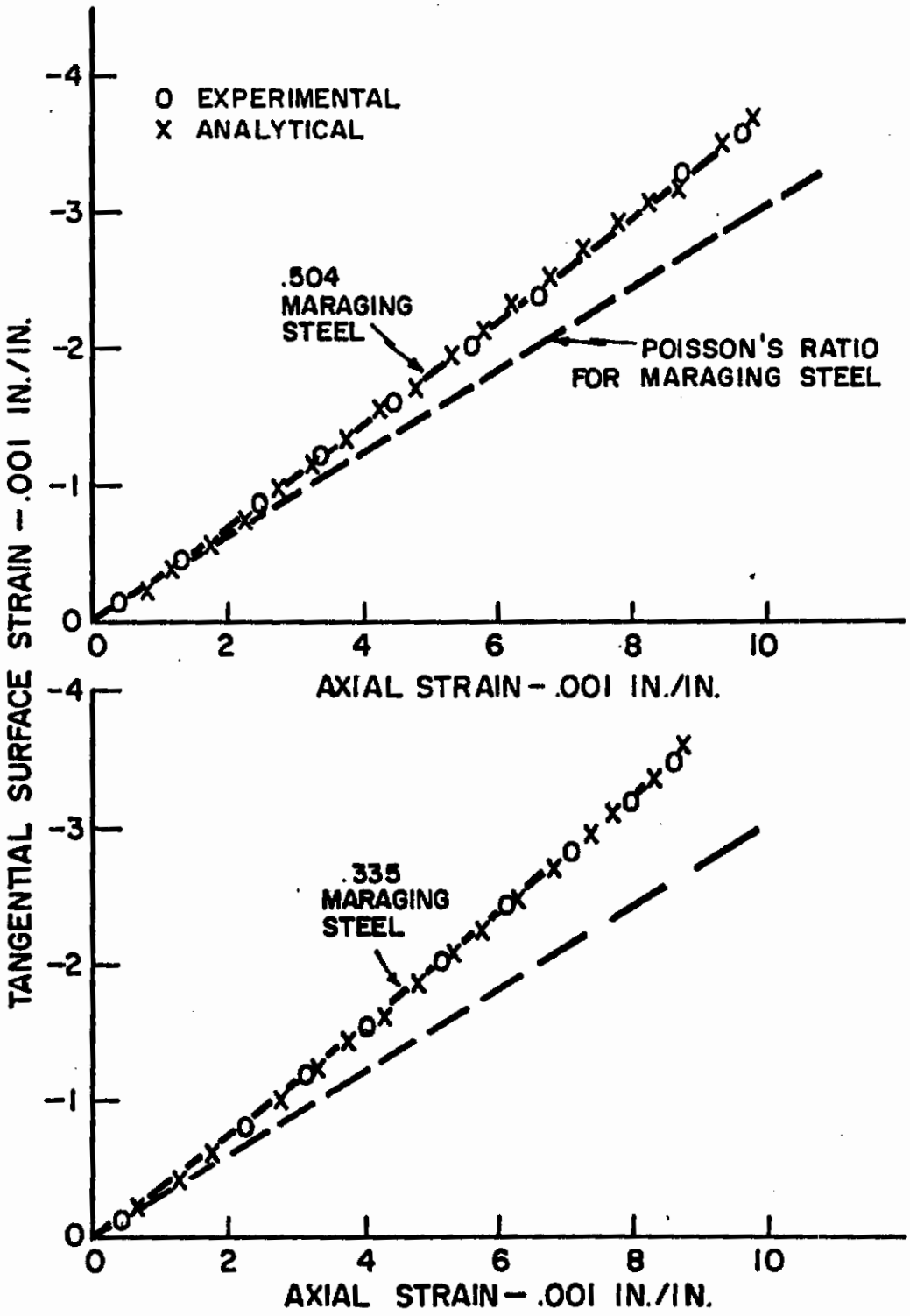

Figure 77

Surface Tangential Strain-Axial Strain Curves for Reloading Maraging Steel-OFHC Copper Composites Which Were Prestrained Into Stage III.

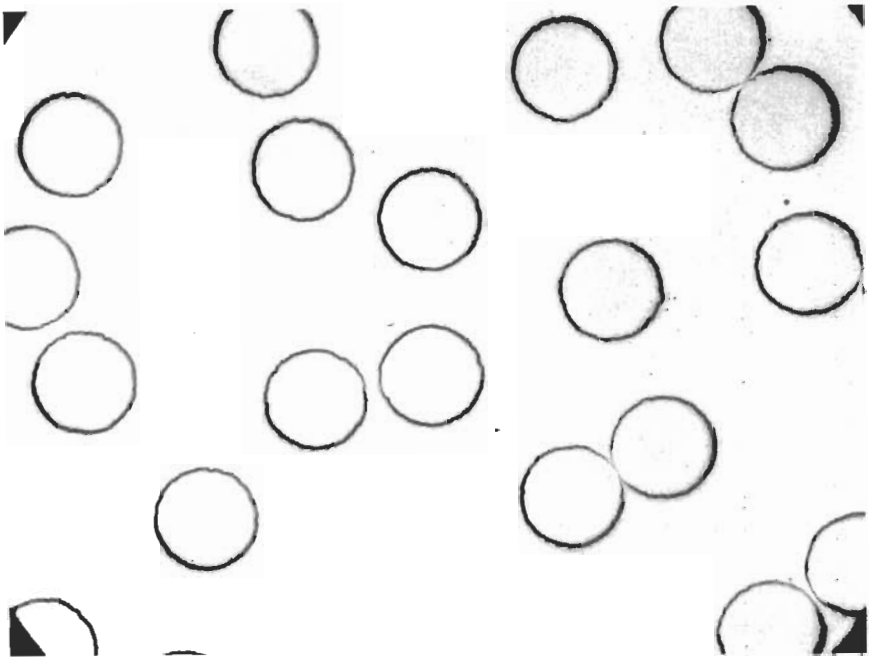

Figure 78

Typical Fiber Spacing in 20.75 Volume Percent Tungsten-Copper Composites.

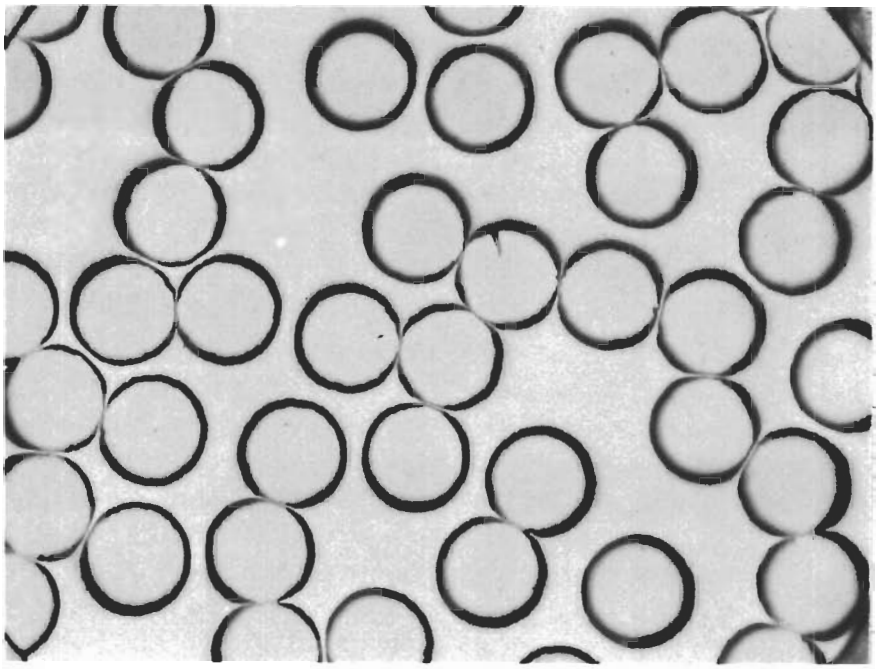

Figure 79

Typical Fiber Spacing in 43 Volume Percent Tungsten-Copper Composites.

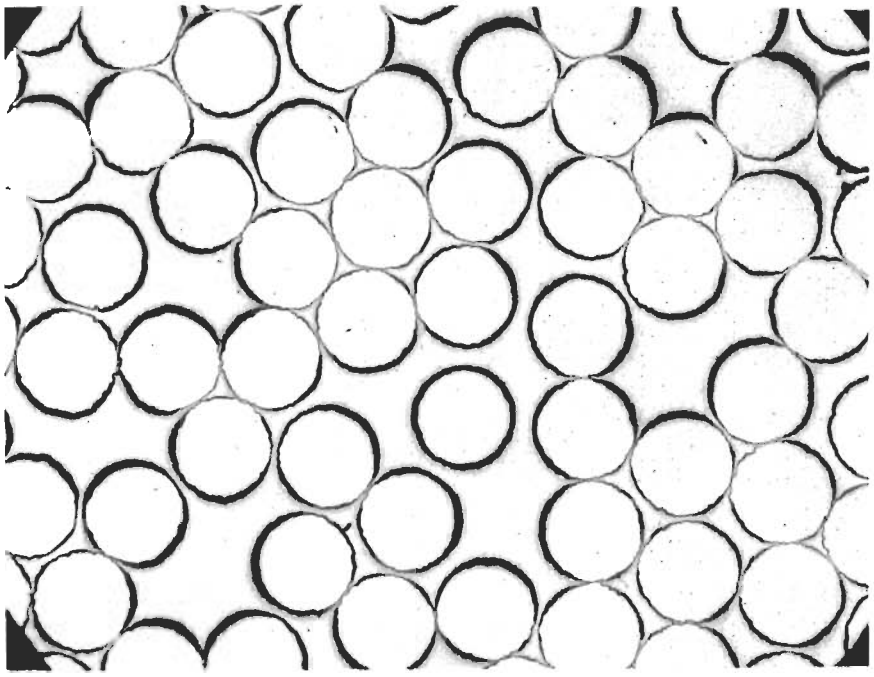

Figure 80

Typical Fiber Spacing in 64 Volume Percent Tungsten-Copper Composites.

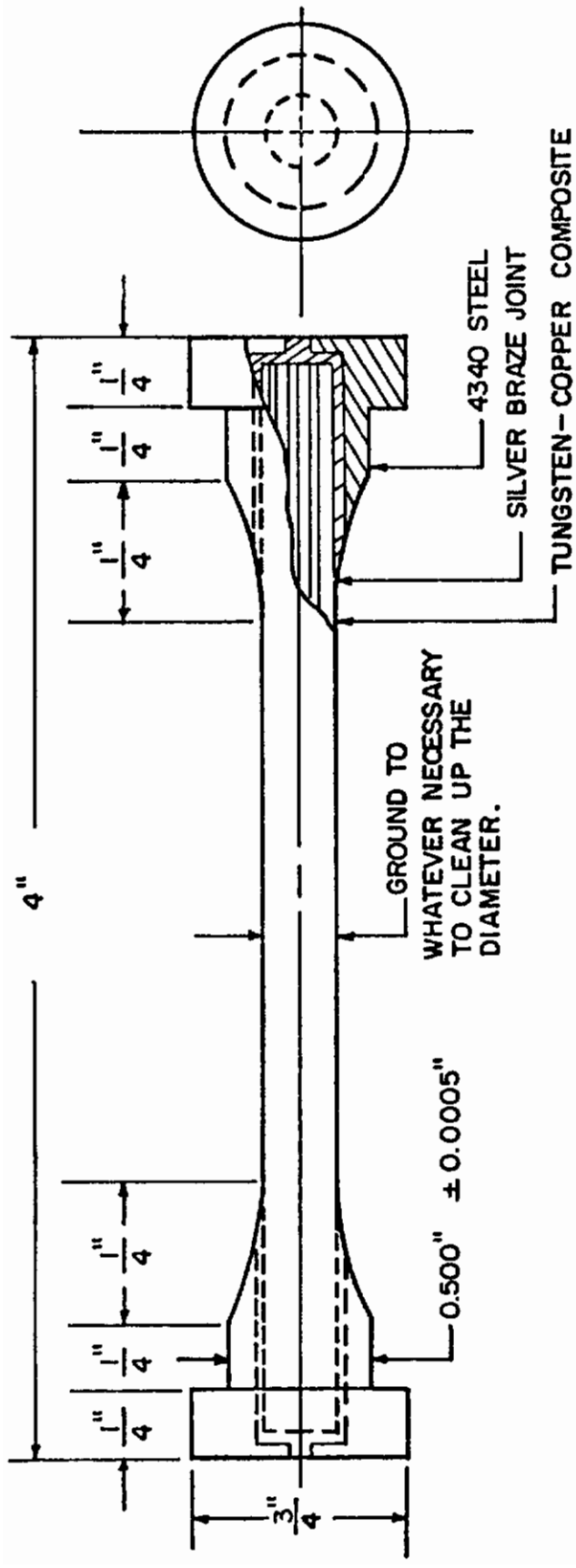

Figure 81

Tensile Specimen Configuration Used for Tungsten-Copper Filamentary Composites.

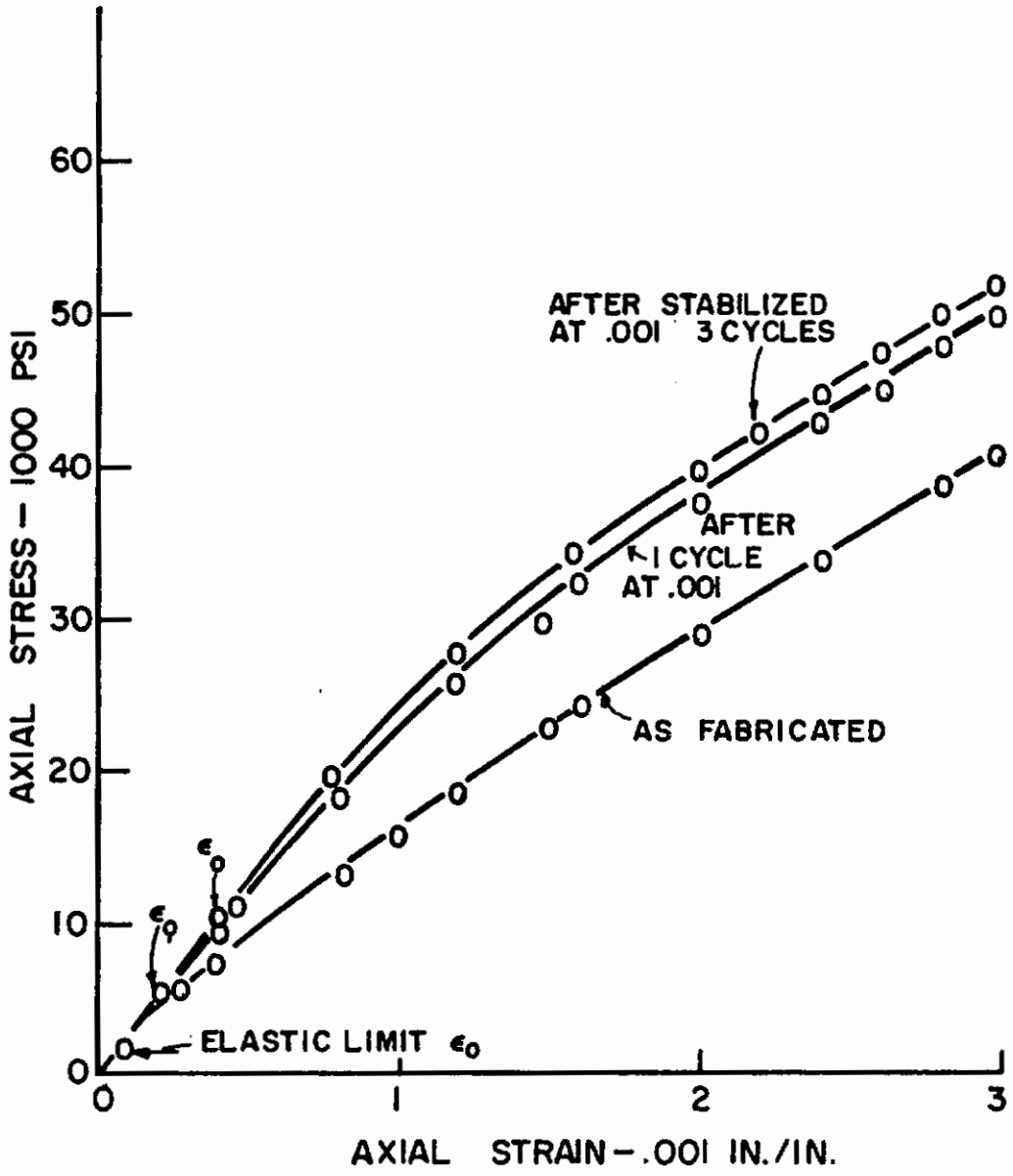

Figure 82

Effect of .001 Prestrain on the Tensile Behavior of 20.75 Volume Percent Tungsten-Copper Composites.

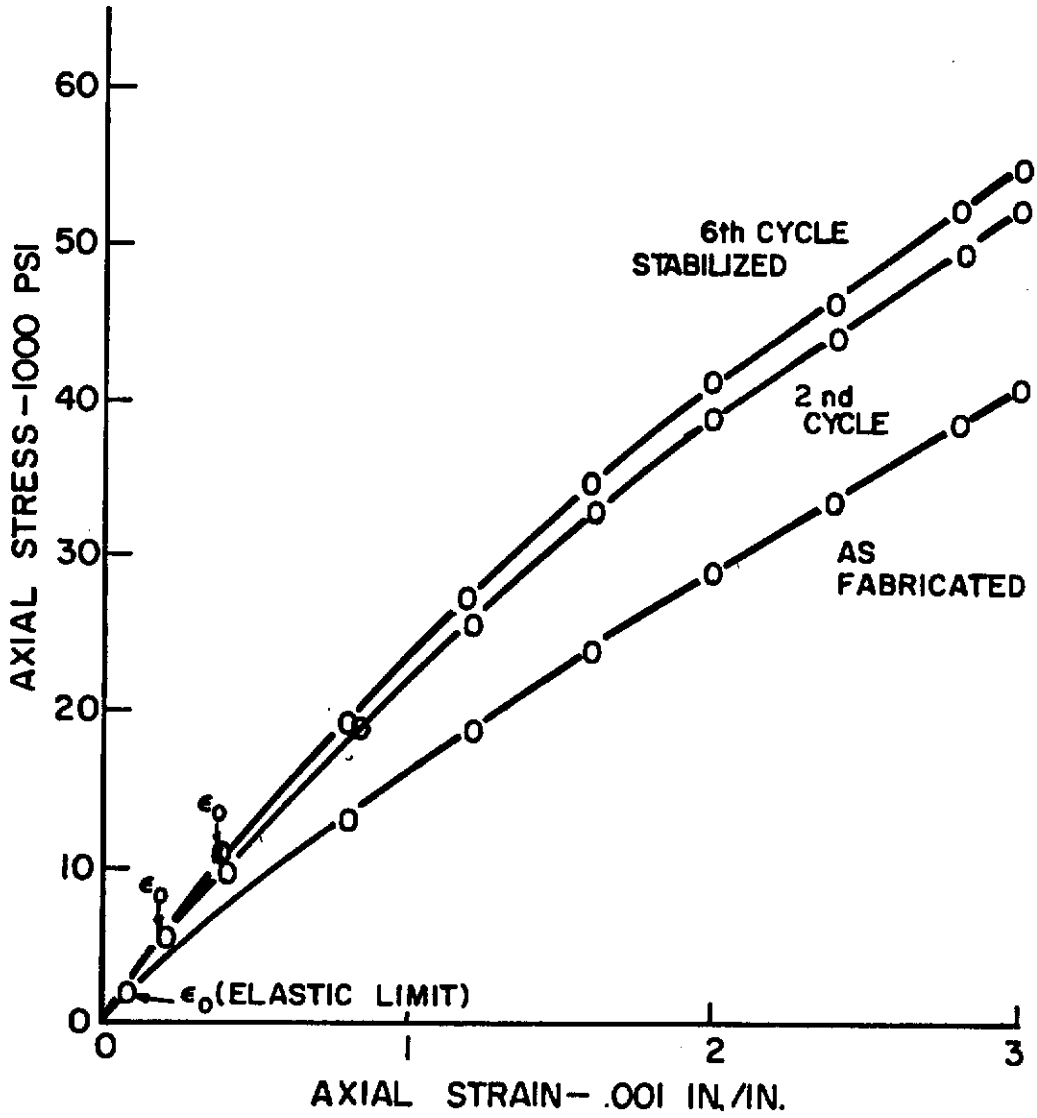

Figure 83

Effect of .003 Prestrain on the Tensile Behavior of 20.75 Volume Percent Tungsten-Copper Composites.

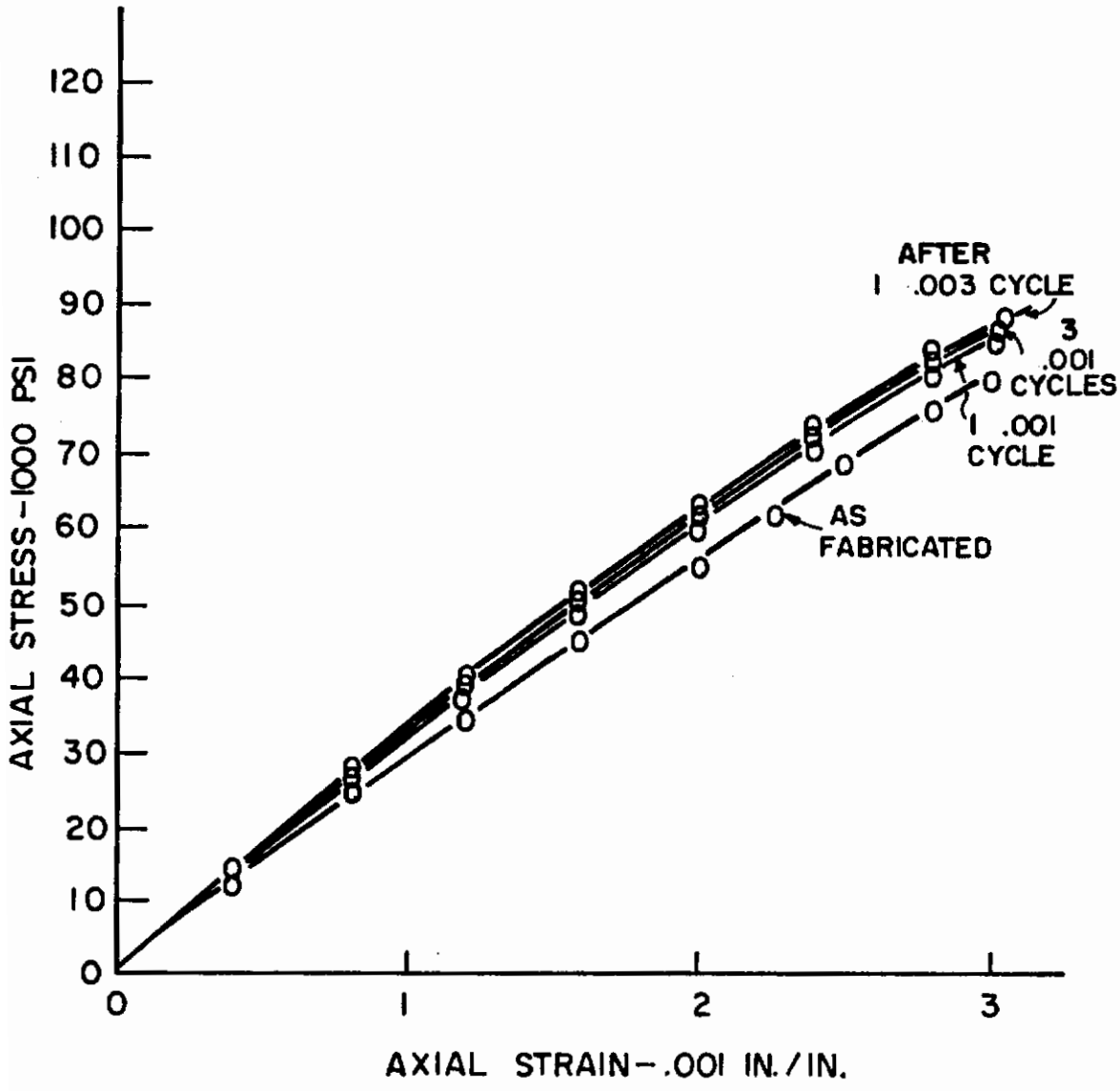

Figure 84

Effect of Prestraining on the Tensile Behavior of 43 Volume Percent Tungsten-Copper Composites.

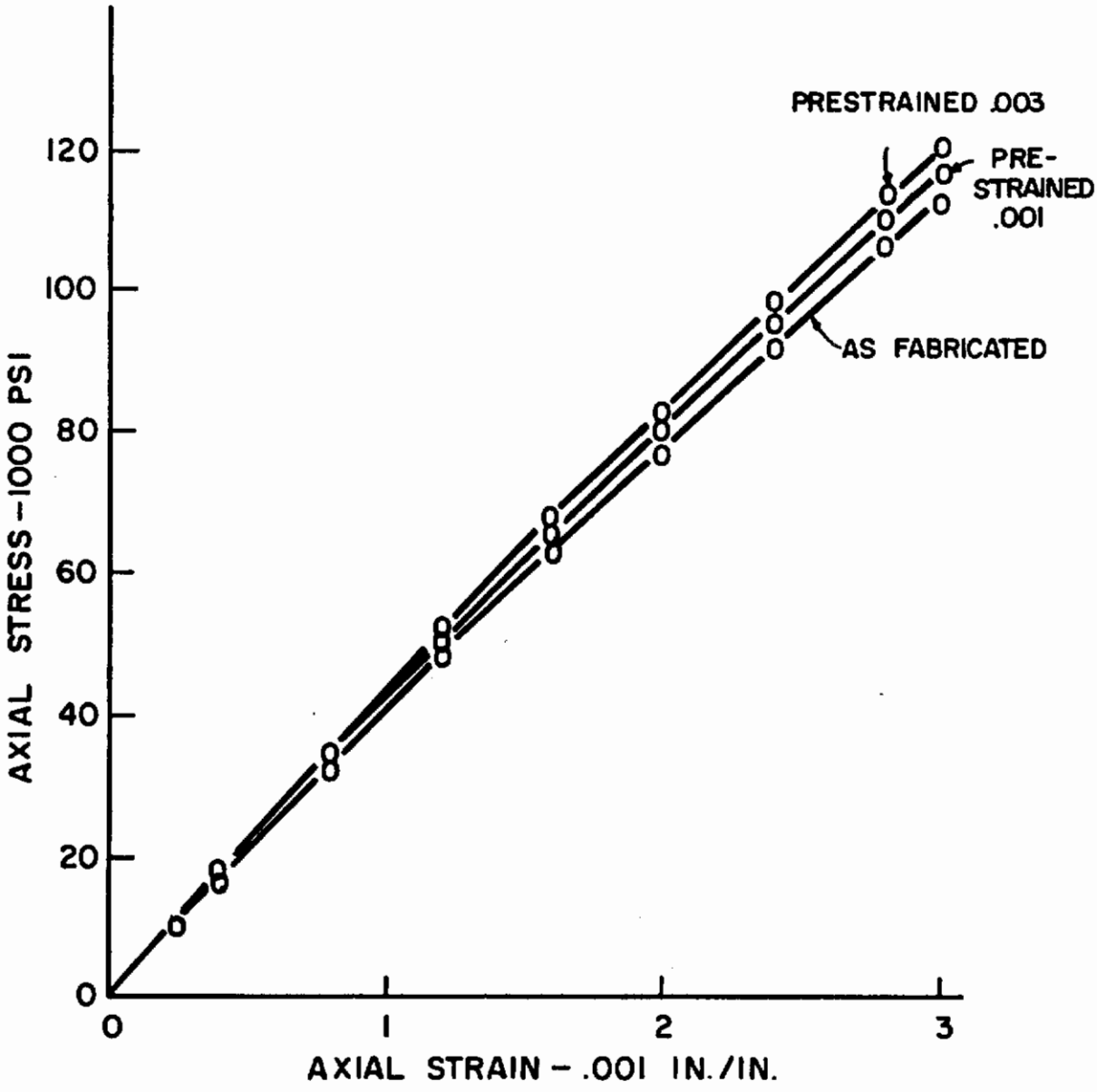

Figure 85

Effect of Prestraining on the Tensile Behavior of 64 Volume Percent Tungsten-Copper Composites.

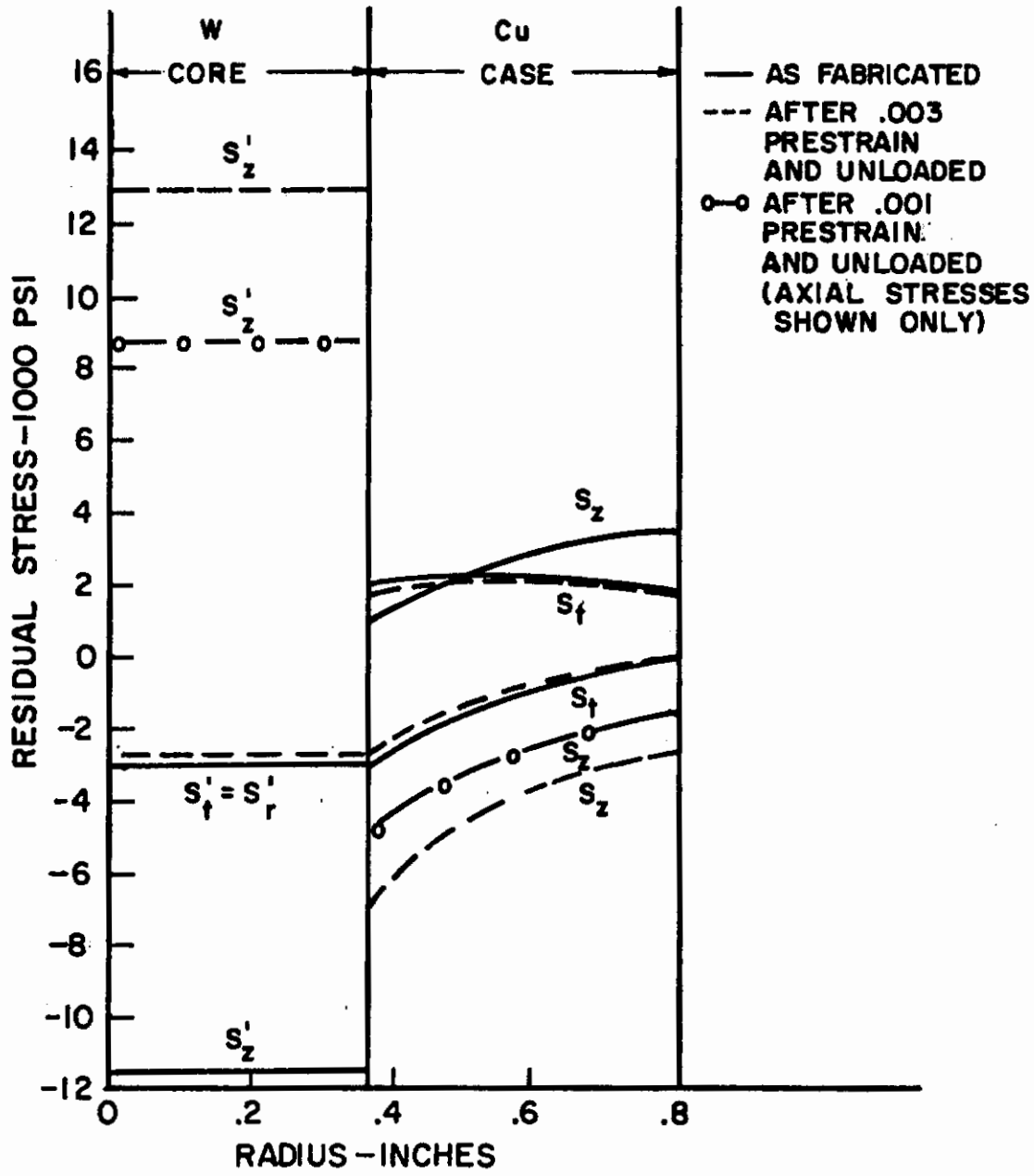

Figure 86

Effect of Prestraining on the Residual Stress State of 20.75 Volume Percent Tungsten-Copper Filamentary Composites.

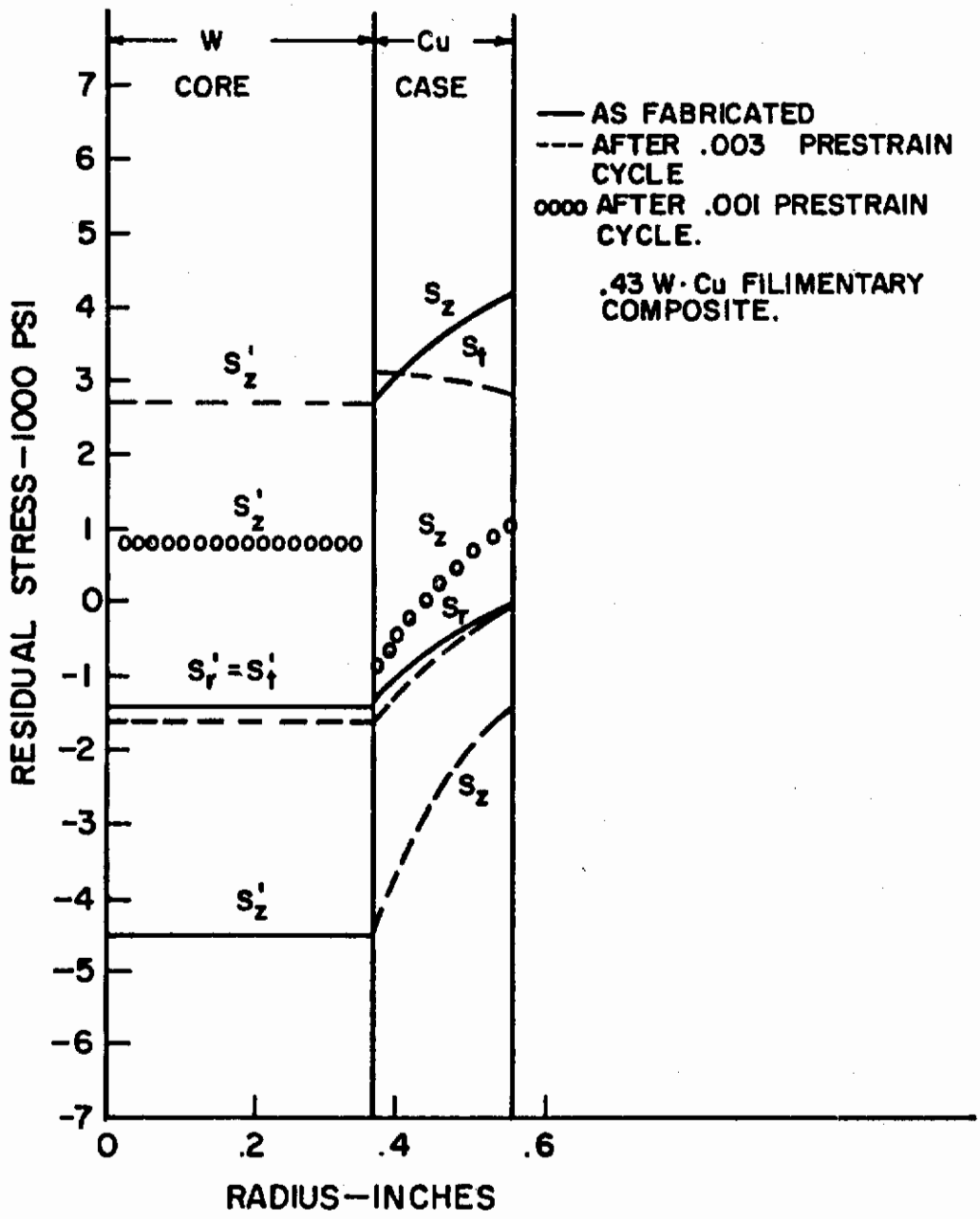

Figure 87

Effect of Prestraining on the Residual Stress State of 43 Volume Percent Tungsten-Copper Filamentary Composites.

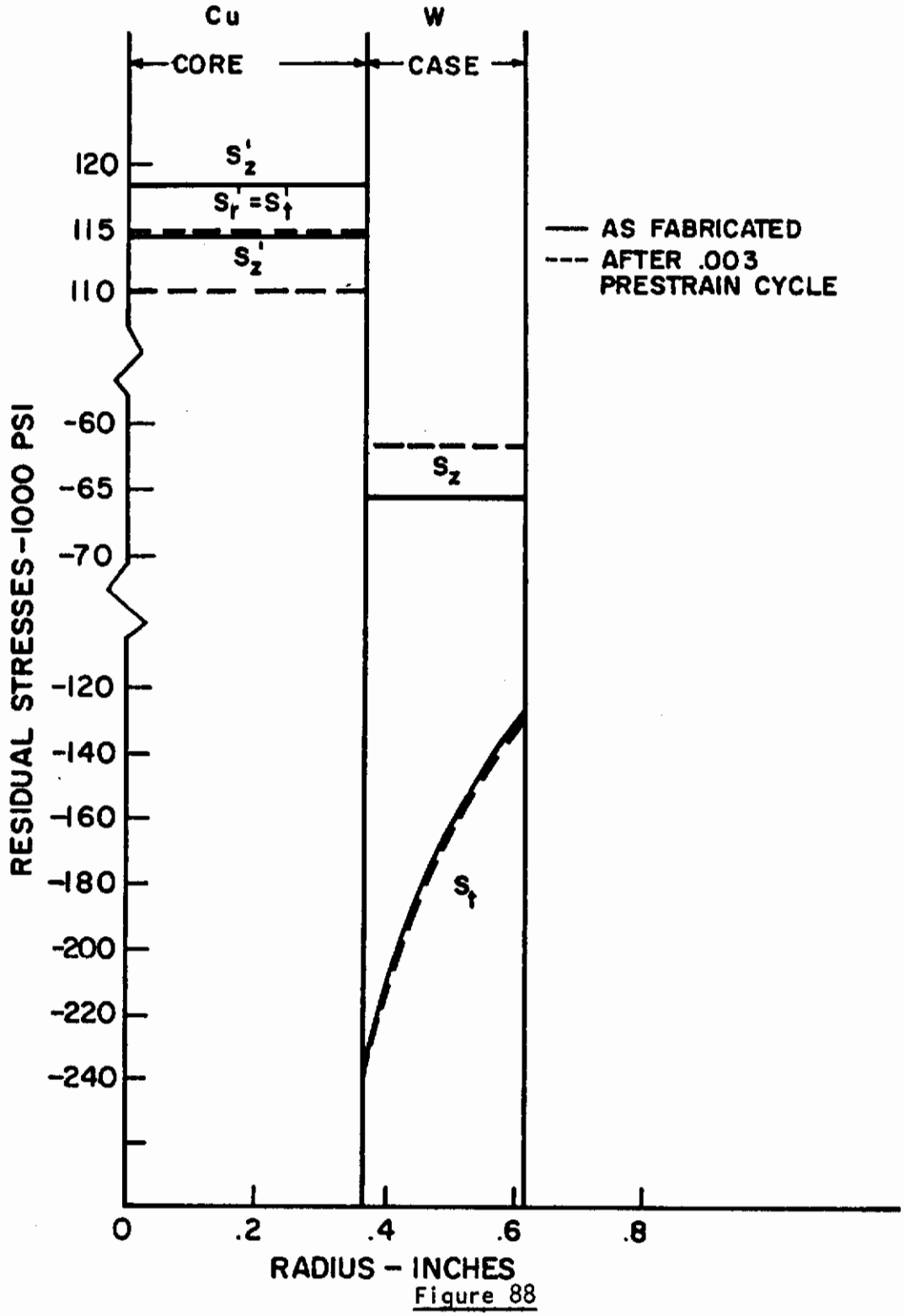

Figure 88

Effect of Prestraining on the Residual Stress State of 64 Volume Percent Tungsten-Copper Filamentary Composites.

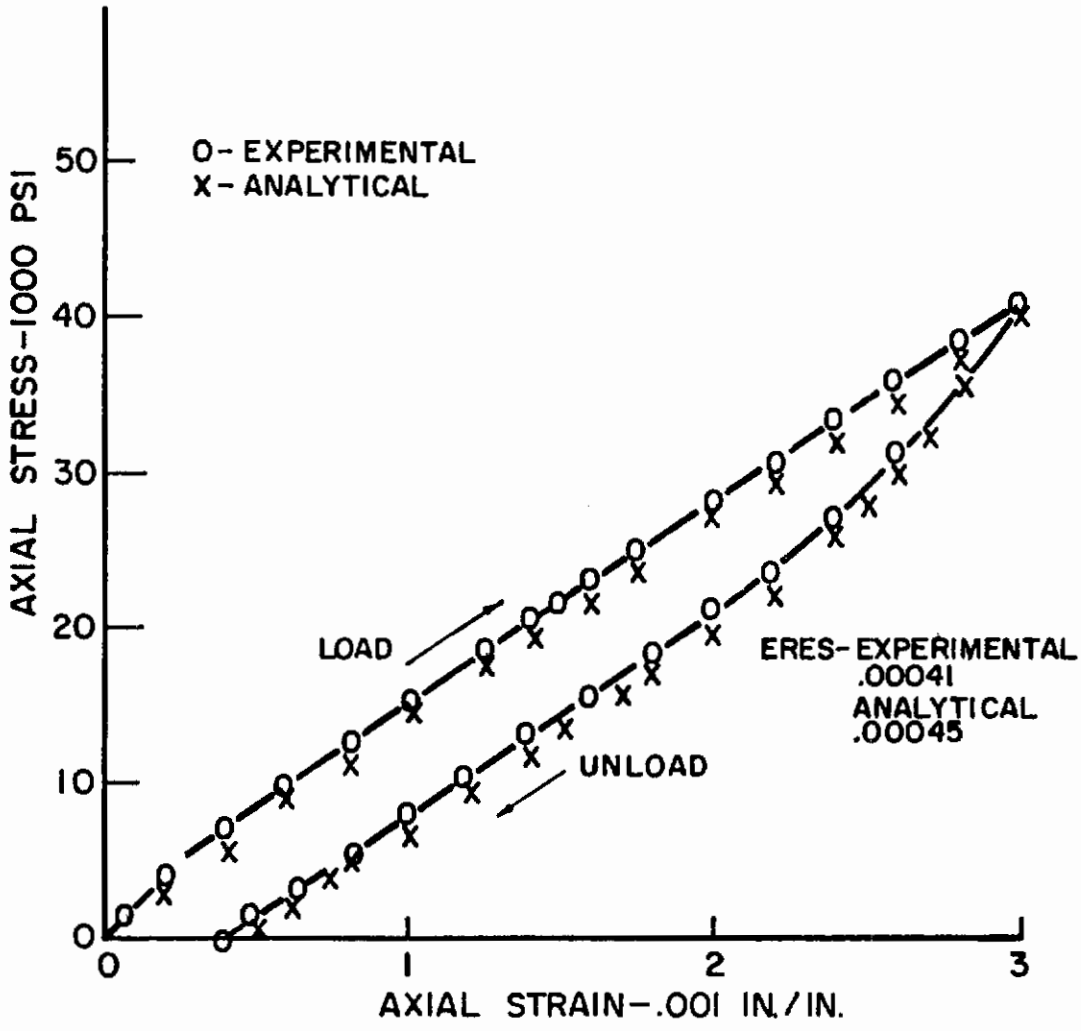

Figure 89

Analytical Prediction of .003 Prestrain Cycle for 20.75 Volume Percent Tungsten-Copper Filamentary Composites.

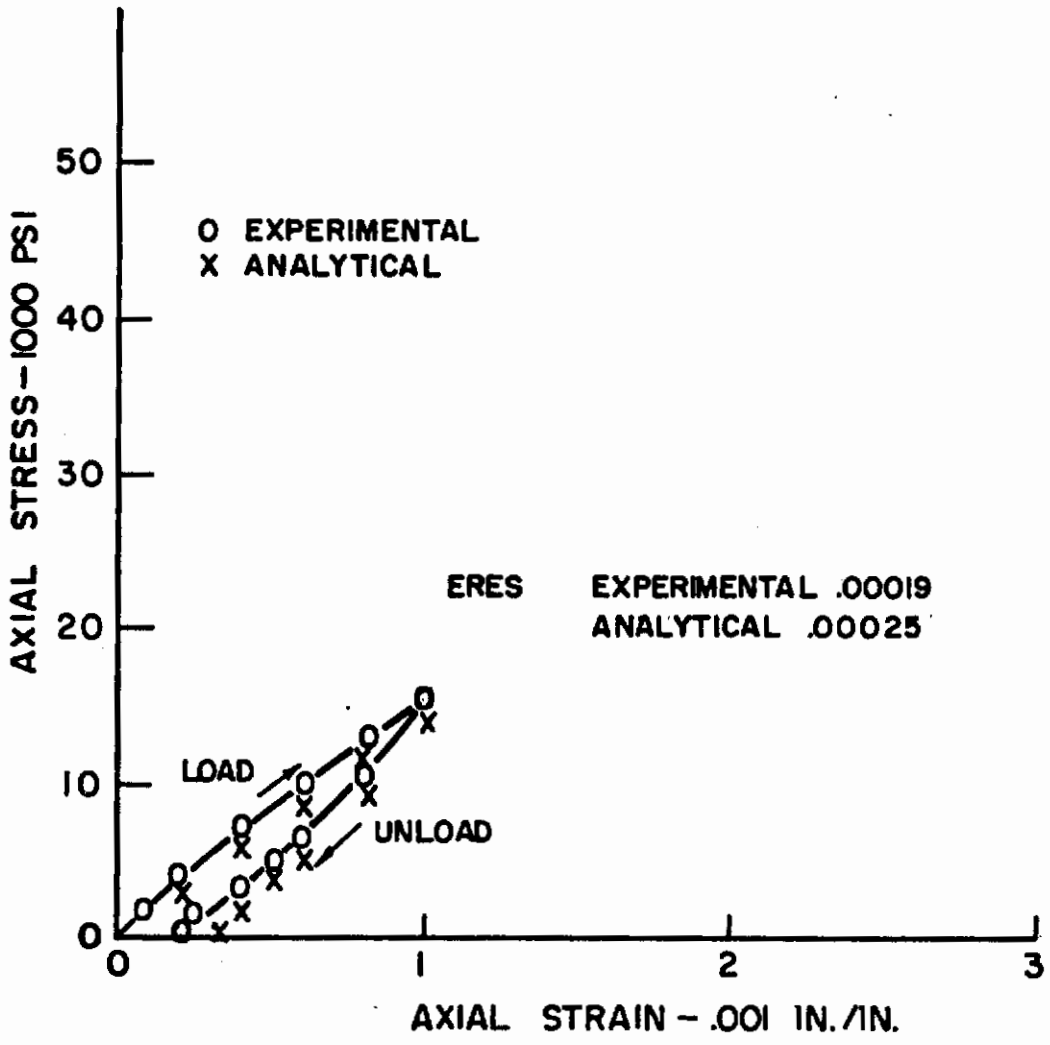

Figure 90

Analytcial Prediction of .001 Prestrain Cycle for 20.75 Volume Percent Tungsten-Copper Filamentary Composites.

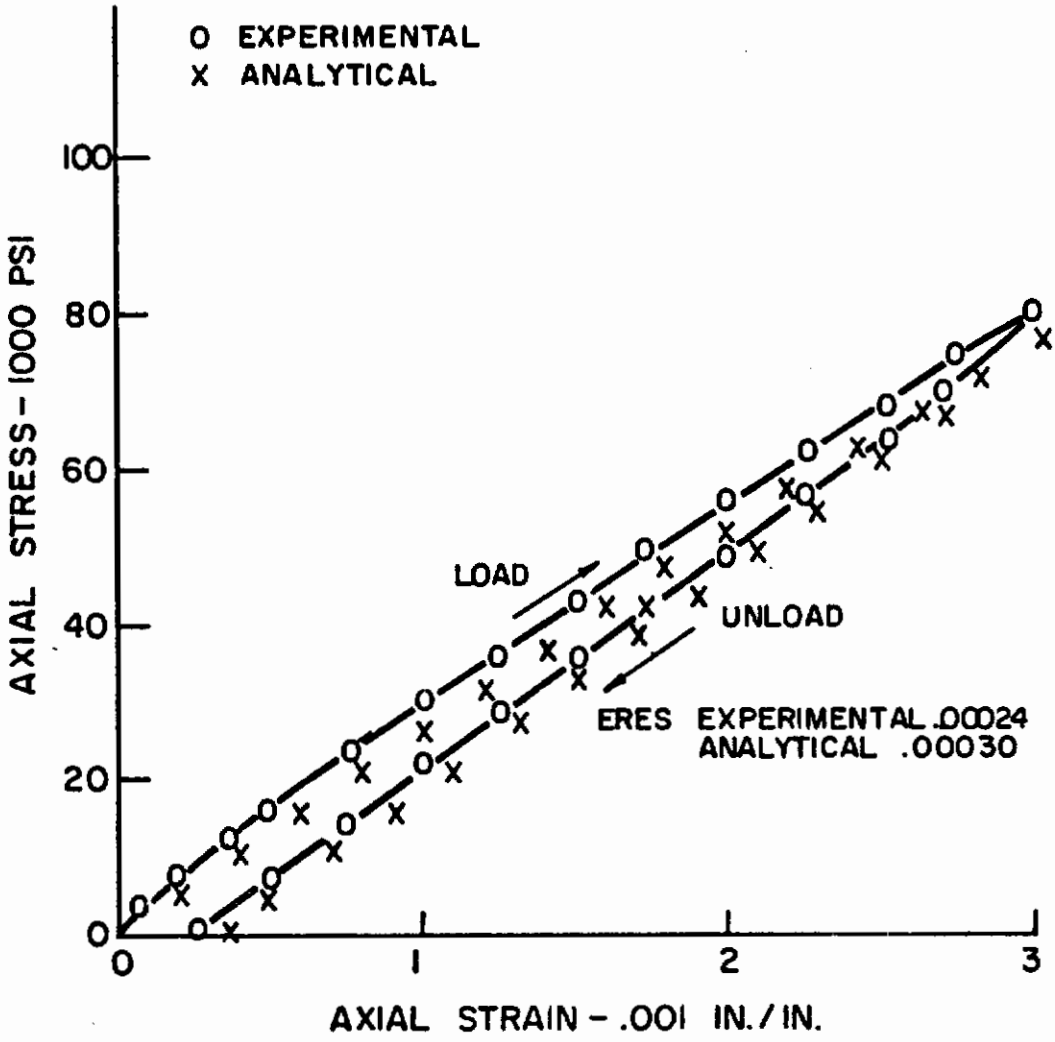

Figure 91

Analytical Prediction of .003 Prestrain Cycle for 43 Volume Percent Tungsten-Copper Filamentary Composites.

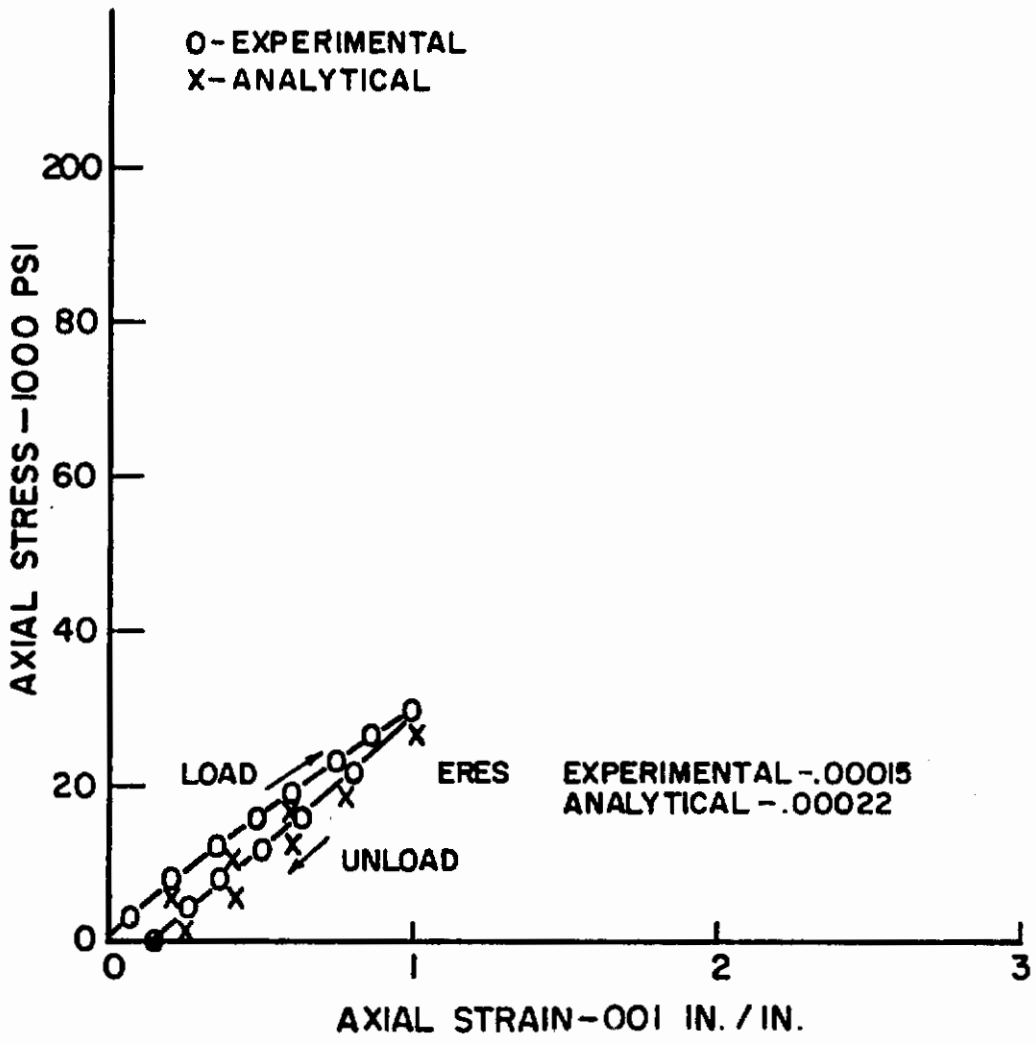

Figure 92

Analytical Prediction of .001 Prestrain Cycle for 43 Volume Percent Tungsten-Copper Filamentary Composites.

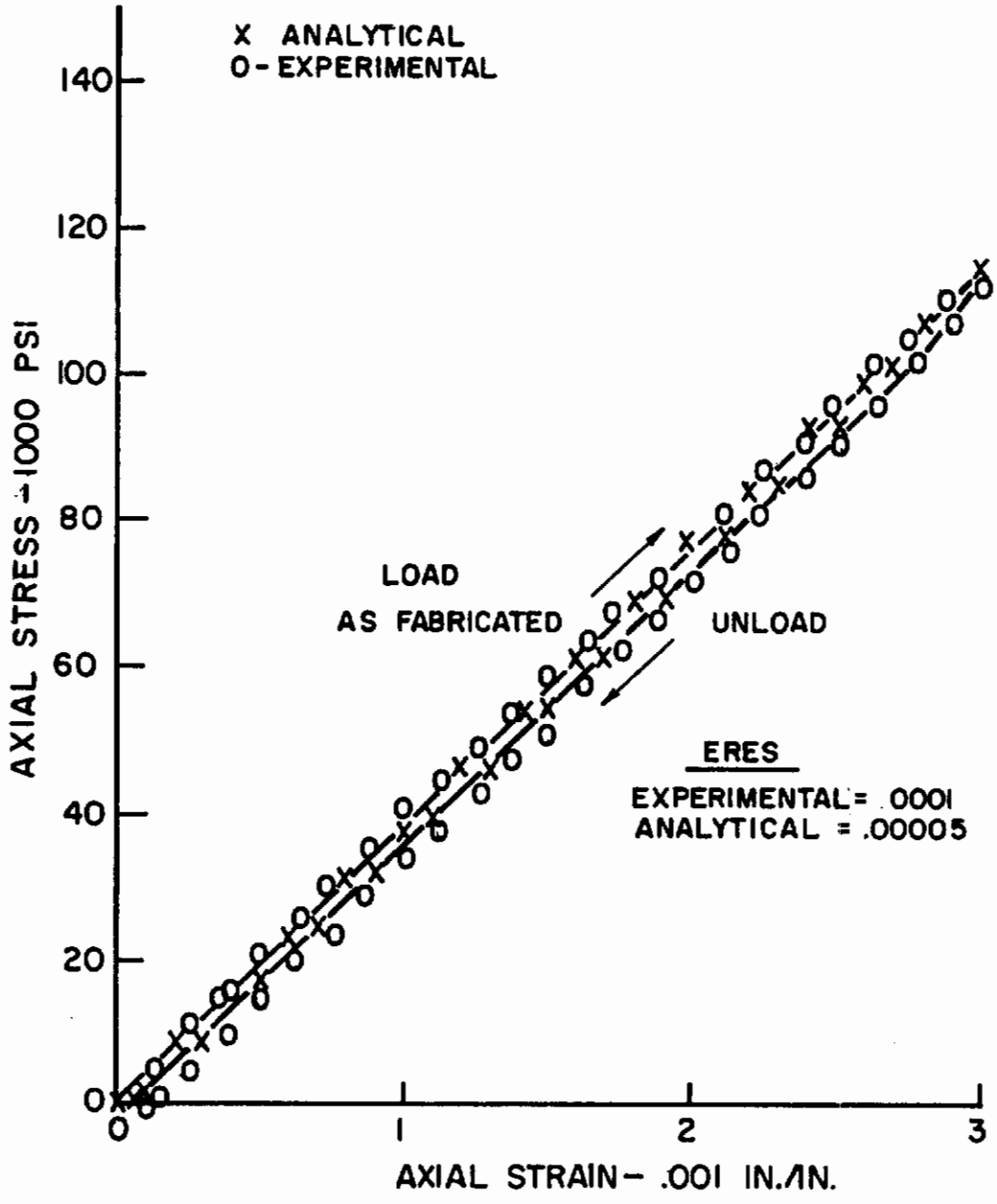

Figure 93

Analytical Prediction of .003 Prestrain Cycle for 64 Volume Percent Tungsten-Copper Filamentary Composites.

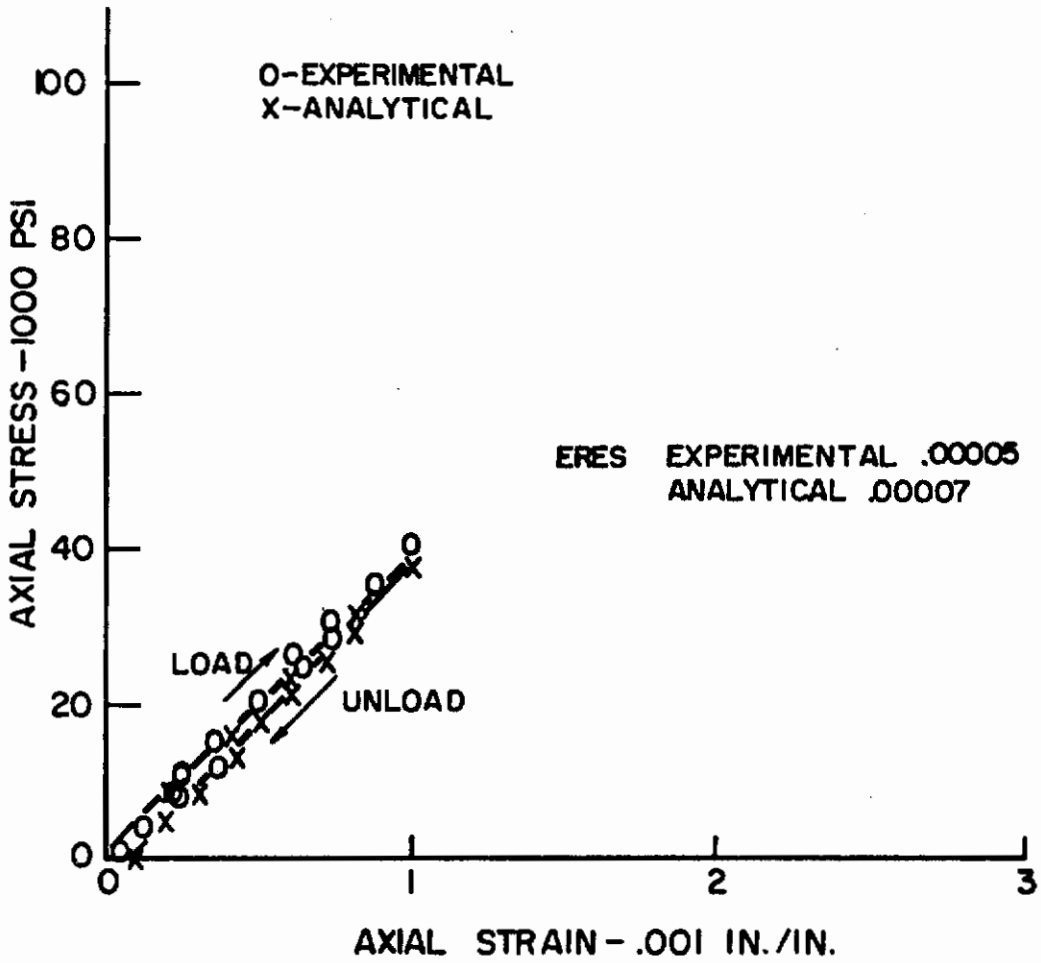

Figure 94

Analytical Prediction of .001 Prestrain Cycle for 64 Volume Percent Tungsten-Copper Filamentary Composites.

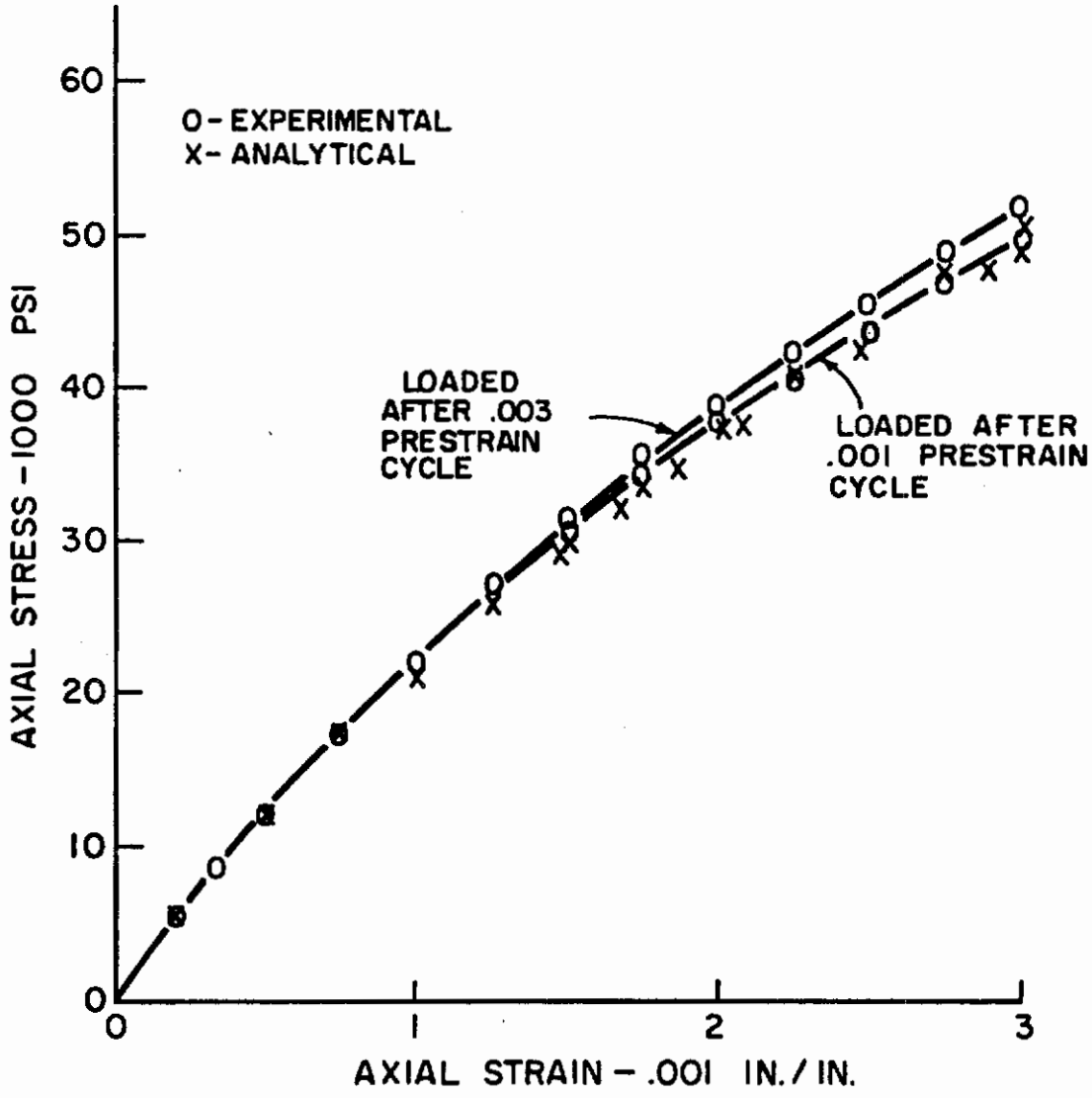

Figure 95

Analytical Predictions of Reloading Stress-Strain Behavior for 20.75 Volume Percent Tungsten-Copper Filamentary Composites.

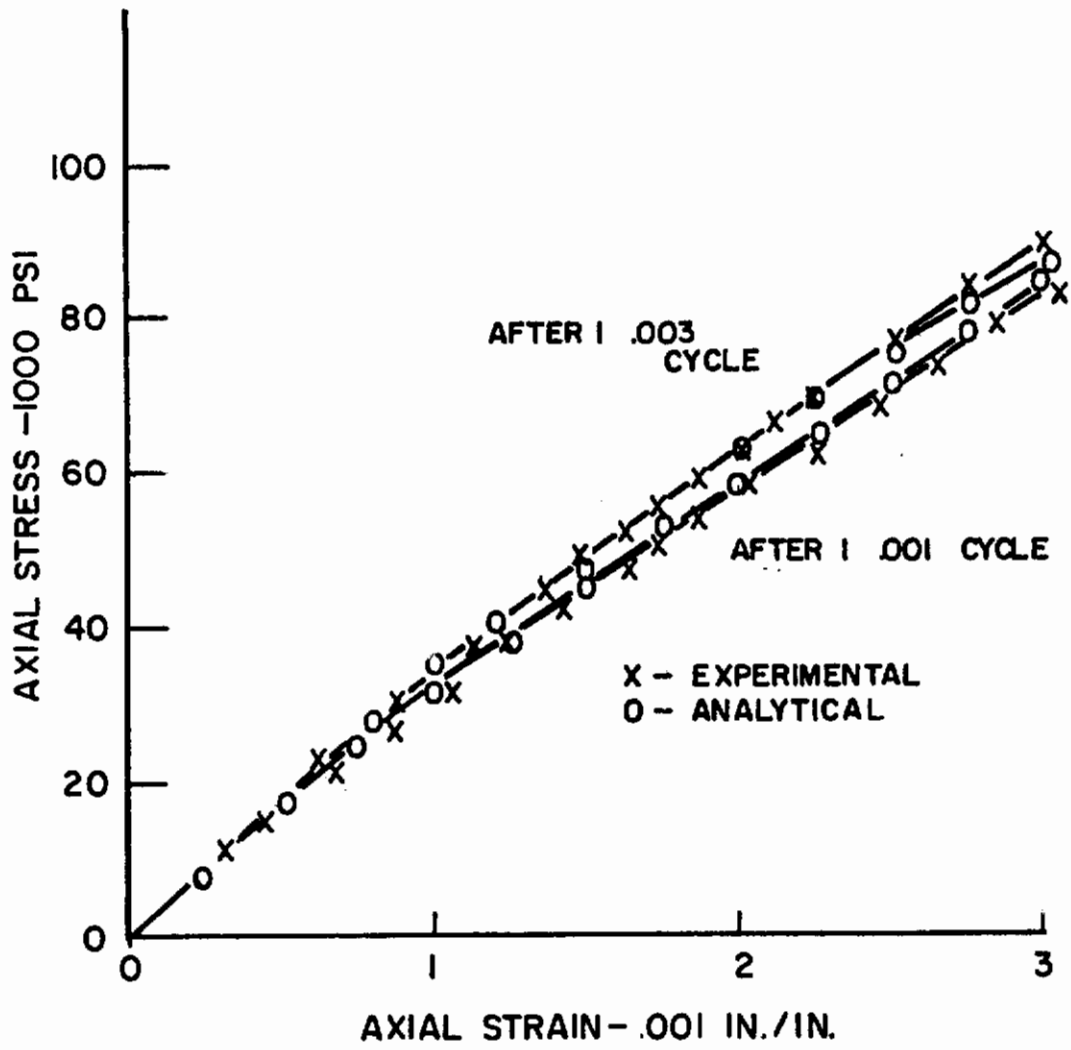

Figure 96

Analytical Predictions of Reloading Stress-Strain Behavior for 43 Volume Percent Tungsten-Copper Filamentary Composites.

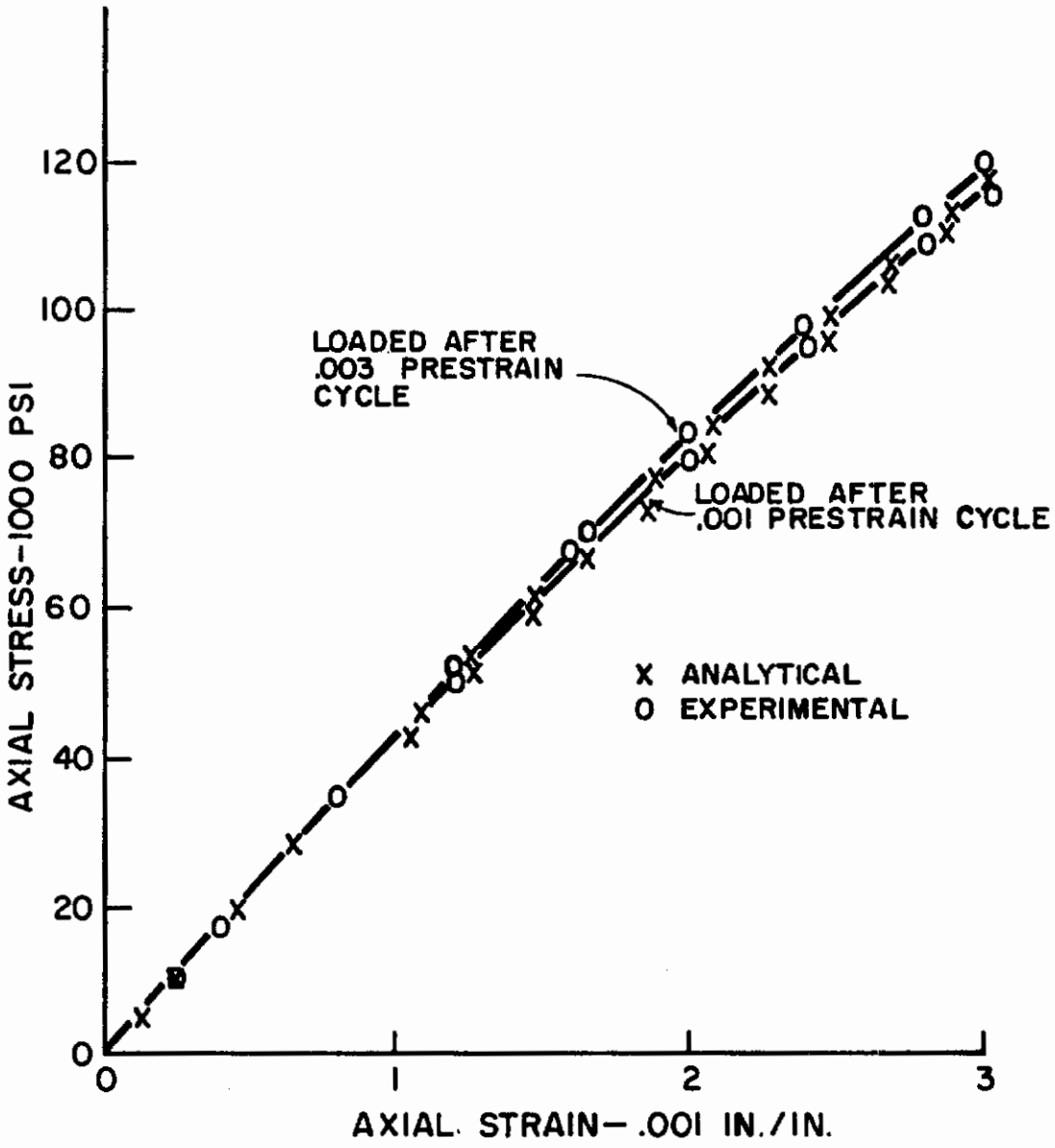

Figure 97

Analytical Predictions of Reloading Stress-Strain Behavior for 64 Volume Percent Tungsten-Copper Filamentary Composites.

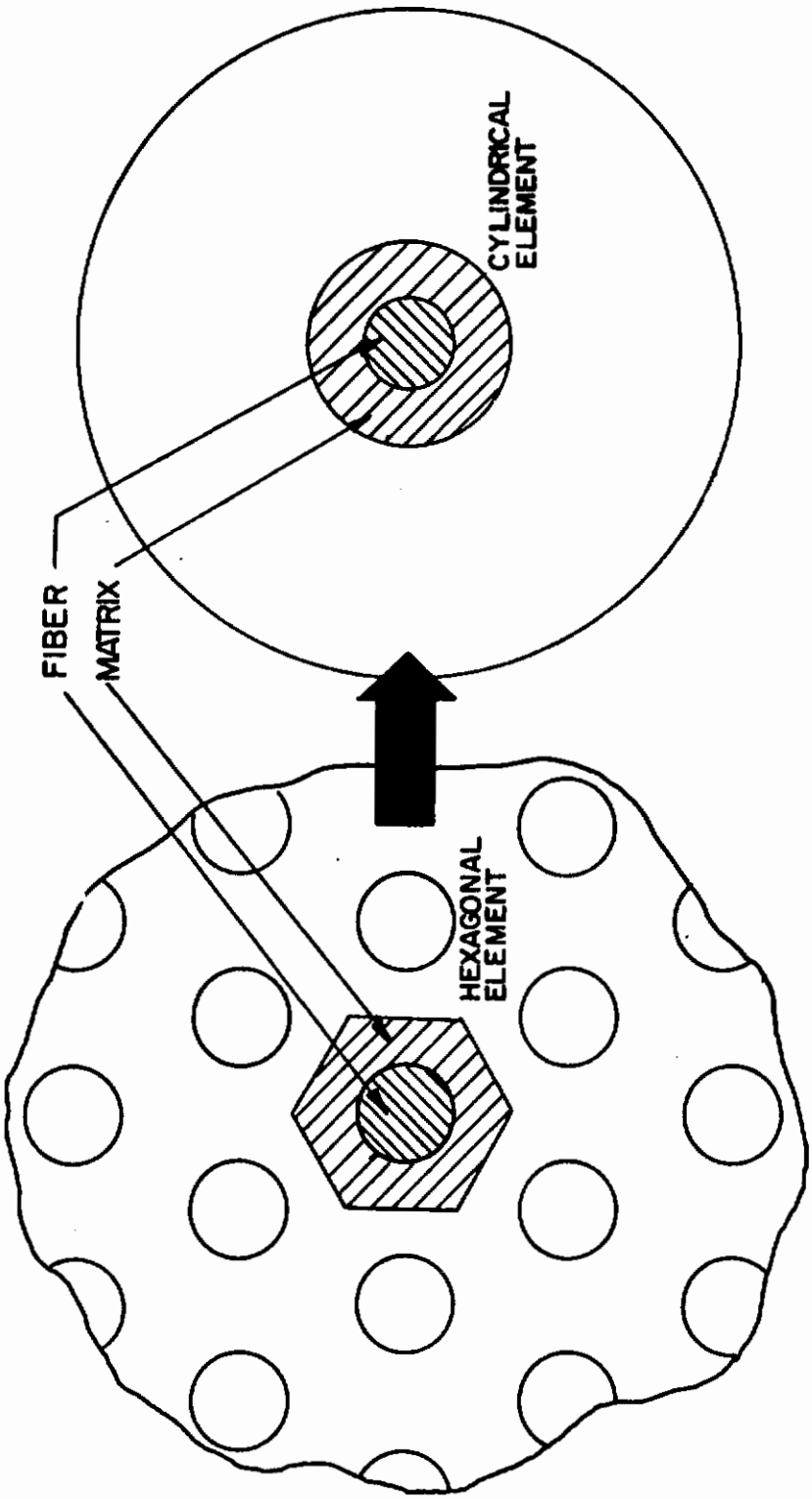

Figure 98

Representation of the Hexagonal Fiber Composite Element by the Cylindrical Element.

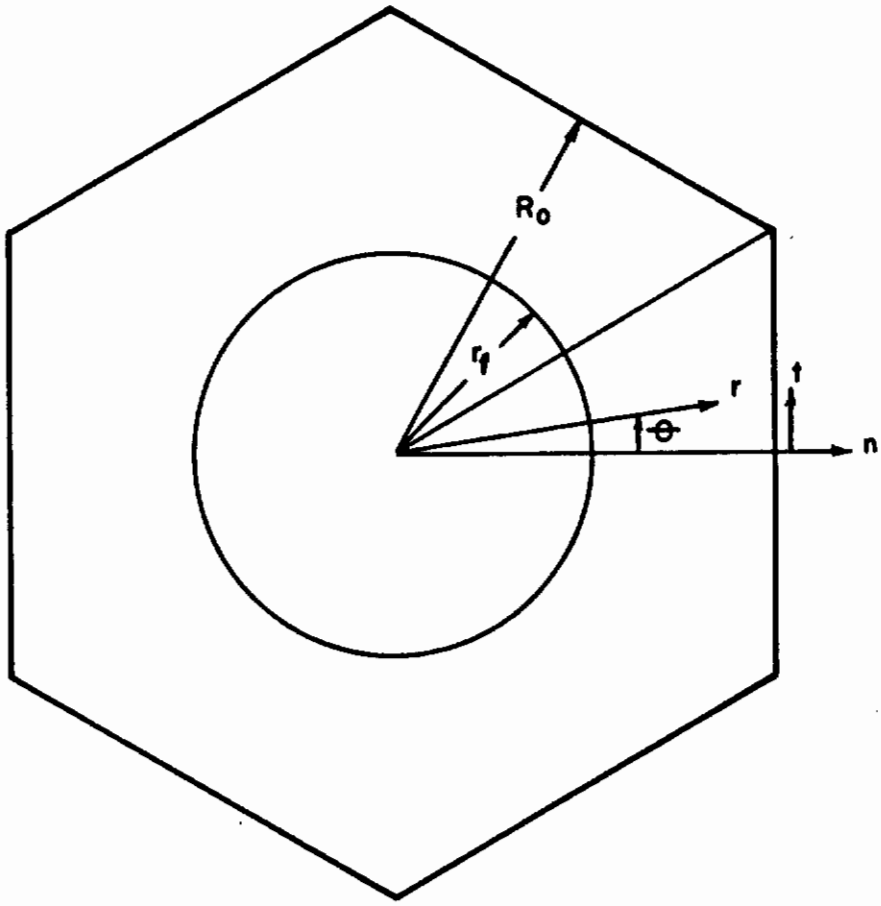

Figure 99

Hexagonal Composite Element with Descriptive Nomenclature.

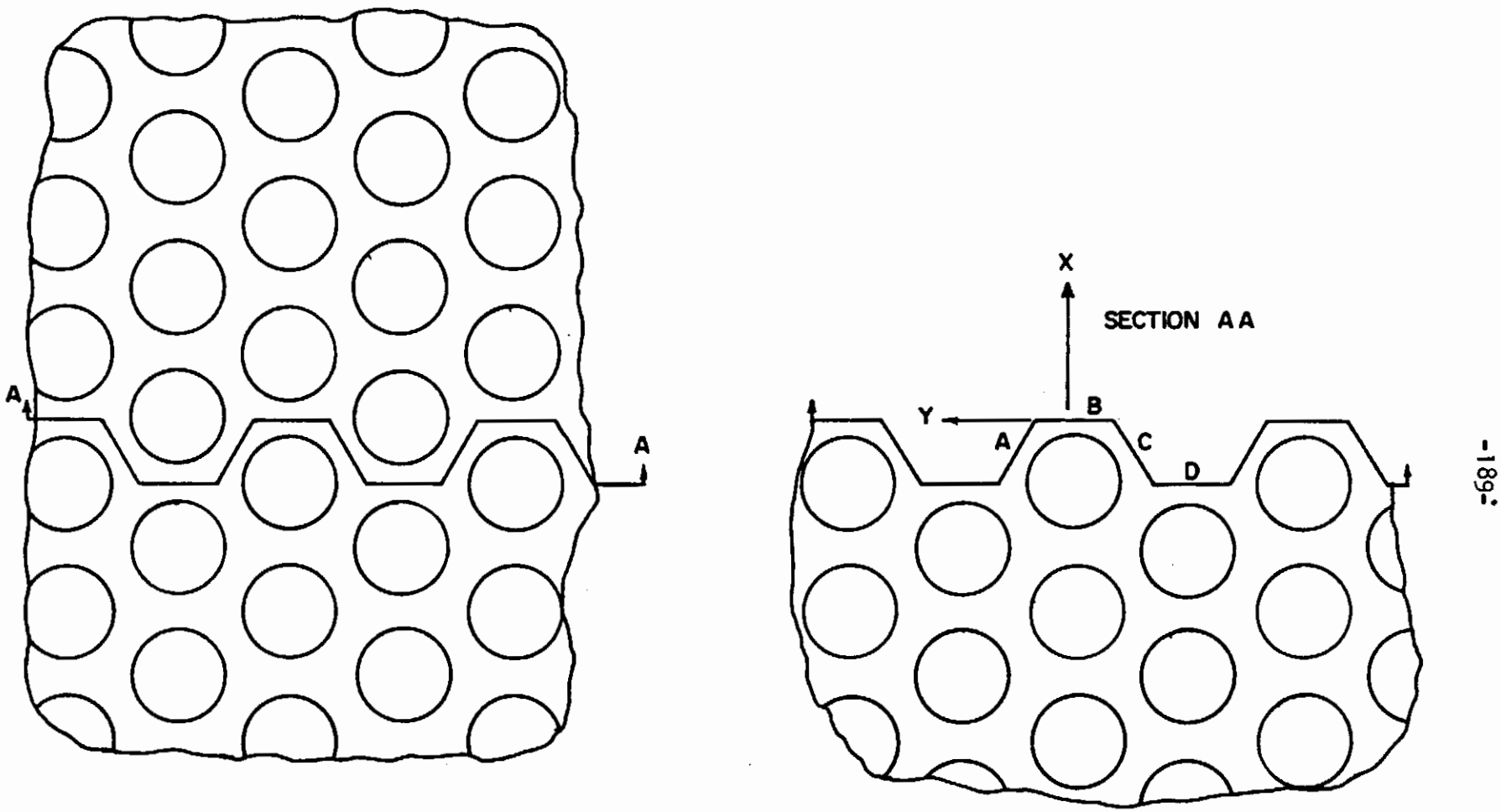

Figure 100

Hexagonally-Packed Fiber Composite Showing Symmetric Cut.

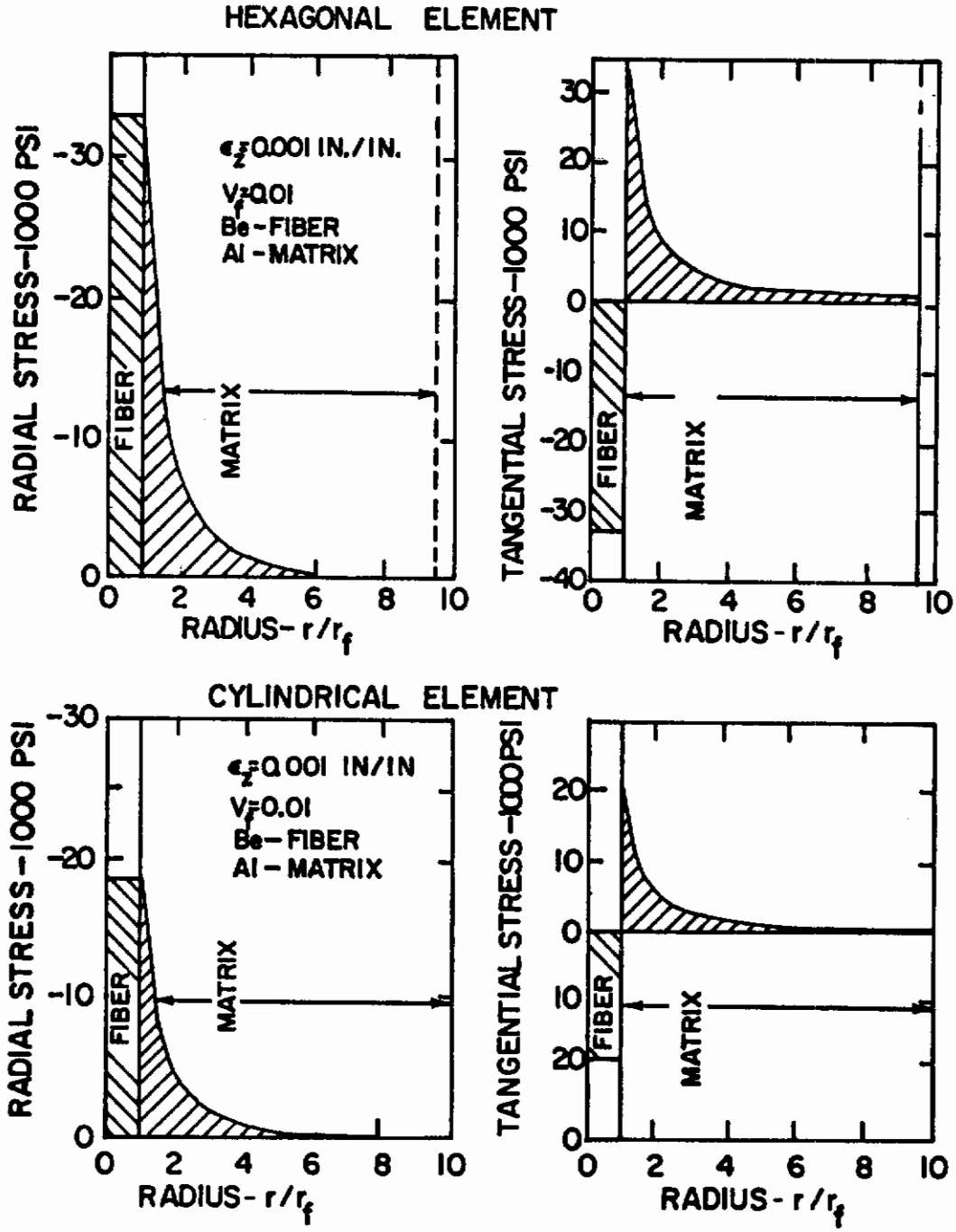

Figure 101

Transverse Stress Distributions in Hexagonal and Cylindrical Elements, V_f = 0.01.

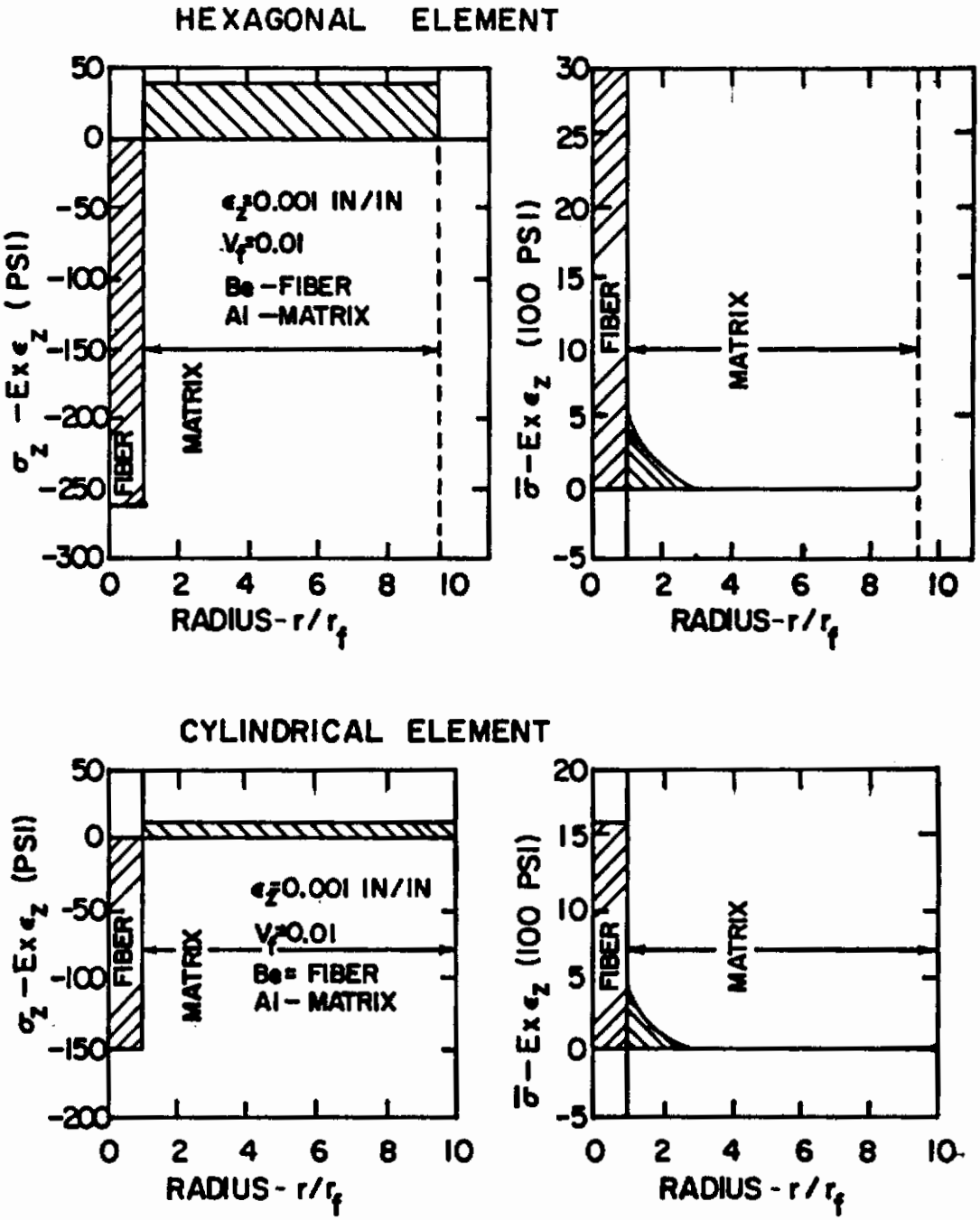

Figure 102

Distribution of ($\sigma_z - E\epsilon_z$) and ($\bar{\sigma} - E\epsilon_z$) for Hexagonal and Cylindrical Elements.

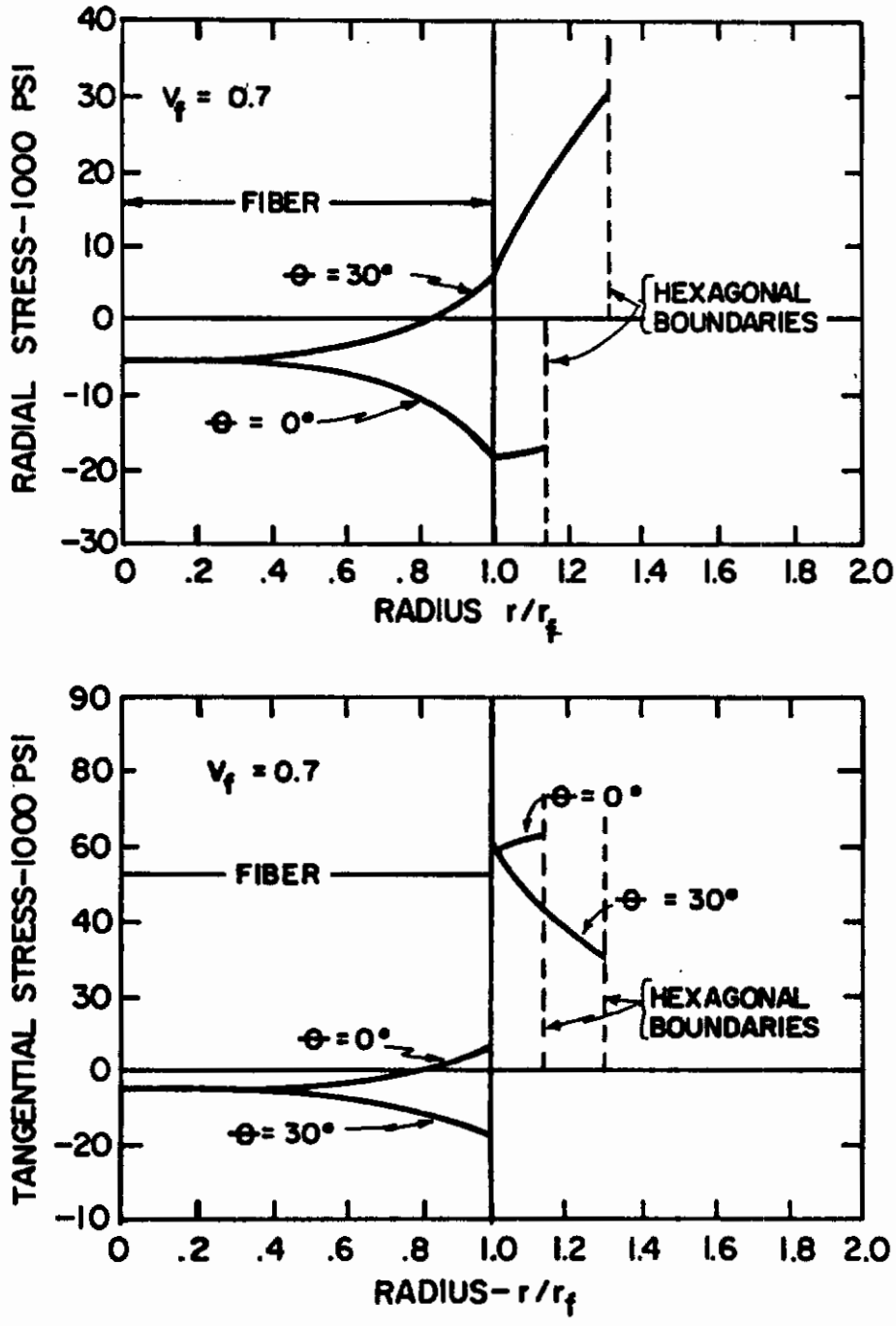

Figure 103

Transverse Stress Distribution in the Hexagonal Element, V_f = 0.70.

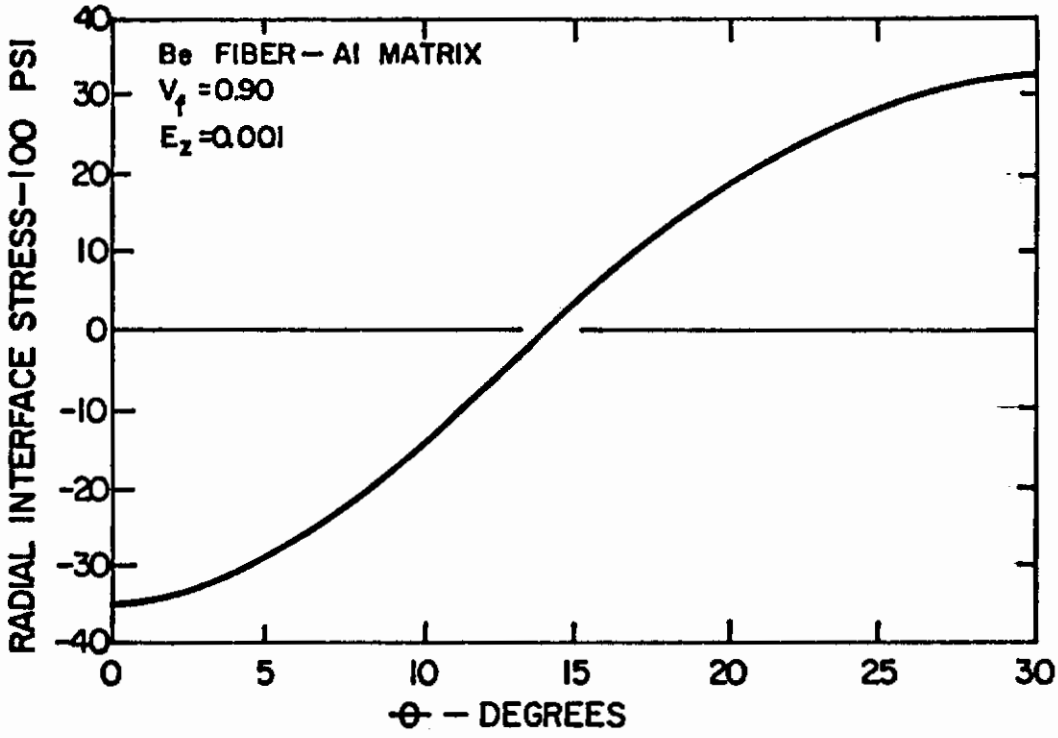

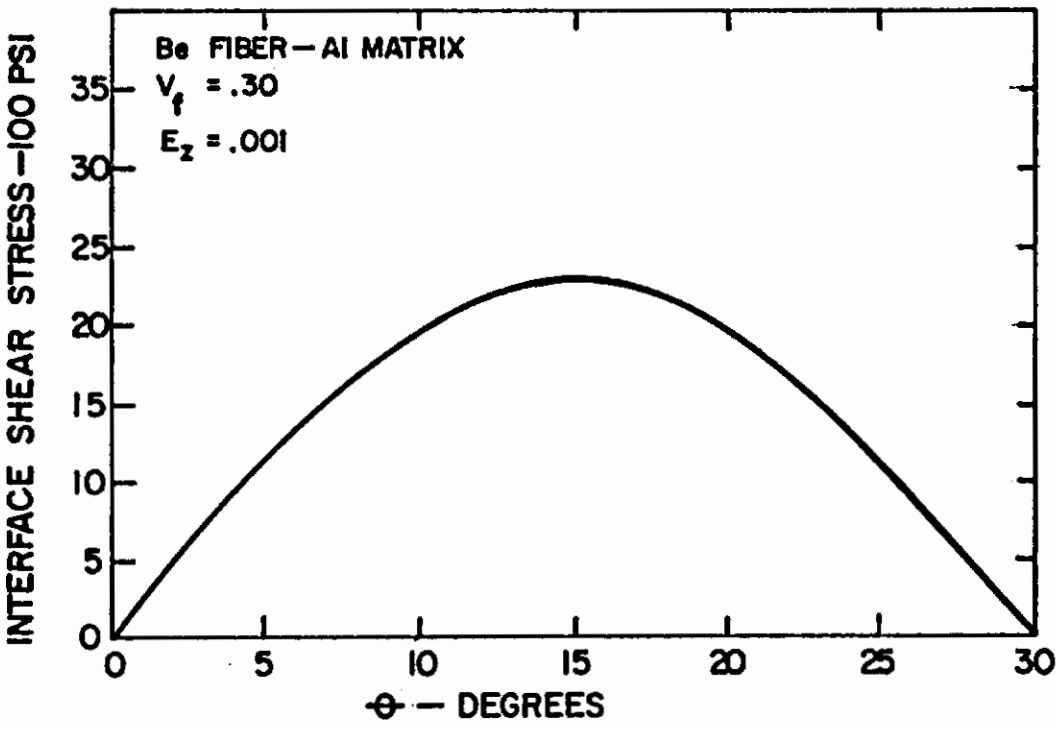

Figure 104

Variation of Radial and Shear Stresses at the Fiber-Matrix Interface.

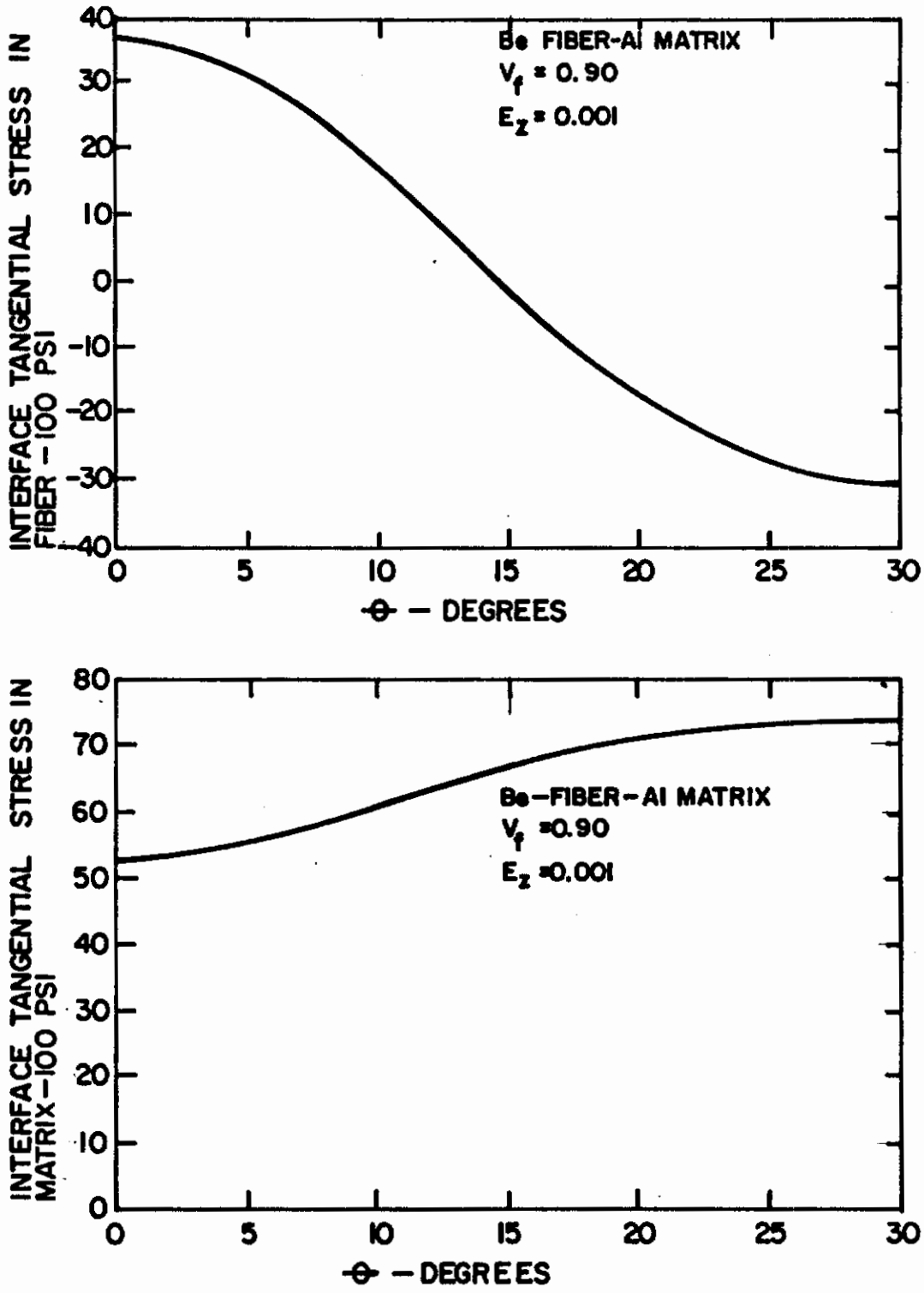

Figure 105

Variation of Tangential Stress in the Fiber and Matrix at the Fiber-Matrix Interface.

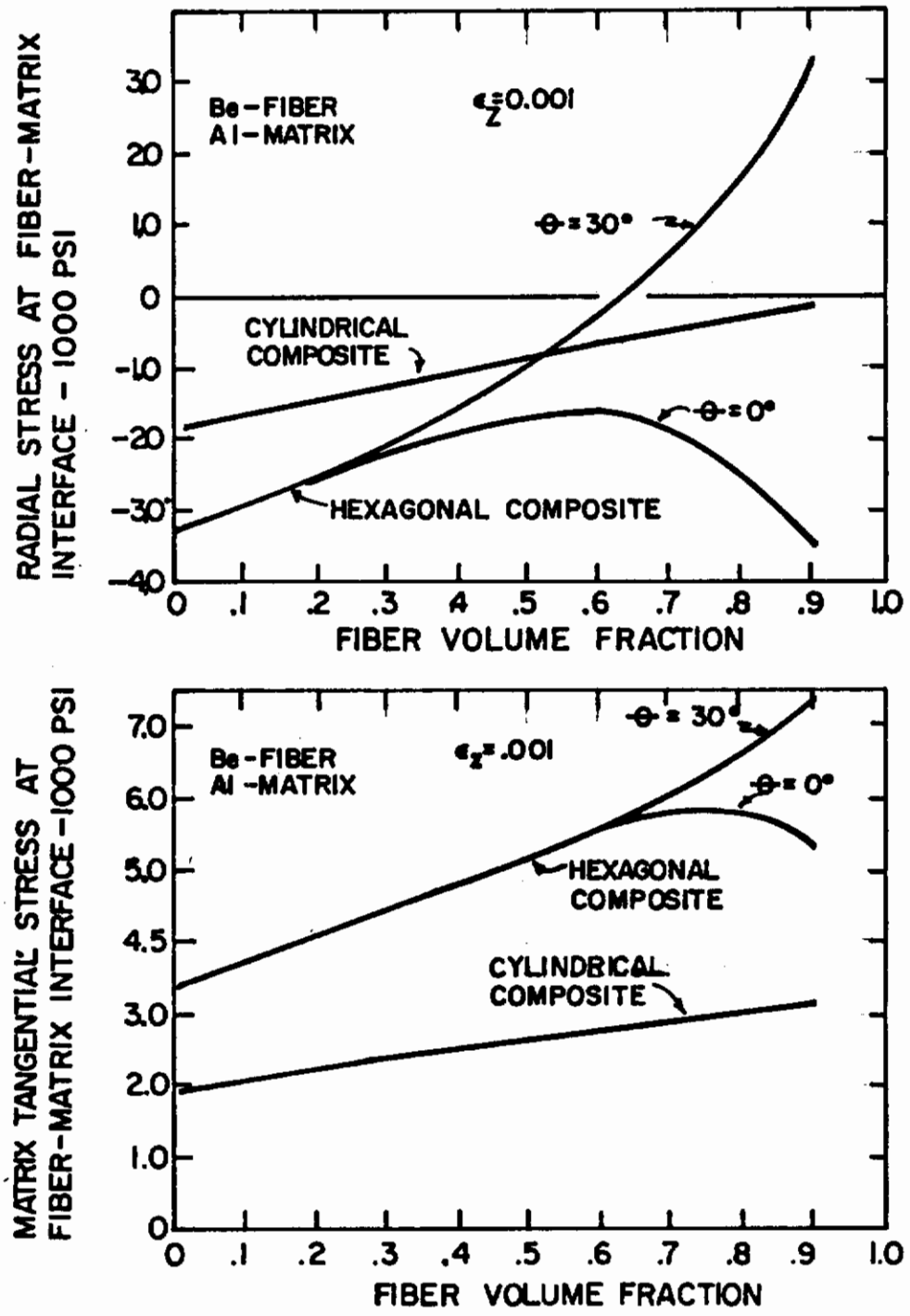

Figure 106

Variation of Interfacial Radial and Tangential Stresses with Fiber Volume Fraction for Hexagonal and Cylindrical Elements, Be-Al Composites System.

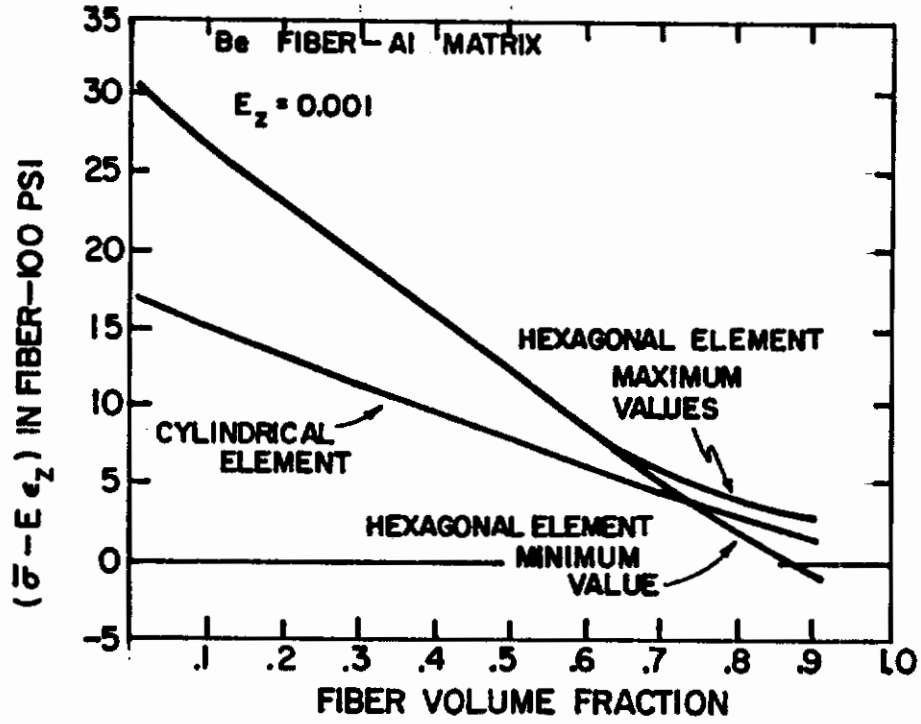

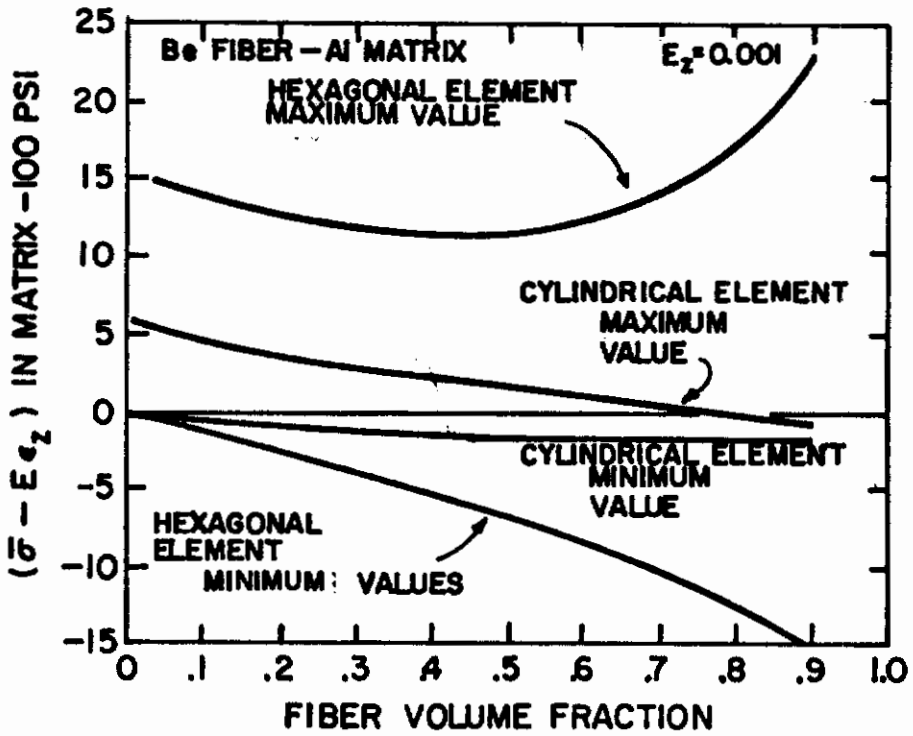

Figure 107

Variation of ($\bar{\sigma}$ - Eϵ_z) in the Fiber and Matrix with Fiber Volume Fraction for Hexagonal and Cylindrical Elements, Be-Al Composite System.

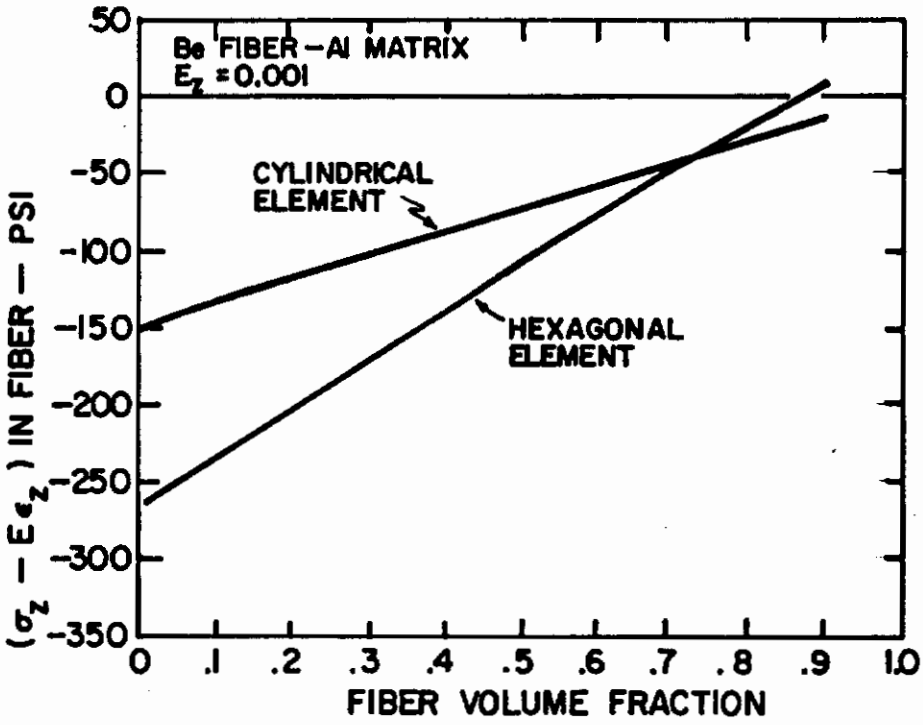

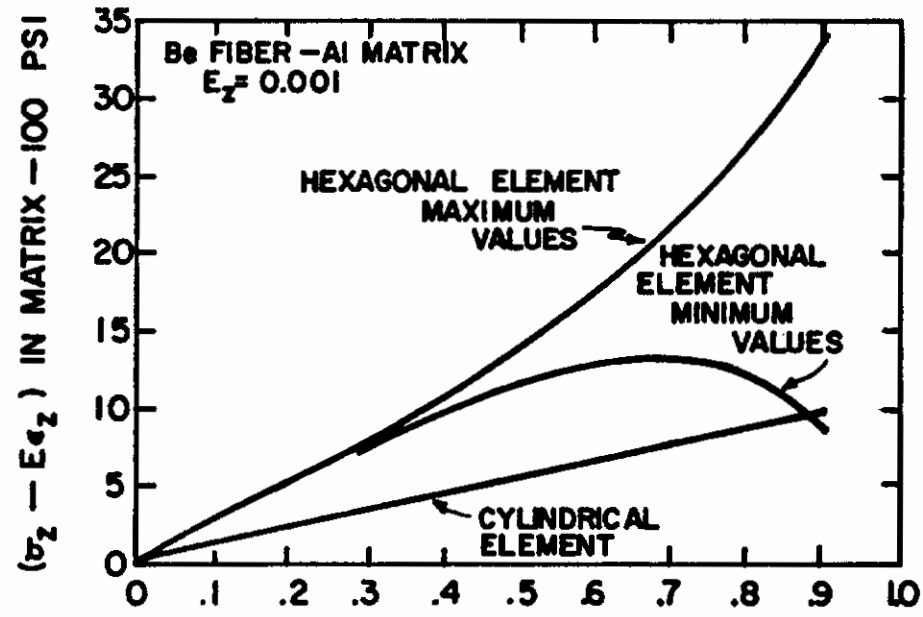

Figure 108

Variation of (σ_z - $E\epsilon_z$) in the Fiber and Matrix with Fiber Volume Fraction for Hexagonal and Cylindrical Elements, Be-Al Composite System.

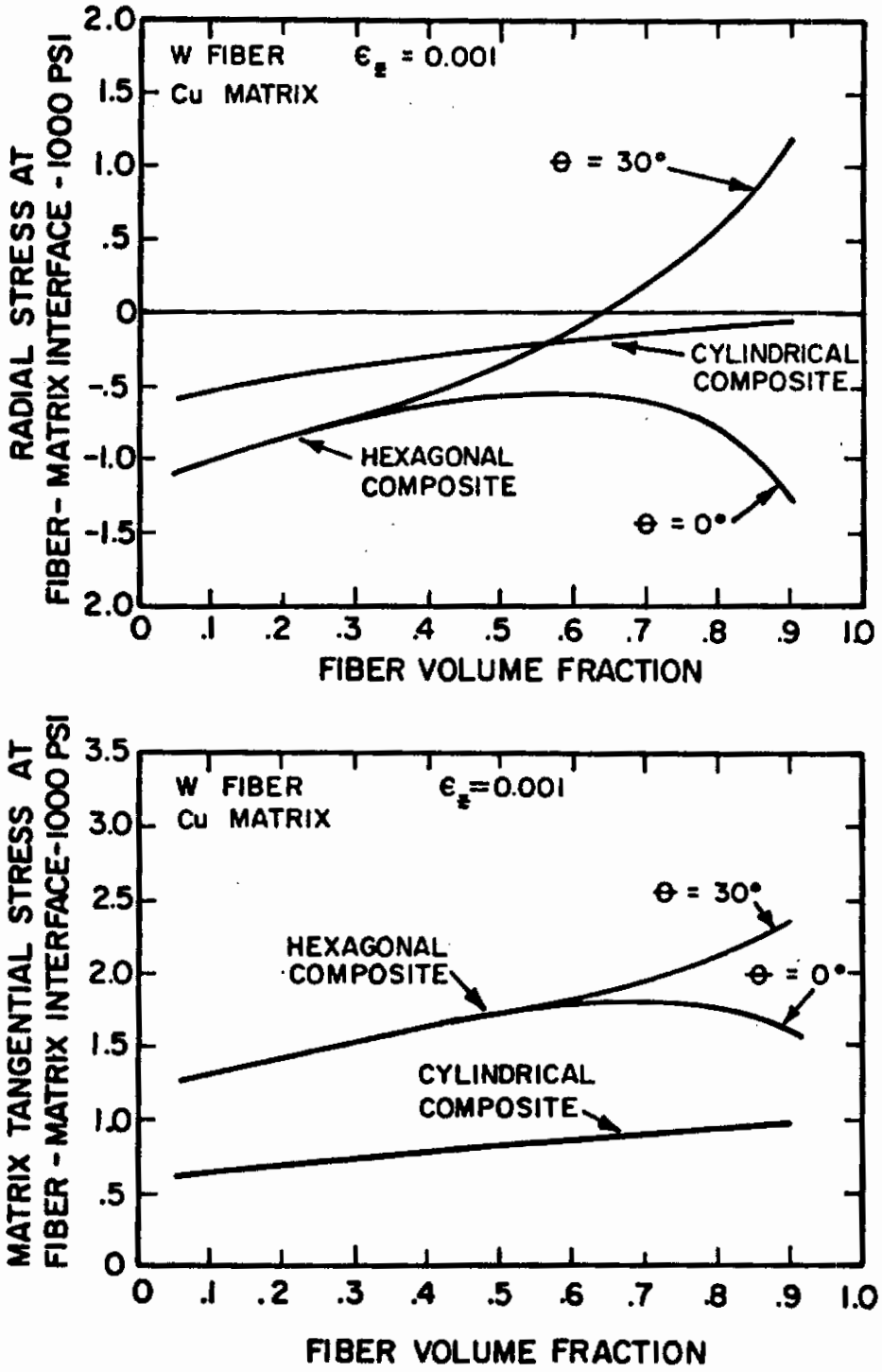

Figure 109

Variation of Interfacial Radial and Tangential Stresses with Fiber Volume Fraction for Hexagonal and Cylindrical Elements, W-Cu Composites System.

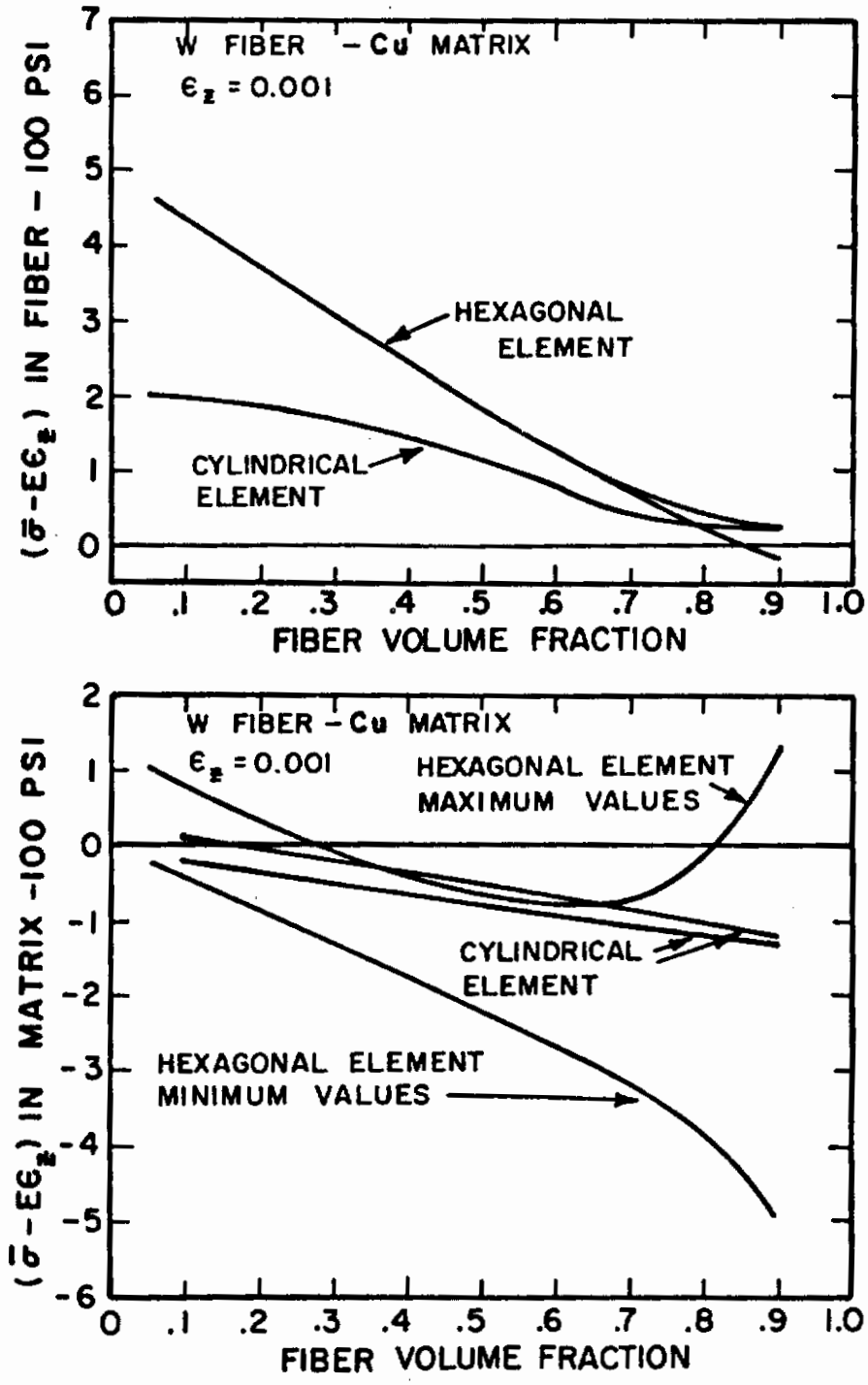

Figure 110

Variation of $(\bar{\sigma} - E\epsilon_z)$ in the Fiber and Matrix with Fiber Volume Fraction for Hexagonal and Cylindrical Elements, W-Cu Composite System.

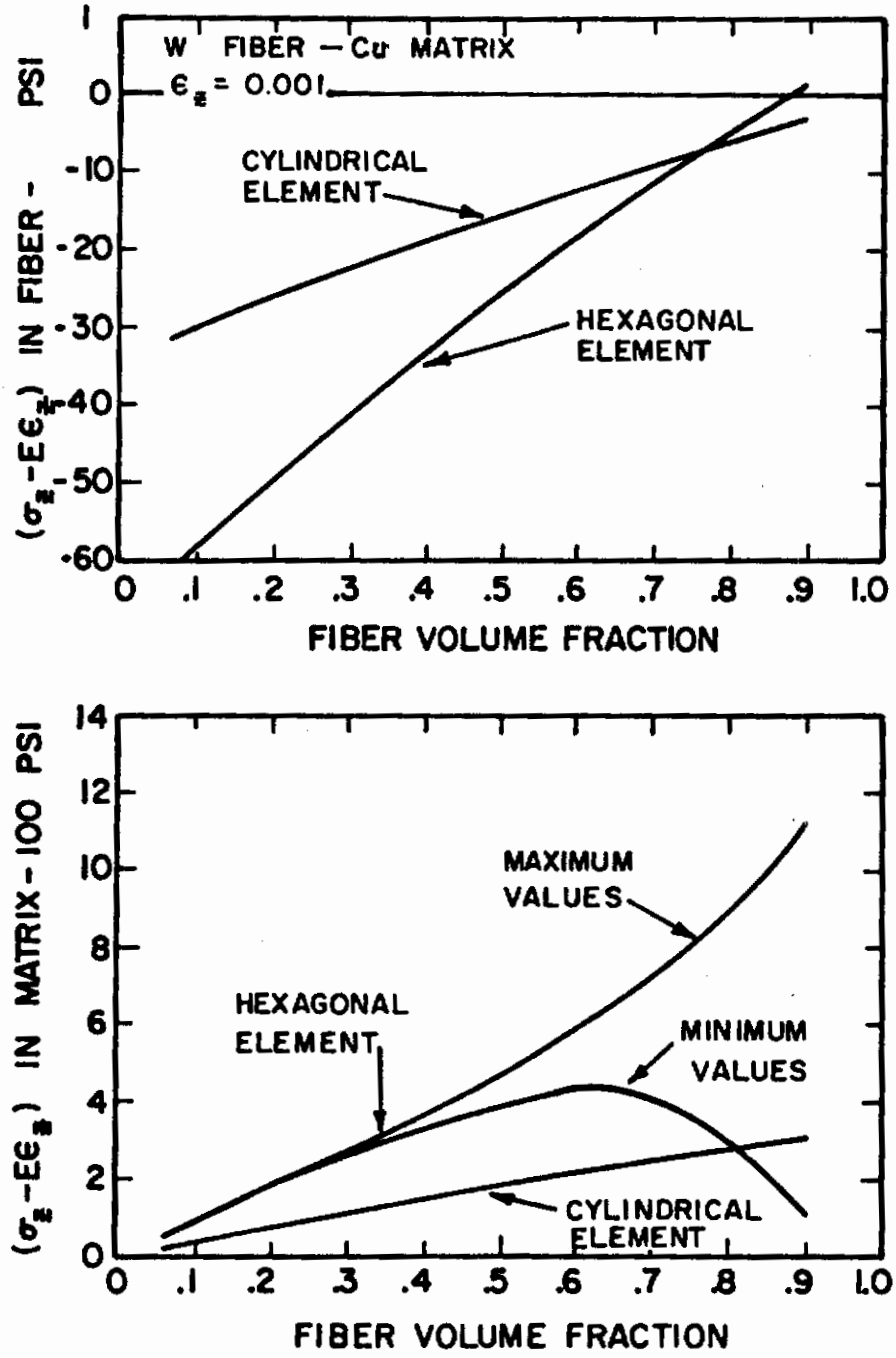

Figure 111

Variation of $(\sigma_z - E\epsilon_z)$ in the Fiber and Matrix with Fiber Volume Fraction for Hexagonal and Cylindrical Elements, W-Cu Compoiste System.

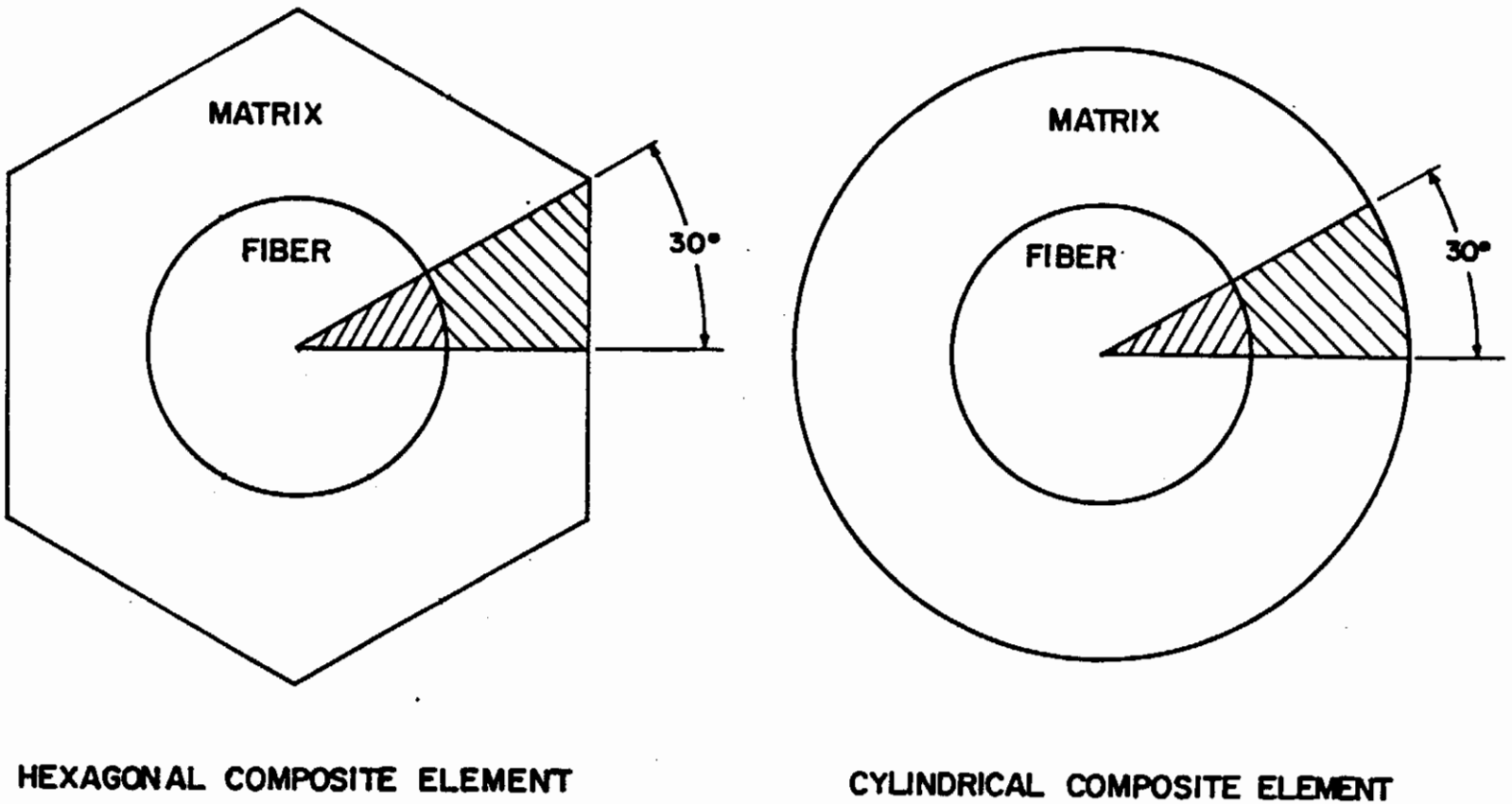

Figure 112

Hexagonal and Cylindrical Elements with 30^{o} Sections Utilized for Comparative Analysis.

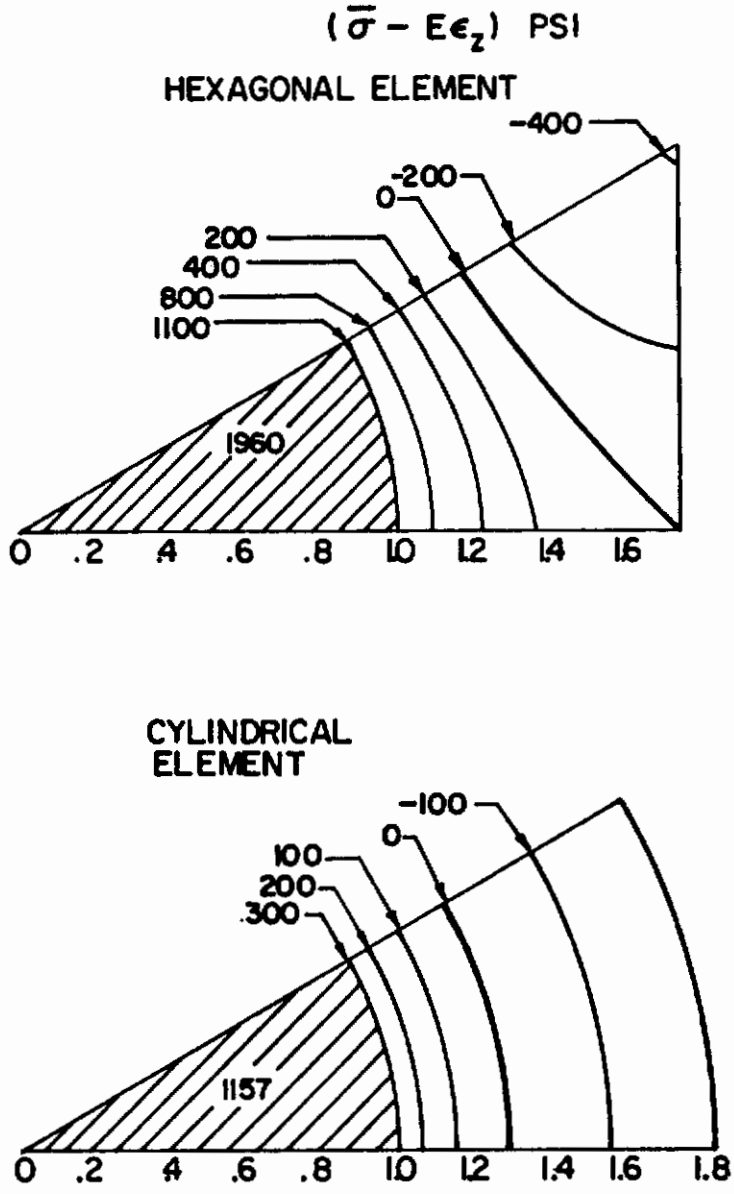

Figure 113

Isograms of $(\bar{\sigma} - E\epsilon_z)$ for Hexagonal and Cylindrical Elements, Be-Al Composite System, $V_f = 0.3$.

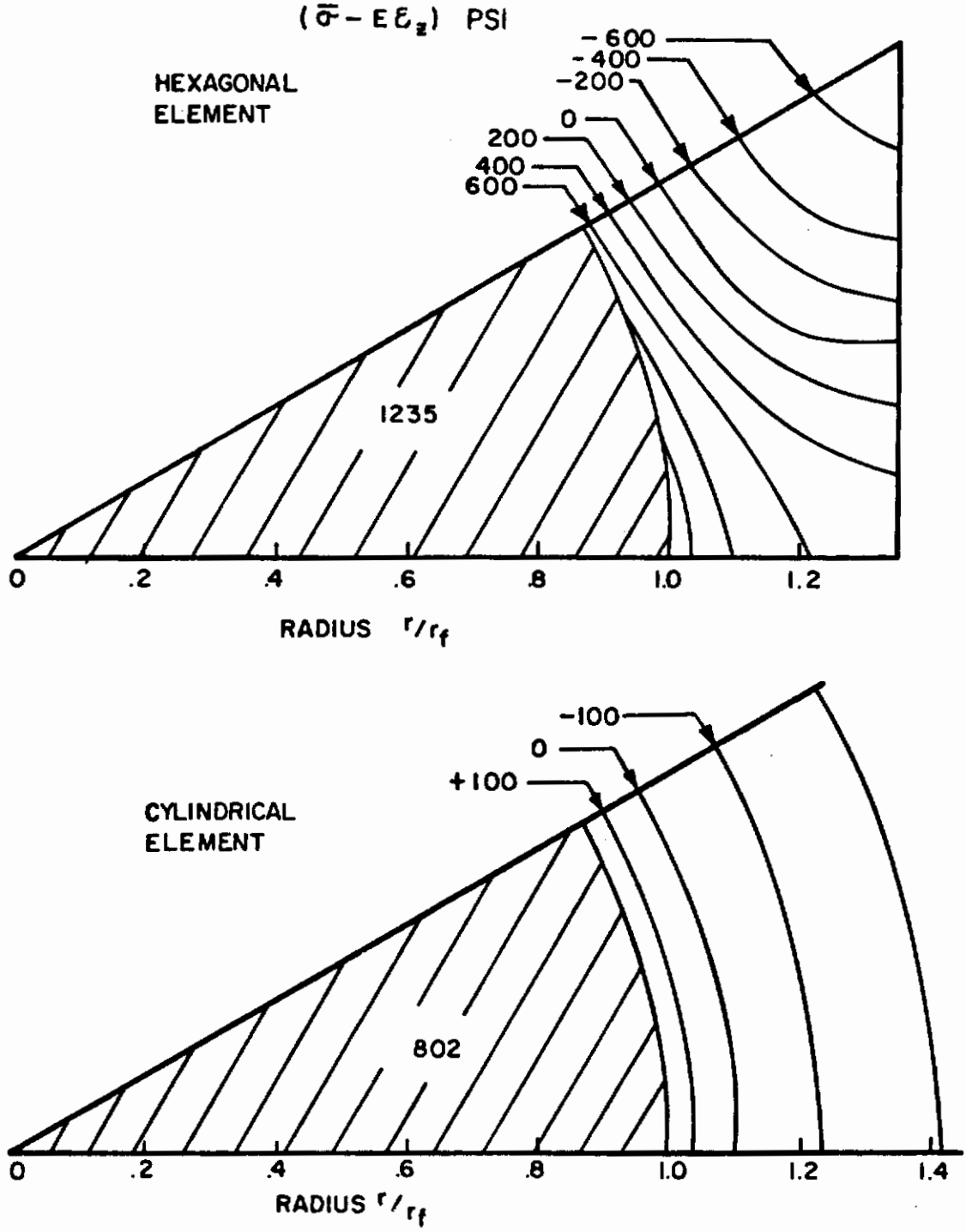

Figure 114

Isograms of $(\bar{\sigma} - E\epsilon_z)$ for Hexagonal and Cylindrical Elements, Be-Al Composite System, $V_f = 0.5$.

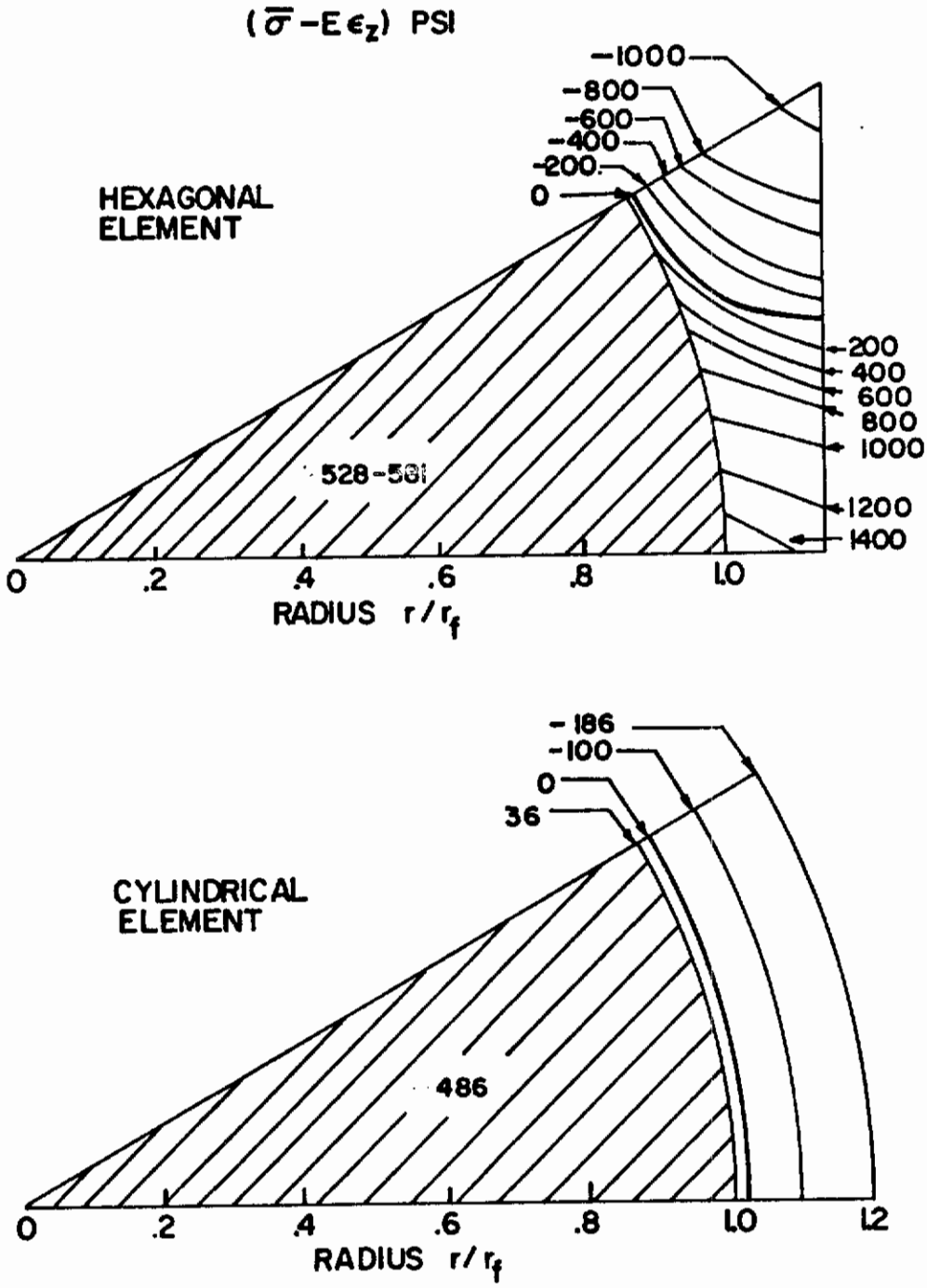

Figure 115

Isograms of $(\bar{\sigma} - E\epsilon_z)$ for Hexagonal and Cylindrical Elements, Be-Al Composite System, $V_f = 0.7$.

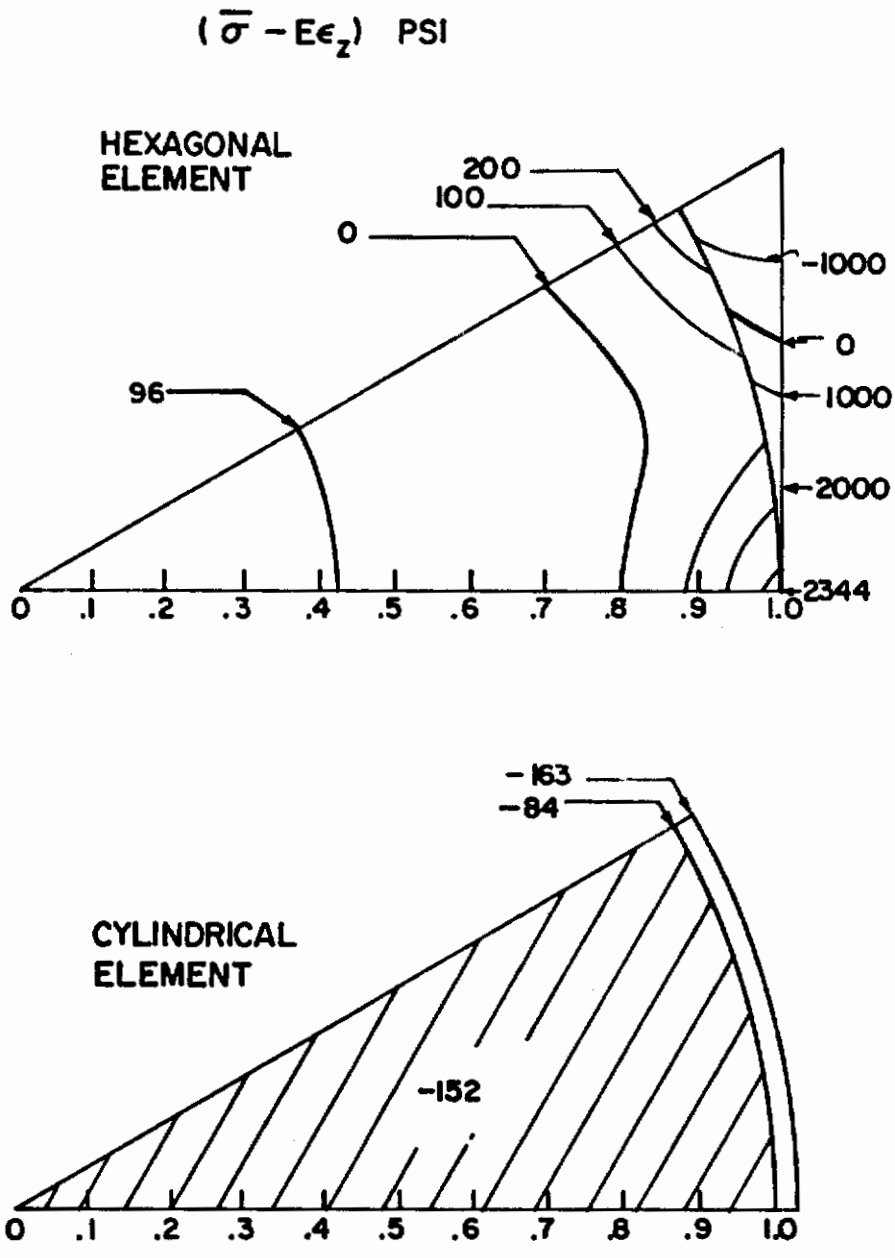

Figure 116

Isograms of $(\overline{\sigma} - E\epsilon_z)$ for Hexagonal and Cylindrical Elements, Be-Al Composite System, $V_f = 0.9$.

$(\sigma_z - E\epsilon)$ PSI

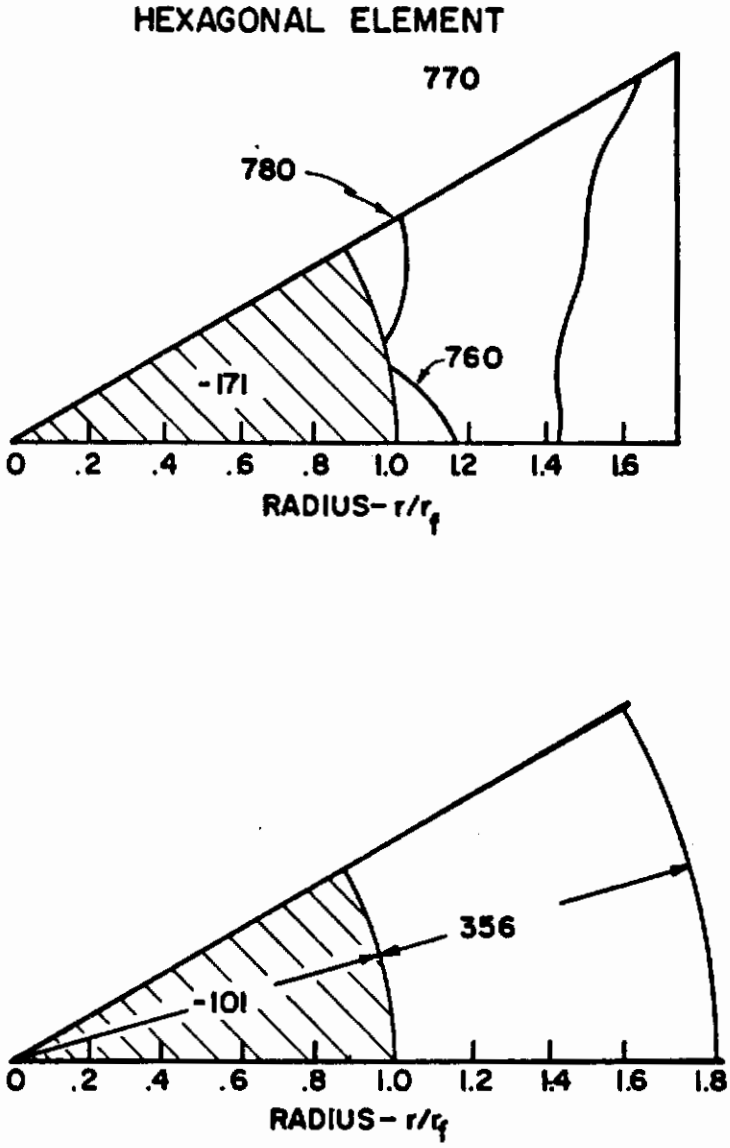

Figure 117

Isograms of $(\sigma_z - E\epsilon_z)$ for Hexagonal and Cylindrical Elements, Be-Al Composite System, $V_f = 0.3$.

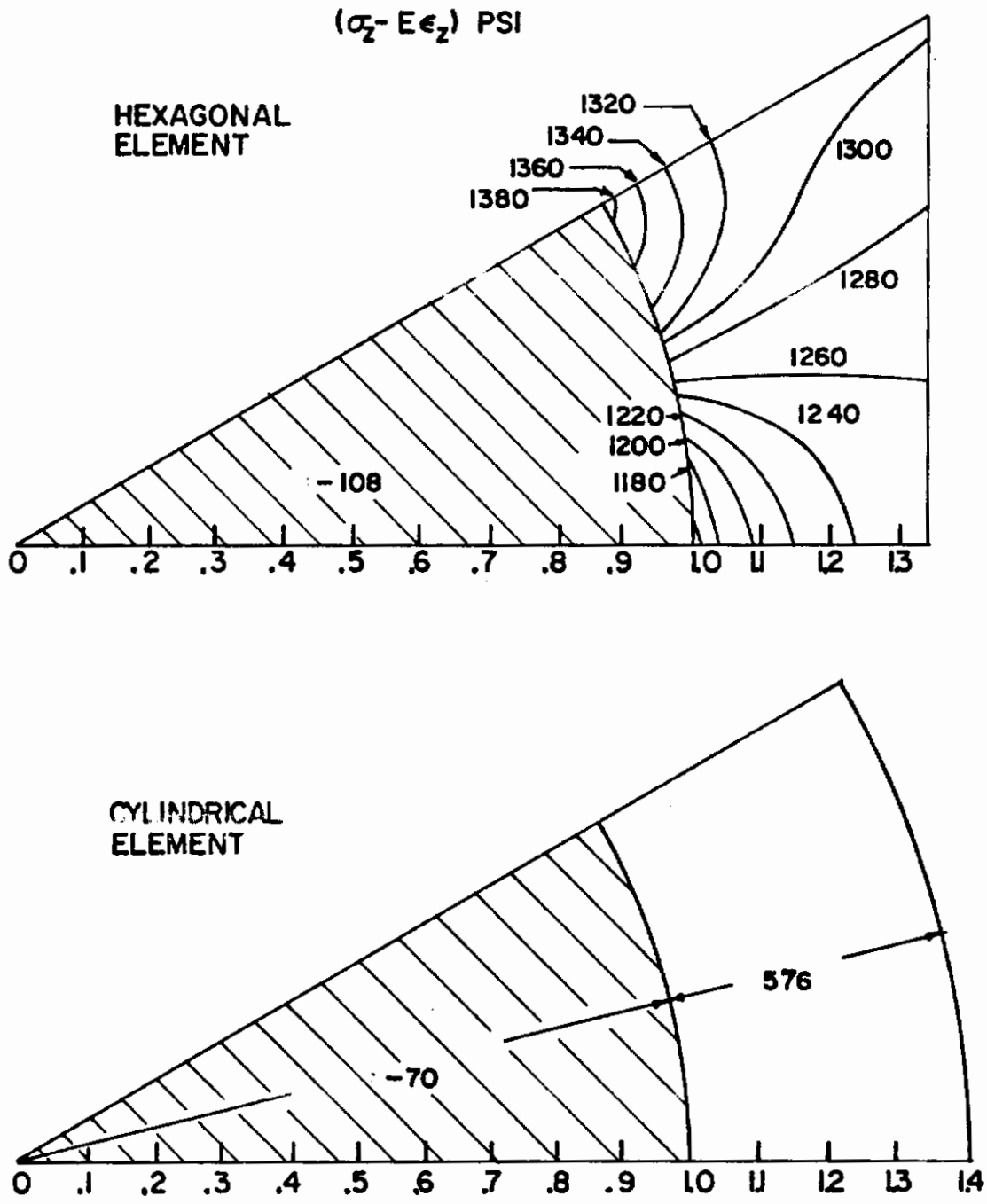

Figure 118

Isograms of (σ_z - $E\epsilon_z$) for Hexagonal and Cylindrical Elements, Be-Al Composite System, V_f = 0.5.

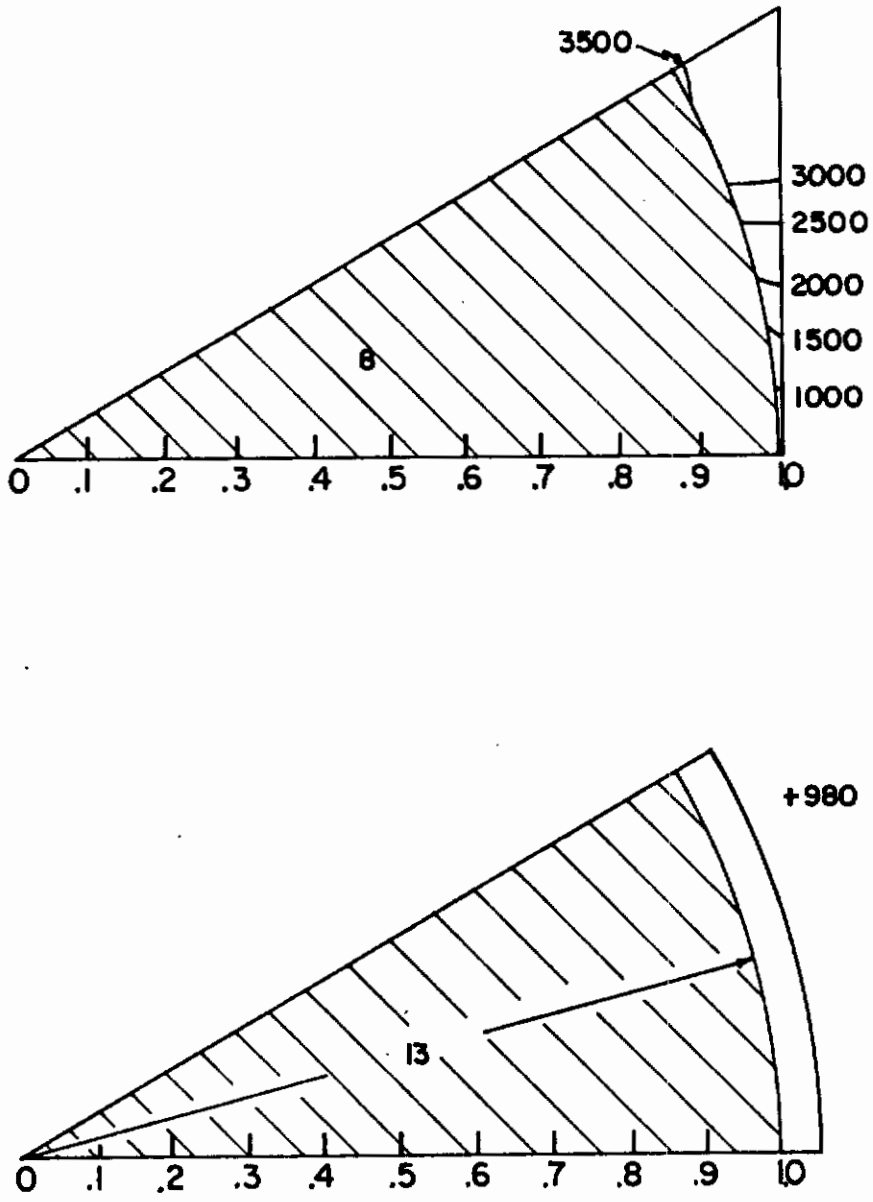

Figure 119

Isograms of (σ_z - $E\epsilon_z$) for Hexagonal and Cylindrical Elements, Be-Al Composite System, V_f = 0.7.

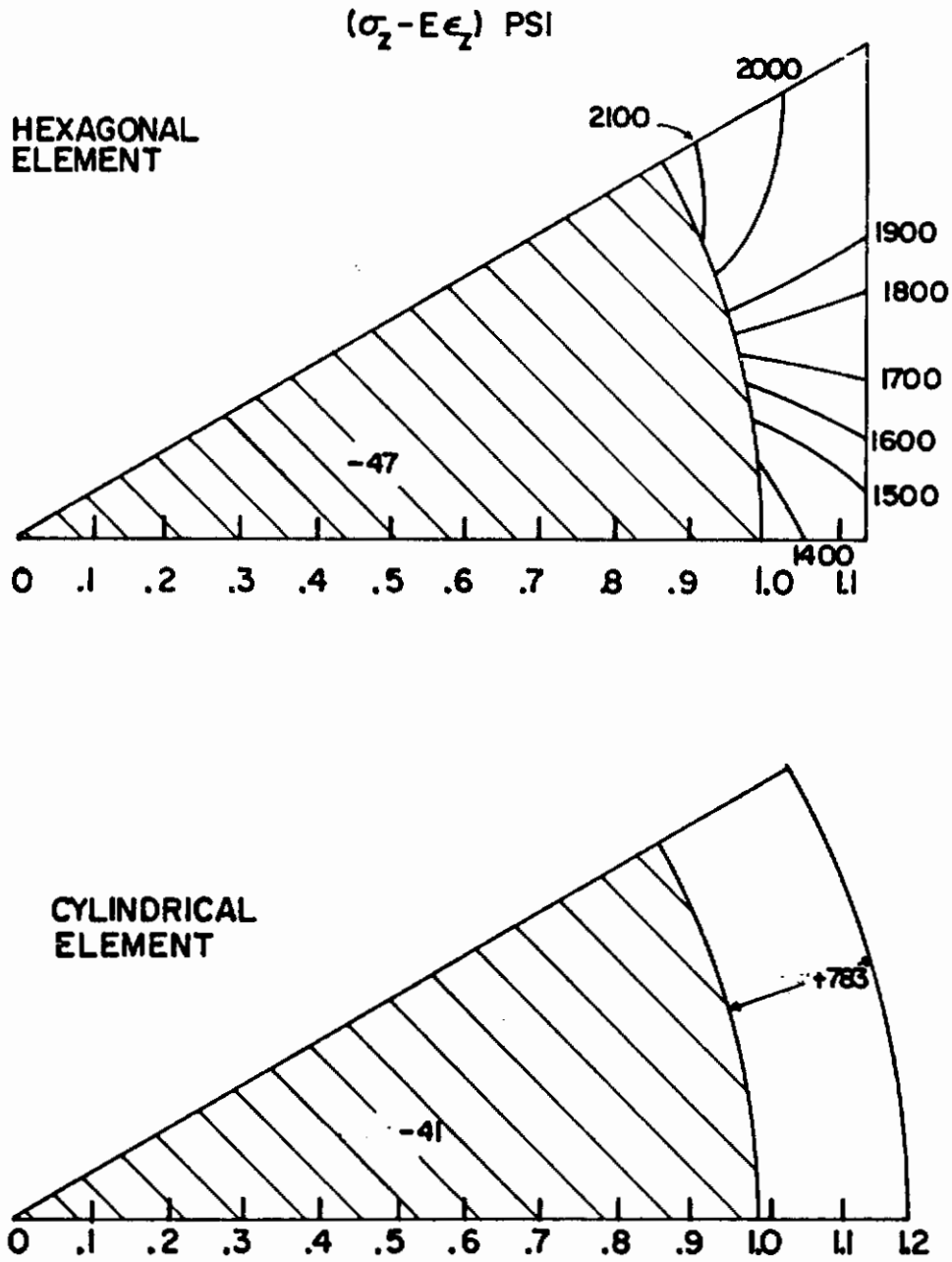

Figure 120

Isograms of (σ_z - E ϵ_z) for Hexagonal and Cylindrical Elements, Be-Al Composite System, V_f = 0.9.

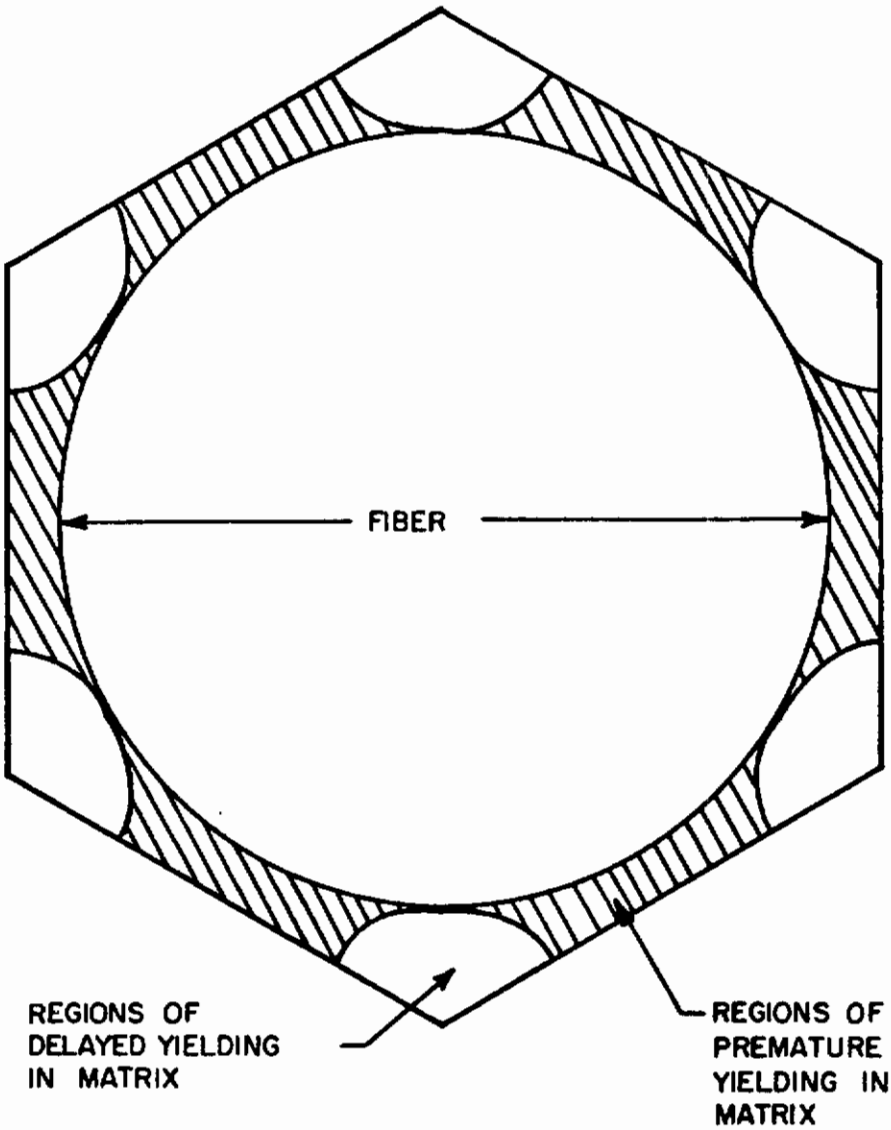

Figure 121

Hexagonal Element with Regions of Premature and Delayed Yielding Indicated, $V_f = 0.7$.

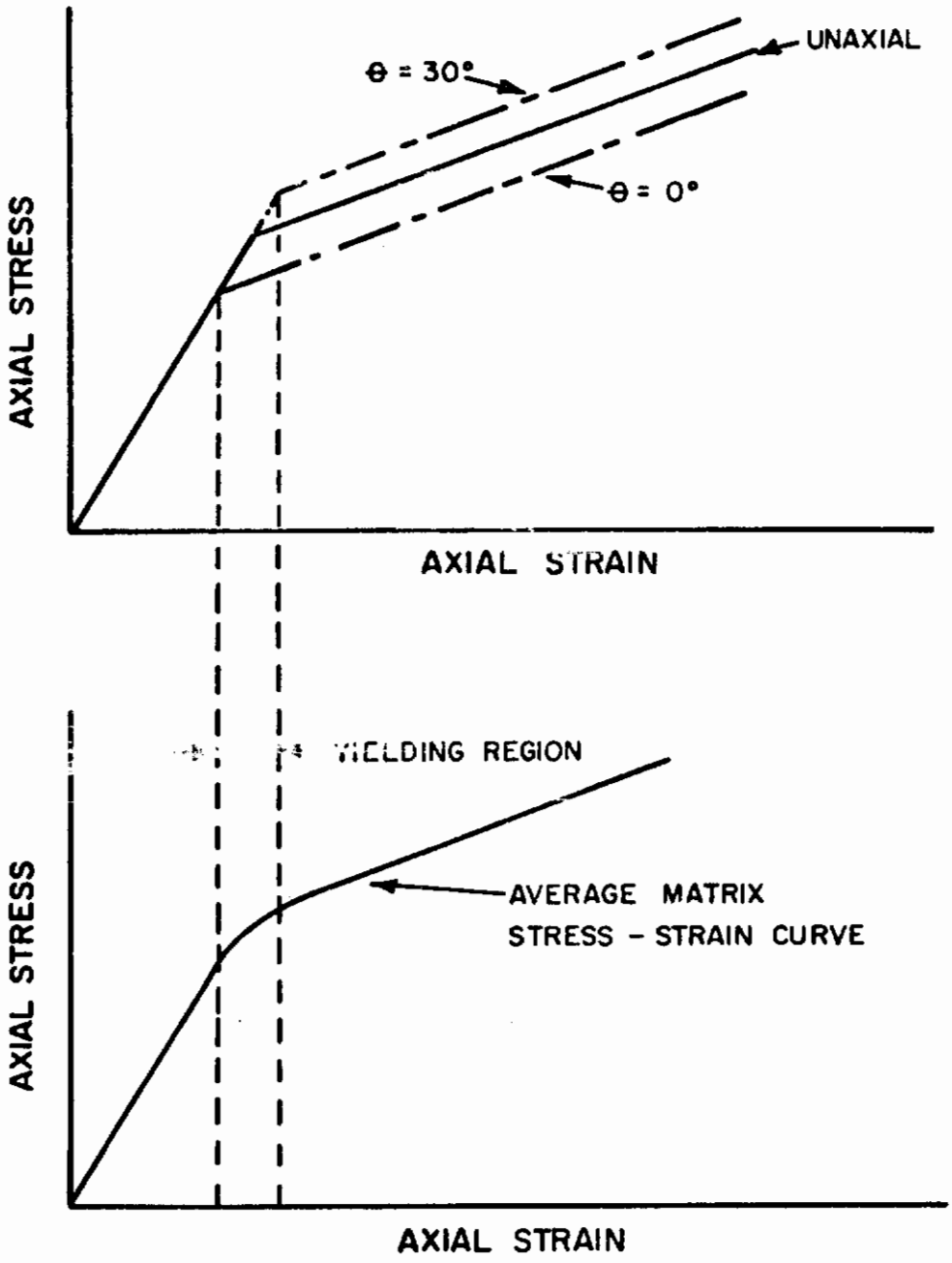

Figure 122

Diagram of the Effect of the Yielding Behavior of the Matrix on the Stress-Strain Characteristics of a Hexagonally-Packed Fiber Composite.

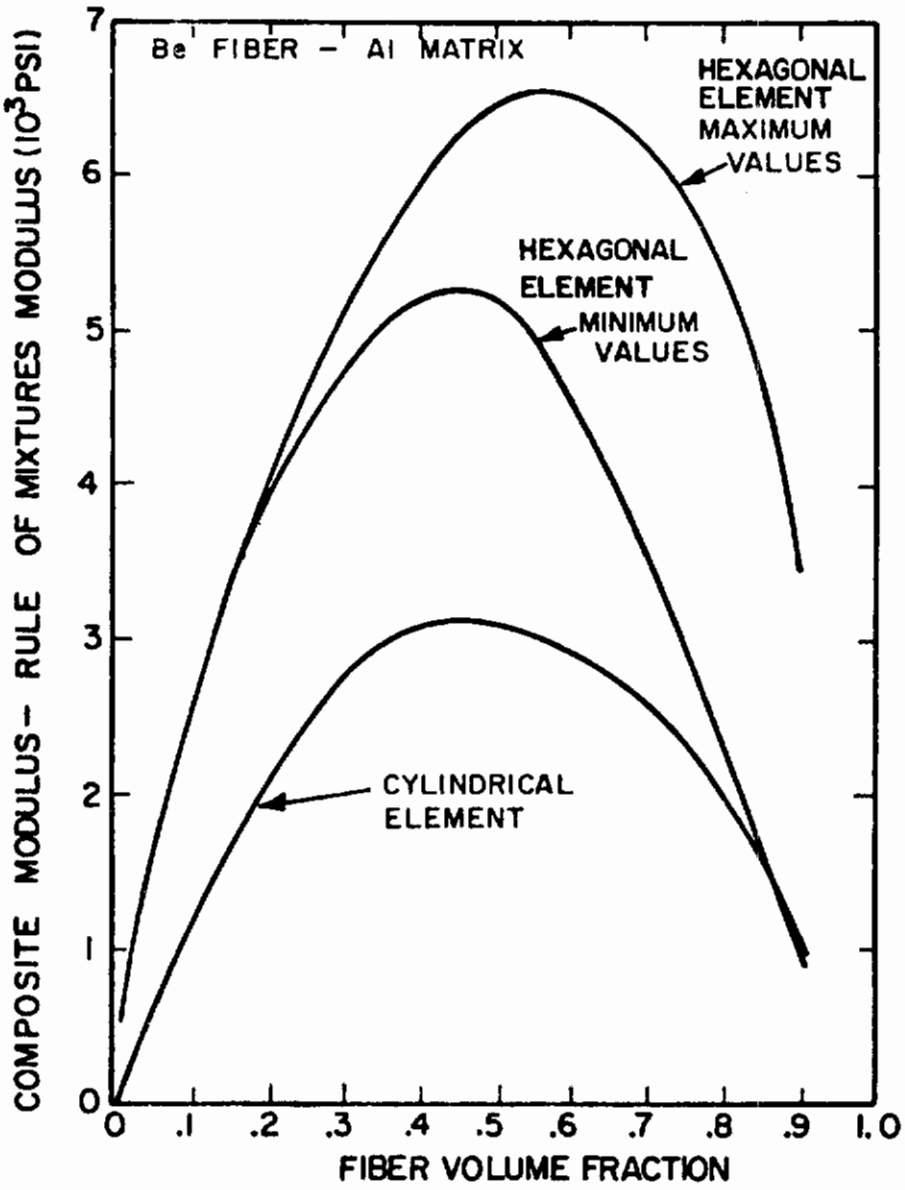

Figure 123

Variation in the Difference Between the Composite Modulus and Rule of Mixtures Modulus with Fiber Volume Fraction.

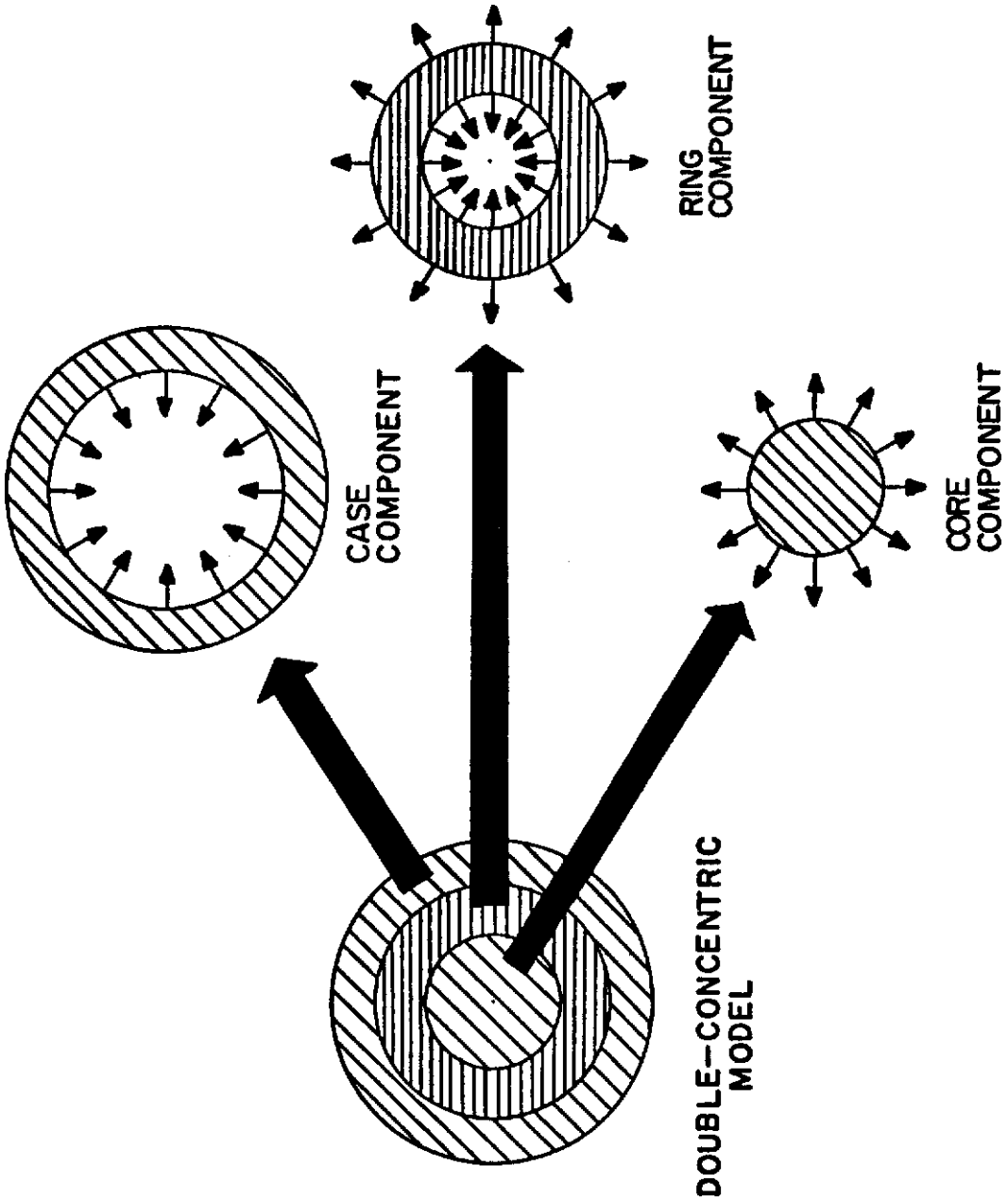

Figure 124

Double-Concentric Model Cross Section with Component Designations.

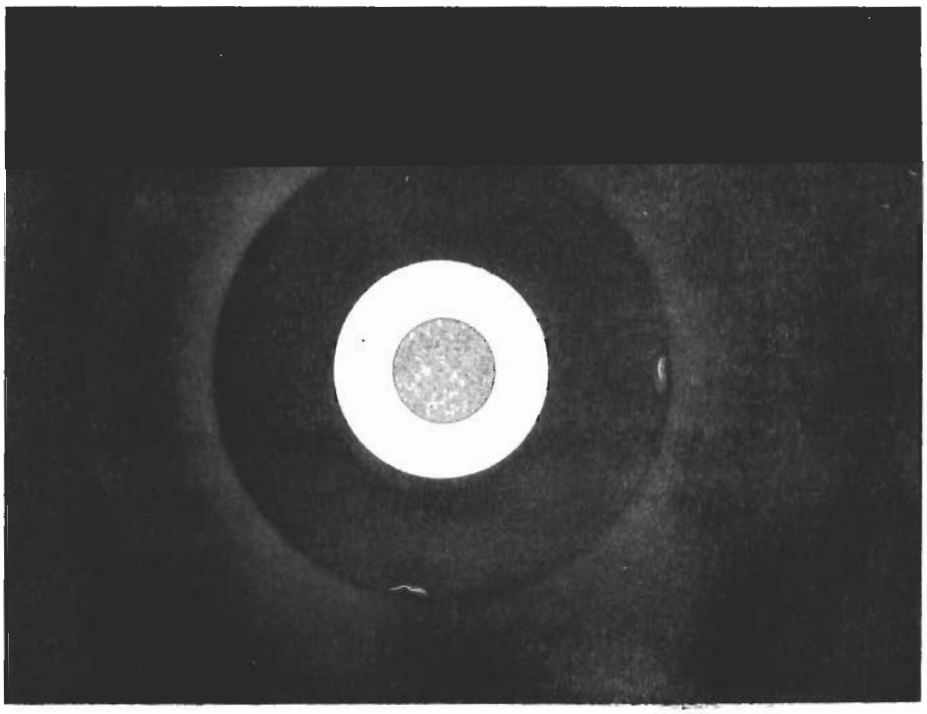

Figure 125

Cross Section of the Maraging Steel - OFHC Copper Double-Concentric Composite.

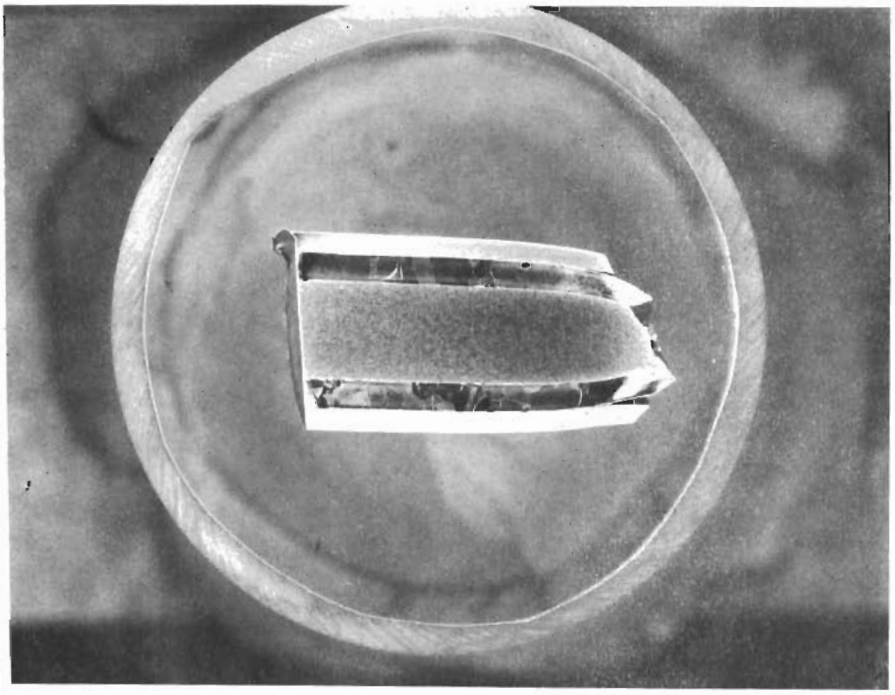

Figure 126

Longitudinal Section Through a Typical Fracture of a Maraging Steel-OFHC Copper Double-Concentric Composite.

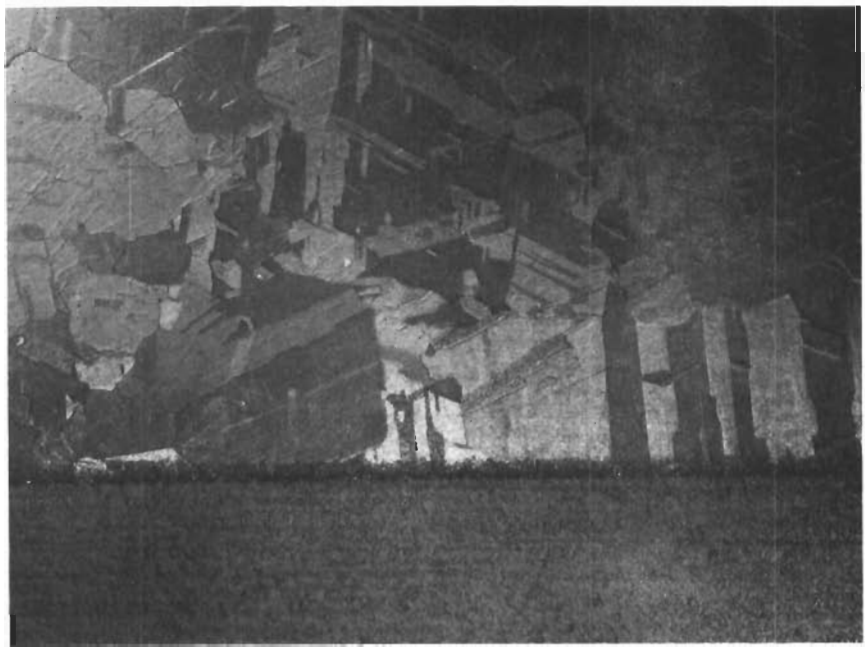

Figure 127

Photomicrographs of the Interfaces of the Maraging Steel-OFHC Copper Double-Concentric Composites.

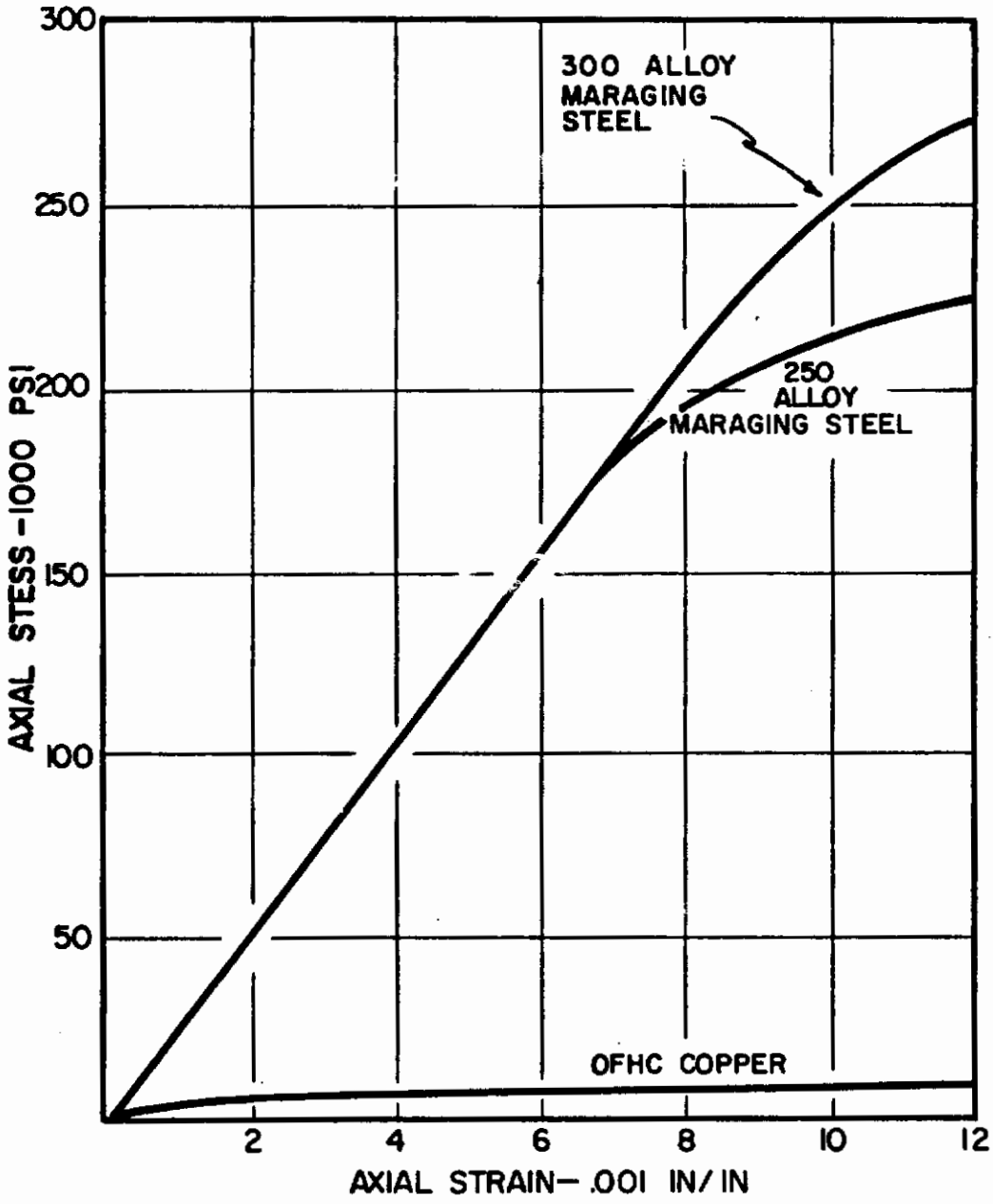

Figure 128

Stress-Strain Curves for the Maraging Steel and OFHC Copper Component Materials.

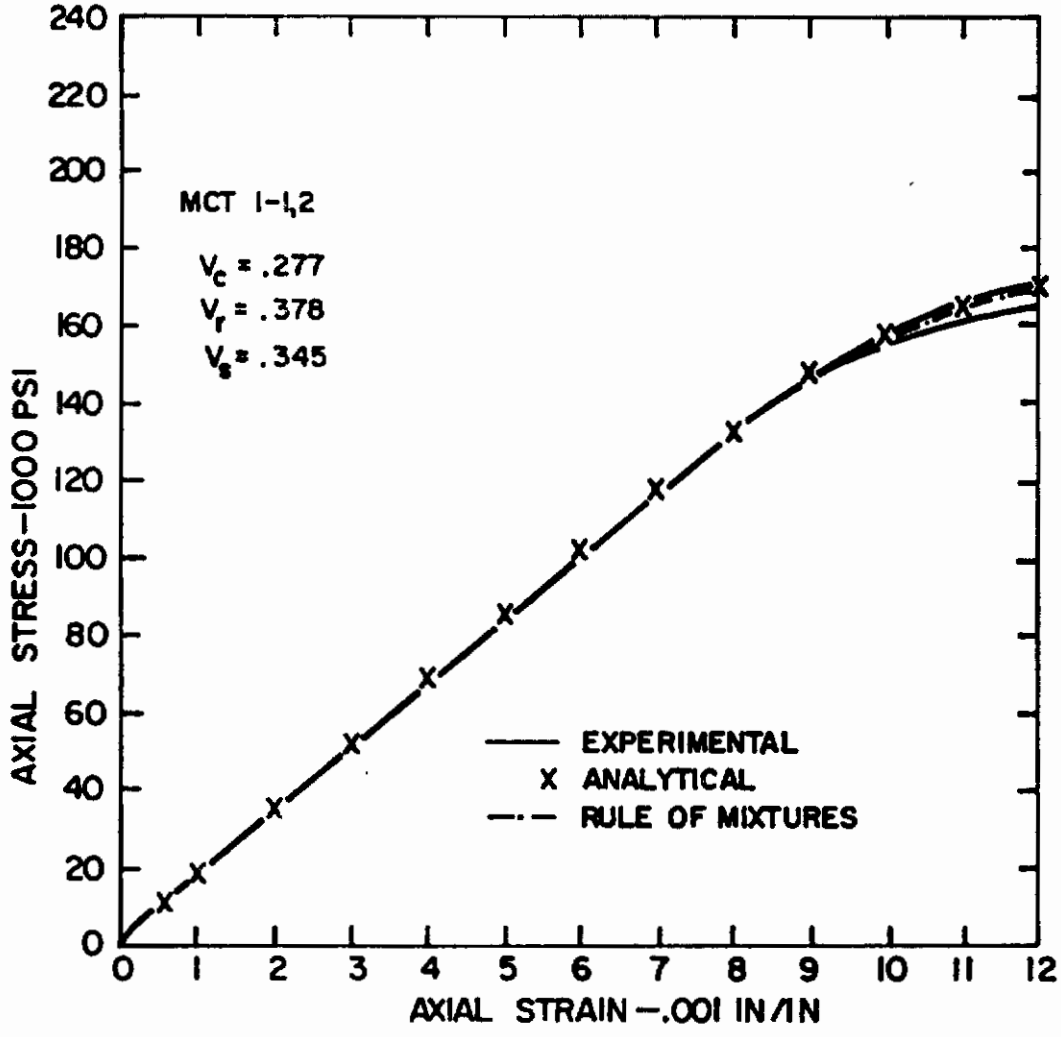

Figure 129

Experimental and Analytical Stress-Strain Curves for the Maraging Steel OFHC Copper Double-Concentric Composites (Samples (MCT 1-1,2).

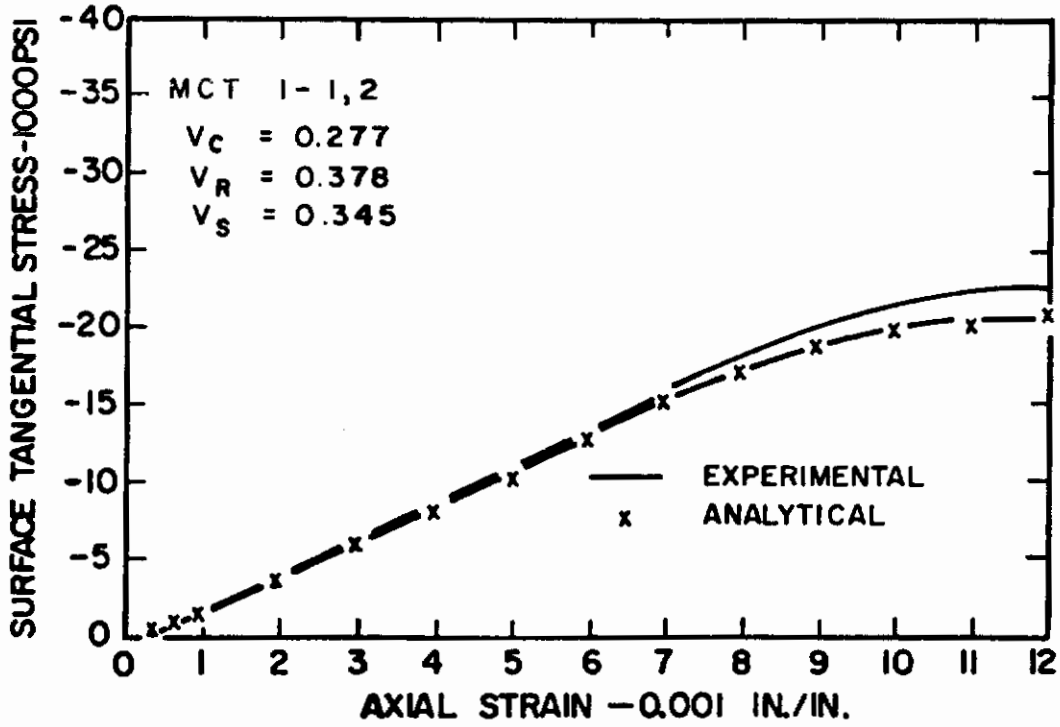

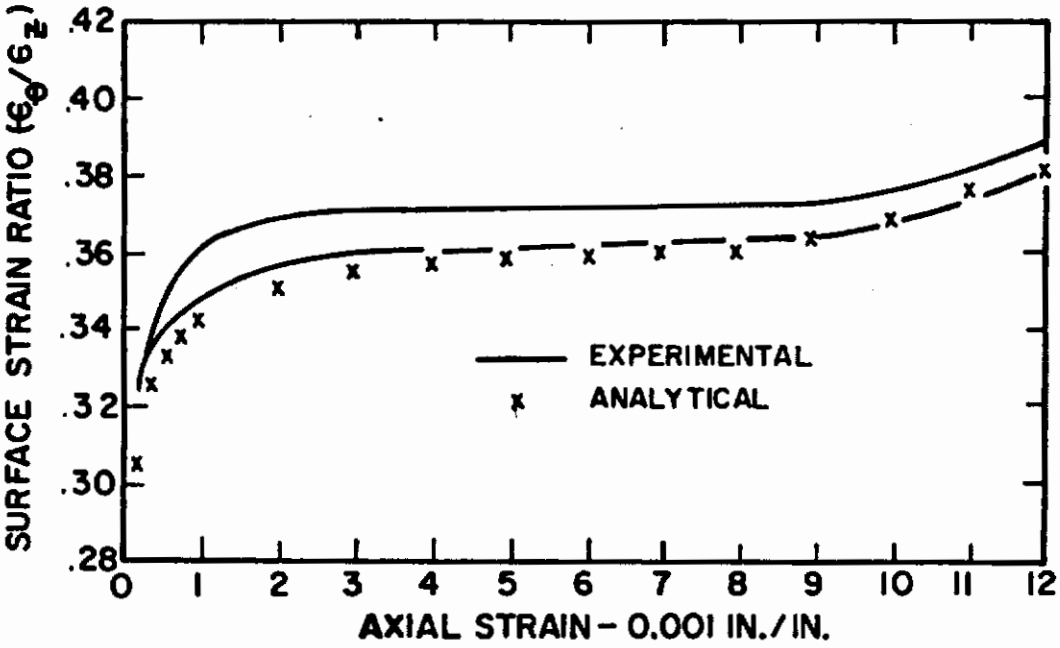

Figure 130

Experimental and Analytical Curves of Surface Tangential Stress and Strain Ratio for Maraging Steel-OFHC Copper Double-Concentric Composites (Samples MCT 1-1,2).

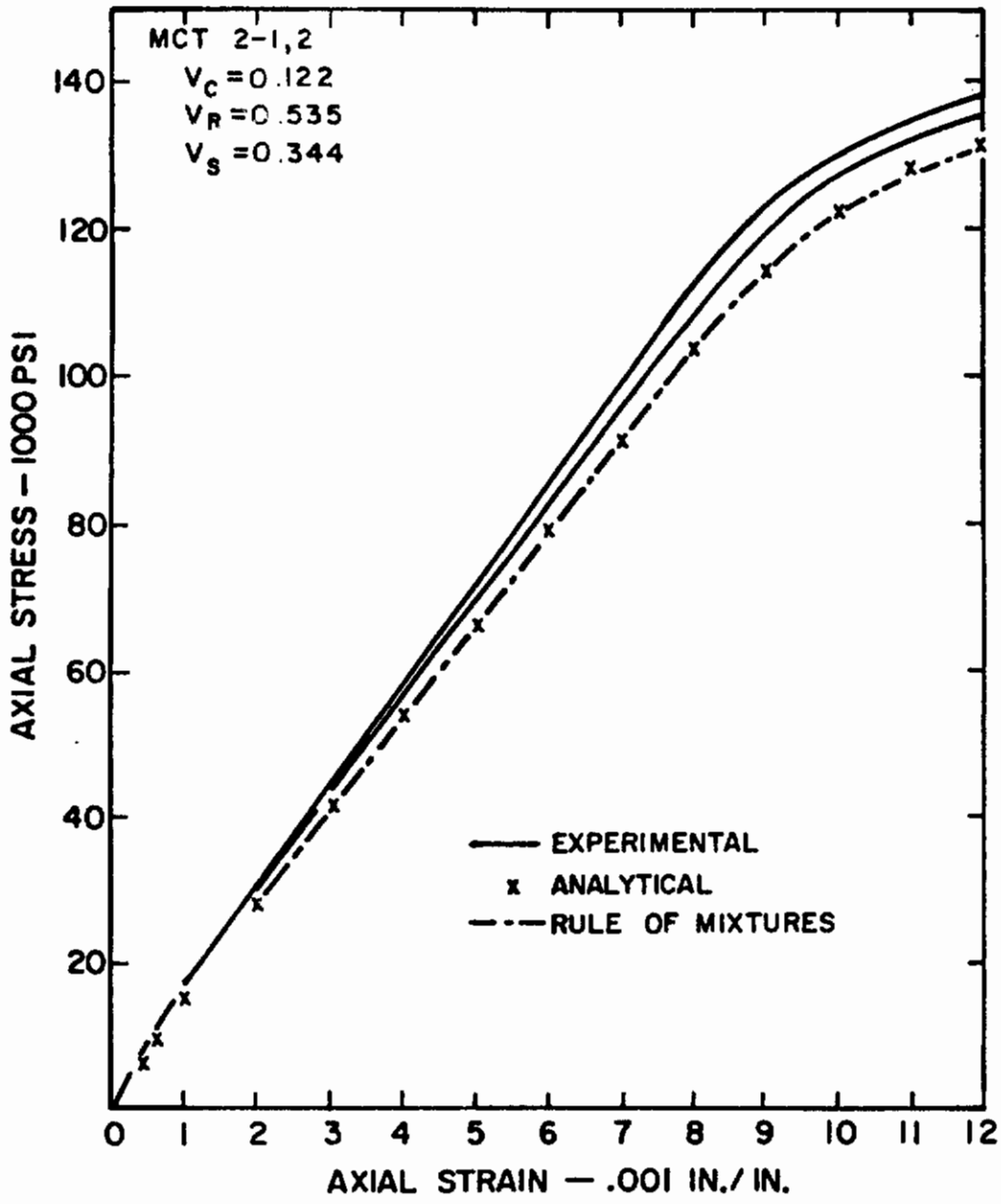

Figure 131

Experimental and Analytical Stress-Strain Curves for the Maraging Steel OFHC Copper Double-Concentric Composites (Samples MCT 2-1,2).

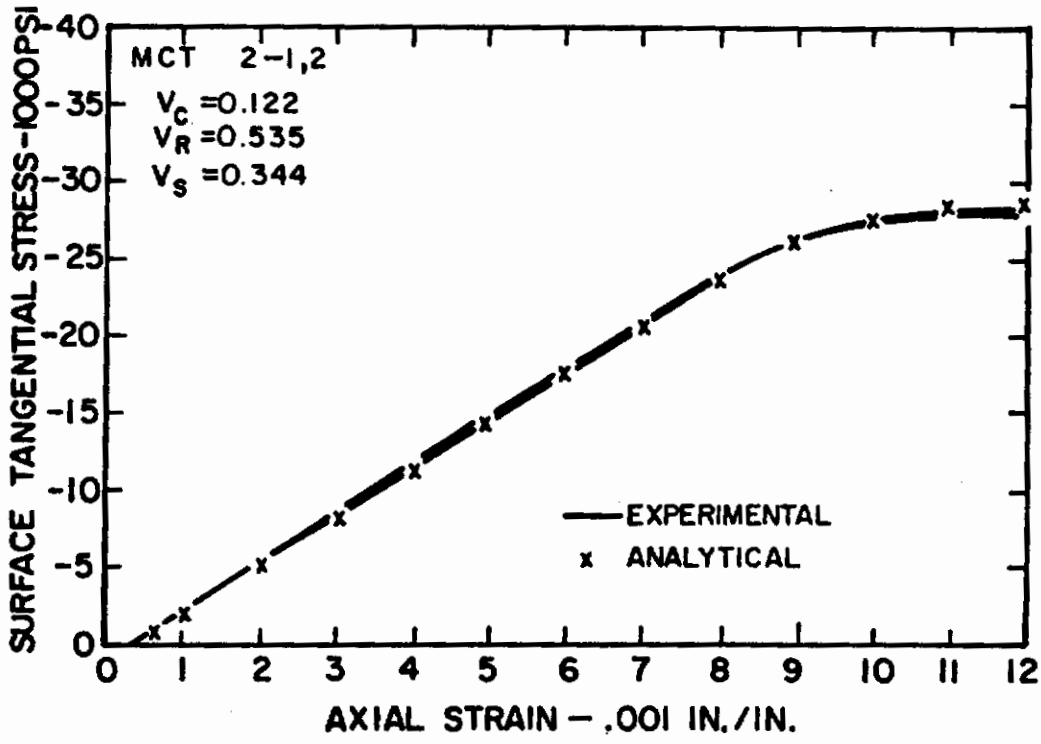

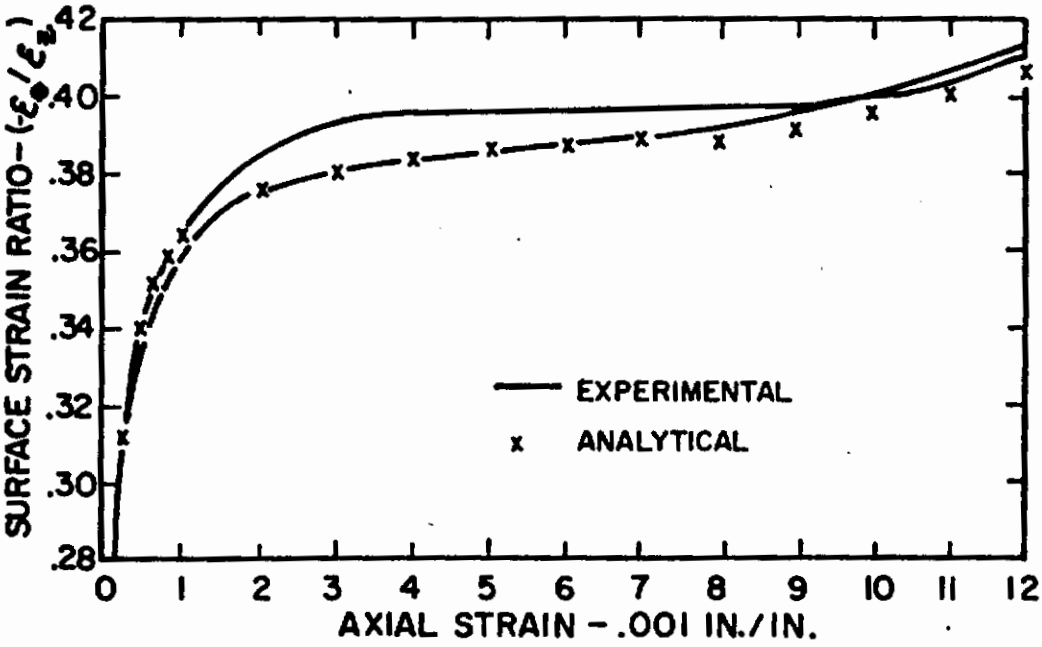

Figure 132

Experimental and Analytical Curves of Surface Tangential Stress and Strain Ratio for Maraging Steel-OFHC Copper Double-Concentric Composites (Samples MCT 2-1,2).

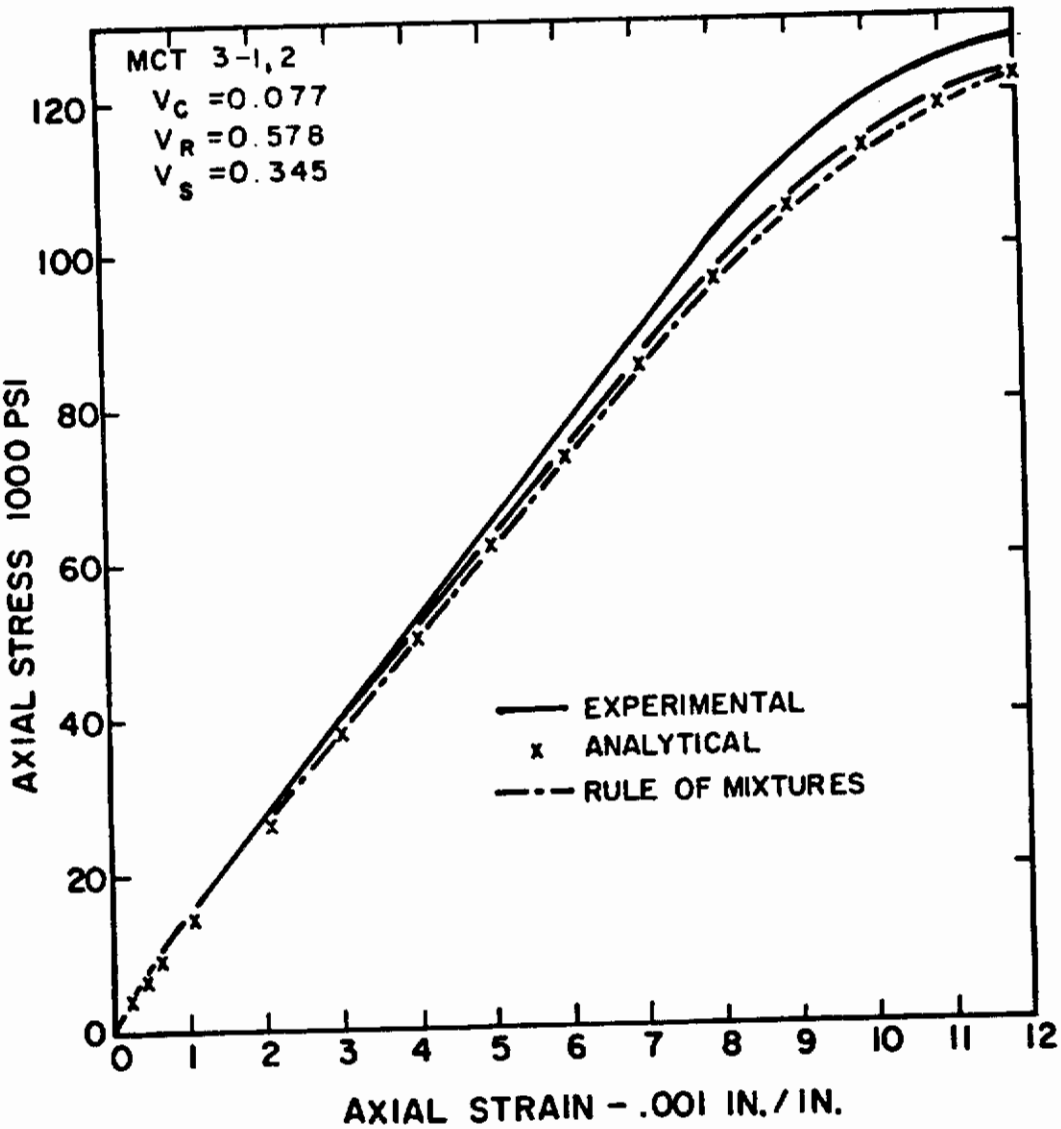

Figure 133

Experimental and Analytical Stress-Strain Curves for the Maraging Steel OFHC Copper Double-Concentric Composites (Samples MCT 3-1,2).

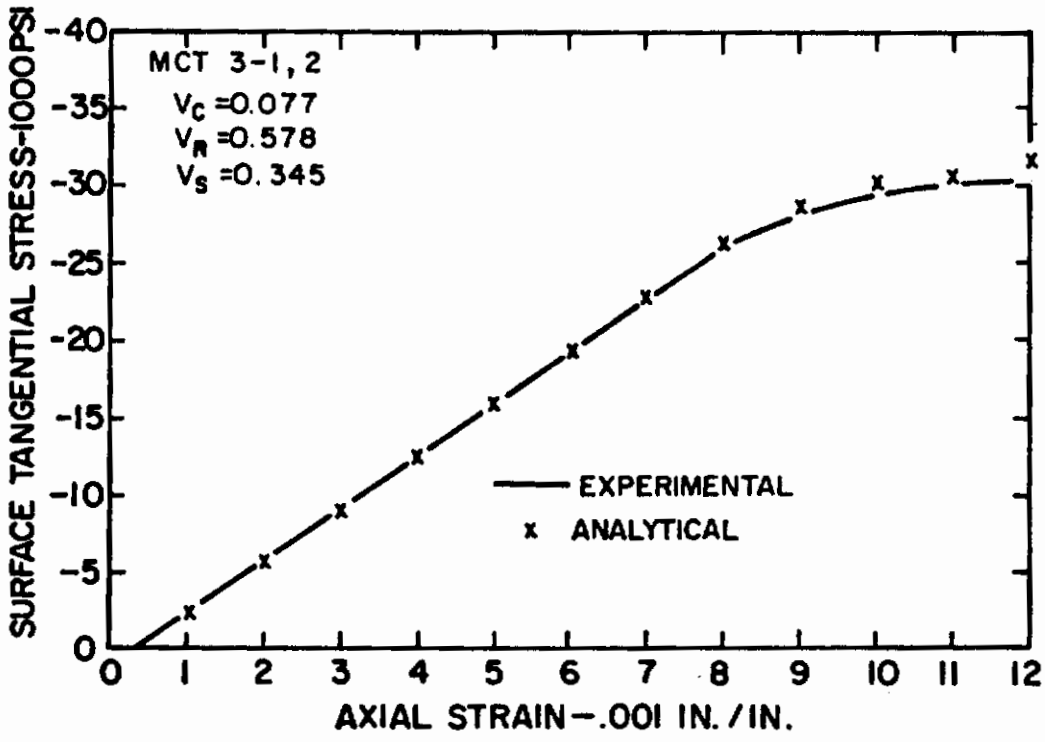

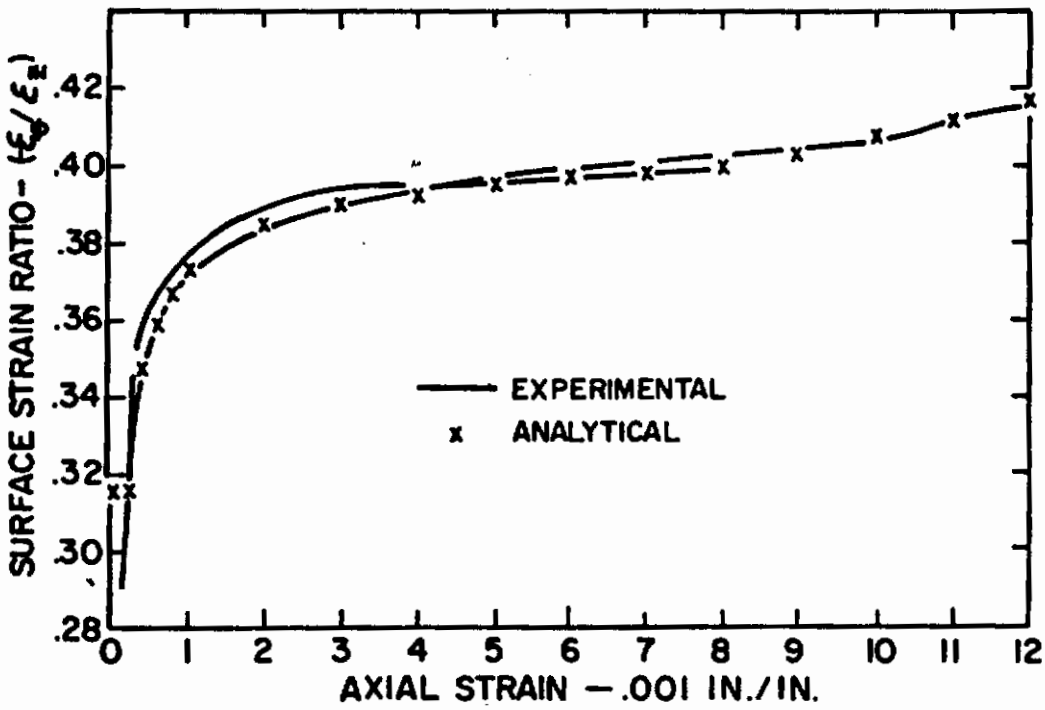

Figure 134

Experimental and Analytical Curves of Surface Tangential Stress and Strain Ratio for Maraging Steel-OFHC Copper Double-Concentric Composites (Samples MCT 3-1,2).

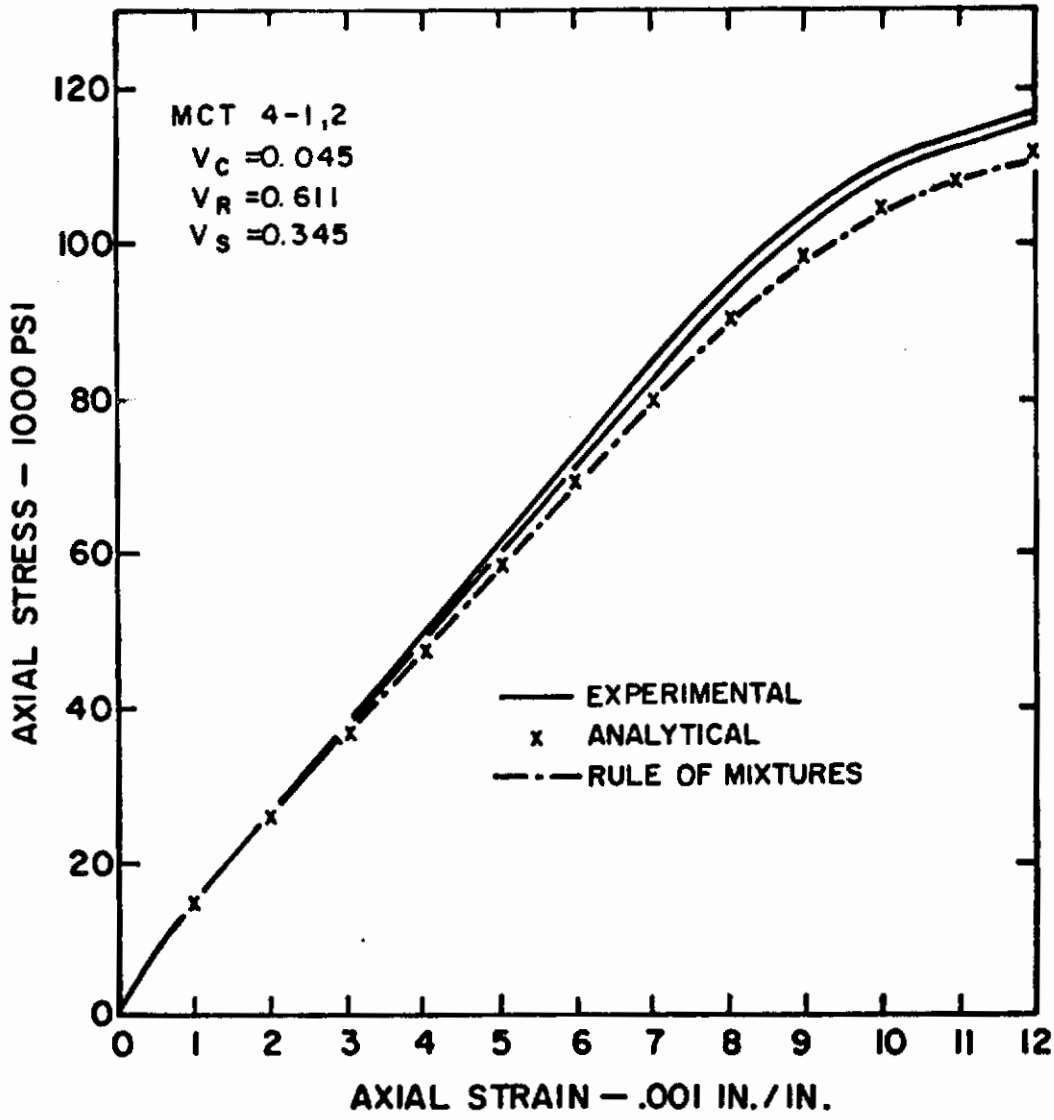

Figure 135

Experimental and Analytical Stress-Strain Curves for the Maraging Steel OFHC Copper Double-Concentric Composites (Samples MCT 4-1,2).

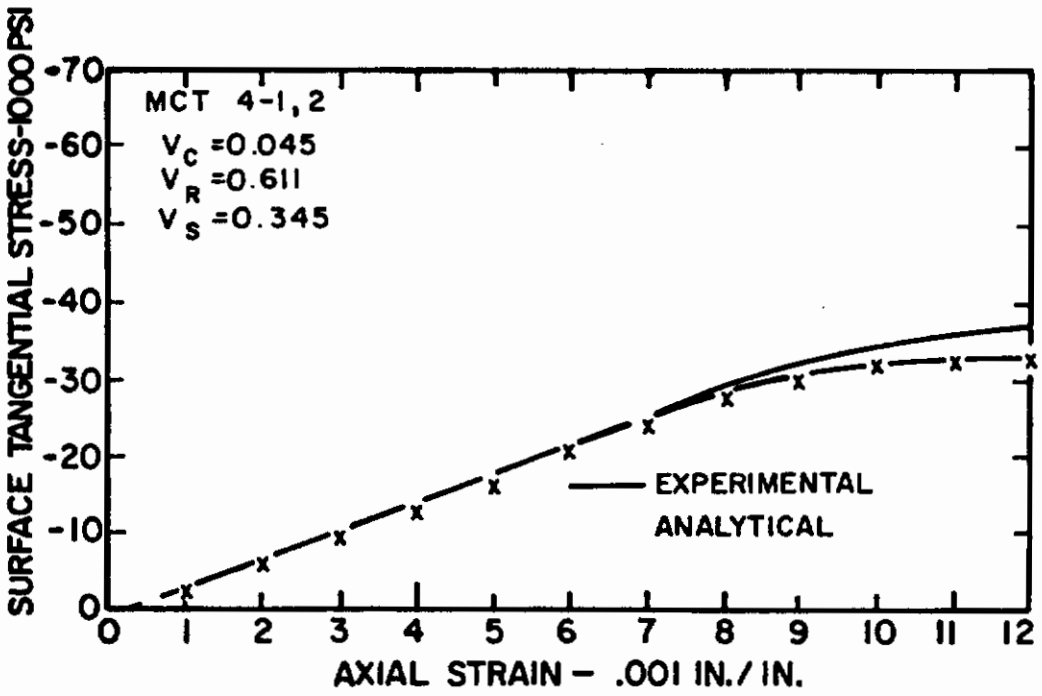

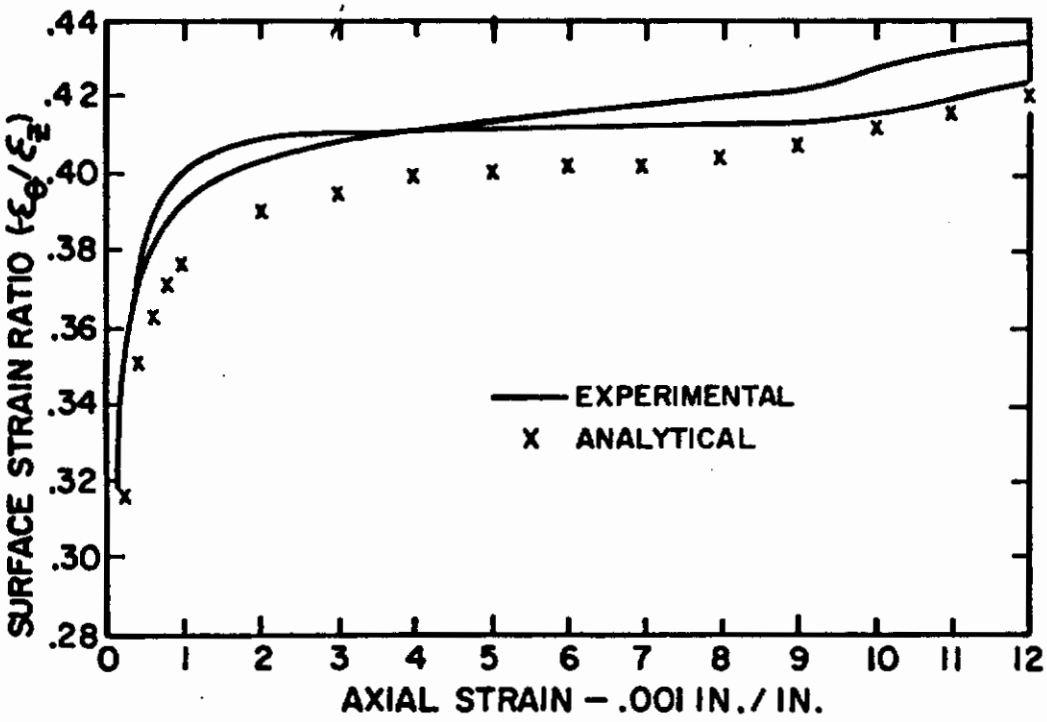

Figure 136

Experimental and Analytical Curves of Surface Tangential Stress and Strain Ratio for Maraging Steel-OFHC Copper Double-Concentric Composites (Samples MCT 4-1-,2).

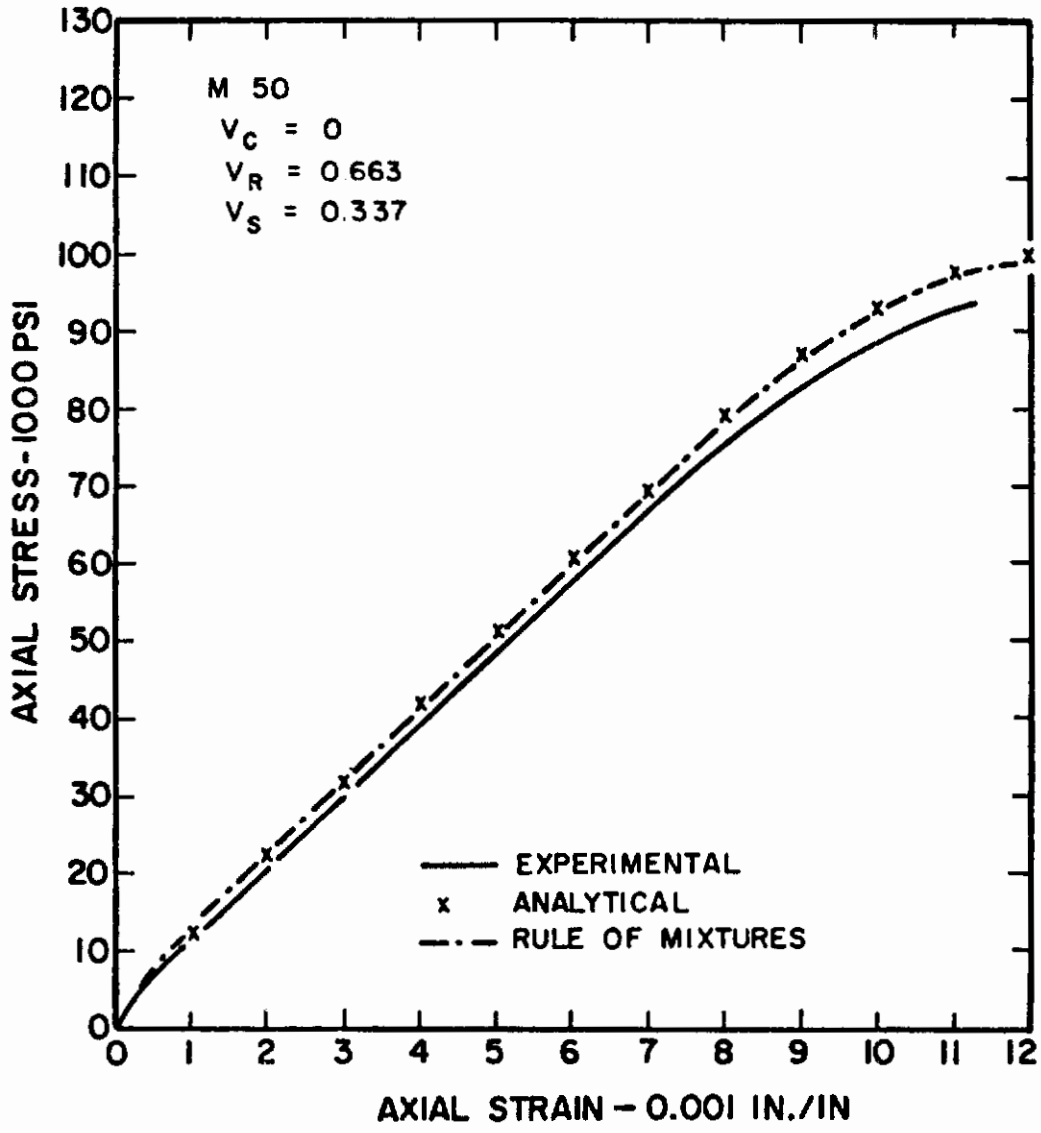

Figure 137

Experimental and Analytical Stress-Strain Curves for the Maraging Steel OFHC Copper Double-Concentric Composites (Sample M 50).

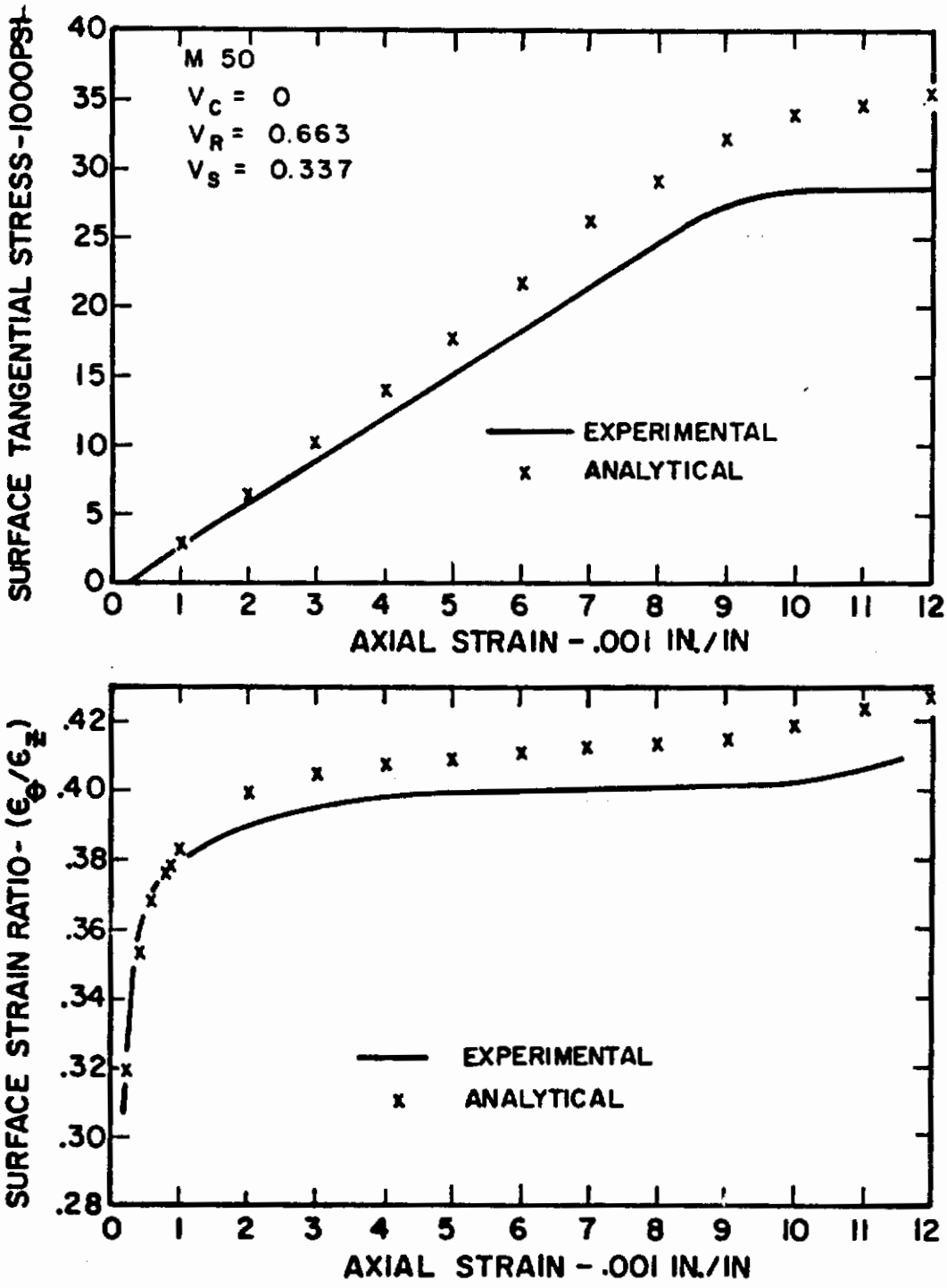

Figure 138

Experimental and Analytical Curves of Surface Tangential Stress and Strain Ratio for Maraging Steel-OFHC Copper Double-Concentric Composites (Sample M 50).

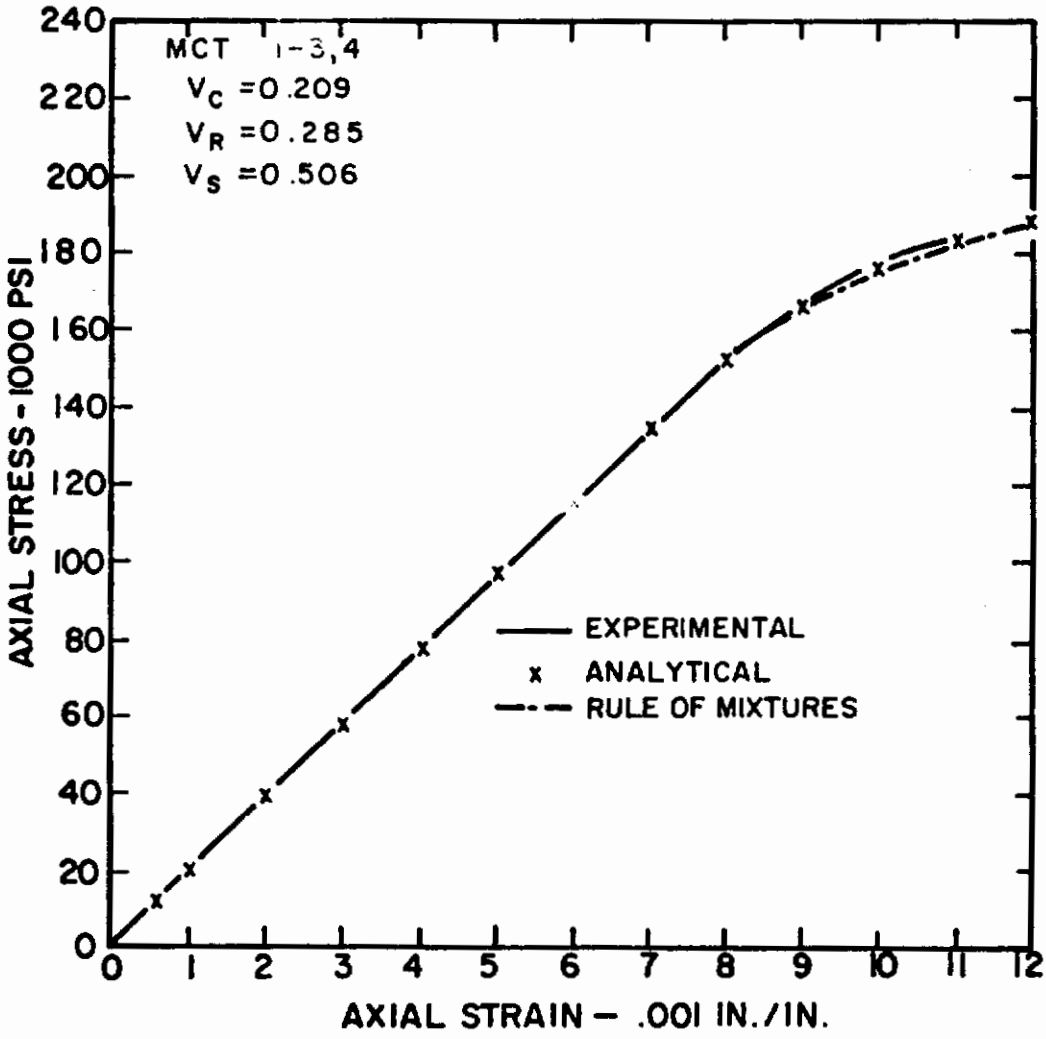

Figure 139

Experimental and Analytical Stress-Strain Curves for the Maraging Steel OFHC Copper Double-Concentric Composites (Samples MCT 1-3,4).

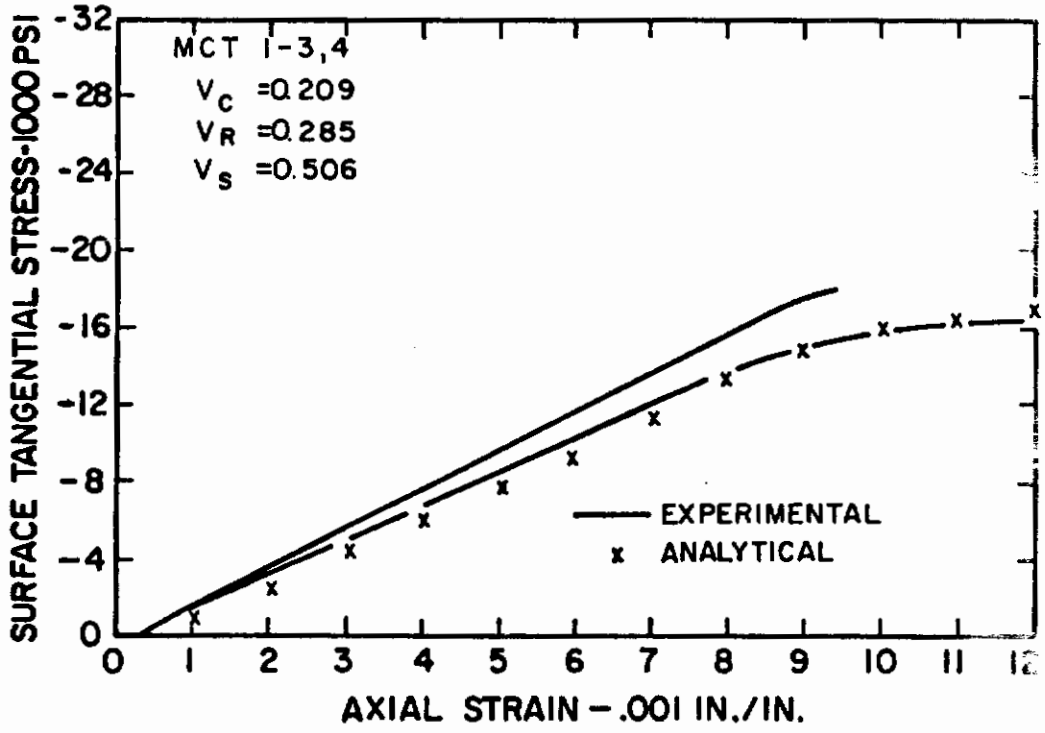

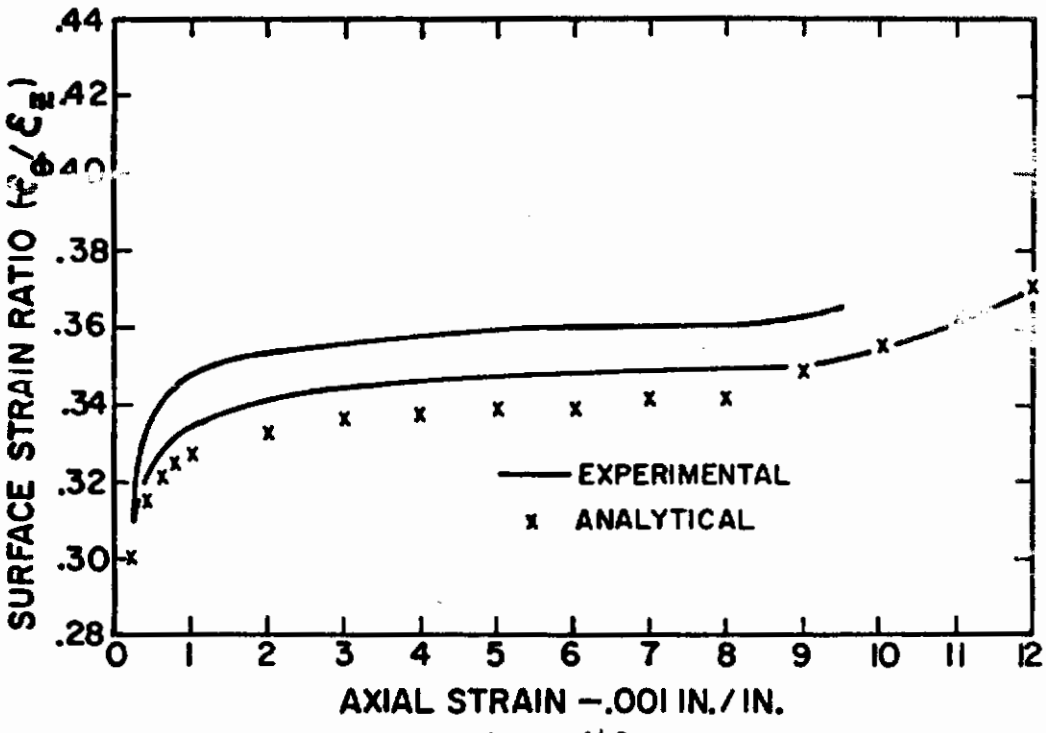

Figure 140

Experimental and Analytical Curves of Surface Tangential Stress and Strain Ratio for Maraging Steel-OFHC Copper Double-Concentric Composites (Samples MCT 1-3,4).

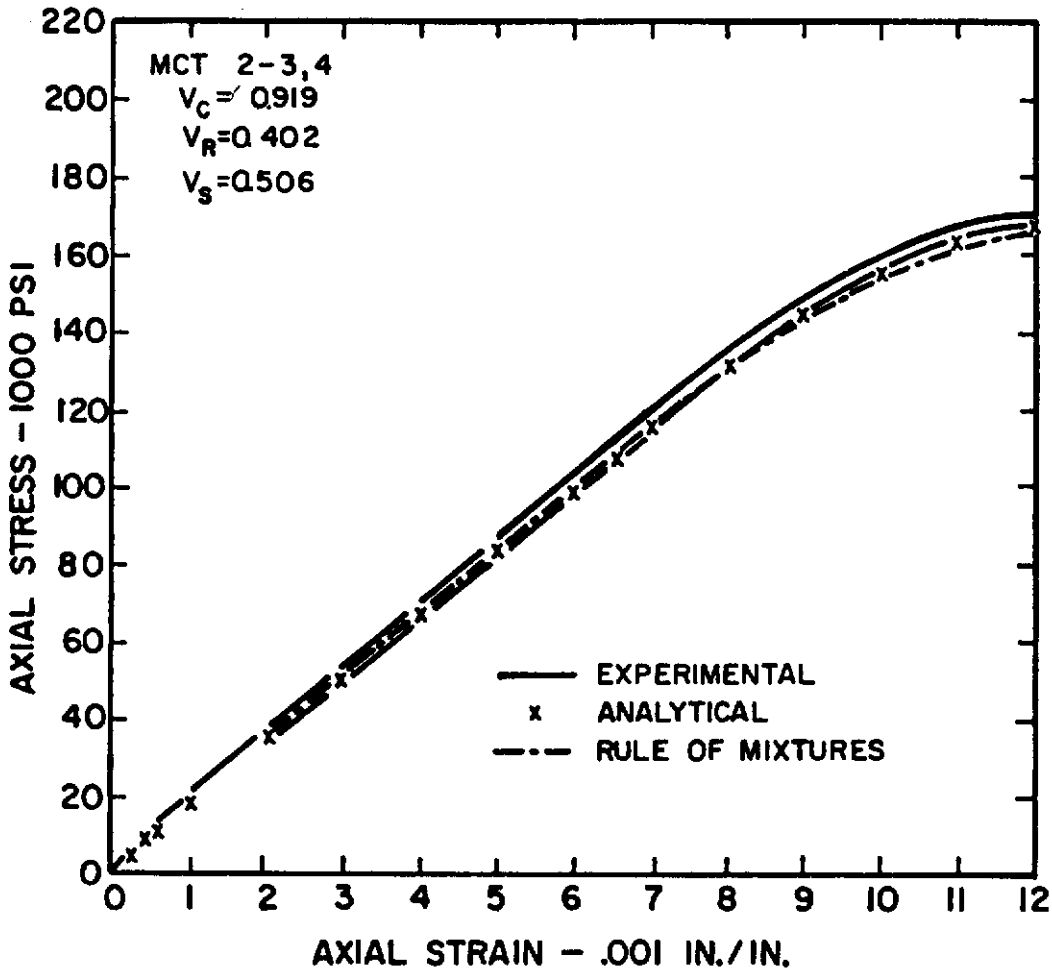

Figure 141

Experimental and Analytical Stress-Strain Curves for the Maraging Steel OFHC Copper Double-Concentric Composites (Samples MCT 2-3,4).

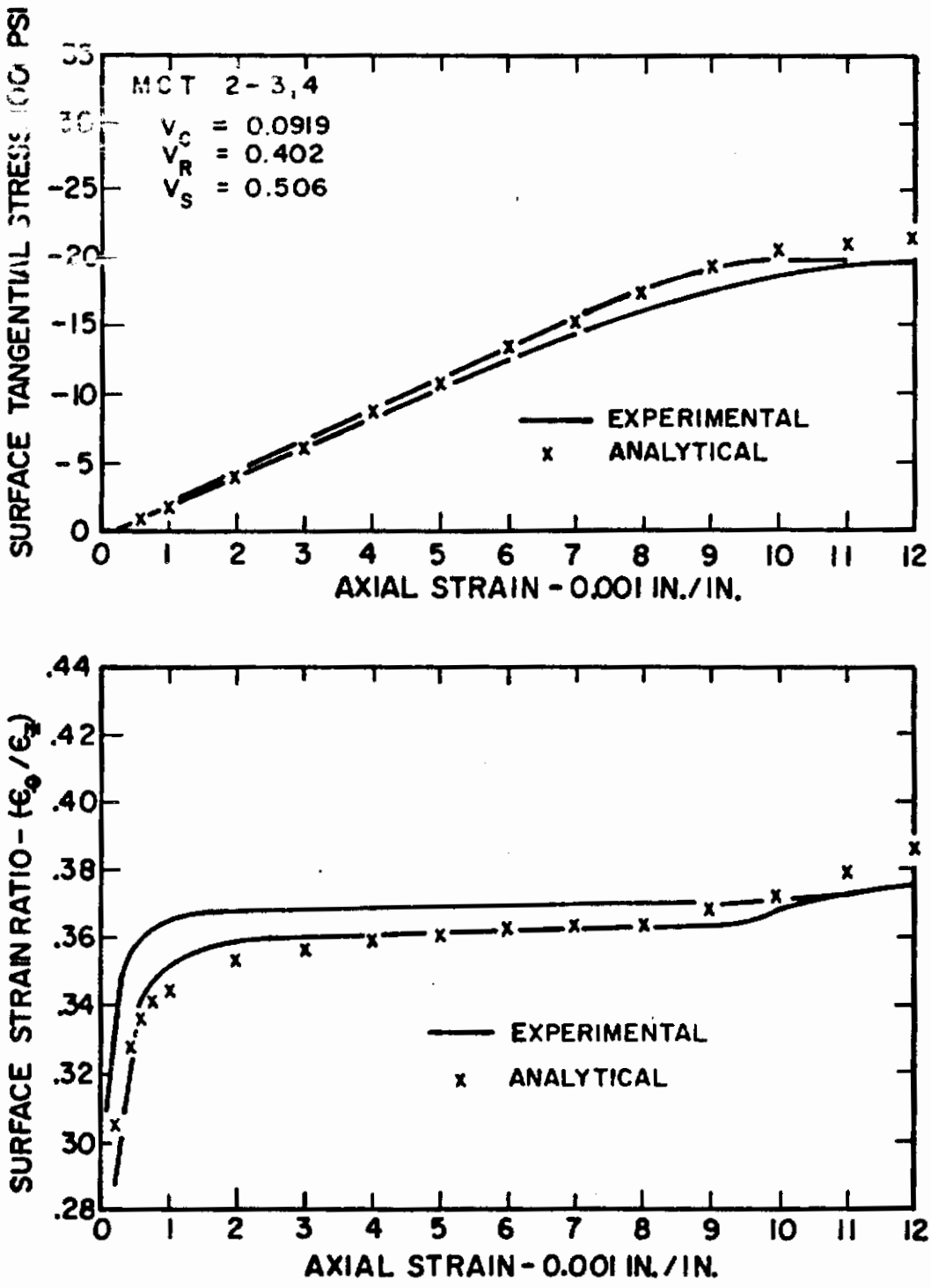

Figure 142

Experimental and Analytical Curves of Surface Tangential Stress and Strain Ratio for Maraging Steel-OFHC Copper Double-Concentric Composites (Samples MCT 2-3,4).

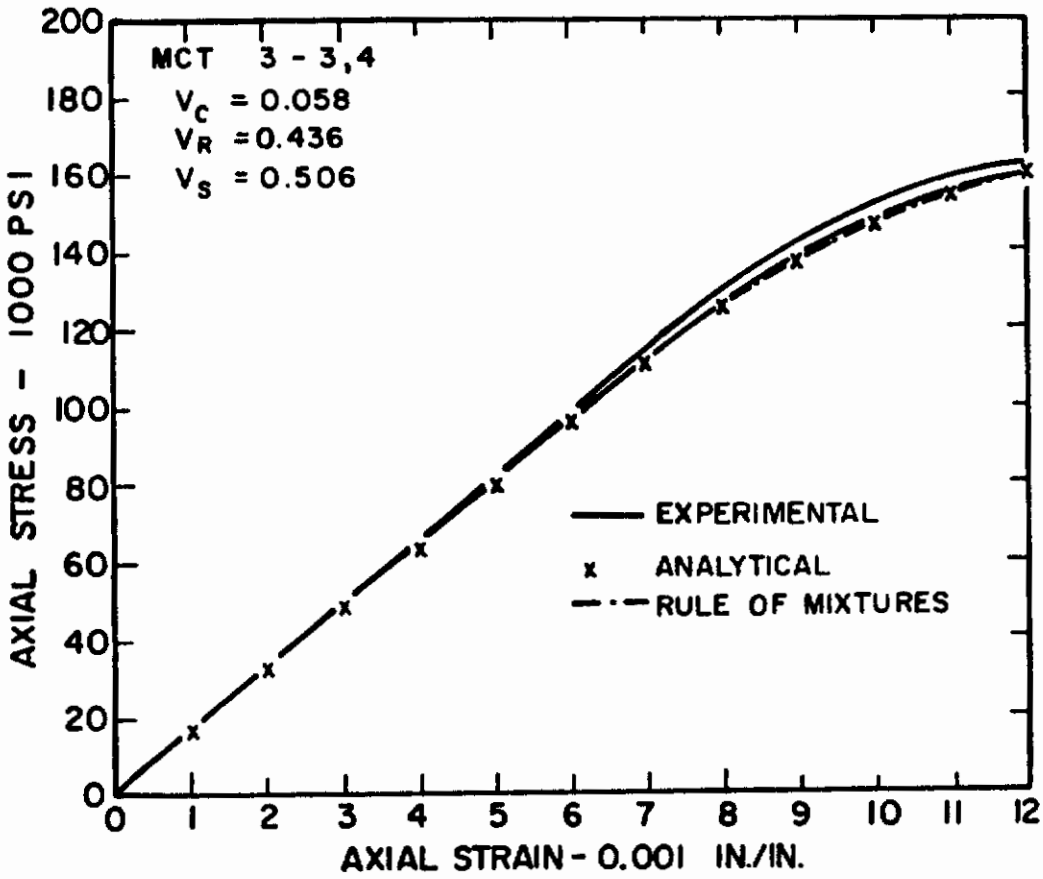

Figure 143

Experimental and Analytical Stress-Strain Curves for the Maraging Steel OFHC Copper Double-Concentric Composites (Samples MCT 3-3,4).

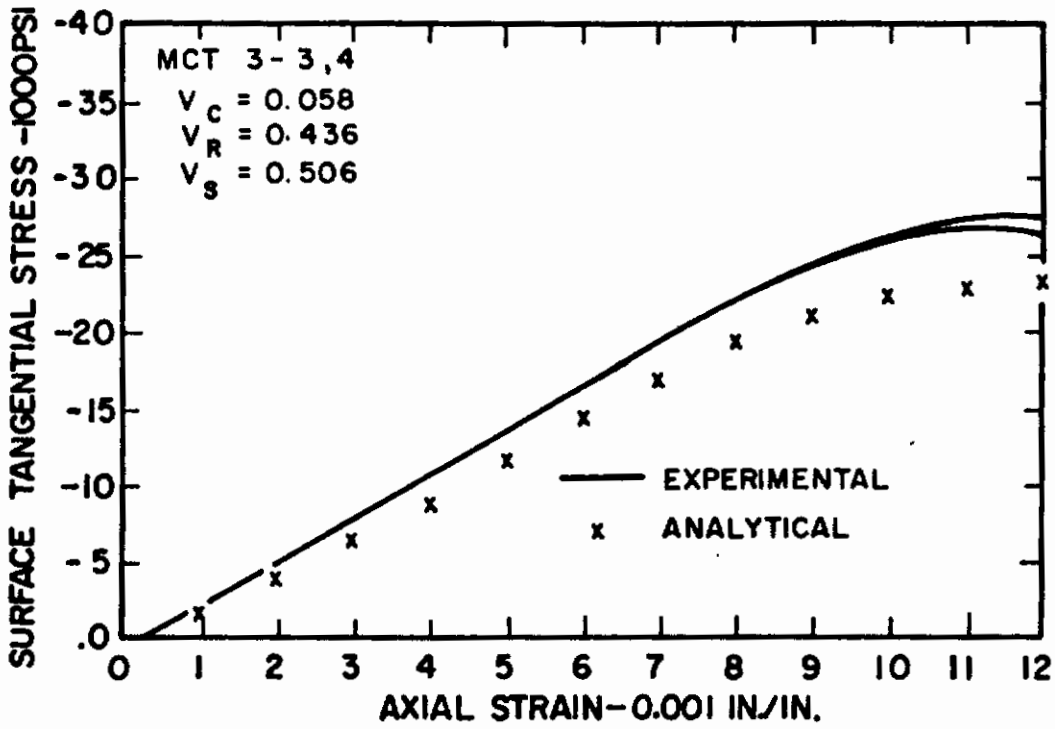

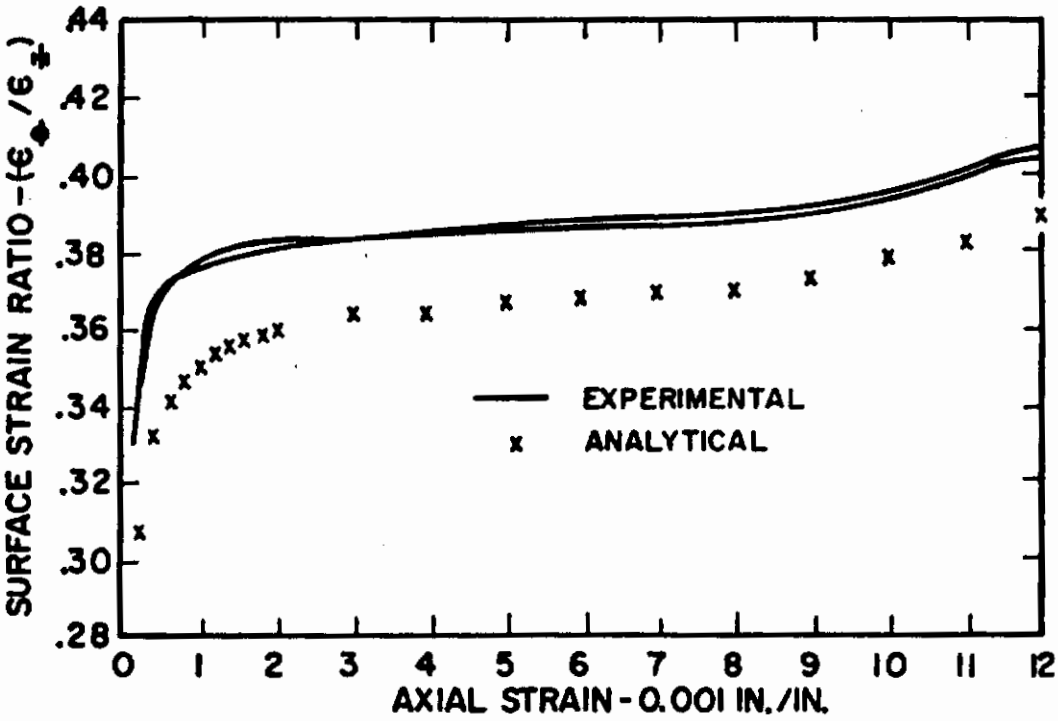

Figure 144

Experimental and Analytical Curves of Surface Tangential Stress and Strain Ratio for Maraging Steel-OFHC Copper Double-Concentric Composites (Samples MCT 3-3,4).

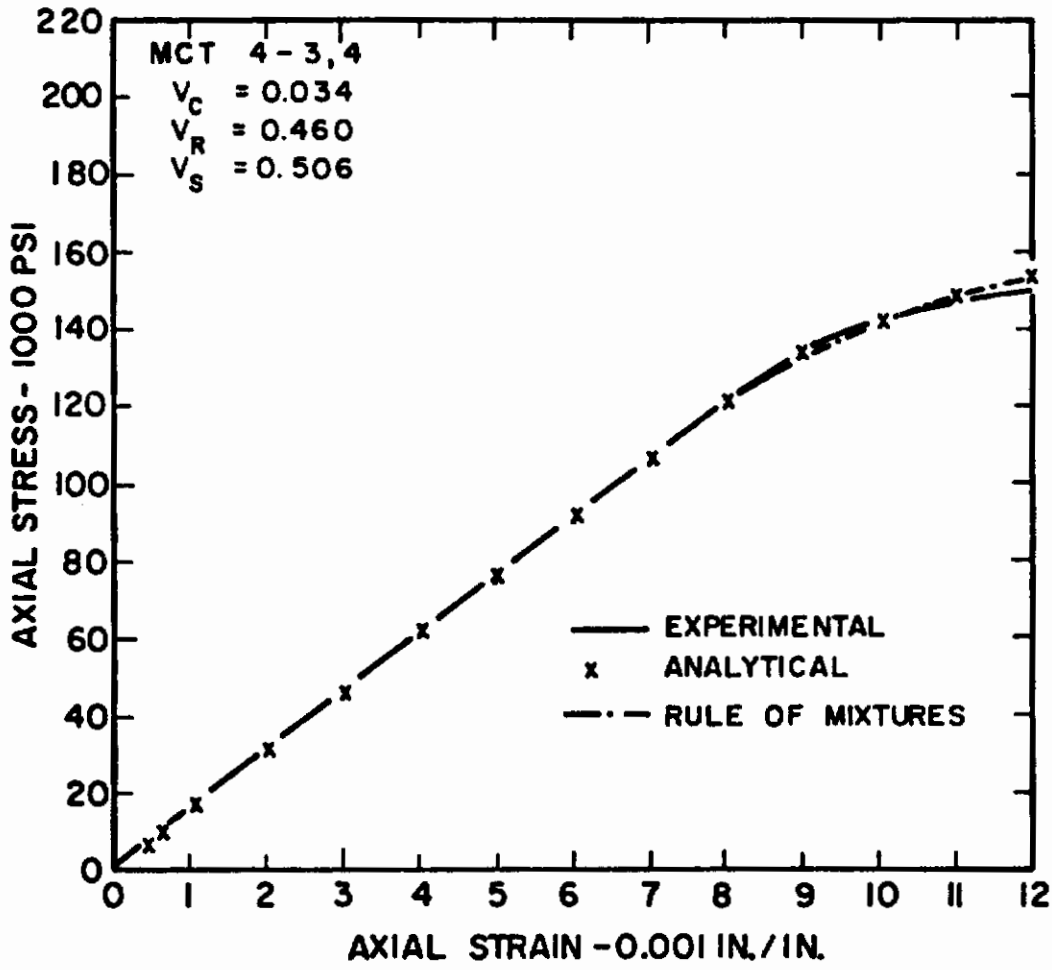

Figure 145

Experimental and Analytical Stress-Strain Curves for the Maraging Steel OFHC Copper Double-Concentric Composites (Samples MCT 4-3,4).

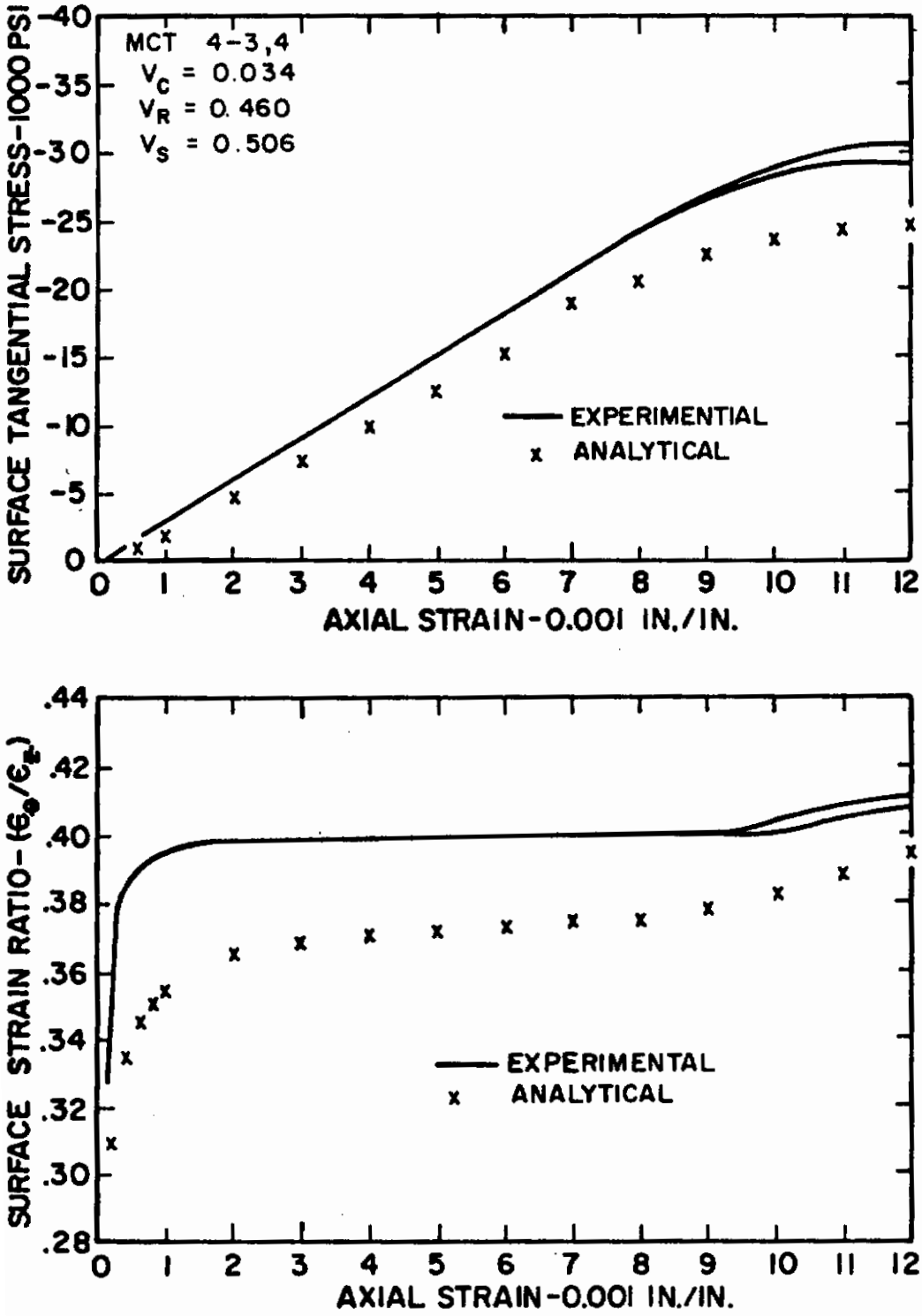

Figure 146

Experimental and Analytical Curves of Surface Tangential Stress and Strain Ratio for Maraging Steel-OFHC Copper Double-Concentric Composites (Samples MCT 4-3,4).

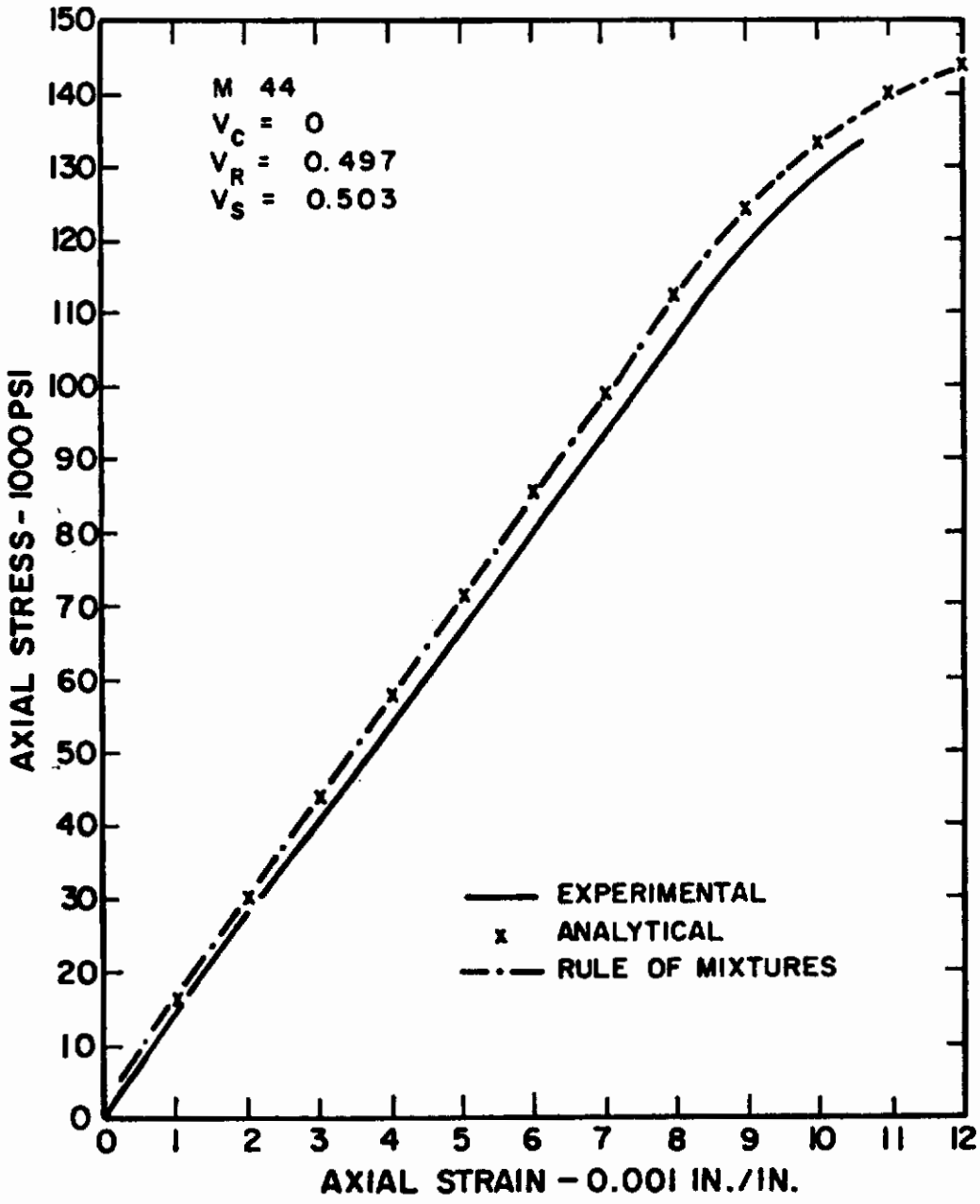

Figure 147

Experimental and Analytical Stress-Strain Curves for the Maraging Steel OFHC Copper Double-Concentric Composites (Sample M 44).

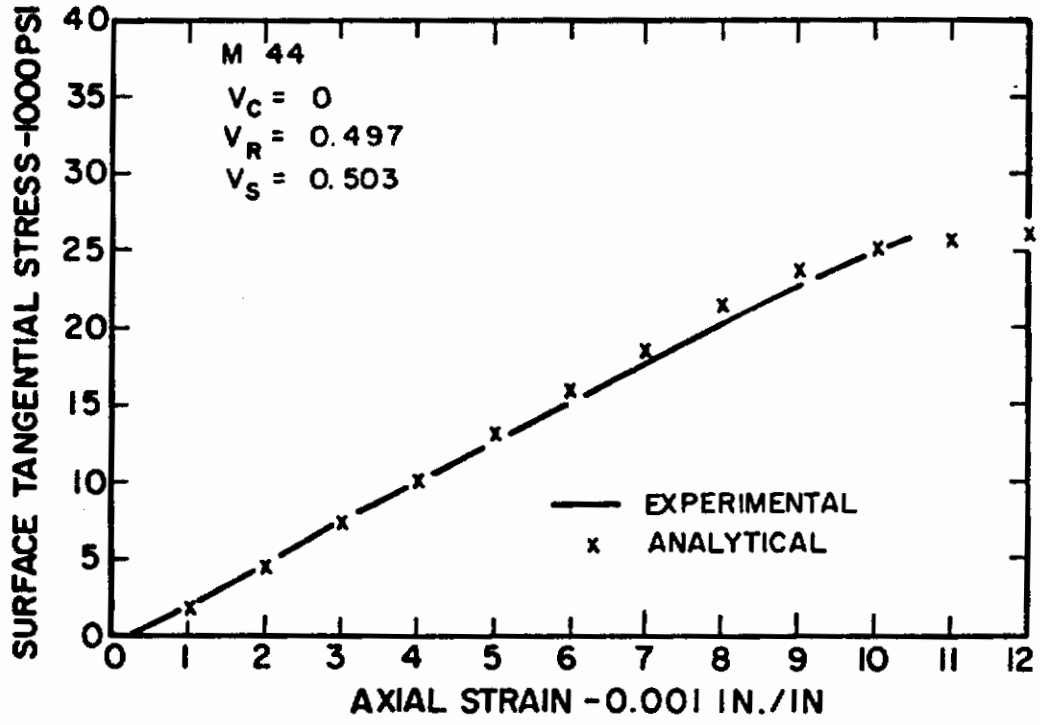

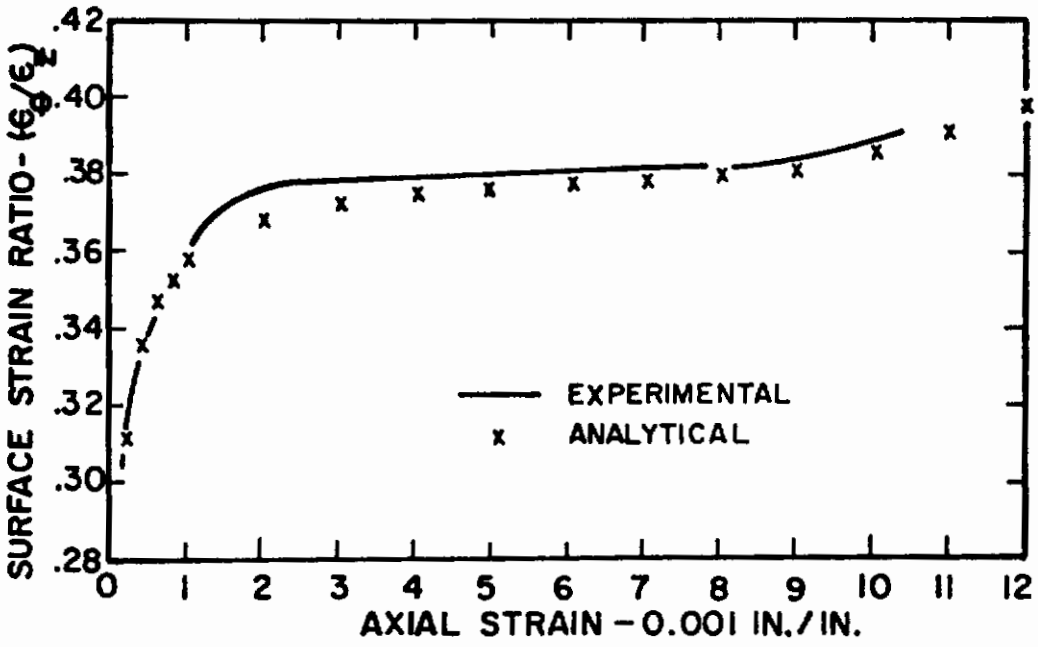

Figure 148

Experimental and Analytical Curves of Surface Tangential Stress and Strain Ratio for Maraging Steel OFHC Copper Double-Concentric Composites (Sample M 44).

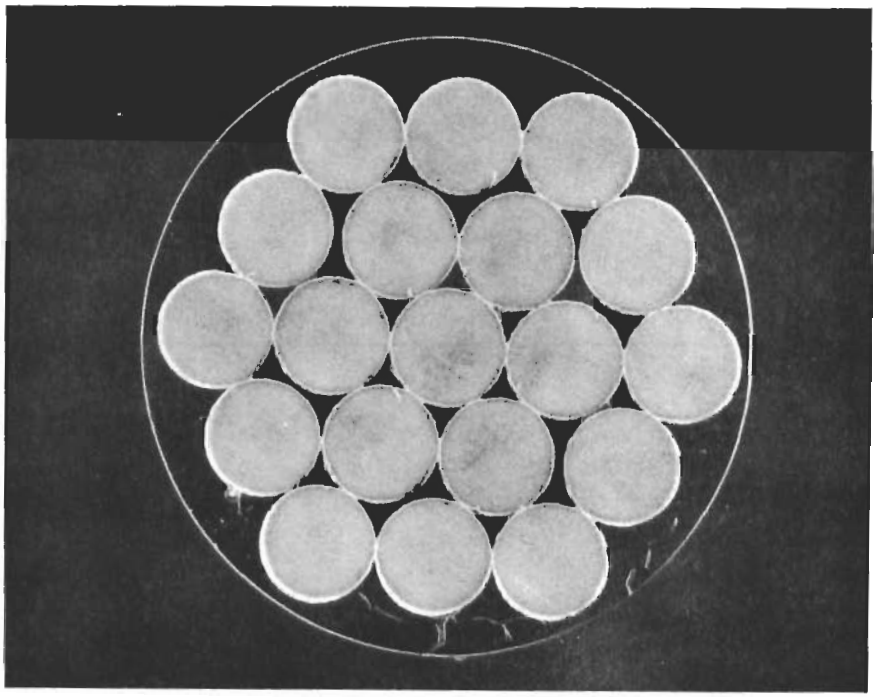

Figure 149

Cross Section of a Typical 50 mil Diameter Tungsten Wire Prototype Composite. This Cross Section Was Taken Immediately Adjacent to the Fracture Surface of a Tested Composite and Some Damage to the Tungsten and Copper Is Evident. V_f = 70.2%.

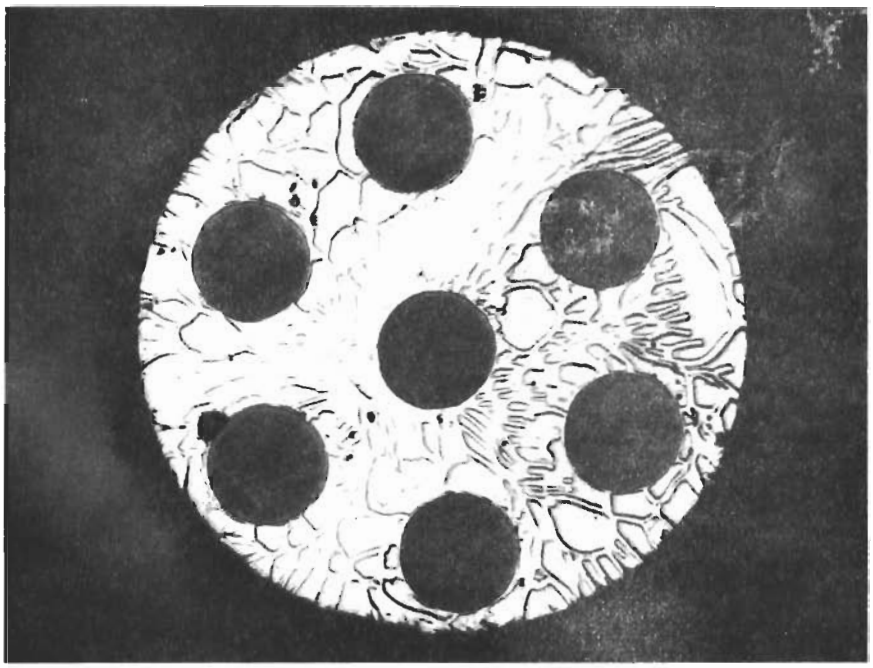

Figure 150

Cross Section of a Typical 50 mil Diameter Tungsten Wire Prototype Composite with the 7-wire Geometry. V_f = 25.9.

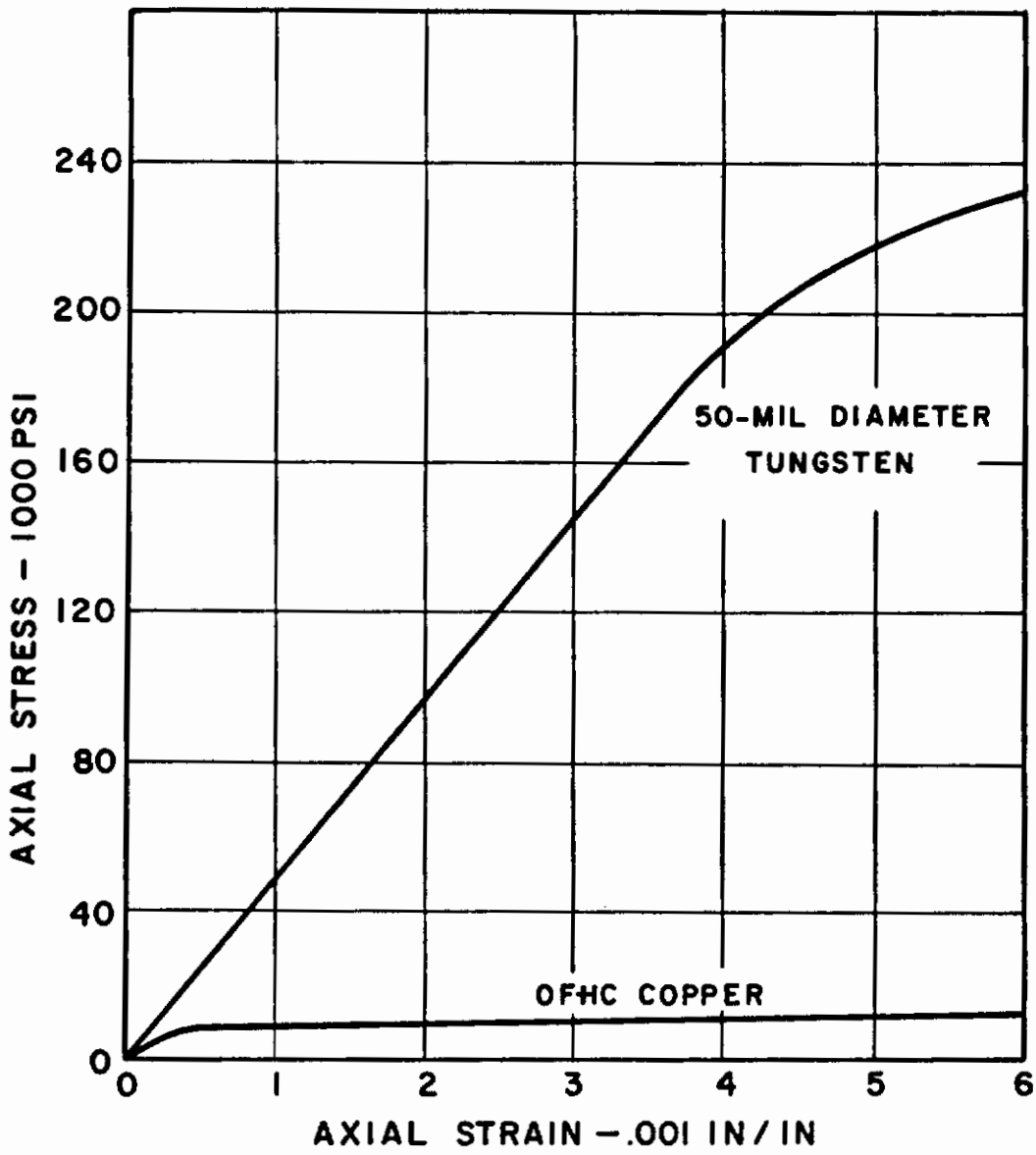

Figure 151

Experimental Stress-Strain Curves for 50 mil Diameter Tungsten Wire and OFHC Copper Used in the Discontinuous Fiber Study.

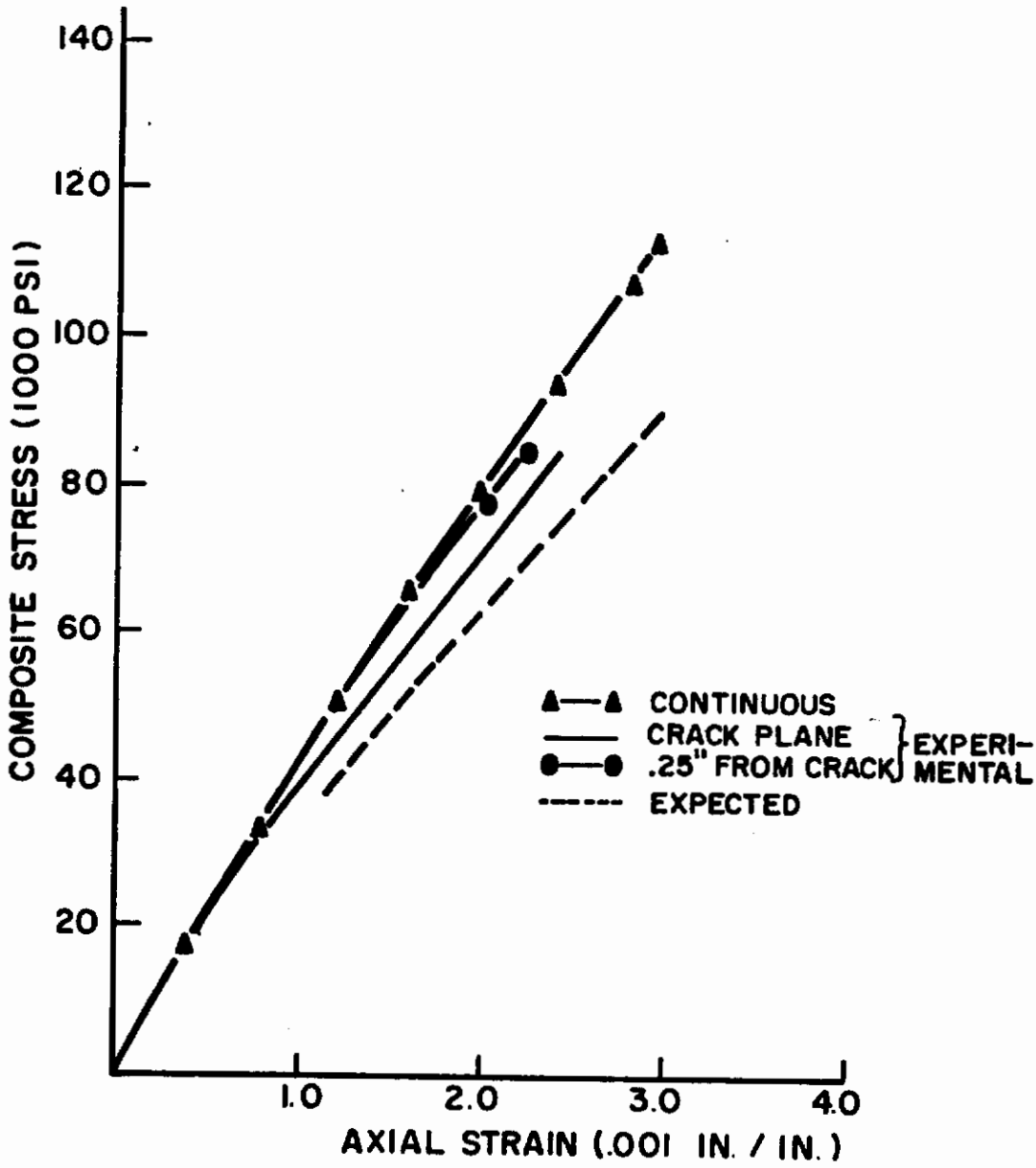

Figure 152

Experimental Stress-Strain Curves for 19 Wire 50 mil Diameter Tungsten-Copper Matrix Composites with a Single Discontinuous Fiber, at Various Locations on the Composites. The Curves for Continuous Fiber Composites and the Expected Behavior Based on the Crack Plane Volume Fraction are Shown for Comparison.

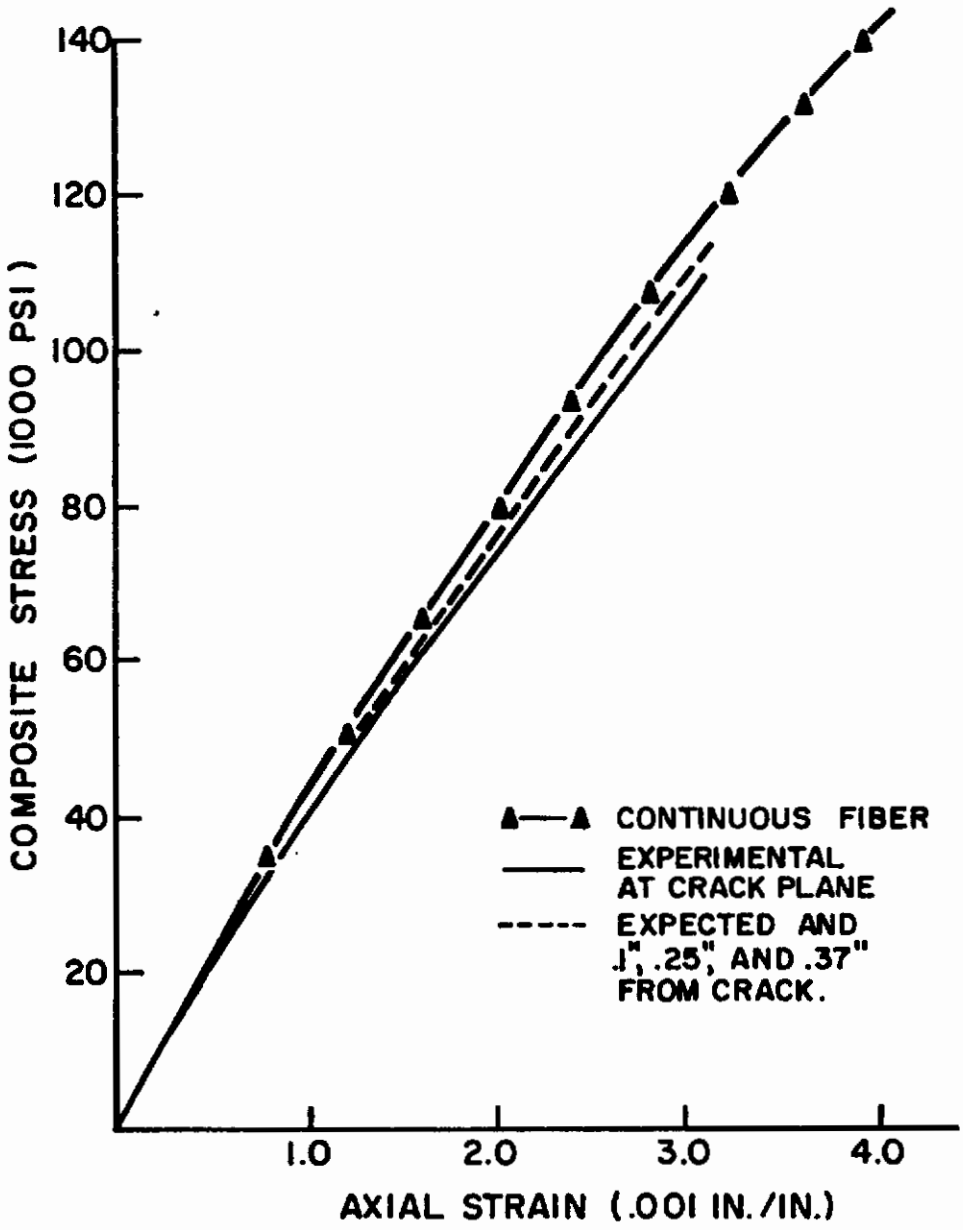

Figure 153

Experimental Stress-Strain Curves for a 19 Wire 50 mil Diameter Tungsten-Copper Composites with Three Discontinuous Fibers Located in the Same Cross Sectional Plane.

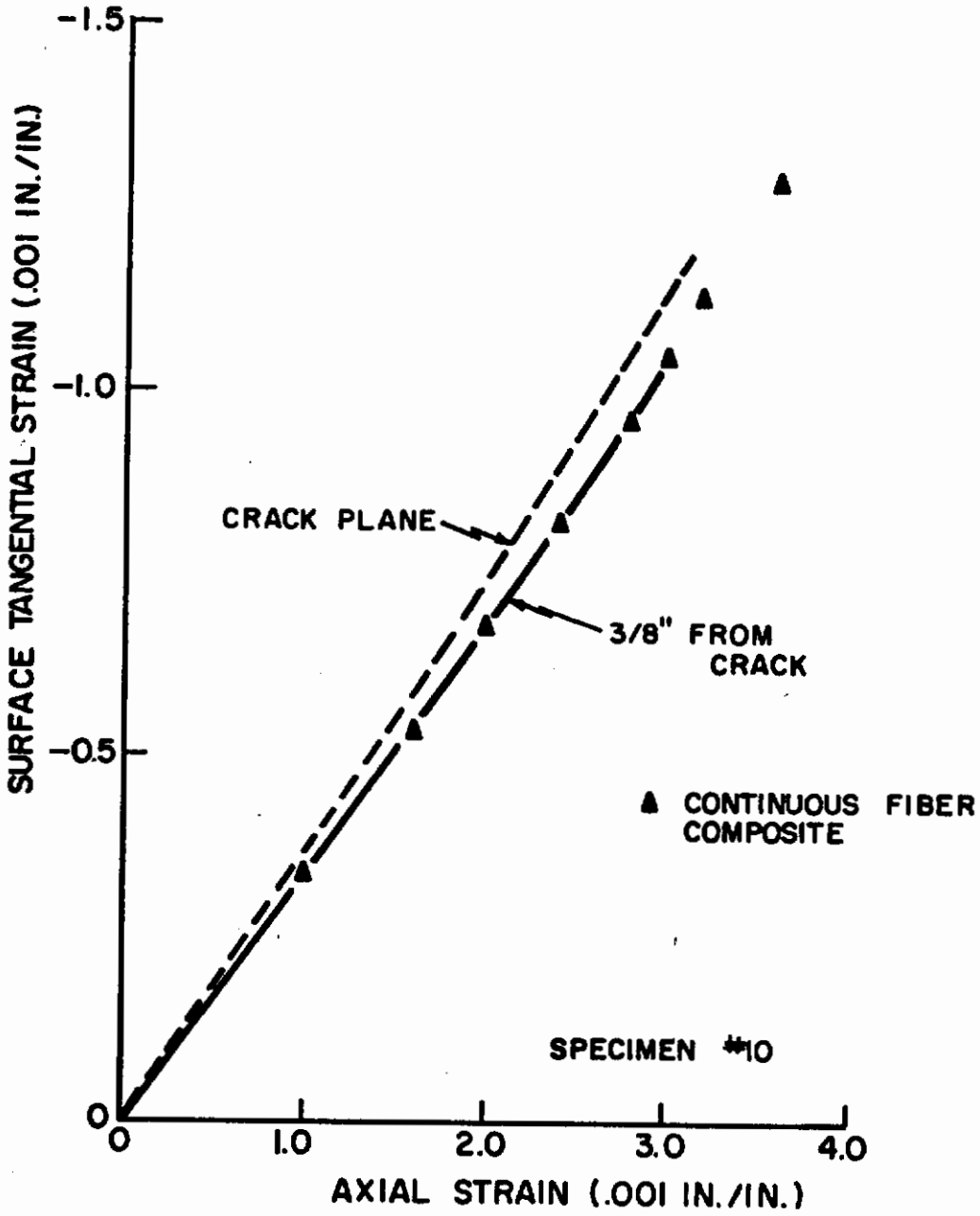

Figure 154

Experimental Stress-Strain Curves for a 19 wire 50 mil Diameter Tungsten-Copper Composites with Four Discontinuous Fibers Located in the Same Cross Sectional Plane.

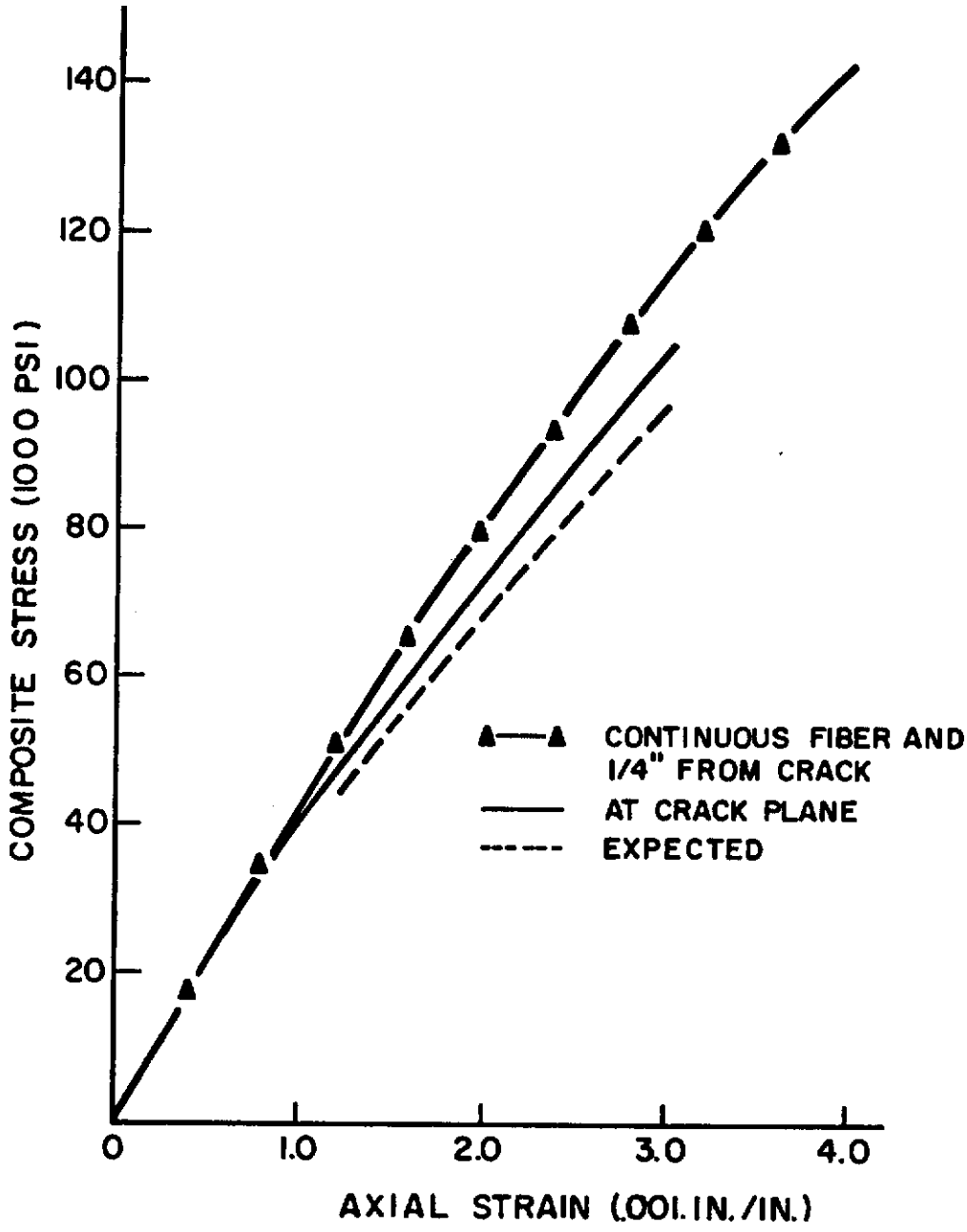

Figure 155

Experimental Curves of Tangential Surface Strain vs. Axial Strain for a 19 wire 50 mil Diameter Tungsten-Copper Composite with one Discontinuous Fiber, and for a Continuous Fiber Composite.

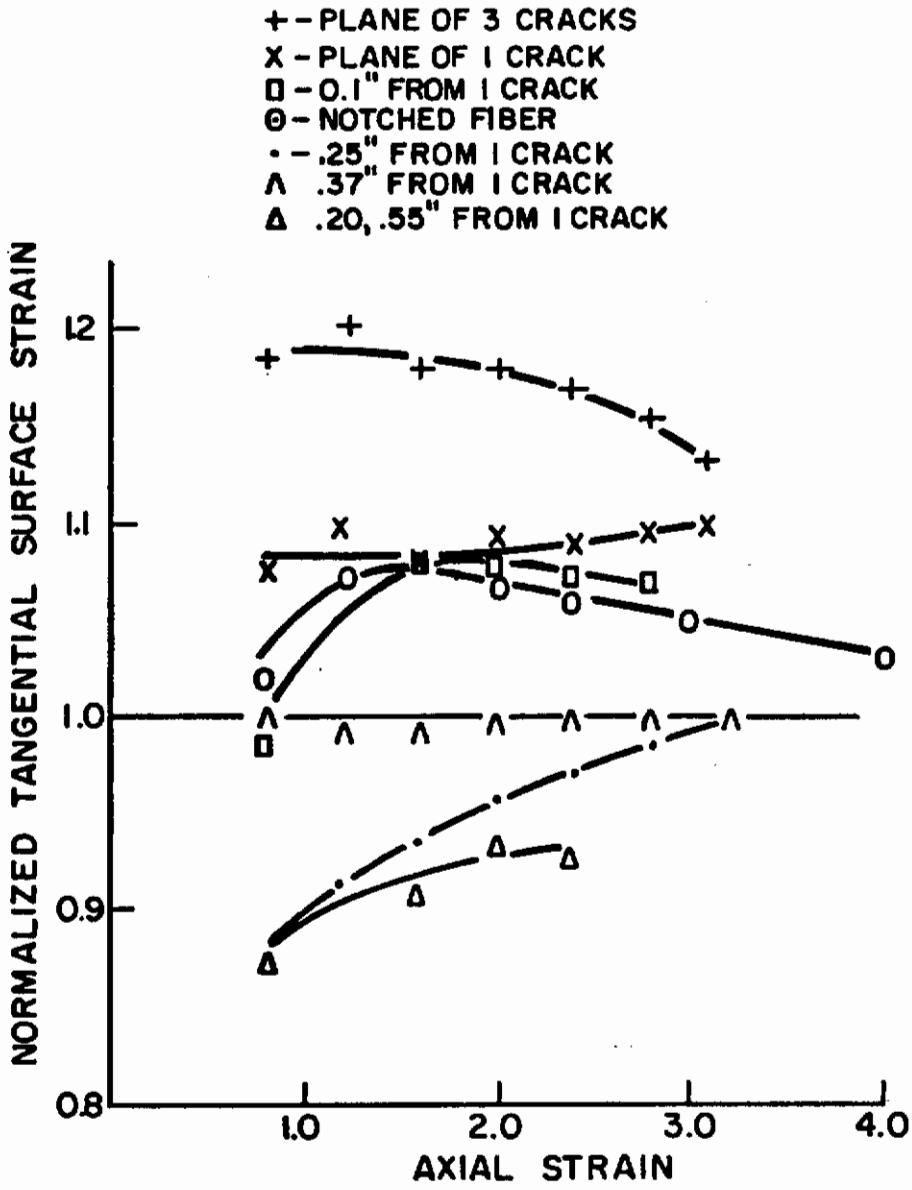

Figure 156

Experimental Curves of Tangential Surface Strain Normalized against Tangential Surface Strain in a 19 Wire Continuous Composite vs. Axial Strain for 19 Wire Tungsten-Copper Discontinuous Fiber Composites of Various Configurations.

APPENDIX I

COMPARISON OF NEW STRESS-STRAIN RELATIONS TO THE PRANDTL-REUSS RELATIONS

In this appendix a comparison is made between the stress-strain relations postulated in this investigation (equation(1)) and Prandtl-Reuss relations of the flow theory.

The Prandtl-Reuss relations in their entirety, in the expanded engineering notation, will be presented first. The plastic strain increment is given by equation (A1) in tensor notation

$$d\epsilon_{ij}^{p} = \frac{3}{2} \frac{d\bar{\epsilon}^{p}}{\bar{\sigma}} S_{ij} \qquad (A1)$$

and the elastic strain increment by Hooke's law

$$d\epsilon_{ij}^{e} = \frac{1+\nu}{E} d\sigma_{ij} - \delta_{ij} \frac{\nu}{E} d\theta \qquad (A2)$$

from the postulate of the separation of total strain into elastic and plastic components the total increment is determined as,

$$d\epsilon_{ij} = \frac{3}{2} \frac{d\epsilon_{ij}^{p}}{\bar{\sigma}} S_{ij} + \frac{1+\nu}{E} d\sigma_{ij} - \delta_{ij} \frac{\nu}{E} d\theta \qquad (A3)$$

To gain physical insight to these relations, they will be written in the expanded form in principal coordinates

$$\begin{aligned}
d\epsilon_1 &= \frac{d\bar{\epsilon}^{p}}{\bar{\sigma}} [\sigma_1 - 1/2(\sigma_2+\sigma_3)] + \frac{1}{E}[d\sigma_1 - \nu(d\theta + d\theta)] \\
d\epsilon_2 &= \frac{d\bar{\epsilon}^{p}}{\bar{\sigma}} [\sigma_2 - 1/2(\sigma_1+\sigma_3)] + \frac{1}{E}[d\sigma_2 - \nu(d\sigma_1 + d\sigma_3)] \\
d\epsilon_3 &= \frac{d\bar{\epsilon}^{p}}{\bar{\sigma}} [\sigma_3 - 1/2(\sigma_1+\sigma_2)] + \frac{1}{E}[d\sigma_3 - \nu(d\sigma_1 + d\sigma_2)]
\end{aligned} \qquad (A4)$$

The first term on the right hand side of equation (A4) denotes the plastic strain increment. It is a function of the current state of stress, not of the stress increment. The second term represents the elastic strain increments. The terms $d\bar{\epsilon}^p$ and $\bar{\sigma}$ are defined in the text by equations (2) and (4) respectively. Figure 157(a) represents the graphical interpretation of the quantity $(\bar{\sigma}/d\bar{\epsilon}^p)$ from the effective stress-plastic strain curve. It is seen to be equal to the term P''. Equation (A4) can therefore be written as

$$d\epsilon_1 = \frac{1}{P''}\left[\sigma_1 - 1/2(\sigma_2+\sigma_3)\right] + \frac{1}{E}\left[d\sigma_1 - \nu(d\sigma_2+d\sigma_3)\right] \quad (A5)$$

with $d\epsilon_2$ and $d\epsilon_3$ given by the suitable permutation of the subscripts 1, 2, and 3.

The stress-strain relations postulated in this study (equation (1)) give the following relation for the total strain increments:

$$\begin{aligned} d\epsilon_1 &= \frac{1}{P}\left[d\sigma_1 - m(d\sigma_2+d\sigma_3)\right] \\ d\epsilon_2 &= \frac{1}{P}\left[d\sigma_2 - m(d\sigma_1+d\sigma_3)\right] \\ d\epsilon_3 &= \frac{1}{P}\left[d\sigma_3 - m(d\sigma_1+d\sigma_2)\right] \end{aligned} \quad (A6)$$

P is represented in Figure 157 (b) and is seen to be equal to $(d\bar{\sigma}/d\bar{\epsilon})$. In the present stress-strain relations, the split of the elastic and plastic strain increment is contained in the definition of m (Reference [1]). If this equation is substituted into the above stress-strain relations, the total strain increments can be split into their elastic and plastic parts by the following mathematical development:

$$d\epsilon_1 = \frac{1}{P}\left[d\sigma_1 - m(d\sigma_2+d\sigma_3)\right] \quad (A7)$$

$$P = \frac{d\bar{\sigma}}{d\bar{\epsilon}} \quad (A8)$$

$$m = \nu\frac{d\bar{\epsilon}^e}{d\bar{\epsilon}} + 1/2\,\frac{d\bar{\epsilon}^p}{d\bar{\epsilon}} \quad (A9)$$

Substituting P and m into $d\epsilon_1$, results in

$$d\epsilon_1 = \frac{d\bar{\epsilon}}{d\bar{\sigma}} \left[d\sigma_1 - (d\sigma_2 + d\sigma_3)\nu \frac{d\bar{\epsilon}^e}{d\bar{\epsilon}} - (d\sigma_2 + d\sigma_3)\, 1/2 \frac{d\bar{\epsilon}^p}{d\bar{\epsilon}} \right] \quad (A10)$$

But

$$d\bar{\epsilon} = d\bar{\epsilon}^e + d\bar{\epsilon}^p$$

and equation (A10)

becomes

$$d\epsilon_1 = \frac{d\bar{\epsilon}^p}{d\bar{\sigma}} \left[d\sigma_1 - 1/2(d\sigma_2 + d\sigma_3) \right] + \frac{d\bar{\epsilon}^e}{d\bar{\sigma}} \left[d\sigma_1 - \nu(d\sigma_2 + d\sigma_3) \right] \quad (A11)$$

From Figure 97(b)

$$\frac{d\bar{\sigma}}{d\bar{\epsilon}^p} = p' \qquad \frac{d\bar{\sigma}}{d\bar{\epsilon}^e} = E$$

$$\frac{p'}{p''} = \frac{d\bar{\sigma}}{\bar{\sigma}}$$

Hence equation (A11) becomes

$$d\epsilon_1 = \frac{1}{E} \left[d\sigma_1 - \nu(d\sigma_2 + d\sigma_3) \right] + \frac{1}{p''} \frac{\bar{\sigma}}{d\bar{\sigma}} \left[d\sigma_1 - 1/2(d\sigma_2 + d\sigma_3) \right] \quad (A12)$$

where the first term on the right hand side corresponds to the elastic strain increment and the second term to the plastic strain increment.

It is apparent that these stress-strain relations predict that both the elastic and the plastic strain increments are functions of the stress increment. This prediction is unlike that of the Prandtl-Reuss relations (equation (A5)).

In examining the differences between the Prandtl-Reuss relations and the presently developed relations, it is necessary to compare only the plastic strain increments since it is apparent from equations (A5) and (A11) that the elastic strain increments are identical. At this point, it is once again convenient to resort to the short-hand tensor notation. The plastic strain increment of the Prandtl-Reuss relations can be written as

$$d\epsilon^{p}_{ij}{}_{P-R} = \frac{3}{2}\ \frac{1}{p''}\ S_{ij}$$

$$d\epsilon_{ij}{}_{P-R} = \frac{3}{2}\ \frac{d\bar{\epsilon}^{p}}{\bar{\sigma}}\ S_{ij} \quad \text{or} \tag{A13}$$

The subscript P-R refers to Prandtl-Reuss. The presently predicted plastic strain increment (denoted by the subscript *) can be written as

$$d\epsilon^{p}_{ij}{}_{*} = \frac{3}{2}\ \frac{1}{p''}\ \frac{\bar{\sigma}}{d\bar{\sigma}}\ dS_{ij}$$

$$\text{or} \tag{A14}$$

$$d\epsilon^{p}_{ij}{}_{*} = \frac{3}{2}\ \frac{d\bar{\epsilon}^{p}}{d\bar{\sigma}}\ dS_{ij}$$

It is immediately apparent that equation (A13) and (A14) can predict the same plastic strain increment only when the tensors S_{ij} and dS_{ij} are coaxial. This condition, in terms of the geometrical π -plane representation [3, 5], restricts the possibility for coincidence to radial or porportional loading only.

In the special case of proportional loading, the development below will show that the predictions of the two equations are indeed identical. For proportional loading all the stresses increase in constant ratio, and therefore

$$\sigma_{ij} = K'\,\sigma^{\circ}_{ij} \tag{A15}$$

where σ°_{ij} is the initial stress state and K' is a monotonically increasing function of time.

$$S^{\circ}_{ij} = \sigma^{\circ}_{ij} - \frac{1}{3}\ \delta_{ij}\ \sigma^{\circ}_{KK} \tag{A16}$$

$$S_{ij} = \sigma_{ij} - \frac{1}{3}\ \delta_{ij}\sigma_{KK} = K'\sigma^{\circ}_{ij} - \frac{1}{3}\ \delta_{ij}\ K'\sigma^{\circ}_{KK} = K'\ S^{\circ}_{ij}$$

$$\bar{\sigma} = \left(\frac{3}{2} S_{ij}\ S_{ij}\right)^{1/2} = K' \left(\frac{3}{2} S^{\circ}_{ij}\ S^{\circ}_{ij}\right)^{1/2} = K'\ \bar{\sigma}^{\circ} \tag{A17}$$

$$d\,S_{ij} = S_{ij} - S^{\circ}_{ij}$$

$$d\,S_{ij} = K' S^{\circ}_{ij} - S^{\circ}_{ij} = S^{\circ}_{ij}\ (K'-1) \tag{A18}$$

$$d\,\bar{\sigma} = \left(\frac{3}{2}\, dS_{ij}\ \ dS_{ij}\right)^{1/2} = \left(\frac{3}{2} (K'-1)^2\ S^{\circ}_{ij}\ \ S^{\circ}_{ij}\right)^{1/2} = (K'-1)\,\bar{\sigma}^{\circ} \tag{A19}$$

Substituting euqations (A16-19) into equations (A13) and A14) leads to

$$d\epsilon^{p}_{ij}{}_{P-R} = \frac{3}{2}\ d\bar{\epsilon}^{p}\ \frac{K' S^{\circ}_{ij}}{K'\bar{\sigma}^{\circ}}$$

$$d\epsilon^{p}_{ij}{}_{P-R} = \frac{3}{2}\ d\bar{\epsilon}^{p}\ \frac{S^{\circ}_{ij}}{\bar{\sigma}^{\circ}} \tag{A20}$$

and

$$d\epsilon^{p}_{ij}{}_{*} = \frac{3}{2}\ d\bar{\epsilon}^{p}\ \frac{(K'-1)\,S_{ij}}{(K'-1)\,\bar{\sigma}^{\circ}}$$

$$d\epsilon^{p}_{ij}{}_{*} = \frac{3}{2}\ d\bar{\epsilon}^{p}\ \frac{S^{\circ}_{ij}}{\bar{\sigma}^{\circ}} \tag{A21}$$

Therefore, in the case of proportional loading, equations (A13) and (A14) become equivalent and the stress-strain relations of equations (A1) and (1), referring to the Prandtl-Reuss relations and the newly postulated relations, become indentical. In the case of general loading where the tensors S_{ij} and dS_{ij} are not coincident,

the plastic strain increment of equation (A14) will not be normal to the yield surface as in the case for equation (A13) [3] and equation (A12) will predict somewhat larger total strains than equation (A9).

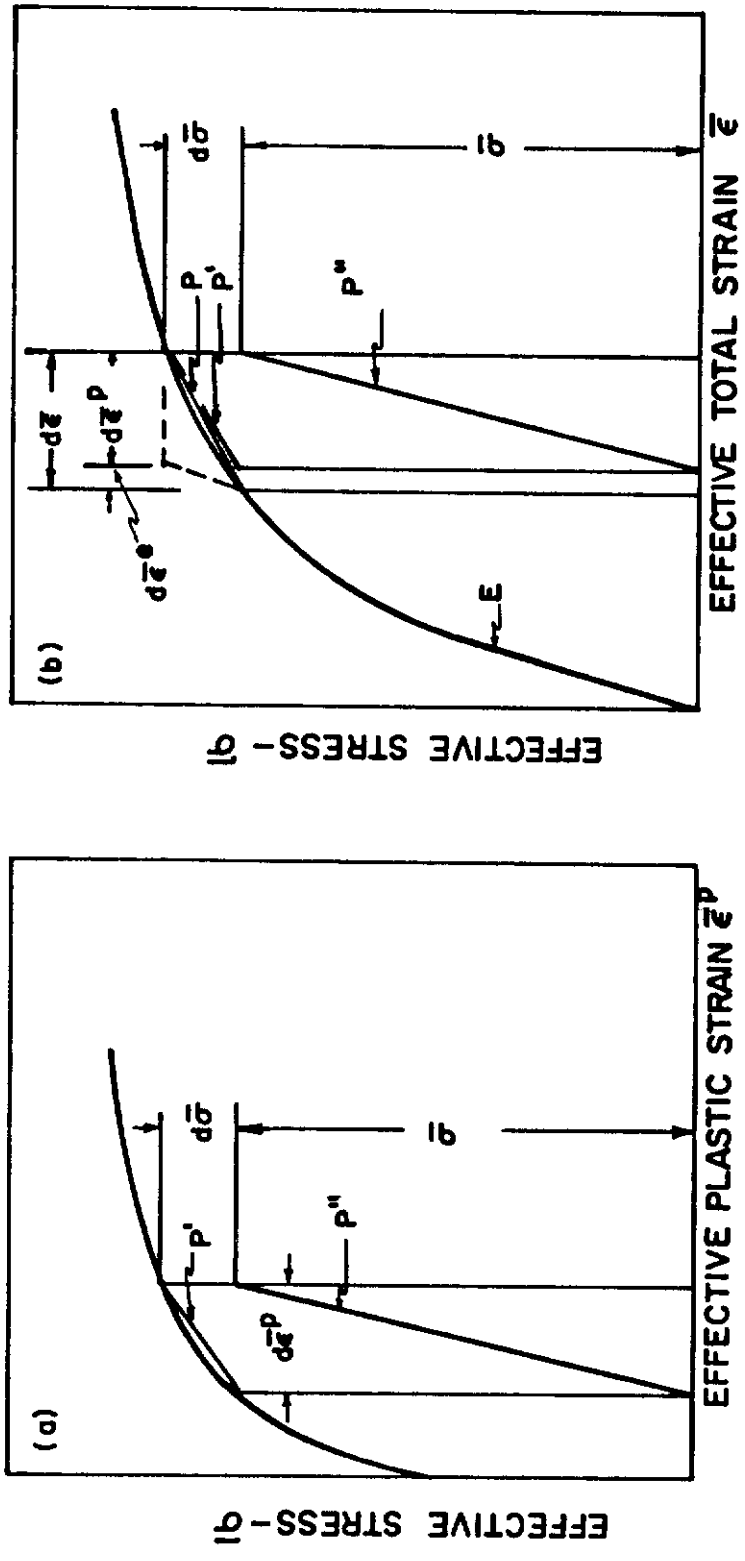

Figure 157

Comparison of Effective Stress-Plastic Strain Curve to Effective Stress-Total Strain Curve.

APPENDIX II

ELASTICITY SOLUTION OF AN "N"-RING COMPOSITE CYLINDER UNDER AXIAL LOAD

A general elasticity solution to a problem is a necessary prerequisite for the plasticity analysis developed in the text. In this appendix, a rigorous elasticity solution to a composite cylinder subjected to axial loads is developed. Figure 158 graphically represents the "N" ring composite cylinder under investigation.

The solution will be achieved subject to the following assumptions:

1. The cylinder is infinitely long - no end-effects
2. The axial strain is uniform across the composite cross-section - plane sections remain plane
3. The individual components are perfectly bonded at the interface
4. There are no body forces acting on this system

Solution of the problem will be achieved in cylindrical (polar) coordinates because of the axial symmetry of the problem. The most direct method of solution for this type of problem is that of expressing the equilibrium of forces equations in terms of the displacements and then solving the resulting differential equation with regard to the boundary conditions of the problem.

The equilibrium of forces equations for this problem reduce from their general form of

$$\sigma_{ij,j} = 0$$

to

$$\frac{d\sigma_r}{dr} + \frac{\sigma_r - \sigma_t}{r} = 0 \qquad \text{(A22)}$$

Compatibility can be satisfied by expressing the strains in terms of the displacements rather than vice versa. In the present situation, the tangential displacement and all the shear strains are equal to zero because of the axial symmetry. The three normal (and in this case, principal) strains can be expressed in terms of the radial and axial displacements, u and w, as follows:

$$\epsilon_z = \frac{dw}{dz} = \text{CONSTANT}$$
$$\epsilon_r = \frac{du}{dr} \qquad (A23)$$
$$\epsilon_t = \frac{u}{r}$$

Expressing Hooke's law in terms of stresses

$$\sigma_{ij} = \frac{E}{1+\nu}\,\epsilon_{ij} + \delta_{ij}\,\nu K \epsilon_{KK} \qquad (A24)$$

where

$$K = \frac{E}{(1+\nu)(1-2\nu)} \qquad (A25)$$

and substituting into the equilibrium equation (A22) results in the following differential equation

$$\frac{d^2u}{dr^2} + \frac{1}{r}\frac{du}{dr} - \frac{u}{r^2} = 0 \qquad (A26)$$

which can be solved for the radial displacement to give

$$u = C_1 r + \frac{C_2}{r} \qquad (A27)$$

Note that the three dimensional problem of elasticity has been reduced to a one dimensional (one variable) differential equation. This simplification is a direct result of the axial symmetry of the problem and the fact that the axial strain, ϵ_z, is assumed to be constant both across the composite cross section and along the composite length.

Equation (A27) for the radial displacement applies to all individual components of the composite cylinder. It can be expressed in general as

$$u_i = C_1^i r + \frac{C_2^i}{r} \qquad \text{(A28)}$$

where "i" refers to the particular components as graphically illustrated in Figure 158.

Solution of the problem now rests upon the determination of the constants C_1^i and C_2^i by the application of the available boundary conditions. It is apparent that two boundary conditions are required for each component. The necessary boundary conditions can be derived from the following requirements:

1. Compatibility requires that the displacements at all the component interfaces be continuous.

2. Equilibrium of forces requires that the radial stresses across all the component interfaces be continuous

3. Physical reasoning requires that all displacements be finite.

The first requirement results in the following sets of equations:

$$U_i = U_{i+1} \quad \text{AT} \quad r_i$$

$$C_1^i r_i + \frac{C_2^i}{r_i} = C_1^{i+1} r_i + \frac{C_2^{i+1}}{r_i} \qquad \text{FOR } i = 0,1,\ldots N-1 \qquad \text{(A29)}$$

where N is the number of rings in the composite case and the r_i's are defined in Figure 158. Hence requirement number one results in N equations.

The second requirement results in the following sets of equations:

$$\sigma_r^i = \sigma_r^{i+1} \qquad \text{at } r_i \text{ for } i=0, 1,\ldots\ldots N \qquad \text{(A30)}$$

where σ_r^{N+1} at r_N is the radial stress outside the composite cylinder, which must be zero since the composite lateral surface is free of any constraints. These equations are meaningless unless σ_r^i are expressed in terms of the constants C_1^i and C_2^i.

In the initial solution, it was necessary to express the stresses in terms of the radial displacement. These relations were not given at the time but they will be stated now without derivation. Substitution of equation (A23) into (A24) leads to the following relations:

$$\begin{aligned}
\sigma_r &= K\left[\nu \frac{du}{dr} + (1-\nu)\frac{u}{r} + \nu\epsilon_z\right] \\
\sigma_t &= K\left[(1-\nu)\frac{du}{dr} + \nu\frac{u}{r} + \nu\epsilon_z\right] \\
\sigma_z &= K\left[\nu \frac{du}{dr} + \nu\frac{u}{r} + (1-\nu)\epsilon_z\right]
\end{aligned} \tag{A31}$$

Substitution of equation (A27) and (A23) results in the following expressions for the entire stress and strain distribution in each component:

$$\begin{aligned}
\sigma_r &= K\left[C_1 - \frac{C_2}{r^2}(1-2\nu) + \nu\epsilon_z\right] \\
\sigma_t &= K\left[C_1 + \frac{C_2}{r^2}(1-2\nu) + \nu\epsilon_z\right] \\
\sigma_z &= K\left[2\nu C_1 + (1-\nu)\epsilon_z\right] \\
\epsilon_r &= C_1 - \frac{C_2}{r^2} \\
\epsilon_t &= C_1 + \frac{C_2}{r^2}
\end{aligned} \tag{A32}$$

Substitution of σ_r of equation (A32) into the boundary condition equation (A30), taking into consideration the stresses in each individual element, results in

$$K_i C_1^i - K_{i+1}^{i+1} C_1^{i+1} - \frac{1}{r_1^2}\left[K_i(1-2\nu_i) C_2^i - K_{i+1} (1-2\nu_{i+1}) C_2^{i+1}\right] =$$

$$(K_{i+1} \nu_{i+1} - K_i \nu_i) \epsilon_z \qquad \text{for } i=0,1,\ldots.N \qquad \text{(A33)}$$

Equation (A33) represents a set of N+1 equations.

Consideration of the third requirement for boundary conditions results in one additional equation

$$C_2^o = 0 \qquad \text{(A34)}$$

A look at equation (A28) will show that this is a necessary condition to avoid a singularity at the origin of the cylinder. From a physical viewpoint it is necessary to avoid an infinite displacement at the origin.

It is interesting to note that condition (A34) forces all stresses and strains in the inner member (core) to be constant with radius (and in particular $\sigma_r{}^o = \sigma_t{}^o$) for any loading conditions. A result of this fact which utilized in the text is that the core will always experience proportional loading, no matter what the loading conditions are.

The combination of equations (A29), and (A33), and (A34) can be seen to constitute a set of 2N+2 equations with 2N+2 unknowns. Solution of the complete elasticity problem can hence be achieved by solving this set of equations simultaneously and substituting the resulting answers for the constants into equation (A32) for each individual component of the composite.

For computational convenience the unknown constants $C_1{}^i$ and $C_2{}^i$ will be replaced by the following notation:

$$C_1^i = C_{2i+1}$$

and

$$C_2^i = C_{2i+2}$$

If this substitution is made in equations (A29,33,34) they can be arranged in the following manner:

$$\begin{aligned}
&a_{11}\,C_1 + a_{12}C_2 + \cdots + a_{1,2N+2}\,C_{2N+2} = b_1 \\
&a_{21}\,C_1 + a_{22}C_2 + \cdots + a_{2,2N+2}\,C_{2N+2} = b_2 \\
&\vdots \qquad\qquad\qquad\qquad\qquad\qquad\qquad\qquad\qquad\qquad\qquad\qquad \vdots \qquad (A35) \\
&a_{2N+2,1}\,C_1 + \cdots + a_{2N+2,2N+2}\,C_{2N+2} = b_{2N+2}
\end{aligned}$$

where the a_{ij} are the appropriate coefficients of the unknown constants and the b_i are the collection of all terms which do not include any constants.

This system of equations can be written in matrix form as follows:

$$[C]\ [A] = [B]$$

where

$$[C] = \begin{bmatrix} C_1 \\ C_2 \\ \vdots \\ C_{2N+2} \end{bmatrix} \qquad [B] = \begin{bmatrix} b_1 \\ b_2 \\ \vdots \\ b_{2N+2} \end{bmatrix}$$

and

$$[A] = \begin{bmatrix} a_{11} & a_{12} & \cdots & a_{1,2N+2} \\ a_{21} & a_{22} & \cdots & a_{2,2N+2} \\ \vdots & & & \vdots \\ a_{2N+2,1} & a_{2N+2,2} & \cdots & a_{2N+2,2N+2} \end{bmatrix}$$

Matrices [A] and [B] are known from equations (A29, 33, 34) in terms of property constants and geometrical terms. Matrix [C] is the matrix of unknown coefficients. The method of Gaussian elimination [18] is now employed to solve for the matrix [C]. This is accomplished by the use of a computer programmed Gaussian elimination method. The answers, of course, are numerical. They have to be substituted into equation (A32) to define the entire stress and strain distribution in the composite upon axial loading.

To provide some physical insight to the character of the solution, a sample of the matrices [A] and [B] for a composite of 4 rings in the case material is presented in Table 9.

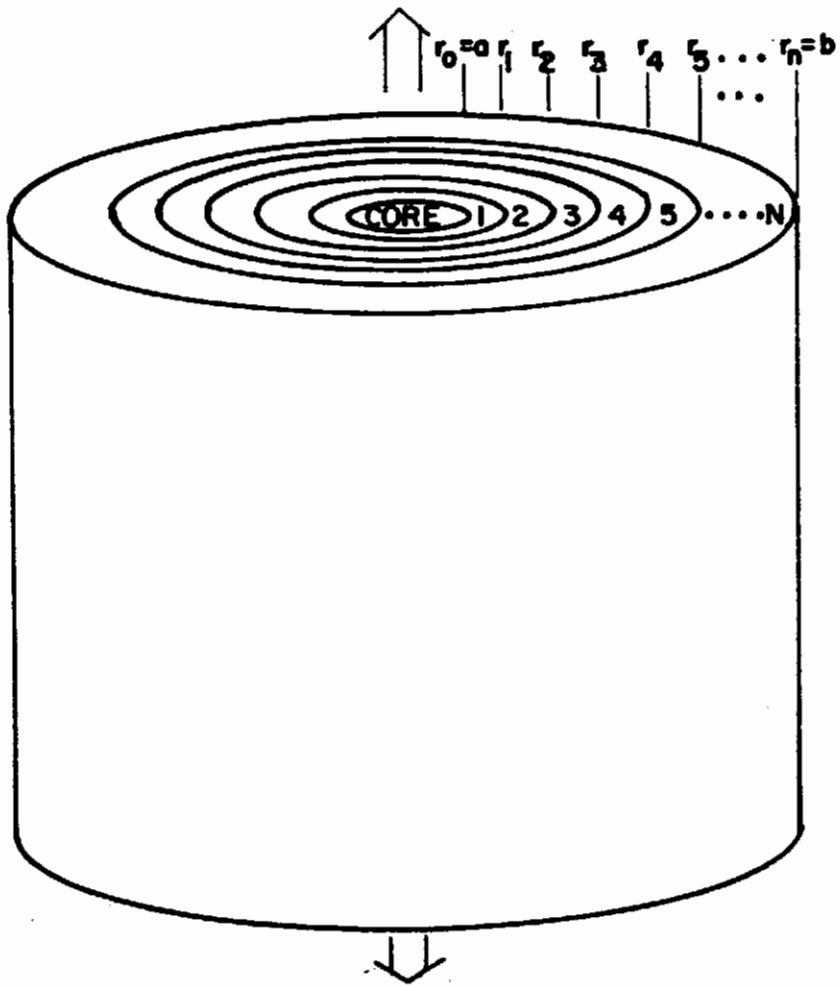

Figure 158

Composite Cylinder Consisting of a Core and "N" Rings in the Case (The Load is Applied Uniformly Across the Composite Cross Section).

[A]										[B]
0	1	0	0	0	0	0	0	0	0	0
r_0	0	$-r_0$	r_0^{-1}	0	0	0	0	0	0	0
0	0	r_1	r_1^{-1}	$-r_1$	$-r_1^{-1}$	0	0	0	0	0
0	0	0	0	r_2	r_2^{-1}	$-r_2$	$-r_2^{-1}$	0	0	0
0	0	0	0	0	0	r_3	r_3^{-1}	$-r_3$	$-r_3^{-1}$	0
K_0	0	$-K_1$	$\frac{K_1(1-2\nu_1)}{r_0^2}$	0	0	0	0	0	0	$\epsilon_z(K_1\nu_1-K_0\nu_0)$
0	0	K_1	$\frac{-K_1(1-2\nu_1)}{r_1^2}$	$-K_2$	$\frac{K_2(1-2\nu_2)}{r_1^2}$	0	0	0	0	$\epsilon_z(K_2\nu_2-K_1\nu_1)$
0	0	0	0	K_2	$\frac{-K_2(1-2\nu_2)}{r_2^2}$	$-K_3$	$\frac{K_3(1-2\nu_3)}{r_2^2}$	0	0	$\epsilon_z(K_3\nu_3-K_2\nu_2)$
0	0	0	0	0	0	K_3	$\frac{-K_3(1-2\nu_3)}{r_3^2}$	$-K_4$	$\frac{K_4(1-2\nu_4)}{r_3^2}$	$\epsilon_z(K_4\nu_4-K_3\nu_3)$
0	0	0	0	0	0	0	0	K_4	$\frac{-K_4(1-2\nu_4)}{r_4^2}$	$-K_4\nu_4\epsilon_z$

TABLE 9

Coefficient Matrices for the Elasticity Solution of a Composite Cylinder in Axial Tension (N=4)

APPENDIX III

DETERMINATION OF RESIDUAL STRESSES FROM MEASURED STRAINS

In this appendix, a method for determining the residual stress distributions in as-fabricated composite cylinders from the measured strain data of the drilling-out operation is developed.

In a manner analagous to that used by Sachs (20), the initially present residual stresses (σ_{ij}) will be determined from the calculation of the stresses removed during the drilling operation (σ_{ij}') and the stresses remaining after the drilling operation (σ_{ij}''). The stresses initially present can then be designated as

$$\sigma_{ij} = \sigma_{ij}' + \sigma_{ij}'' \tag{A40}$$

In the section on composite fabrication in the text, it was shown that the residual stresses originate only as a result of the difference in thermal expansion coefficients between the components. The drilling-out of composite discs and the splitting of the steel shell remaining after the removal of the copper core demonstrated that there are no stresses remaining in the case after the removal of the core, hence,

$$\sigma_{ij}'' = 0 \tag{A41}$$

The initial stress distribution is determined by the calculation of the stresses removed during the drilling-out of the copper core. Only the strains measured after the entire removal of the core will be utilized in this development.

Consider first the axial stress removed during drilling. The effect of the removal of the axial stress in the core material can be calculated by determining its effect on the stress at the outside surface (radius b). If the previous assumption of infinite composite length is made, the stress change due to the removal of the core will be uniformly distributed over the remaining cross section (the case). Hence, the removed stress can be related to the stress at the outside surface by

$$\sigma_z' = -\sigma_z^* \tag{A42}$$

The negative sign is required because σ_z^* is a stress change causing

the measured strain changes, while σ_z' is an amount of stress removed by the drilling-out operation.

The stress changes at the outside surface can be related to the measured surface strains ϵ_z and ϵ_t by applying Hooke's law with

$$\sigma_z^* = \frac{E}{(1-\nu^2)} (\epsilon_z + \nu \epsilon_t) \tag{A43}$$

$$\sigma_t^* = \frac{E}{(1-\nu^2)} (\epsilon_t + \nu \epsilon_z) \tag{A44}$$

Substituting (A43) into (A42) gives the axial stress at any point in the case relieved by the drilling as

$$\sigma_z' = -\frac{E}{(1-\nu^2)} (\epsilon_z + \nu \epsilon_t) \tag{A45}$$

The same kind of procedure can be used to find σ_t', i.e., the effect at radius b due to drilling-out the core (radius a) is noted. Before drilling, the case has a radial tension (tension is chosen by convention) at the interface. After drilling, the interface becomes a free surface and the radial stress becomes equal to zero. Removing this tensile stress by drilling has the same effect as imposing an internal pressure on the case at radius a. The tangential stress anywhere in the case material is given by the standard Lame-solution for pressurized thick-walled cylinders (21):

$$\sigma_t' = \frac{Pa^2}{b^2-a^2} \left(1 + \frac{b^2}{r^2}\right) \tag{A46}$$

where p is the effective internal pressure.

The tangential stress at the outside surface (r=b) is then given by

$$\sigma_t^* = 2 \frac{Pa^2}{b^2-a^2} \tag{A47}$$

and hence

$$\sigma_t' = 1/2 \left(1+\frac{b^2}{r^2}\right)\sigma_t^* \tag{A48}$$

Substituting equation (A44) for σ_t^* and changing sign for the same reason as in equation (A42) results in the follwing expression:

$$\sigma_t' = -1/2 \left(1+\frac{b^2}{r^2}\right)\left(\frac{E}{1-\nu^2}\right)\left(\epsilon_t + \nu\epsilon_z\right) \tag{A49}$$

The radial stress σ_r' is determined in the same way as σ_t'. Applying the radial stress equation of the Lame-solution results in

$$\sigma_r' = \frac{Pa^2}{(b^2-a^2)}\left(1-\frac{b^2}{r^2}\right) \tag{A50}$$

The radial stress can be related to the tangential stress at the surface by substituting equation (A47) into (A50)

$$\sigma_r' = \frac{r^2-b^2}{2r^2}\sigma_t^* \tag{A51}$$

Substitution of equation (A44) into (A51) and changing sign results in

$$\sigma_r' = -\frac{r^2-b^2}{2r^2}\left(\frac{E}{1-\nu^2}\right)\left(\epsilon_t + \nu\epsilon_z\right) \tag{A52}$$

Equation (A45), (A49), and (A52) completely determine the residual stresses relieved in the case material by the drilling out of the core. From equations (A40) and (A41) it is apparent that the above equations also represent the residual stresses initially present in the case. To determine the residual stresses initially present in the core, use must be made of the boundary conditions which govern all composite cylinder behavior.

First, consideration of the continuity of the radial stress across the case-core interface results in the determination of the transverse stresses in the core. In Appendix II the radial and tangential stresses in the core were shown to be equal in the core for any type of loading. Both of the stresses therefore are equal to the radial stress in the case at radius a. From equation (A52) substitution of a for r results in

$$\sigma_r^{CORE} = \sigma_t^{CASE} = -\left(\frac{a^2-b^2}{2a^2}\right)\left(\frac{E}{1-\nu^2}\right)(\epsilon_t + \nu\epsilon_z) \qquad (A53)$$

The axial stress in the core can be determined from the condition of equilibrium of forces in the axial direction. After fabrication there is no resultant force in the axial direction, hence

$$A_c\,\sigma_z^{CORE} + A_s\,\sigma_z^{CASE} = 0$$

where A_c and A_s are the area fractions of the core and case respectively. Substituting equation (A45) for σ_z^{case} and the appropriate relations for A_c and A_s results in the following expression for the axial stress in the core:

$$\sigma_z^{CORE} = -\left(\frac{b^2-a^2}{a^2}\right)\sigma_z^{CASE}$$

$$\sigma_z^{CORE} = \left(\frac{b^2-a^2}{a^2}\right)\left(\frac{E}{1-\nu^2}\right)(\epsilon_z + \nu\epsilon_t) \qquad (A54)$$

Equation (A53-54)) along with equations (A45), (A49), and (A52) determine the entire residual stress distribution existing in the as-fabricated and machined composite tensile specimen. A numerical evaluation of these stresses is dependent only upon the pertinent geometric and elastic properties of the composite, the dimensions of the composite, and the measured surface strains from the drilling-out operation.

APPENDIX IV

ELASTICITY SOLUTION OF AN "N"-RING COMPOSITE CYLINDER UNDER THERMAL LOADING

The solution to this problem will be achieved in a manner similar to that of Appendix II which treated the same problem for axial loading. Much of the formalism is the same with the following exceptions:

1. The stress-strain relations must include a thermal strain term

2. The axial strain is no longer a known quantity but instead becomes an additional unknown

The same assumptions as those stated in Appendix II apply for this problem.

Hooke's law upon the inclusion of thermal strains becomes

$$\epsilon_{ij} = \frac{1+\nu}{E}\sigma_{ij} - \delta_{ij}\left(\frac{\nu}{E}\theta - \alpha T\right) \tag{A55}$$

or expressing stresses in terms of strains

$$\sigma_{ij} = \frac{E}{1+\nu}(\epsilon_{ij} - \delta_{ij}\alpha T) + \delta_{ij}\nu K(\epsilon_{ii} - 3\alpha T) \tag{A56}$$

where

$$K = \frac{E}{(1+\nu)(1-2\nu)} \quad \text{AND} \quad \epsilon_{ii} = \epsilon_r + \epsilon_t + \epsilon_z$$

In the expanded engineering notation equation (A56) becomes

$$\begin{aligned}
\sigma_r &= K[\epsilon_r(1-\nu) + \nu\epsilon_t + \nu\epsilon_z - (1+\nu)\alpha T] \\
\sigma_t &= K[\epsilon_t(1-\nu) + \nu\epsilon_r + \nu\epsilon_z - (1+\nu)\alpha T] \\
\sigma_z &= K[\epsilon_z(1-\nu) + \nu\epsilon_r + \nu\epsilon_t - (1+\nu)\alpha T]
\end{aligned} \tag{A57}$$

where α is the thermal expansion coefficient and T is the temperature above or below some arbitrary reference temperature.

Replacing ϵ_r and ϵ_t by their definition in terms of the radial displacment u (equation (A23)) results in

$$\sigma_r = K\left[(1-\nu)\frac{du}{dr} + \nu\frac{u}{r} + \nu\epsilon_z - (1+\nu)\alpha T\right]$$

$$\sigma_t = K\left[\nu\frac{du}{dr} + (1-\nu)\frac{u}{r} + \nu\epsilon_z - (1+\nu)\alpha T\right] \qquad \text{(A58)}$$

$$\sigma_z = K\left[\nu\frac{du}{dr} + \nu\frac{u}{r} + (1-\nu)\epsilon_z - (1+\nu)\alpha T\right]$$

substitution of equation (A58) into the equilibrium equation of the composite cylinder (equation (A22)) yields the following differential equation:

$$\frac{d^2u}{dr^2} + \frac{1}{r}\frac{du}{dr} - \frac{u}{r^2} = 0 \qquad \text{(A59)}$$

which is identical to the controlling equilibrium equation (A26) for the axial loading case. This result indicates that the difference in the thermal and axial loading problems arises only after the application of the boundary conditions. The solution to equation (A59) is

$$U = C_1 r + \frac{C_2}{r} \qquad \text{(A60)}$$

Equation (A60) applies to all individual components of the composite cylinder and in general it can be expressed as

$$U_i = C_1^i r + \frac{C_2^i}{r} \qquad \text{(A61)}$$

where "i" refers to the particular components graphically illustrated in Figure 158. Solution of the problem again, as in the axial case, rests upon the determination of C_1^i and C_2^i which constitute 2N+2 unknowns for a composite with N rings in the case.

In this problem, however, one additional unknown, namely the axial strain ϵ_z, is present. Consequently, one boundary condition requirement must be added to the three presented in Appendix II (all of which are still applicable). The additional requirement is

a result of the necessity for the equilibrium of forces in the axial direction. Since upon thermal loading, the composite is not restrained in the axial direction, the resultant forces in the composite acting on the cylinder ends must equal to zero. Mathematically this can be expressed as follows:

$$\sum_{i=0}^{N} \int_{r_{i-1}}^{r_i} \sigma_z^i \, r \, dr = 0 \qquad \text{(A62)}$$

where r_{i-1} is defined as zero.

The subsequent development will express all the boundary conditions in terms of the unknown constants C_1^i, C_2^i and ϵ_z. It is apparent that 2N+3 equations must be found to solve these constants.

First, it is necessary to express equation (A58) and (A23) in terms of these constants

$$\begin{aligned}
\sigma_r &= K\left[C_1 - \frac{C_2}{r^2}(1-2\nu) + \nu\epsilon_z - (1+\nu)\alpha T\right] \\
\sigma_t &= K\left[C_1 + \frac{C_2}{r^2}(1-2\nu) + \nu\epsilon_z - (1+\nu)\alpha T\right] \qquad \text{(A63)} \\
\sigma_z &= K\left[C_1 \cdot 2\nu + (1-\nu)\epsilon_z - (1+\nu)\alpha T\right] \\
\epsilon_t &= C_1 + \frac{C_2}{r^2} \qquad \epsilon_r = C_1 - \frac{C_2}{r^2}
\end{aligned}$$

From equation (A63) it can be seen that σ_z is not a function of composite radius within each particular component. Hence, the intergration of equation (A62) can be replaced as follows:

$$\sum_{i=0}^{N} \left(\frac{r_i^2 - r_{i-1}^2}{r_N^2}\right) \sigma_z^i = 0 \qquad \text{(A64)}$$

Substituting σ_z of equation (A63) into (A64) for each component results in

$$\sum_{i=0}^{N} \left(\frac{r_i^2 - r_{i-1}^2}{r_N^2} \right) K_i \left[2\nu \; C_1^i + (1-\nu)\epsilon_z - (1+\nu_i)\alpha_i T \right] = 0 \qquad \text{(A65)}$$

This equation represents one of the 2N+3 equations necessary for the solution of the problem. It is the only one which is different from the development of Appendix II for axial loading.

Applying boundary requirement number one of Appendix II (which states that the radial displacements have to be continuous at the interfaces) results in a set of N equations identical to equation (A29),

$$C_1^i \cdot r_i + \frac{C_2^i}{r_i} = C_1^{i+1} r_i + \frac{C_2^{i+1}}{r_i} \quad \text{for} \quad i=0,1,\ldots\ldots\ldots N-1 \qquad \text{(A66)}$$

Application of the second requirement that the radial stresses be continuous at the components interfaces specifies

$$\sigma_r^i = \sigma_r^{i+1} \qquad \text{at } r_i \text{ for } i=0,1,\ldots.N$$

where (as in Appendix II) σ_r^{N+1} is equal to zero. Substitution of σ_r of equation (A63) into this relation for each component results in the following set of N+1 equations:

$$K_i \; C_1^i - K_{i+1} C_1^{i+1} - \frac{1}{r_i^2} \left[K_i (1-2\nu_i) C_2^i - K_{i+1} (1+2\nu_{i+1}) C_2^{i+1} \right]$$

$$- \epsilon_z \left[K_{i+1} \cdot \nu_{i+1} - K_i \nu_i \right] = T \left[K_i \alpha_i (1+\nu_i) - \right. \qquad \text{(A67)}$$

$$\left. K_{i+1} \alpha_{i+1} (1+\nu_{i+1}) \right] \qquad \text{for } i=0,1,\ldots.N$$

Application of requirement three of finite displacements results in the same equation as (A34),

$$C_2^o = 0 \tag{A68}$$

Equations (A65-68) represent 2N+3 simultaneous equations in the 2N+3 unknown constants C_1^i, C_2^i and ϵ_z (for i=0,1,.....N). Their simultaneous solution and back substitution into equation (A63) gives the entire stress and strain distribution in the composite cylinder upon changing the temperature from some arbitrary reference temperature to temperature T.

It is important to note that in general all the elastic and physical constants of equations (A63) can be functions of temperature. In such a case, the appropriate function would simply replace the elastic or physical constant in equation (A63) and in all the boundary condition equations.

To obtain a numerical solution to the above problem for the case of constant elastic and physical properties, the method of Gaussian elimination is applied to the 2N+3 simultaneous equations. Again for computational convenience, as in Appendix II, the following bookkeeping changes are made:

$$\begin{aligned} C_1^i &= C_{2i+1} \\ C_2^i &= C_{2i+2} \\ \epsilon_z &= C_{2i+3} \end{aligned} \tag{A69}$$

Substitution of equation (A69) into the boundary condition equations of (A65-68) results in a system of equations similar to that presented in equation (A35) of Appendix II. Solution is achieved in a manner identical to that of Appendix II. Table 10 represent the matrices [A] and [B] for the temperature loading problem for a composite of 4 rings in the case material. Note that matrix [A] now has dimensions of 2N+3 by 2N+3 and matrix [B] is a column matrix with 2N+3 entries.

Close examination of Tables 9 and 10 shows that if T=0 and ϵ_z is a known constant, the column a_1, 2N+3 becomes the matrix [B] and Tables 9 and 10 coincide.

[A]											[B]
0	1	0	0	0	0	0	0	0	0	0	0
r_0	0	$-r_0$	$-r_0^{-1}$	0	0	0	0	0	0	0	0
0	0	r_1	r_1^{-1}	$-r_1$	$-r_1^{-1}$	0	0	0	0	0	0
0	0	0	0	r_2	r_2^{-1}	$-r_2$	$-r_2^{-1}$	0	0	0	0
0	0	0	0	0	0	r_3	r_3^{-1}	$-r_3$	$-r_3^{-1}$	0	0
K_0	0	$-K_1$	$\frac{K_1(1-2\nu_1)}{r_0^2}$	0	0	0	0	0	0	$K_0\nu_0 - K_1\nu_1$	$T[K_0(1+\nu_0)\alpha_0 - K_1(1+\nu_1)\alpha_1]$
0	0	K_1	$\frac{-K_1(1-2\nu_1)}{r_1^2}$	$-K_2$	$\frac{K_2(1-2\nu_2)}{r_1^2}$	0	0	0	0	$K_1\nu_1 - K_2\nu_2$	$T[K_1(1+\nu_1)\alpha_1 - K_2(1+\nu_2)\alpha_2]$
0	0	0	0	K_2	$\frac{-K_2(1-2\nu_2)}{r_2^2}$	$-K_3$	$\frac{K_3(1-2\nu_3)}{r_2^2}$	0	0	$K_2\nu_2 - K_3\nu_3$	$T[K_2(1+\nu_2)\alpha_2 - K_3(1+\nu_3)\alpha_3]$
0	0	0	0	0	0	K_3	$\frac{-K_3(1-2\nu_3)}{r_3^2}$	$-K_4$	$\frac{K_4(1-2\nu_4)}{r_3^2}$	$K_3\nu_3 - K_4\nu_4$	$T[K_3(1+\nu_3)\alpha_3 - K_4(1+\nu_4)\alpha_4]$
0	0	0	0	0	0	0	0	K_4	$\frac{-K_4(1-2\nu_4)}{r_4^2}$	$K_4\nu_4$	$T[K_4(1+\nu_4)\alpha_4]$
$2\nu_0 K_0 \cdot (r_0^2 - r_{-1}^2)$	0	$2\nu_1 K_1 \cdot (r_1^2 - r_0^2)$	0	$2\nu_2 K_2 \cdot (r_2^2 - r_1^2)$	0	$2\nu_3 K_3 \cdot (r_3^2 - r_2^2)$	0	$2\nu_4 K_4 \cdot (r_4^2 - r_3^2)$	0	$K_0(1-\nu_0)(r_0^2 - r_{-1}^2) + K_1(1-\nu_1)(r_1^2 - r_0^2) + K_2(1-\nu_2)(r_2^2 - r_1^2) + K_3(1-\nu_3)(r_3^2 - r_2^2) + K_4(1-\nu_4)(r_4^2 - r_3^2)$	$K_0(1+\nu_0)\alpha_0 T(r_0^2 - r_{-1}^2) + K_1(1+\nu_1)\alpha_1 T(r_1^2 - r_0^2) + K_2(1+\nu_2)\alpha_2 T(r_2^2 - r_1^2) + K_3(1+\nu_3)\alpha_3 T(r_3^2 - r_2^2) + K_4(1+\nu_4)\alpha_4 T(r_4^2 - r_3^2)$

TABLE 10

Coefficient Matrices for the Elasticity Solution of a Composite Cylinder for Thermal Loading (N=4)

APPENDIX V

THE TEMPERATURE VARIATION OF MECHANICAL AND PHYSICAL PROPERTIES USED IN THE PLASTICITY ANALYSIS OF THERMAL LOADING

In the temperature range of the thermal loading analysis, there is an appreciable variation of mechanical and physical properties. These variations were included in the analytical predictions of the induced residual stress state during the cooling of composite cylinders.

During the thermal loading process the strains induced were high enough to cause plastic flow in the copper core, but not high enough to cause yielding in either of the case components used in the present study. The property changes necessary to describe the behavior of the 4340 and maraging steels were therefore limited to specifying the temperature variations in E, ν, and α. The copper, on the other hand, needed specification of these properties as well as the change of the entire stress-strain curve with temperature.

All property data as a function of temperature were obtained from the available literature. Examination of the available data revealed that it was possible, without introducing appreciable error, to approximate all properties to be linear functions of temperature. Hence the elastic modulus, for instance, can be represented by the following relation:

$$E = E_{RT} + C_E \, (T - T_{RT})$$

where E represents the modulus at a given temperature T, E_{RT} represents the room temperature modulus, C_E the rate of change of the modulus with temperature, and T_{RT} the room temperature. Similar relations were assumed to hold for ν and α.

All room temperature properties were experimentally determined in this study. The rate of change of these properties were taken from the available literature and they are presented in Table 1 for the base components utilized in this study.

Characterization of the plastically behaving copper core properties with temperature is more difficult. For all thermal loading problems the room temperature stress-strain curve is approximated by three linear regions as shown in Figure 10.

Characterization of the temperature variation of this curve was based on experimental data presented in References [55] and [56] It is accomplished by approximating the strain limits of each region and the slopes of each region as linear functions of temperature. The slope of the first region is the elastic modulus and its variation has already been specified in Table 1. The strain limit of the first relation represents the elastic strain limit. Its variation with temperature along with those of the slopes of the other regions is presented in Table 11. The resulting stress-strain curve for various temperatures is presented in Figure 10.

TABLE 11

PROPERTY CHANGES WITH TEMPERATURE
FOR OFHC COPPER

Material	Linear Rate Of Change of Elastic Strain Limit with Temperature	Linear Rate of Change of Slope B_1 with Temperature	Linear Rate of Change of Slope B_2 with Temperature
OFHC Copper	-2.0×10^{-7} in/in/^{o}F	-3.125×10^{3} psi/^{o}F	-3.51×10^{2} psi/^{o}F

APPENDIX VI

RESIDUAL STRESS CHANGES DURING MACHINING

During the fabrication of a composite cylinder residual stresses are induced during cooling as result of the difference in thermal expansion coefficients between the case and the core components. These residual stresses can be calculated by the approximate analytical method described in Section III. The calculation of the stresses is based on the radius r=b of Figure 159 which is 0.010" greater than the final test section diameter f. Removal of the material from radius b to f results in a change of the original stress distribution. The objective of this section is development of relations with which to determine the stresses removed during the machining operation. The calculation of these stresses will be based on knowledge of the residual stress distribution existing in the composite prior to machining.

Removal of the external layer by machining relieves the axial stress in the case. The stress change must be redistributed over the remaining composite. The residual stresses relieved by the machining action are therefore equivalent to the stresses induced if the remaining composite would be subjected to an axial force of $-\int_b^f \sigma_z^* \, r \, dr$, where σ_z^* is the axial stress initially present in the case at r=f. σ_z^* is known from the temperature loading analysis.

Machining also relieves the radial tension at r=f, designated as σ_r^*. The residual stresses removed by this machining action are equivalent to the stresses induced in the remaining composite under an external pressure of σ_r^*.

All the stresses relieved in the composite during machining can therefore be found by solving the composite cylinder problem (with the outside radius equal to f) for the case of an imposed axial force of $F = \int_f^b \sigma_z^* \, r \, dr$ and external pressure of σ_r^* at r=f.

Solution to this problem is similar to that developed for axial loading of a composite with N+1 components in Appendix II. In this situation, there are only two components, the core with r=a and case with r=f (see Figure 159). All initial assumptions are identical. The governing differential equation (A26) is the same and hence the solution in terms of the radial displacement is the same, i.e.,

$$U_i = C_1^i \, r + \frac{C_2^i}{r} \qquad \text{(A70)}$$

The boundary conditions are not identical. For the present problem they are given by

$$\begin{aligned}
&\text{a. } U < \infty \\
&\text{b. } U_0 = U_1 \qquad \text{at } r=a \\
&\text{c. } \sigma_r^0 = \sigma_r^1 \qquad \text{at } r=a \\
&\text{d. } \sigma_r = \sigma_r^* \qquad \text{at } r=f \\
&\text{e. } \int_0^a \sigma_z^0\, r\,dr + \int_a^f \sigma_z^1\, r\,dr = -\int_f^b \sigma_z^*\, r\,dr
\end{aligned} \tag{A71}$$

The first three of these are the same as those in Appendix II. The last two, however, are governed by the new conditions of an effective external pressure and axial force.

The equations relating the stresses to the constants $C_1^{\,i}$ and $C_1^{\,i}$ are given by equation (A32). Substitution of these equations into the above conditions permits the expression of the boundary conditions in terms of the unknown constants. Boundary condition (a) requires

$$C_2^0 = 0 \tag{A72}$$

Boundary condition (b) results in the following equation:

$$C_1^0 a = C_1^1 a + \frac{C_2^1}{a} \tag{A73}$$

application of condition (c) requires

$$K_0\left[C_1^0 + \nu_0 \epsilon_z\right] = K_1\left[C_1^1 - (1-2\nu_1)\frac{C_2^1}{a^2} + \nu_1 \epsilon_z\right]$$

$$K_0 C_1^0 - K_1 C_1^1 + (1-2\nu_1)\frac{K_1}{a^2} C_2^1 + \epsilon_z(K_0 \nu_0 - K_1 \nu_1) = 0 \tag{A74}$$

or

Condition (d) requires that

$$\sigma_r^I = \sigma_r^* \qquad \text{at } r=f$$

Hence

$$K_1 \left[C_1^I - (1-2\nu_1) \frac{C_2^I}{f^2} + \nu_1 \epsilon_z \right] = \sigma_r^*$$

and

$$C_1^I - \left(\frac{1-2\nu_1}{f^2}\right) C_2^I + \nu_1 \epsilon_z = \frac{\sigma_r^*}{K_1} \qquad \text{(A75)}$$

Condition (e) can be simplified by the fact that the axial stresses in the core and case upon thermal loading are not a function of radius. Hence condtion (e) becomes

$$\sigma_z^0 \; a^2 + \sigma_z^I (f^2 - a^2) = -\sigma_z^* (b^2 - f^2)$$

and substitution of σ_z from equation (A32) results in the following expression:

$$K_0 a^2 \left[2\nu_0 C_1^0 + (1-\nu_0) \epsilon_z \right] + K_1 (f^2 - a^2) \left[2\nu_1 C_1^I + (1-\nu_1) \epsilon_z \right]$$

$$= - \sigma_z^* (b^2 - f^2)$$

or

$$2K_0 a^2 \nu_0 C_1^0 + 2K_1 (f^2 - a^2) \nu_1 C_1^I + \epsilon_z \left[K_0 a^2 (1-\nu_0) - \right.$$

$$\left. K_1 (f^2 - a^2)(1-\nu_1) \right] = - \sigma_z^* (b^2 - f^2) \qquad \text{(A76)}$$

Equations (A72-76) represent five equations with five unknowns (C_1^i, C_1^i, ϵ_z for i=0,1). Solution of these equations can now be obtained by the Gaussian elimination method described in Appendix II. Making the following notation changes

$$C_1^i = C_{2i+1}$$

$$C_2^i = C_{2i+2}$$

$$\epsilon_z = C_{2i+3}$$

allows the matrices [A] and [B], defined in Appendix II, to be determined. Note that, as in the case of thermal loading in Appendix IV, the matrix [A] includes the coefficients of the axial strain term ϵ_z because it is also an unknown. The matrices [A] and [B] are presented in Table 12.

Upon solution of all constants, the stresses and strains relieved in the case and core during machining can be calculated by substituting the calculated constants into equation (A32) of Appendix II.

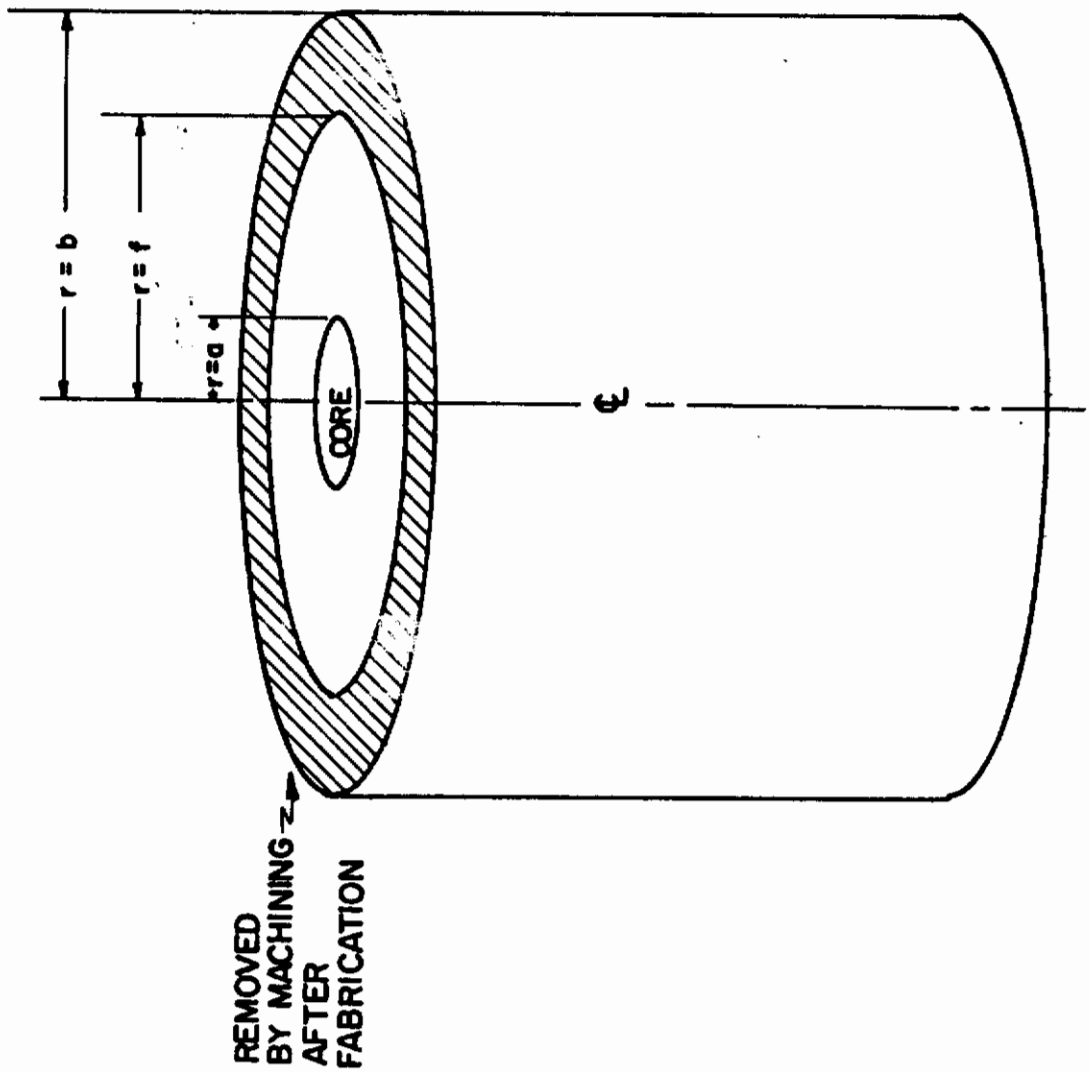

Figure 159

Composite Cylinder Showing the Dimensions Before and After Machining.

[A]

0	1	0	0	0
a	0	$-a$	$-a^{-1}$	0
0	0	1	$\frac{-(1-2z_1)}{f^2}$	z_1
K_0	0	$-K_1$	$K_1\left(\frac{1-2z_1}{a^2}\right)$	$K_0 z_0 - K_1 z_1$
$2K_0 v_0 a^2$	0	$2K_1 v_1 (f^2-a^2)$	0	$K_0(1-z_0)a^2 - K_1(1-z_1)(f^2-a^2)$

[B]

0
0
$\frac{\sigma_r^*}{K_1}$
0
$-(b^2-f^2)\sigma_z^*$

TABLE 12

Coefficient Matrices for the Elasticity Solution of a Composite Cylinder Subject to Removal of Material by Machining

APPENDIX VII

COMPUTATION OF SURFACE TANGENTIAL STRESSES

The computation of the surface tangential stresses from the measured values of ϵ_z and ϵ_θ for the double-concentric model composites requires the consideration of plastic deformations as well as elastic since the composites were strained until all components deformed plastically. Since the strains were measured on the case component, this analysis applied only to that component.

The analytical procedure reviewed here utilizes the method of successive elastic solutions as described in detail by Mendelson [3]. The form of the stress-strain equations includes plastic strain contributions:

$$\epsilon_z = \frac{1}{E}\left[\sigma_z - \nu\,(\sigma_r + \sigma_\theta)\right] + \epsilon_z^p + \Delta\epsilon_z^p$$

$$\epsilon_r = \frac{1}{E}\left[\sigma_r - \nu\,(\sigma_z + \sigma_\theta)\right] + \epsilon_r^p + \Delta\epsilon_r^p \qquad \text{(A77)}$$

$$\epsilon_\theta = \frac{1}{E}\left[\sigma_\theta - \nu\,(\sigma_z + \sigma_r)\right] + \epsilon_\theta^p + \Delta\epsilon_\theta^p$$

where ϵ_z^p, ϵ_r^p, and ϵ_θ^p are total plastic strains up to a current loading increment, and $\Delta\epsilon_z^p$, $\Delta\epsilon_r^p$, and $\Delta\epsilon_\theta^p$ are the plastic strain increments due to the current increment of loading.

These plastic strain increments are related to the stresses through the Prandtl-Reuss relations

$$\Delta\epsilon_z^p = \frac{\Delta\epsilon_p}{2\bar{\sigma}}\,(2\sigma_z - \sigma_r - \sigma_\theta)$$

$$\Delta\epsilon_\theta^p = \frac{\Delta\epsilon_p}{2\bar{\sigma}}\,(2\sigma_\theta - \sigma_r - \sigma_z) \qquad \text{(A78)}$$

$$\Delta\epsilon_r^p = \frac{\Delta\epsilon_p}{2\bar{\sigma}}\,(2\sigma_r - \sigma_z - \sigma_\theta)$$

where

$$\Delta\epsilon_p = \frac{\sqrt{2}}{3}\left[(\Delta\epsilon_z^p - \Delta\epsilon_r^p)^2 + (\Delta\epsilon_r^p - \Delta\epsilon_\theta^p)^2 + (\Delta\epsilon_\theta^p - \Delta\epsilon_z^p)^2\right]^{1/2} \quad \text{(A79)}$$

and

$$\bar{\sigma} = \frac{1}{\sqrt{2}}\left[(\sigma_z - \sigma_r)^2 + (\sigma_r - \sigma_\theta)^2 + (\sigma_\theta - \sigma_z)^2\right]^{1/2} \quad \text{(A80)}$$

Rewriting equations (A77) in terms of stresses,

$$\sigma_z = \lambda(\epsilon_r + \epsilon_\theta + \epsilon_z) + 2\mu(\epsilon_z - \epsilon_z^p - \Delta\epsilon_z^p) \quad \text{(A81)}$$

$$\sigma_r = \lambda(\epsilon_r + \epsilon_\theta + \epsilon_z) + 2\mu(\epsilon_r - \epsilon_r^p - \Delta\epsilon_r^p) \quad \text{(A82)}$$

$$\bar{\sigma}_\theta = \lambda(\epsilon + \epsilon_\theta + \epsilon_z) + 2\mu(\epsilon_\theta - \epsilon_\theta^p - \Delta\epsilon_\theta^p) \quad \text{(A83)}$$

where

$$\lambda = \frac{\nu E}{(1+\nu)(1-2\nu)}$$

$$\mu = \frac{E}{2(1+\nu)}$$

The surface radial stress must be zero, which allows the evaluation of the unmeasured surface radial strain in terms of the two measured strains and its plastic contribution,

$$\epsilon_r = 2\mu(\epsilon_r^p + \Delta\epsilon_r^p) - \frac{\lambda(\epsilon_\theta + \epsilon_z)}{\lambda + 2G} \quad \text{(A84)}$$

Now, provided that the values of the plastic strains are known, the surface stresses σ_z and σ_θ may be computed from equations (A81) and (A83). If the surface stresses are below the yield point, the values of the plastic strains are zero and the stresses are computed directly. If, however, the effective stress $\bar{\sigma}$ is above the yield stress then the iteration method of successive elastic solutions is used. In this method, values of the incremental plastic strains ($\Delta\epsilon_r^p$, $\Delta\epsilon_\theta^p$, and $\Delta\epsilon_z^p$) are assumed for the first iteration. The stresses are computed from equations (A81) - (A83), and $\Delta\epsilon_p$ is determined from equation (A79). A value of $\bar{\sigma}$ is determined from the stress-strain curve; a new set of incremental plastic strains

may be determined from equations A78. These new values of incremental strains allow the above computational procedure to be followed once again, with the resulting stresses and strains closer to the correct value.

This process is continued until convergence is obtained; i.e., until two successive sets of strain increments are less than some prescribed value.

A computer program was prepared to conduct the required calculations described above. Values of surface strains, ϵ_z and ϵ_θ were determined experimentally at various axial loads, and the corresponding surface stresses computed for each increment. The plastic strain-hardening curves were evaluated as fifth order polynominals which permitted the accurate determination of the effective stress from the effective strains. The iteration process was terminated when successive strain increments were within a value 10^{-9} in/in.

UNCLASSIFIED

Security Classification

DOCUMENT CONTROL DATA - R&D

(Security classification of title, body of abstract and indexing annotation must be entered when the overall report is classified)

1. ORIGINATING ACTIVITY *(Corporate author)* Case Western Reserve University University Circle Cleveland, Ohio 44106	2a. REPORT SECURITY CLASSIFICATION Unclassified 2b. GROUP

3. REPORT TITLE

Analytical Approach to Composite Behavior

4. DESCRIPTIVE NOTES *(Type of report and inclusive dates)*

Summary Technical Report

5. AUTHOR(S) *(Last name, first name, initial)*

L.J. Ebert, R.J. Fedor, C.H. Hamilton, S. S. Hecker, P.K. Wright

6. REPORT DATE	7a. TOTAL NO. OF PAGES	7b. NO. OF REFS
March 1969	283	56

8a. CONTRACT OR GRANT NO. F33615-67-C-1487 b. PROJECT NO. 7353 c. Task No: 735301 d.	9a. ORIGINATOR'S REPORT NUMBER(S) 9b. OTHER REPORT NO(S) *(Any other numbers that may be assigned this report)* AFML-TR-69-129

10. AVAILABILITY/LIMITATION NOTICES This document is subject to special export controls and each transmittal to foreign governments or foreign nationals may be made only with prior approval of the Metals and Ceramics Division (MAMS), Air Force Materials Laboratory, Wright-Patterson AFB, Ohio 45433

11. SUPPLEMENTARY NOTES	12. SPONSORING MILITARY ACTIVITY
	AFML (MAMS) Wright-Patterson AFB, Ohio 45433

13. ABSTRACT The applicability of the binary composite model has been completely generalized for any combination and arrangement of materials. This refinement has eliminated the previous restriction where only composite cylinders in which the core member would yield before the case member could be treated analytically. It was found that the residual stresses in the composite induced during cooling from fabrication temperatures needed to be analyzed and incorporated into subsequent axial loading predictions. The residual stresses, which result from dissimilar thermal expansions of the components of composites, were predicted analytically and compared to the experimentally determined values for OFHC copper core with a 4340 steel case and OFHC copper core with a maraging steel case. The effect of tensile prestraining on the residual stress states and on subsequent stress-strain behavior of binary composites and tungsten-copper filamentary composites was experimentally investigated and analytically predicted. The fabrication-induced residual stresses were sufficiently altered to cause a substantial rise in the tensile flow stress curves upon reloading. Prestrains into the elastic-plastic behavioral region were emphasized. A double concentric model was developed to assess the seriousness of the presence of an unconstrained outer surface of the models. The double concentric model can also be used to predict the behavior under axial loading of composites which contain an interaction layer or diffusion protection coating at the fiber-matrix interface. This model has been developed for both elastic and strain-hardening plastic deformation in the components of the composites. Presentation of experimental data (of double-concentric model composites) completes the verification of this approach. The elastic response of a two component composite cylinder uniformly

DD FORM 1 JAN 64 1473

Unclassified

Security Classification

14. KEY WORDS	LINK A		LINK B		LINK C	
	ROLE	WT	ROLE	WT	ROLE	W
1. Fiber Composites						
2. Rheological Interactions						
3. Metal Matrix						
4. Plasticity Analysis						
5. Micromechanics						
6. Residual Stresses						
7. Tungsten Filaments						
8. Discontinuous Fibers						
9. Prestraining						

INSTRUCTIONS

1. ORIGINATING ACTIVITY: Enter the name and address of the contractor, subcontractor, grantee, Department of Defense activity or other organization *(corporate author)* issuing the report.

2*a*. REPORT SECURITY CLASSIFICATION: Enter the overall security classification of the report. Indicate whether "Restricted Data" is included. Marking is to be in accordance with appropriate security regulations.

2*b*. GROUP: Automatic downgrading is specified in DoD Directive 5200.10 and Armed Forces Industrial Manual. Enter the group number. Also, when applicable, show that optional markings have been used for Group 3 and Group 4 as authorized.

3. REPORT TITLE: Enter the complete report title in all capital letters. Titles in all cases should be unclassified. If a meaningful title cannot be selected without classification, show title classification in all capitals in parenthesis immediately following the title.

4. DESCRIPTIVE NOTES: If appropriate, enter the type of report, e.g., interim, progress, summary, annual, or final. Give the inclusive dates when a specific reporting period is covered.

5. AUTHOR(S): Enter the name(s) of author(s) as shown on or in the report. Enter last name, first name, middle initial. If military, show rank and branch of service. The name of the principal author is an absolute minimum requirement.

6. REPORT DATE: Enter the date of the report as day, month, year; or month, year. If more than one date appears on the report, use date of publication.

7*a*. TOTAL NUMBER OF PAGES: The total page count should follow normal pagination procedures, i.e., enter the number of pages containing information.

7*b*. NUMBER OF REFERENCES: Enter the total number of references cited in the report.

8*a*. CONTRACT OR GRANT NUMBER: If appropriate, enter the applicable number of the contract or grant under which the report was written.

8*b*, 8*c*, & 8*d*. PROJECT NUMBER: Enter the appropriate military department identification, such as project number, subproject number, system numbers, task number, etc.

9*a*. ORIGINATOR'S REPORT NUMBER(S): Enter the official report number by which the document will be identified and controlled by the originating activity. This number must be unique to this report.

9*b*. OTHER REPORT NUMBER(S): If the report has been assigned any other report numbers *(either by the originator or by the sponsor)*, also enter this number(s).

10. AVAILABILITY/LIMITATION NOTICES: Enter any limitations on further dissemination of the report, other than those imposed by security classification, using standard statements such as:

(1) "Qualified requesters may obtain copies of this report from DDC."

(2) "Foreign announcement and dissemination of this report by DDC is not authorized."

(3) "U. S. Government agencies may obtain copies of this report directly from DDC. Other qualified DDC users shall request through _____."

(4) "U. S. military agencies may obtain copies of this report directly from DDC. Other qualified users shall request through _____."

(5) "All distribution of this report is controlled. Qualified DDC users shall request through _____."

If the report has been furnished to the Office of Technical Services, Department of Commerce, for sale to the public, indicate this fact and enter the price, if known.

11. SUPPLEMENTARY NOTES: Use for additional explanatory notes.

12. SPONSORING MILITARY ACTIVITY: Enter the name of the departmental project office or laboratory sponsoring *(paying for)* the research and development. Include address.

13. ABSTRACT: Enter an abstract giving a brief and factual summary of the document indicative of the report, even though it may also appear elsewhere in the body of the technical report. If additional space is required, a continuation sheet shall be attached.

It is highly desirable that the abstract of classified reports be unclassified. Each paragraph of the abstract shall end with an indication of the military security classification of the information in the paragraph, represented as *(TS)*, *(S)*, *(C)*, or *(U)*.

There is no limitation on the length of the abstract. However, the suggested length is from 150 to 225 words.

14. KEY WORDS: Key words are technically meaningful terms or short phrases that characterize a report and may be used as index entries for cataloging the report. Key words must be selected so that no security classification is required. Identifiers, such as equipment model designation, trade name, military project code name, geographic location, may be used as key words but will be followed by an indication of technical context. The assignment of links, rules, and weights is optional.

13. ABSTRACT
loaded along its axis was compared analytically to a corresponding hexagonal fiber composite element. The analytical comparison of the elastic behavior of the composite elements provided justification and identified limitations for the use of the cylindrical approximation to the hexagonal geometry for the yielding and subsequent plastic deformation of the matrix component. The comparative elastic analysis considered the micro-stress field and its effect on the composite modulus and yielding behavior. Experimental data are given for the study of effects in prototype (50 mil tungsten wires in copper matrix) fiber composites. Composites of both 7 and 19 wires were assembled to represent loose and close packed conditions, with precut discontinuous tungsten wires being included in different numbers and geometric configurations.